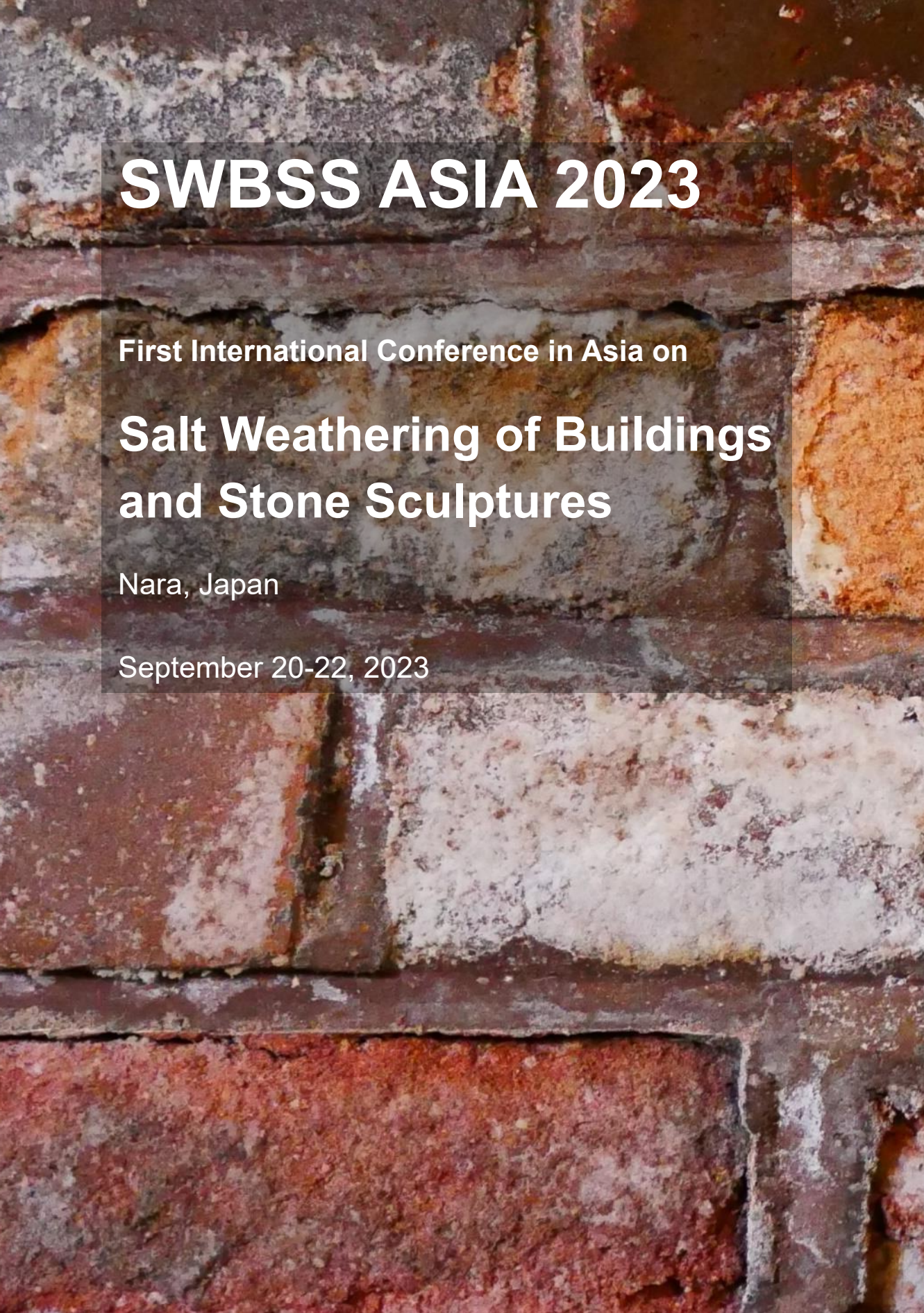

SWBSS ASIA 2023

First International Conference in Asia on

Salt Weathering of Buildings and Stone Sculptures

Nara, Japan

September 20-22, 2023

SWBSS ASIA 2023

First International Conference in Asia on

Salt Weathering of Buildings and

Stone Sculptures

Nara National Research Institute for Cultural Properties
Nara, Japan

September 20-22, 2023

Edited by
Masaru Abuku, Nobumitsu Takatori

Title:
Proceedings of SWBSS ASIA 2023

First International Conference in Asia on
Salt Weathering of Buildings and Stone Sculptures

Nara National Research Institute for Cultural Properties
Nara, Japan

September 20-22, 2023

Editors:
Masaru Abuku
Nobumitsu Takatori

Publisher:
SWBSS ASIA 2023 Organizing Committee
Kowakae 3-4-1, Higashi-Osaka, 577-8502 Osaka, Japan
Laboratory of Building Physics, Faculty of Architecture, Kindai University

Cover design:
Kiln Plaza, INAX MUSEUMS, photographed by Masaru Abuku

ISBN 978-4-600-01329-5

Preface

Welcome to Japan and SWBSS ASIA 2023!

SWBSS is the conference series “Salt Weathering of Buildings and Stone Sculptures,” started in 2008. The past series were held in Copenhagen (2008), Limassol (2011), Brussel (2014), Potsdam (2017), and Delft (2021). The conference aims at bringing together conservators, restorers, engineers, architects, academics, students and experienced researchers to contribute thereby to the promotion of research and development within the field of salt weathering of porous materials. So far this conference series has been held only in European countries. However, research of salt weathering of porous materials is becoming more and more important worldwide. This is because this complex weathering phenomenon is seen in various locations and this research field specifically requires interdisciplinary research. I believe that these aspects of salt weathering will certainly lead to advancing the new frontier for different research fields, which will finally result in a better solution to weathering of porous materials. For such reasons, an idea of SWBSS ASIA as a conference series to be held in Asian countries was proposed in Potsdam, Germany, in 2017. The first meeting in Asia, SWBSS ASIA 2023, was announced in Delft, the Netherlands, in 2021. I am very glad that we received around 30 contributions, consisting of full papers and extended abstracts, from 10 countries. This clearly confirms the relevance of the conference.

This event would have never been possible without the collaboration of many experts. I would like to thank the international scientific committee members for the time to review submitted manuscripts, which ensured the scientific quality of the proceedings. A special thanks should also go to the local organizing committee members who largely contributed to preparation of the conference.

Last but not least, I would like to express my deepest gratitude to The Kajima Foundation, The Kyoto University Foundation, Mitsuwa Frontech Corp., and Research Center of Computational Mechanics, Inc. for the financial support, and Kindai University, Kyoto University, Mukogawa Women’s University, Nara National Research Institute for Cultural Properties, and Nara Visitors Bureau for the support.

I sincerely hope you will enjoy the conference!

Masaru Abuku
Conference Chair, SWBSS ASIA 2023
Faculty of Architecture, Kindai University

International Scientific Committee

Hannelore Derluyn, CNRS, France
Sebastiaan Godts, Royal Institute for Cultural Heritage, Brussels (IRPA / KIK), Belgium
Shuichi Hokoi, Kyoto University, Japan
Takeshi Ishizaki, Tohoku University of Art and Design, Japan
Yonghui Li, Southeast University, China
Barbara Lubelli, Delft University of Technology, The Netherlands
Hongjie Luo, Shanghai University, China
Yukinori Matsukura, University of Tsukuba, Japan
Inge Rörig-Dalgaard, Technical Univeristy of Denmark, Denmark
Masato Sato, National Research Institute for Earth Science and Disaster Resilience, Japan
Michael Steiger, University of Hamburg, Germany
Magdalini Theodoridou, Newcastle University, UK

Organizing Committee

Masaru Abuku, Kindai University
Chiaki Oguchi, Saitama University
Daisuke Ogura, Kyoto University
Nobumitsu Takatori, Kyoto University
Tomoko Uno, Mukogawa Women's University
Soichiro Wakiya, Nara National Research Institute for Cultural Properties

Financial Sponsor

The Kajima Foundation
The Kyoto University Foundation
Mitsuwa Frontech Corp.
Research Center of Computational Mechanics, Inc.

Sponsor

Kindai University
Kyoto University
Mukogawa Women’s University
Nara National Research Institute for Cultural Properties
Nara Visitors Bureau

Table of contents

2. LABORATORY INVESTIGATIONS AND EXPERIMENTAL TECHNIQUES

SOLUBLE SALTS IN BUILDING MATERIALS: FROM SAMPLING TO INTERPRETATION

Michael Steiger[1]

KEYWORDS

Sources of salts, salt mobility, salt mixtures, modeling

1 INTRODUCTION

Soluble salts are commonly present in natural rocks and soils but also in building materials, e.g. natural stone, brick or concrete. Most of these salts are highly soluble and hygroscopic. Depending on the environmental conditions they may be present in a porous material in dissolved form as pore solution and are then subject to transport. Under dry conditions, as water evaporates from the pore solution, salts may crystallize out and form efflorescences (on the surface) or subflorescences (within the pore space). Other relevant phase changes apart from evaporation–condensation at the air–solution interface and crystallization–dissolution at the crystal–solution interface are changes of the state of hydration of salts and the crystallization of ice, i.e. the freeze–thaw equilibrium (Figure 1).

The pressure generated by crystal growth of salts in confined spaces of porous building materials such as stone, brick and concrete is generally recognized as a major cause of damage in ancient monuments and modern buildings [1]. Crystal growth in porous materials is the result of phase changes that are induced by variation of ambient temperature and relative humidity, RH. Unfavorable conditions of temperature and RH may result in repeated cycles of crystallization–deliquescence, hydration–dehydration and freezing–thawing, respectively. Under such conditions, building materials and natural rocks are subject to rapid decay.

The relevant phases involving single salts are well characterized and it is easy to predict unfavorable climatic conditions that might accelerate salt damage processses. However, contamination of buildings or sculptures with just one salt is very uncommon. Usually, objects are contaminated with complex salt mixtures that are also subject to complex transport processes and permanent interaction with the environment. In this contribution we try to discuss briefly appropriate analytical

[1] University of Hamburg, Department of Chemistry
Michael.Steiger@uni-hamburg,de

and data evaluation approaches in order to predict the behavior of complex salt mixtures and the dynamics of the damage process.

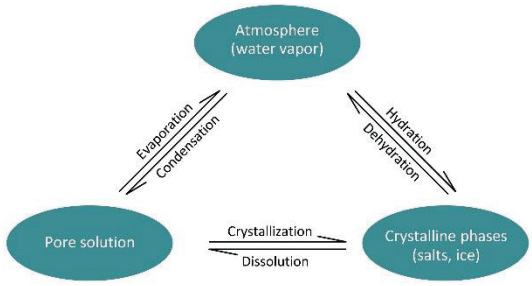

Figure 1: Phase Equilibria in porous materials (reference [1] modified).

2 SOURCES OF SALTS

Deposition of acidic air pollutants is an important source of salt enrichment in building materials. The major anions associated with atmospheric acid-forming species are sulfate and nitrate. Therefore, the processes described in the previous section lead to the enrichment of sulfates and nitrates of calcium in the case of mortars and calcitic stones, as well as those of sodium, potassium, and magnesium in the case of other stone materials. In addition to these salts formed through chemical reactions, there is also a direct input of salts from the atmosphere. For example, in a marine environment, sea salt is present in the atmosphere. On a global scale, emissions of sea salt droplets ejected from the oceans are considered as one of the most important primary sources of the atmospheric aerosol particles. Sea salt particles will undergo both wet and dry deposition, the major processes leading to their enrichment in building materials.

Another very important source of salts in buildings is ground moisture carried into masonry by rising damp in the absence of damp-proof coursing. Considering a structure in hydraulic contact with the saturated ground, water is absorbed and slowly moves upwards in the wall. Above ground level, the wall is subject to evaporation, and rising damp is a result of the competition between the rate of capillary absorption and the evaporation rate [2]. While water can leave the structure by evaporation, the salts dissolved in the water infiltrating a wall remain there and accumulate. The major constituents of natural ground and surface waters that can penetrate building materials are sodium, potassium, magnesium, calcium, chloride, sulfate, and bicarbonate. Additional constituents may be leached from surface soils. For example, nitrate is an important contaminant in surface soils, originating from the use of fertilizers, animal waste, and the oxidation of organic nitrogen.

Other important sources include deicing salts (mainly NaCl, sometimes $MgCl_2$ and $CaCl_2$) and alkaline construction and restoration materials (mainly alkali hydroxides and carbonates). Finally, the former use of a building may lead to specific contaminations like in the case stables (nitrates) or storage houses, e.g. for rock salt (NaCl) or gun powder (KNO_3).

3 MOBILITY AND DISTRIBUTION IN MASONRY

Depending on the nature of the sources, the salt mixtures that are found in building materials are formed by several different ions. Typically, chlorides, nitrates, sulfates, carbonates, and bicarbonates of sodium, potassium, magnesium, and calcium are the most common ones. These salts are commonly referred to as "soluble salts". However, their solubilities differ by orders of magnitude and, consequently, the components of such complex salt mixtures may be either present in dissolved form, i.e. in pore solutions, or as crystalline salts within the pore system. Salts dissolved in a pore solution are subject to capillary transport, for instance, with rising ground moisture or rainwater penetrating the stone. In contrast, crystallized salts are less mobile and may accumulate.

Mobility may be conveniently defined here as the maximum amount of a salt present in a porous material that can just be dissolved if the pore space is completely filled with water. Salt mobilities can be calculated from the concentration and density of the saturated salt solution, and the porosity and density of the porous material. As an example, Figure 2 depicts smoothed values of the mobilities of halite (NaCl) and gypsum ($CaSO_4 \cdot 2H_2O$) as a function of the water accessible pore space of natural building stones. Comparing the mobilities with typical concentrations in buildings, it can be concluded that NaCl in the pore space will be completely dissolved and mobilized in all but the most extreme situations if water penetrates the material, e.g. after a rain shower. In contrast, typical gypsum concentrations in building materials are far exceeding the mobilities shown in Figure 2, frequently by several orders of magnitude. Thus, even if the pore space is completely filled with water only a very small fraction of gypsum can be mobilized. In effect, gypsum tends to be accumulated in crystalline form which is typically resulting in the formation of strong gradients as gypsum remains where it is formed. More soluble salts like NaCl are usually mobile and can be transported with rain water resulting in more even distributions in masonry.

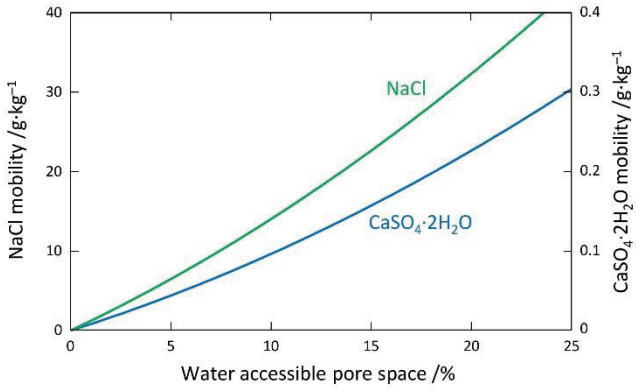

Figure 2: Maximum content of NaCl (halite) and $CaSO_4 \cdot 2H_2O$ (gypsum) that can just be dissolved if the pore space is completely filled with water.

In general, the various sources and pathways of salt infiltration, the mobility of the individual salts, the availability of liquid water for transport (e.g. rain water, surface

or roof run-off waters, rising damp etc.) and the drying behaviour of the materials lead to distinct distributions patterns of salt in masonry with pronounced horizontal and vertical gradients. Some examples are shown in Figure 3.

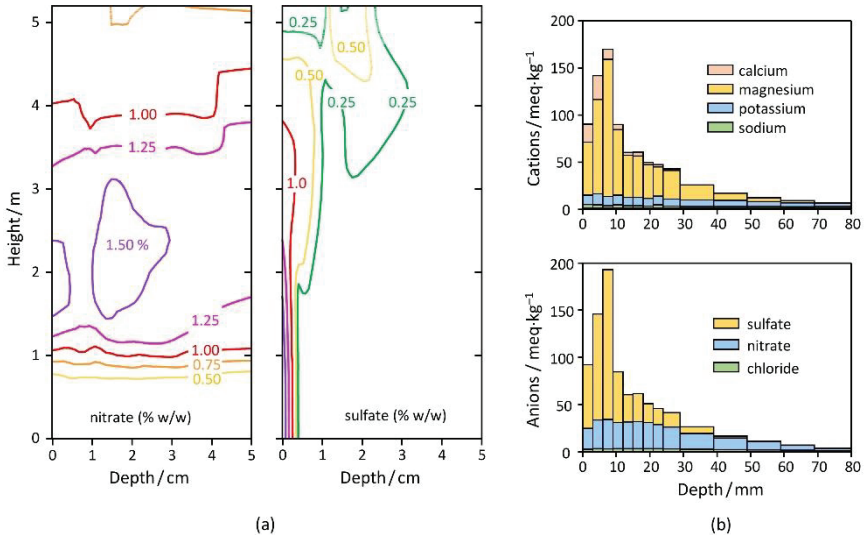

Figure 3: (a) Distribution of sulfate and nitrate in masonry affected by both rising damp and deposition from the atmosphere (Birkenfeld Convent). (b) Depth profile of salts in sandstone masonry with distinct maximum of salt load below the stone surface (Weissenstein Castle, Pommersfelden, modified from reference [1]).

4 ANALYSIS OF SALTS

The dynamics of salt damage in porous materials is largely determined by the interaction of the salt mixture present in the pore space and the surrounding atmosphere, i.e. temperature and relative humidity. Therefore, an analytical approach to characterize the salt contamination of an object has to take into consideration the dynamics of these interactions which requires an analytical strategy. For example, a correctly devised sampling strategy is needed to ensure that the right samples are taken in an appropriate manner. Considering the profiles shown in Figure 3, it is hardly possible to understand the full complexity of the salt systems in these two buildings by just analysing a single surface sample. Therefore, a sampling strategy has to take into account the likely spatial and temporal variability of the object's salt distribution, the construction and condition of the object, and the prevailing environmental conditions.

There are two main strategies that consider the dynamics of salt systems in building materials. The first one is known as the long-term monitoring approach [3,4]. This approach mainly focuses on mapping, monitoring of climatic conditions and observation and non-destructive analysis of salt efflorescences which may then allow to derive appropriate climatic conditions to minimize damage processes. A second approach is based on quantitative analysis of all relevant ions comprising the salt system and the application of chemical equilibrium models (e.g. such as ECOS–RUNSALT) which allow to predict the crystallization pathways even for complex

salt mixtures, and also the environmental conditions for salt phase transitions (e.g. [5]). It is then possible to define for an object the safe ranges of climatic conditions, i.e. temperature and relative humidities, under which salt damage can be avoided or at least minimized.

An example of such a calculation is shown in Figure 4. It is obvious that such a modelling approach is particularly useful as a predictive tool. In instances where other measures to prevent salt damage, e.g. desalination, are not applicable, preventive conservation through environmental control might be the only option to reduce the incidence of salt damage. Following appropriate measurements of the salt contamination of an object, it is possible through careful application of a thermodynamic model to predict the temperature and relative humidity conditions that would minimize the frequency of undesired phase changes inducing crystal growth, and hence damage. In the example shown in Figure 3, typical fluctuations in ambient RH in an outdoor environment (i.e. 50–80 % RH) cause cyclic dissolution and crystallization of KNO_3 and damage has to be expected. Additional crystallization of the other salts only occurs at very low RH. However, although such events are less frequent they may cause severe damage as a large amount of salt crystallizes in a pore space that is already partially filled with niter and gypsum.

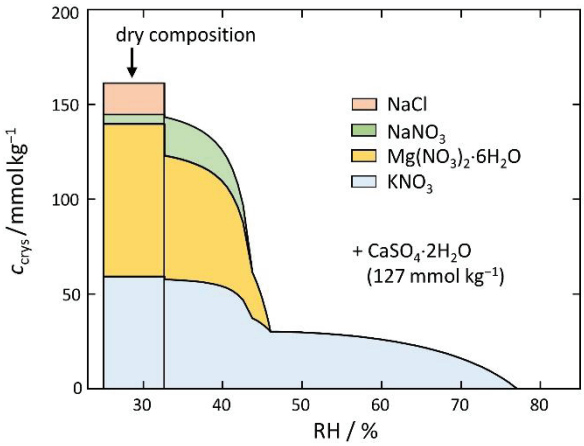

Figure 4: Crystallization pathway at 25 °C of a salt mixture found at Birkenfeld Convent (cf. Figure 3, stone surface at 3 m height) as calculated with an equilibrium model; c_{cryst} is the amount of crystalline solids present in the sample at the respective RH ($CaSO_4 \cdot 2H_2O$ is permanently crystalline).

The successful application of an equilibrium model depends largely on the quality of the input data, which in turn are grossly affected by how the samples are collected, and how they are analyzed. Furthermore, a thermodynamic model requires quantitative analytical measurements, and assumes that from these the composition of the salt mixture is known exactly. The latter assumption is usually not fulfilled as the mixture composition data is based on measurements and is therefore limited by what can be measured, and the accuracy of those measurements. Therefore, the first step in a careful study always has to be a quality check of the input data [6,7].

Though equilibrium models can be extremely useful, there are also limitations that have to be considered. First of all, such models need to be validated. For example, some issues of ECOS–RUNSALT are well known [5]. Second, thermodynamic models assume that the salt–water system is at equilibrium, and as such, the models only predict equilibrium pathways. However, in reality this is not necessarily the case. Kinetic influences can result in the formation of metastable phases (which are less stable than the equilibrium ones, but quicker to form), plus the effects of supersaturation (as crystallisation does not occur precisely at saturation but at some unspecified point beyond) are not accounted for by ECOS–RUNSALT. This however, may be easily overcome in future model generations. For example, thermodynamic models turned out be very useful to calculate metastable crystallization pathways [8,9] or to calculate thermodynamic supersaturations from concentrations in supersaturated solutions [10–12].

Apart from the damage processes triggered by salt crystallization, dissolved salts also strongly influence the water uptake and moisture transport properties of building materials. For instance, due to their hygroscopicity salts strongly affect the sorption isotherm of a material and dissolved salts alter the capillary transport properties, e.g. solution density and viscosity, of the pore liquid. Finally, salts present in crystalline form change the pore structure, i.e. the pore size distribution and the permeability of materials. Therefore, in moisture transport models an accurate representation of the behavior of salts and salt mixtures is required. This includes (1) an appropriate model for the representation of the thermodynamic properties of aqueous pore solutions and (2) the ability to treat the relevant solid–liquid phase equilibria. In principle, the same thermodynamic models used to determine the crystallization sequence can be also used to predict the hygroscopic moisture uptake and moisture saturation. However, such calculations are not provided by ECOS–RUNSALT. Future developments should therefore focus on more flexible programs than currently available. It might also be possible to combine chemical models with humidity and moisture transport models.

REFERENCES

[1] M. Steiger, A.E. Charola, K. Sterflinger, „Weathering and deterioration," In: S. Siegesmund and R. Snethlage, Eds., "Stone in architecture - Properties, Durability", 5th ed. Springer, 2014, pp. 225–316.

[2] C. Hall, W.D. Hoff, „Rising damp: capillary rise dynamics in walls," *Proc. Roy. Soc. A* vol. 463, pp. 1871–1884, 2007.

[3] S. Laue, "Salt weathering of porous structures related to climate changes," *Restor.* Build*. Monum.* vol. 11, pp. 381–390, 2005.

[4] K. Zehnder, "Long-term monitoring of wall paintings affected by soluble salts, *Environ. Geol*. vol. 52, pp. 353–367, 2007.

[5] S. Godts, M. Steiger, S.A. Orr, T. De Kock, J. Desarnaud, H. De Clercq, V. Cnudde, "Modeling Salt Behavior with ECOS/RUNSALT: Terminology, Methodology, Limitations, and Solutions," *Heritage* vol. 5, pp. 3648–3663, 2022

[6] M. Steiger, A. Sawdy, "Modelling the crystallisation behaviour of mixed salt systems: Input data requirements," In: *12th International Congress on the Deterioration and Conservation of Stone*, Columbia University, New York, 2012.

[7] S. Godts, M. Steiger, S.A. Orr, T. De Kock, J. Desarnaud, H. De Clercq, V. Cnudde, "Charge balance calculations for mixed salt systems applied to a large dataset from the built environment," *Sci. Data* vol. 9, 324, 2022.

[8] N. Lindström, N. Heitmann, K. Linnow, M. Steiger M., "Crystallization behavior of $NaNO_3$–Na_2SO_4 salt mixtures in sandstone and comparison to single salt behaviour," *Appl. Geochem.* vol. 63, pp. 116–132, 2015.

[9] N. Lindström, T. Talreja, K. Linnow, A. Stahlbuhk, M. Steiger, "Crystallization behavior of Na_2SO_4–$MgSO_4$ salt mixtures in sandstone and comparison to single salt behaviour," *Appl. Geochem*. vol. 69, pp. 50–70, 2016.

[10] Y. Shen, K. Linnow, M. Steiger, "Crystallization behavior and damage potential of Na_2SO_4–NaCl mixtures in porous building materials," *Cryst. Growth Des*. vol. 20, 5974–5985, 2020.

[11] A. Stahlbuhk, M. Steiger, "Damage potential and supersaturation of KNO_3 and relevance in the field of salt damage to porous building material," *Constr. Build. Mater*. vol. 325, 126516, 2022

[12] A. Stahlbuhk, M. Steiger, "Investigations on the damage potential of salts precipitating from mixed electrolytes," in *Proceedings of SWBSS Asia 2023* (*International Conference on Salt Weathering of Buildings and Stone Sculptures*).

THE MIGRATION AND CRYSTALLIZATION BEHAVIOR OF SALT SOLUTION IN TRADITIONAL INORGANIC POROUS MATERIALS

Luo Hongjie[1], Zhao Jing[2], Li Qiang[1,2], and Huang Xiao[1]

KEYWORDS

Salt Damage, Nature Porous Inorganic Materials, Synchrotron & Micro-CT, Visible Research Method, Whisker, Salt Safe Removal

ABSTRACT

Salt damage is one of the biggest problems not only to inorganic cultural heritages such as earthen ruins, ancient masonries and potteries, etc. but also to modern masonries, highways, saline-alkali soils, etc. The behavior of salt solution migration and crystallization in nature inorganic porous materials under different salt solutions and environments is the fundamental and key problem for people to develop appropriate plans to prevent and eliminate salt damages correctly. For this reason, we applied μ-CT, visible research method, etc. to simulate and study salt damage in the past few years, in order to make clearer the rule of salt solution migration, crystallization, and damage to the simulated samples, reveal the formation mechanism of salt whiskers, and validate several techniques for safe removal of salt solution and crystal in the body of inorganic porous materials.

[1] Institute for the Conservation of Cultural Heritage, Shanghai University, Shanghai 200444, China, hongjieluo@shu.edu.cn; xhuang@shu.edu.cn

[2] Ancient Ceramics Research Center, Shanghai Institute of Ceramics, Chinese Academy of Sciences, Shanghai 200050, China

CAVERNOUS WEATHERING ALONG A CLIMATIC GRADIENT: FROM KARST SOLUTION TO SALT CRYSTALLIZATION (PRELIMINARY RESULTS)

Nurit Shtober-Zisu[1], Nimrod Wieler[2], Tomáš Weiss[3], and Jakub Mareš[3]

KEYWORDS

Inland notches, Tafoni, Salt weathering, Cavernous weathering, Uranine-probe

ABSTRACT

The accepted conceptual model for the formation of cavernous rock weathering involves the presence of permeable rocks subjected to atmospheric conditions. However, despite the common underlying lithology, field observations reveal various morphologies of cavities. In this study, we focus on the origin and role of moisture in cavernous weathering of exposed carbonate rocks of comparable features throughout the various climatic zones with precipitation ranging between 50 to 600 mm/y. Preliminary results show that in all climate zones, the mechanical properties are constantly weaker within the cavity compared to the caprock and base, or the exposed rocks where no cavity exists. However, the depth of the capillary water is negatively correlated with annual precipitation: at 600 mm/y EF (Evaporation Front) is at rock surface, while at 20 mm/y EF is completely missing and the rocks are dry. These preliminary measurements indicate that rock moisture necessary for chemical and salt weathering comes from rain precipitation in wetter regions, whereas in more arid regions, dew plays a significant role. Salt weathering dominates the erosional processes in the arid and hyper-arid zone, forming irregular sizes and shapes of the cavities, while dissolution and flaking is the main process responsible for the smooth and relatively regular morphology of the Mediterranean Inland notches.

[1] School of Environmental Sciences, University of Haifa, Israel
nshtober@research.haifa.ac.il
[2] Archaeological Res. Dept., Israeli Antiquities Authority, Jerusalem, Israel
[3] Faculty of Science, Charles University, Prague, Czech Republic

1 INTRODUCTION

Cavernous weathering is one of the most frequently occurring weathering patterns observed in various regions across the globe, including humid, arid, cold, hot, coastal, and inland sites [1]. The accepted conceptual model for the formation of inland cavernous rock weathering in carbonate rocks involves the presence of permeable rocks that are subjected to soluble salts and repeated episodes of drying–rewetting cycles [2, 3]. The proposed mechanisms assume that cavernous weathering results from physico-chemical processes including salt crystallization [4], incipient fractures [5], exfoliation [6], or stress erosion [7].

In Israel, the prevalence of cavernous features is accented and includes all three climate types characteristic of the country. However, the morphology of the cavities differs between the various sites, despite the common underlying lithology. The formation process suggested in the Mediterranean climate (400-850 mm annual precipitation) combines chemical, mechanical, and biogenic weathering cycles [8], mechanical decay in semi-arid climates (~200 mm annual precipitation) [6], and salt weathering in arid and hyper-arid regions (20-100 mm annual precipitation) [9] (Fig.1). Yet, no study dealt with the role of moisture in the cavernous weathering of exposed limestone and dolomite rocks of comparable features in a range of climates from Mediterranean to hyper-arid.

The rainfall regime across Israel presents a very steep rainfall gradient both from north to south and from west the mountain ridge to the Jordan Rift Valley in the east, making the region a natural laboratory for the study of spatial variability of various geomorphic phenomena along a climate gradient. Thus, in this study, we focus on the origin and role of moisture in cavernous weathering of exposed carbonate rocks of comparable features throughout the various climatic zones with precipitation ranging between 50 to 600 mm/y.

2 METHODOLOGY

To test our hypotheses, we applied a holistic approach combining field observations, and geological, geotechnical, and environmental characterization to elucidate the origin, and role of moisture, temperature and salts in carbonate cavernous weathering along a climatic gradient. Using a 10 mm wide drill bit, we drilled at various depths (2, 4, 8, 16, 32 cm) of the rock, following this procedure: 1) drilling to the respective depth (0-1 cm) collecting dust for salt analysis; 2) measuring T and RH in the respective depths of the hole until semi-steady state was reached; 3) measuring the depth of the capillary water by the uranine-probe (Fig 2) [10]. Mechanical properties were measured by the drilling resistance and the tensile strength (by pulling epoxy-glued T-profiles to the rock's surface).

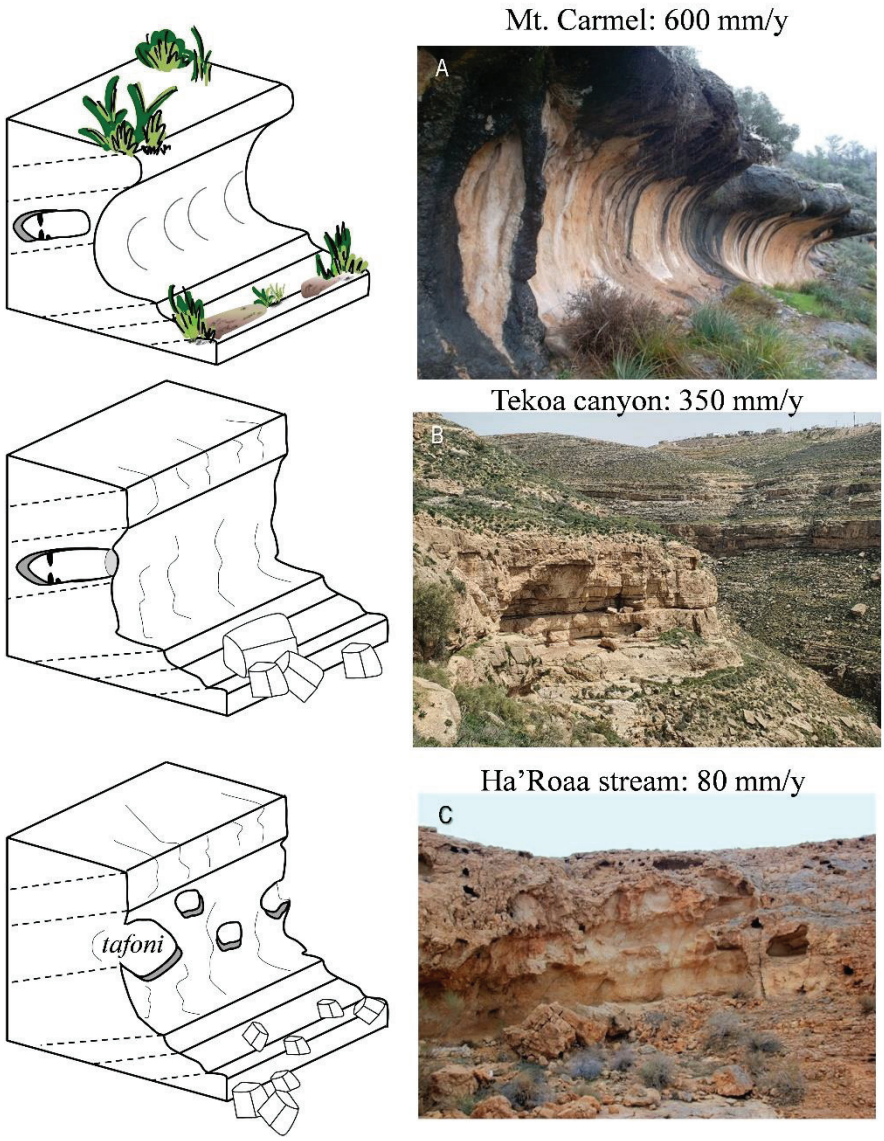

Figure 1. Typical cavernous weathering along a climatic gradient in Israe: A- Hot summer Mediterranean climate; B- Hot semi-arid climate; C- Hot desert climate. (Modified after [6]).

3 STUDY AREA

Most of the exposed sequence forming the mountainous backbone of Israel was deposited during the Cretaceous period through the Eocene epoch, when a huge carbonate platform extended between the open Tethys Sea in the northwest and the

Arabo-Nubian Massif in the southeast. Deposition on the platform was controlled by two main factors: barrier-reefs that partly isolated the platform from the open sea, and local shelf basins that developed within the platform. As a result, different lithostratigraphic sequences evolved in geographically close regions. The Tethyan sedimentary succession is composed therefore of a thick (900–1000 m) sequence of hard, karstic, and permeable limestone and dolomite interbedded with argillaceous impermeable beds, representing a variety of carbonate shallow marine sediments.

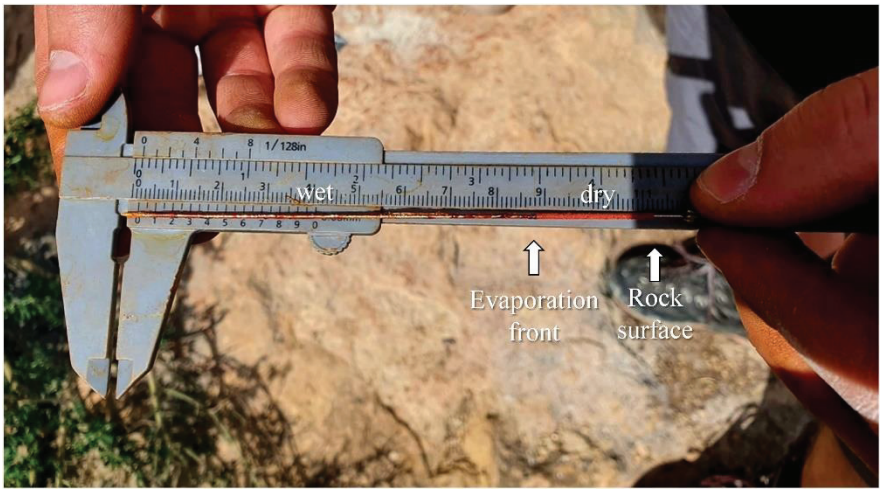

Figure 2. Uranine probe used to measure the depth of the capillary water. Probe is wet from 2.5 cm inwards, proving the location of the Evaporation front.

4 PRELIMINARY RESULTS

Preliminary results show that in all cases and all climate zones, the mechanical properties are constantly weaker in the cavity compared to the caprock and base, or the exposed rocks where no cavity exists. However, the depth of the capillary water is negatively correlated with annual precipitation: at 600 mm/y and also at 350 mm/y EF (Evaporation Front) is at the rock surface, while at 100 mm/y and also 20 mm/y EF is completely missing and the rocks are dry. Relative humidity indicates daily variability in hyper-arid environments, due to dew daily variability, while in the Mediterranean zone rock humidity is attributed to the annual rainfall. Our preliminary measurements indicate that rock moisture necessary for chemical and salt weathering comes from rain precipitation in wetter regions, whereas in more arid regions, dew (or just higher relative humidity) also plays a significant role. This leads to the likely situation that salt weathering dominates the erosional processes in the arid and hyper-arid zone, forming irregular sizes and shapes of the cavities, while dissolution and flaking is the main process responsible for the smooth and relatively regular morphology of the Mediterranean inland notches.

5 REFERENCES

[1] J. Bruthans, M. Filippi, M. Slavík, and E. Svobodová, "Origin of honeycombs: Testing the hydraulic and case hardening hypotheses", *Geomorphology*, vol. 303, pp. 68–83, 2018.

[2] A.S. Goudie, E. Wright, and H.A. Viles, "The roles of salt (sodium nitrate) and fog in weathering: a laboratory simulation of conditions in the northern Atacama Desert, Chile", *Catena*, vol. 48, pp. 255–266, 2002.

[3] B.J. Smith, P.A. Warke, J.P. McGreevy, and H.L. Kane, "Salt-weathering simulations under hot desert conditions: agents of enlightenment or perpetuators of preconceptions?", *Geomorphology*, vol. 67, pp. 211–227, 2005.

[4] G.W. Scherer, "Stress from crystallization of salt", *Cement and Concrete Research*, vol. 34, pp. 1613–1624, 2004

[5] R. Amit, J.B.J. Harrison, Y. Enzel, and N. Porat, "Soils as a tool for estimating ages of Quaternary fault scarps in a hyperarid environment – the southern Arava valley, the Dead Sea Rift, Israel", Catena, vol. 28, pp. 21–45, 1996.

[6] N. Shtober-Zisu, H. Amasha, and A. Frumkin, "Inland notches: lithological characteristics and climatic implications of subaerial cavernous landforms in Israel", *Earth Surface Processes and Landforms*, vo. 42, no. 12, pp. 1820-1832, 2017.

[7] J. Bruthans, J. Soukup, J. Vaculikova, M. Filippi, J. Schweigstillova, A.L. Mayo, J. Rihosek, Sandstone landforms shaped by negative feedback between stress and erosion", *Nature Geoscience*, vol. 7, no. 8, pp. 597-601, 2014.

[8] N. Shtober-Zisu, H. Amasha, and A. Frumkin, "Inland notches: Implications for subaerial formation of karstic landforms - An example from the carbonate slopes of Mt. Carmel, Israel", *Geomorphology*, vol. 229, pp. 85-99, 2015.

[9] N. Wieler, H. Ginat, O. Gillor, and R. Angel, "The origin and role of biological rock crusts in rocky desert weathering", *Biogeosciences*, vol. 16, no. 6, pp. 1133-1145, 2019.

[10] T. Weiss, J. Mareš, M. Slavík, and J. Bruthans, "A microdestructive method using dye-coated-probe to visualize capillary, diffusion and evaporation zones in porous materials", *Science of The Total Environment*, vol. 704, no.135339, 2020.

Cavernous weathering along a climatic gradient: from karst solution to salt crystallization (preliminary results)

CHARACTERISATION OF SALT DISTRIBUTION USING A COMBINATION OF NON-DESTRUCTIVE TESTING AND MATERIAL ANALYSIS FOR A 140 YEAR-OLD CONSERVATION SHOPHOUSE IN SINGAPORE

C.W. Wong[1], Ryanne H.S. Tang[1], C.P. Foo, Y.H. Ng, and Y.M. Yeh

KEYWORDS

3D radar scanning, active infrared thermography, microwave moisture tomography, petrography

ABSTRACT

Characterisation and mapping of salt distribution and damage within a traditional Chinese style shophouse built in early 1900s in Singapore are often fraught with difficulties. This is due to a great extent to the construction of such buildings which comprised of a mixture of a large variety of materials and finishes, architecture and layout. Such buildings typically contain a blend of clay brick masonry with cement or lime mortar, ornamented ceramic tiled dado, encaustic cement floor tiles, granite flooring and terracotta tiles. The layout of the buildings often comprises of air well that allows ingress of rain and party walls that share with adjacent units. A combination of these factors had led to non-uniform or untypical pattern and distribution of crystallization of salt on walls in contrast with those commonly found in other historic buildings locally. The salt could have originated from the ground via uprising damp, inherent within the historic masonry wall leached out from penetrating damp or from environmental pollution. The different finishes of varying pore characteristics could also have resulted in unknown redistribution of the salt.

In order to study the pattern and distribution of the recrystallized salts in one of the shophouses in Singapore, a variety of non-destructive methods were employed. These methods were used to map the relative moisture trapped within the walls at different heights and depths and identify zones with concentrated salts by analysing the electric conductance and dielectric property of the walls. The diverse techniques applied include 3-dimensional surface penetrating radar, active thermogra-

[1] MAEK Consulting Pte Ltd, Singapore,
e-mail: wongcw@maek.com.sg, ryannetang@maek.com.sg

phy and microwave tomography. In addition, minor samples were extracted to determine the level of moisture and salts in the wall. Petrographic examination was also conducted on small fragments of plaster and glazed ceramic tiles extracted to identify the nature of salt, examine the extent of salt attack and condition of the material.

This paper discusses the findings of the different approaches undertaken in the study to evaluate the efficacy of the techniques.

1 INTRODUCTION

Pre-war shophouses are unique form of construction in town and cities of Southeast Asia. These are vernacular buildings with narrow frontage of 20 feet or less and depth of 60-70 feet built in terrace without ventilation at the side. [1]. Some have air well within the houses that open directly to the sky to provide natural ventilation and lighting to the interior. (See Figure 1). These shophouses abut each other and hence have specific structural sensitivity. [2]. A number of these buildings were originally meant solely for residential purposes whilst others consist of spaces of business on the lower floor and accommodation on the upper levels. [3]. In Singapore many of these shophouses are protected and conserved and in recent years, many of them have been converted for reuse as hotels, restaurants and other businesses. Many of the conversion in the past involved removal of some of the wall finishes internally, sealing up of the air wells, addition of usable spaces, installation of air conditioner, installation of secondary windows etc. As some of the units are individually owned, the different extents of alterations are commonly encountered in different units, which may alter the micro-climate of the units. In addition the works done in one unit can affect the response of shared elements, namely the party wall and thus the finishes of the neighbouring unit. For example, some of the works had invariably redirected water discharge path, caused condensation or altered the direction of moisture or vapour migration. These had in numerous instances led to unusual and random pattern of damages to the finishes of the party wall, many of which with highly ornamental finishes and historic murals. Key deterioration amongst them is salt crystallization damage.

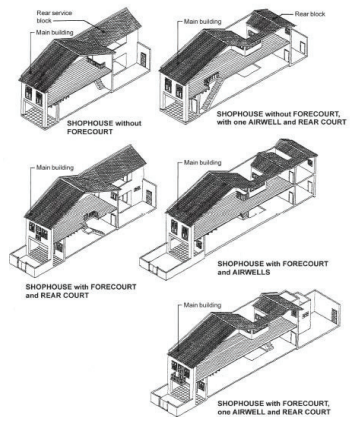

Figure 1 Typology of Shophouses

Whilst salt crystallization attack induced by uprising damp in stand-alone structures commonly follows a certain pattern due to fractionation of the soluble salt brought up from the ground [4] [5] [6], it can be an arduous task trying to trace the zones where salts accumulate in shophouses due to events that had taken place above. Many of these historic shophouses are finished with highly glazed dado tiles which could influenced the hygrothermal balance of the moisture in the wall due to uprising damp. In certain cases when there are no areas where the salt can further migrate, damages to the historic tiles result. Otherwise, the salts get redistributed. Due to the fractionation phenomenon, sulphate salts will result in physical damages

to the wall finishes such as friable plaster and peeling of paintworks. Depending on the environmental condition and hence the drying flux of the wall substrate, the other salts, namely chloride and nitrate may cause physical damages and persistent dampness on the surface of the wall of substrate. [7] In trying to treat the wall, the common approaches taken are to extract powders of the masonry substrate, in this case clay bricks, for total and hygroscopic moisture content and salt content measurement. [8] However, there is a limit as to how many of such sample can be extracted to minimize the extent of damages to the wall. Furthermore, due to the unknown re-distribution of the salts and atypical salt crystallization pattern arising from the various factors described above, it is difficult to determine where the samples should be taken. Indeed, any attempt to damage murals and dado finishes is to be avoided. A trial was thus made using various non-destructive means on one of the typical shophouse that was made available briefly. Three primary methods were used here, namely the infrared thermography, microwave tomography and the ground penetrating radar. Other strategies using poultices to map the salt distribution were looked into but not eventually used here. [9]

Figure 2: a- example of redistributed salt damage on a mural above an internal window; b- concentrated salt crystallization damage on dado tile below an internal window; c- close up view of damaged glazed tile

Figure 3: Left photo – prismatic salt crystals found behind the dado tiles; right photo – efflorescence exuding out from crazes

2 INFRARED THERMOGRAPHY (IRT)

Infrared thermography (IRT) is an established non-destructive technique widely utilized across various engineering disciplines. It involves the measurement of surface temperature differences or changes using an infrared sensor. An infrared camera captures infrared radiation and generates thermal images that contain temperature data for each pixel.

Thermography has the capability to identify the presence of moisture or delamination of plaster up to a depth of 100mm, depending on the rate at which the surrounding environment is heated. It can be performed actively or passively. Active thermography involves the application of controlled external heat excitation to induce surface temperature differences on the object being inspected. Active thermography offers greater flexibility compared to passive thermography due to the availability of various heating techniques that can be employed [10]. It involves controlled heat excitation, allows for internal assessments, and is not constrained by the environmental heating rate. However, the application of IRT in this project is limited to the upper portion of the wall that is not covered by reflective glazed ceramic tiles, as the reflectivity of the Dado tiles significantly impacts the performance of IRT.

Active infrared thermography was conducted on the wall to assess the heat conduction rate across its surface. Discontinuities within an object have an impact on the cooling rate observed on the surface. For instance, in a heating cycle, a delaminated plaster would appear as a hot thermal anomaly since the surface temperature of the delaminated area would be relatively higher compared to other regions.

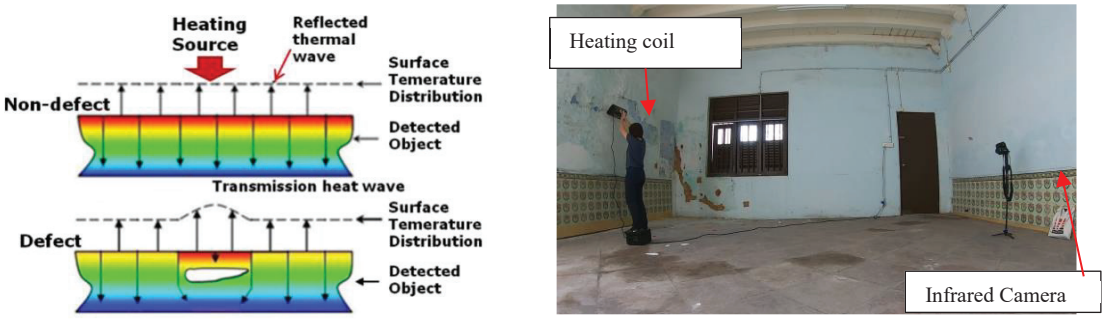

Figure 4 Illustration of thermography principle on delaminated plaster (left), extracted from [11] and set up of the active IRT (right)

3 MICROWAVE MOISTURE TOMOGRAPHY (MT)

Microwave moisture tomography was carried out using the hf-microwave method from GmbH in Leipzig. This is a non-destructive testing method used to determine the real permittivity of the tested material. [12] [13] [14] The apparent permittivity of water ($\varepsilon_{water} = 81$) is much higher than other common building materials (ε_{brick} – 4-7), thus the moisture content leads to significantly higher measurement values. Due to high frequency of microwave, a small loss in permittivity will be detected. As the electric frequency increases, the impact of ohmic loss decreases. In the case where salt is presence in the wall, at high-frequency microwave levels, the contribution of ohmic loss is significantly lower compared to the loss of permittivity. [15]

Areas with high permittivity values will have higher moisture content assuming that a tested wall exhibits relative homogeneity. By creating a moisture profile, it becomes possible to assess the moisture path, aiding in the identification of the moisture source and facilitating the recommendation of appropriate rectification methods.

Microwave measurements were employed to create a moisture distribution map within the wall, aiming to confirm the presence and extent of rising dampness and, when feasible, determine the path of moisture movement. The measurements were conducted using probes at grid spacing intervals of 300 mm, with varying depths probe. See Figure 5.

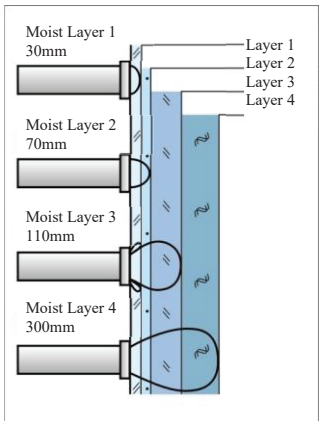

Figure 5 Principle of Microwave Measurement, Extracted from *[33]*

The presence of various types of dampness, including rising damp, hygroscopic moisture, and penetrating damp, can be identified using a high-frequency microwave detector by detecting changes in the permittivity value within the wall.

4 GROUND PENETRATING RADAR

Ground Penetrating Radar (GPR) is a non-destructive technique that utilizes wide-band electromagnetic (EM) pulses to assess subsurface conditions. GPR emits a brief burst of electromagnetic energy, which penetrates into the subsurface. When the energy encounters interfaces between different layers or objects where there are variations in chemical and electrical properties, reflection occurs. This reflection happens due to changes in the speed of the energy. At an interface with a velocity change, a portion of the available energy is reflected back to the antenna, while the remaining energy continues to travel deeper until it encounters another interface. This process repeats until all the available energy is depleted. See Figure 6.

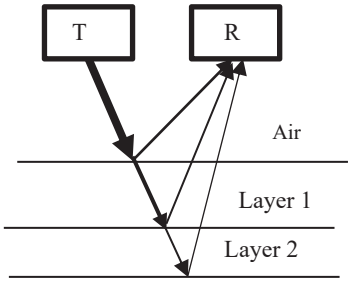

Figure 6 Principle of GPR

In general, the behavior of electromagnetic (EM) waves is governed by three physical properties: conductivity, permittivity, and permeability. These properties are commonly referred to as the dielectric properties of materials. [16]. Among these properties, conductivity and permittivity have a more significant impact on GPR compared to permeability, which can be influenced by magnetic interference.

Permittivity has major effects on the EM waves speed. The permittivity of an electromagnetic wave is a measure of the ability of a material to store electrical energy in an electric field. This means that the oscillating electric fields of the wave for high permittivity material are faster and store more energy. As a result of higher frequency, the wavelength of an electromagnetic wave decreases. The permittivity

of a material is determined by the properties of the atoms and molecules that make up the material. The speed of an electromagnetic wave in a material medium is given by equation below

$$\mathbf{v = c/\sqrt{\varepsilon}} \quad (1)$$

c = the speed of light in vacuum,

ε = *permittivity.*

Values of relative dielectric permittivity for several materials encountered in geological surveys are given in Table 1. [17]

Table 1 Relative dielectric permittivity of geologic materials measured at 100 MHz

Material	Relative Dielectric permittivity (ε_r)	Material	Relative Dielectric permittivity (ε_r)
Air	1	Water	81
Dry Brick	2-5	Dry Mortar	5-10
Saturated Brick	20-80	Saturated Mortar	20-80

Conductivity of materials refers to the ability of free electric charges to transfer when an electric field is applied. This property leads to the dissipation of wave energy. Electrical conductivity is the material property that governs the attenuation of electromagnetic waves, as described by Stratton's theory. [18] [19]. Therefore, when signal attenuation is observed in GPR radargrams, it is likely due to the presence of materials with high conductivity such as when there is presence of electrolytic liquid containing salt. As a result, the electromagnetic wave is absorbed by the conductive material and returns with a weakened signal. Thus, such signal attenuation in electromagnetic (EM) waves can be more pronounced when soluble salt is present in the pores of a material. This tool assists in identifying the presence of electrolytic salt within the wall, even if it is not visible from the surface.

In this study GPR was utilized for 2D and 3D scanning using Proceq GP8800 and GSSI Structural Scan Mini XT. The GPR data was processed using GPR Slice and RADAN 7 software.

5 TEST PROGRAM

The typical layout of the shophouse tested is shown in Figure 7. A number of locations were scanned and tested. For this presentation, two locations are discussed; one without any visual sign of salt damage (L1) whilst another with evidences of salt attack as seen from the badly peeled paintworks, friable plasters and presence of efflorescence (L2). The bottom section of the wall of about 800mm height is finished with glazed tiles whilst the upper section of the wall is finished with lime plaster and paint. The wall substrate is of masonry clay brick construction. The shophouse was constructed in the 1880s.

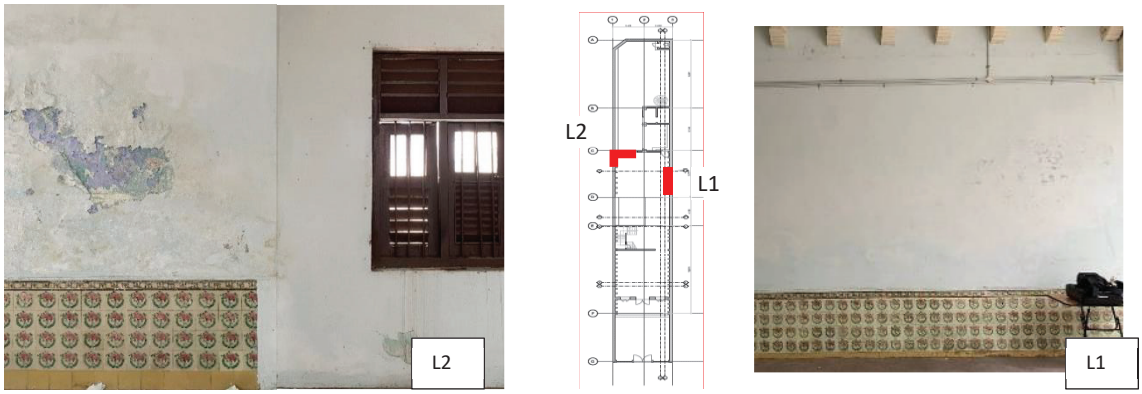

Figure 7 Test Locations

The three different NDT methods were used only at L1 whereas only the microwave and GPR were carried out at L2. In addition, powder samples were extracted for determination of the total and hygroscopic moisture content at L2. The test moisture measurement was made based on BRE Digest 245 [20]. Some powder samples were also subjected to ion chromatography test to determine the nature of the salt. Samples of plaster were also extracted for petrographic examination [21] [22] [23] to identify the damage phenomenon and salt.

6 RESULTS

6.1 LOCATION 1

a. Infrared thermography

Infrared thermography is utilized to capture infrared radiation emitted by materials, which can then be translated into apparent surface temperatures using known emissivity values. For the purpose of infrared thermography inspection, an emissivity value of 0.95 is commonly assigned to opaque materials with low reflectivity. This parameter is employed during the inspection process.

In the specific case of the inspection, the presence of different materials necessitated a focused approach. The reflective dado ceramic tiles and the opaque plaster wall have distinct characteristics. As a result, active thermography technique was specifically applied to the plastered wall, both before and after the heating process. This approach allows for accurate and targeted analysis of the thermal behavior and anomalies within the plastered wall.

The IRT results revealed a notable temperature increase, with a heat band observed on the lower section of the plastered wall. This increase in temperature is likely attributed to the debonding or deterioration of the plaster, potentially caused by salt crystallization. See Figure 4 for the fundamental of infrared thermography. Conversely, the upper part of the wall exhibited relatively lower temperatures following the heating cycle. See Figure 8.

These hot band findings from infrared thermography suggest that the plastered wall, particularly in the region above the ceramic tiles, has delaminated or deteriorated potentially caused by presence of salt within. In contrast, other areas of the wall show a relatively uniform temperature increase without significant anomalies.

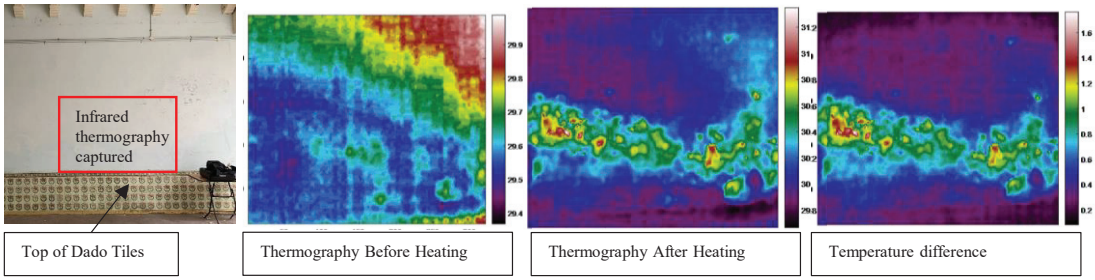

Figure 8 Results of Active Infrared Thermography

b. Microwave moisture

From the microwave moisture mapping, relatively higher moisture content was detected above the "hot" band as observed from the IRT. This probably indicates the presence of trapped moisture, either due to uprising damp or hygroscopic moisture attributed to the presence of salt. The relatively lower moisture content just above the dado tiles where 'hot' band from the IRT (highlighted in black) was noted could have been caused by the presence of deteriorated plaster with larger amount of void thus giving a lower moisture content. See Figure 9. The findings show that the use of microwave can locate trapped moisture deep within a wall which IRT is not able to.

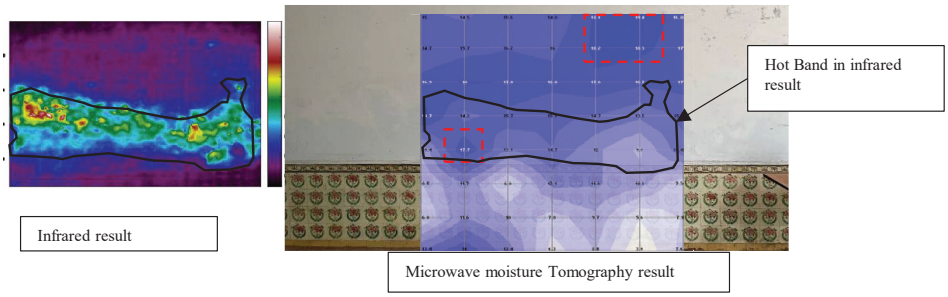

Figure 9 Results of Microwave Moisture Tomography and Infrared

c. Ground penetrating radar

Both radargrams of GPRSW-2-1 and GPRSW-2-2 show signal attenuation at about 1.4 m height and above. It can be seen that the zone with attenuated electromagnetic energy is at a higher height than the area with lower apparent temperature picked up from the active thermography. Based on signal floor output highlighted in green lines, the effective depth detection was generally observed to be consistent but greatly reduce at the height of 1.40 m. This signal floor output indicates the noise

and signal loss from scan to scan and provides an estimate of effective depth penetration of the electromagnetic energy. See Figure 10.
The area with attenuated signal in this case coincided with the area with high relative moisture content from the microwave. This could infer that this area contains salt as well as moisture, possibly hygroscopic moisture as well as moisture from uprising damp. The high moisture level above the dado tiles is thus likely ascribed to the impermeable glazed tiles at the bottom of the wall which had resulted in the moisture being carried up the wall. In addition, the warm and humid condition of the internal environment and thick layers of paintworks would have also led to the moisture migrating up the wall.

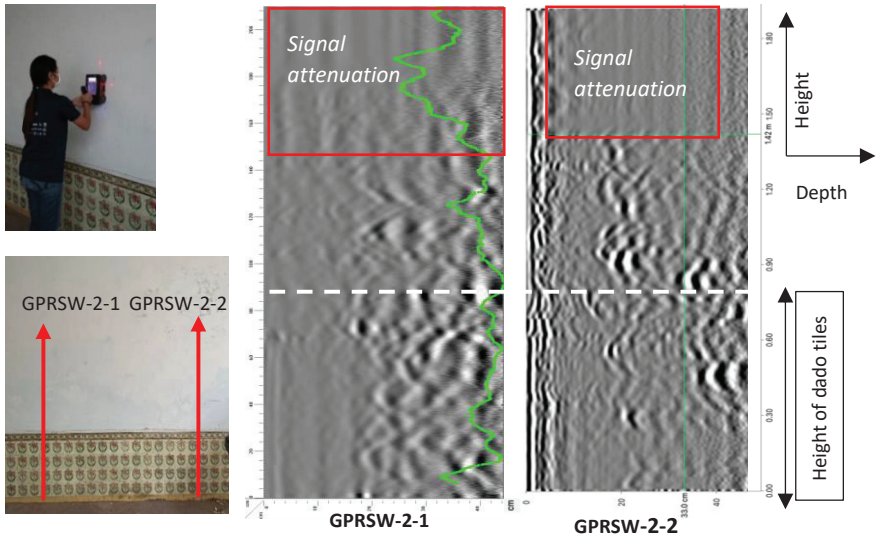

Figure 10 Results of Ground Penetrating Radar

The radargrams obtained from GPRSW-2-1 present valuable insights into the quality of the reflected signals, which can be further evaluated through processing techniques. Within Radan 7 processing tools, the green line observed, known as the signal floor indicator, serves as a reference for estimating the depth at which noise surpasses the signal. This indicator is a common tool in GPR analysis, enabling the determination of effective penetration depth. As electromagnetic waves propagate deeper, they experience absorption and interference from conductive materials, leading to signal attenuation.

In addition to the signal floor indicator, A-scan analysis using an oscilloscope allows for the assessment of polarity shifts. A well-reflected signal exhibits smooth oscillations between positive and negative polarities with a relatively high amplitude. Conversely, attenuated signals display jagged fluctuations between the two polarities, accompanied by minimal amplitudes. See Figure 11.

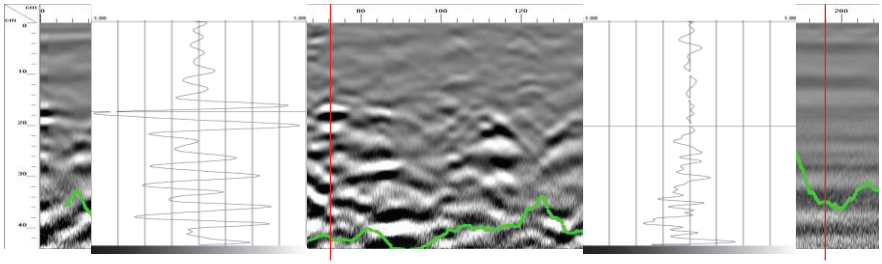

Figure 11: A-Scan analysis

6.2 LOCATION 2

a. Microwave moisture

Higher moisture content was generally observed at the bottom of the moisture tomographs. Up till a height of about 900 mm – 1200 mm for **Side Wall, SW**, and 300 mm – 600 mm for **Back Wall, BW**, moisture content was noted to be higher compared to the top part of the wall, indicating sign of rising dampness. The pattern of moisture distribution appeared consistent throughout the different depths of measurement showing elevated moisture towards the base of the wall. However, steeper in-plane moisture gradient could be noted at deeper measurement depth. This could be because the moisture had evened out around the surface due to evaporation, uniformity of the porosity of the surface layers like the plaster and paintworks or caused by the presence of salt that had accumulated close to the surface zone.

The presence of localized higher moisture content marked in red dotted box are areas subjected to water retention. Higher moisture content was generally observed towards the left side of the moisture tomographs. This suggests water seepage/ingress from the top left of the wall, most likely penetrating damp from the exposed air-well or the neighbouring unit. See Figure 12 and Figure 13

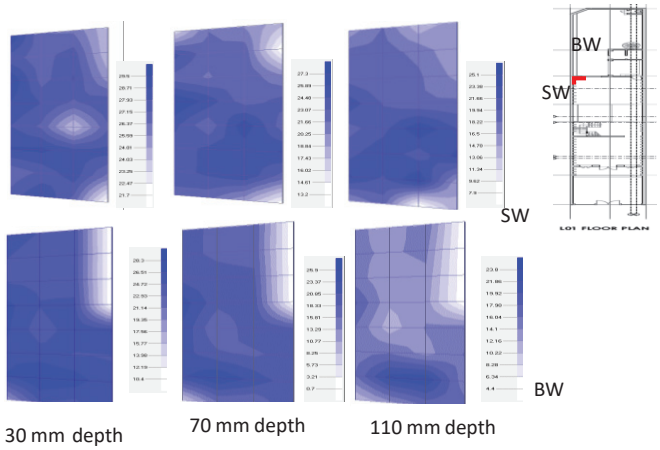

Figure 12: Moisture tomographs at different measurement depths

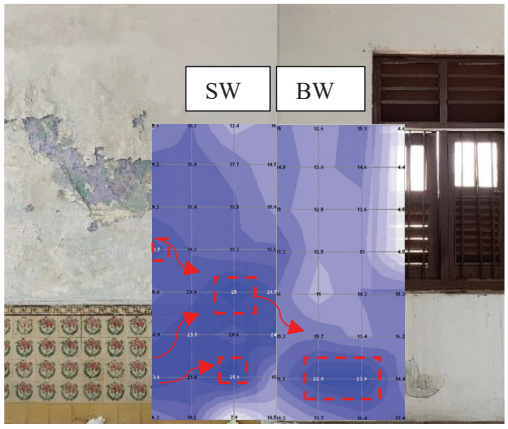

Figure 13: Superimposed moisture tomography at 110mm depth

b. Ground penetrating radar

Signal attenuation was observed higher up the wall, above the wetter zone as seen from the microwave moisture results. In both scans 1 and 2, the radargrams show signal attenuation at about 1.20 m height and above, suggesting presence of electrolyte within the zone. See Figure 14. This signal attenuation is likely caused by the presence of high electrolytic conductivity within the wall in that specific area, typically identifying where larger amount of hygroscopic salts are trapped. This indicates that the salts present in the signal attenuated area are more soluble and remain in a liquid form despite the lower relative moisture content as picked up from the microwave.

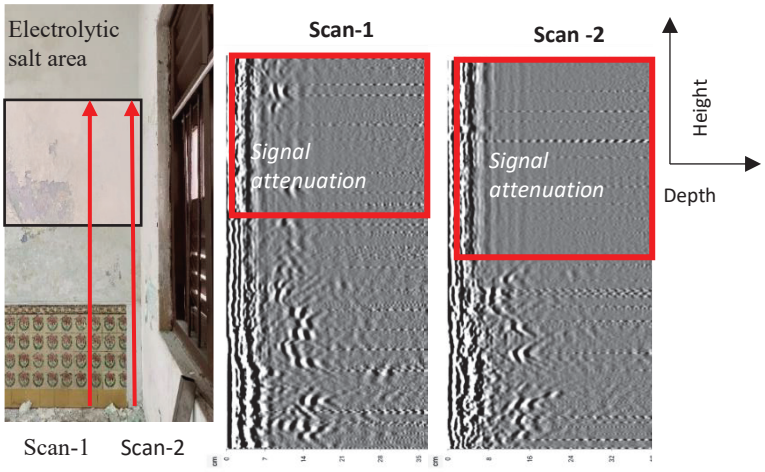

Figure 14 Result of Ground Penetrating Radar at Side Wall, SW

c. Total and Hygroscopic Moisture Test (TMC and HMC)

Powders of the clay brick substrate were extracted from different heights and 2 depths (20-50mm and 100-150mm) for determination of total and hygroscopic moisture content as shown in Figure 15. Above the dado tiled area, the TMC readings are higher than the HMC at both depths. Both the TMC readings deeper in the wall are higher than those near the surface. The highest TMC and HMC readings are found at about 1.3m height which concurred with the microwave moisture results. See Figure 16.

At BW, relatively higher TMC values were encountered at the foot of the wall, as similarly reflected from the microwave moisture findings. The highest TMC and HMC results were however found around 1.3 to 1.6m height. The high TMC values could in fact be the hygroscopic moisture as the humidity of the pores within the wall would likely exceed 75%, the condition which the powders were tested. The presence of thick layers of paint and latter applied cement skim coat could have inhibited drying of the wall. See right photo in Figure 15. This could elucidate the even in-plane moisture distribution from the microwave. It is postulated that there is likely to be greater amount of hygroscopic salt at BW or close to the corner of the wall. This can also be observed from the GPR scan showing attenuated signal higher up the wall at BW.

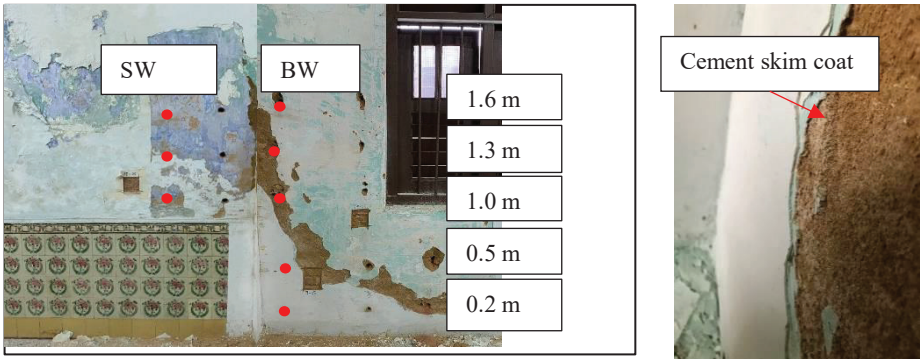

Figure 15: Sampling for TMC and HMC test (left) and presence of cement skim coat (right)

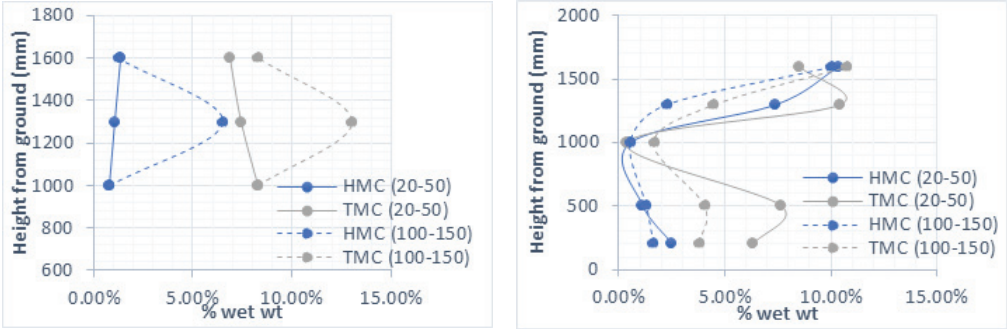

Figure 16: Results of TMC and HMC measurements (left -SW and right- BW)

d. Salt content analysis

The powder samples from BW at 1.6m height and 20-50mm depth were tested to determine the anion salt content using ion chromatography. The results indicate the presence of high chloride and nitrate salt of 0.7 % and 0.8% respectively with medium amount of sulphate salt (0.9%) based on guidelines given WTA. [24]. These could have well been the cause of the high HMC values.

e. Petrographic examination

Samples of deteriorated plasterwork extracted that were subjected to petrographic examination revealed the presence of coarse-grained recrystallized salt crystals. They were detected in numerous locations, namely at the interface between the cement skim coat and the lime plaster as well as within the porous matrix of the plaster. The salts display low birefringe properties, often with a mixture of prismatic crystals and whiskers and have been identified as gypsum and halite. See example in Figure 17. Their discovery at various locations and point to the inhomogeneity of the substrate with regards to the pore characteristics and likely effect of environmental factors, presence of different construction materials and layers and variability in the sources of salt and moisture.

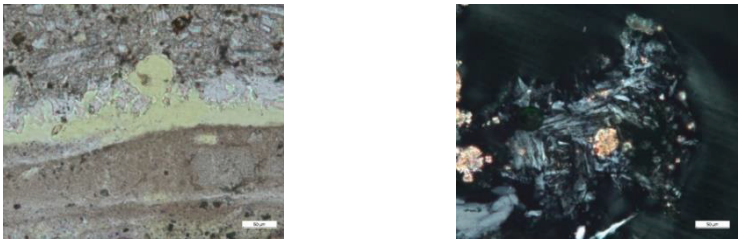

Figure 17: Microscopic images of salt under plane polarized light (left) and cross polarized light (right)

7 CONCLUSION

From the brief trial, it can be seen that by employing a combination of various techniques, it becomes possible to enhance the identification of salt attack, assess its severity, determine the distribution of salt, and evaluate the likelihood and possibly even differentiate the sources moisture ingress, such as rising damp, penetrating damp or others. This multi-technique approach offers a more comprehensive understanding of the condition under investigation. Experiences of the author on other projects had also shown the possibility of using non-destructive means to identify zones with trapped moisture or accumulated hygroscopic salt, and differentiate the zones for different methods of intervention [25]. This approach was found to be particularly useful for shophouses with unique construction and features as discussed. Though the some of the methods have been attempted in some other projects, this is the first time that such a combination of different techniques have been trialed. This is because of time and cost constrained in actual restoration works. Further studies with more live cases will need to be carried out to uncover challenges that can affect the use and effectiveness of the different methods. It should also include their applications in assessing the efficacy of any intervention

with the eventual target to minimize destructive testing like drilling of brick powders, which often need to be repeated several times in tenacious cases.

8 REFERENCES

[1] C. Foo, C. Wong, Y. Ng and R. Jacosalem, "Exploring digital documentation for shophouses in Singapore," in *Documenting, Understanding, preserving Cultural heritage: Humanities adn Digital Technologies Shaping the Future*, 2023.

[2] K. Goh and R. Mair, "Incorporating the existing condition of buildings when assessing potential impact of underground construction," *Underground Singapore,* 2014.

[3] B. S. Yeoh, "Shophouse," in *The Encyclopedia of Urban Studies*, Thousand Oaks, SAGE Publications, Inc., 2010, p. 708.

[4] A. Andreas and Z. Konrad, "Salt weathering on monuments," in *1st int. symposium on the conservation of monuments in the Mediterranean Basin*, Bari, 1989.

[5] A. Arnold and K. Zehnder, "Monitoring wall paintings affected by soluble salts," in *The Conservation of Wall Paintings*, 1987.

[6] H. S. Tang and C. W. Wong, "Managing Recalcitrant Rising Damp and Salt Attack Problems in Heritage Buildings in the Tropics," in *International Academic Forum on Built Heritage: A Cultural Motivator for Urban and Rural Development*, Shanghai, 2017.

[7] T. C. D. Goncalves, *Salt Crystallization in Plastered or Rendered Walls,* Lisbon, 2007.

[8] TU Delft, "https://www.emerisda.eu/wp-content/uploads/2014/07/D-2_3.pdf," 2014. [Online].

[9] I. Egartner and O. Sass, "Using paper pulp poultices in the field and laboratory to analyse salt distribution inbuiling limestones," *Heritage Science,* vol. 4, no. 41, 2016.

[10] W. W. L. W. C. C. L. K. Janet F.C. Shama, "Imaging and condition diagnosis of underground sewer liners via active and passive infrared thermography: A case study in Singapore," *Tunnelling and Underground Space Technology 84,* p. 440–450, 2019.

[11] P. J. W. Z. Zhi Qu, "Development and Application of Infrared Thermography Non-Destructive Testing Techniques," *Damage Detection Systems for Aerospace Applications,* 2020.

[12] G. Gartner, R. Plagge and H. Sonntag, "Determination of moisture content of the outer wall using hf-sensor technology," 2010.

[13] L. Kurik, K. Targo, K. Urve and S. Veljo, "Influencing factors of moisture measurement when using microwave reflection method," in *Energy Procedia*, Trondheim, 2017.

[14] C. Blaue and B. Rousset, "Attempt to use a microwave moisture mapping system (Moist 200B) to control and monitor the water uptake of stones in

the frame of cultural heritage conservation," in *12th International Conference on Microwave and High Frequency Heating*, 2009.

[15] K. Kupfer, "Materialfeuchtemessung, Renningen-Malmsheim," *Expert Verlag,* 1997.

[16] D. Bigman, *Learn GPR.*

[17] L. Conyers and D. Goodman, Ground-Penetrating Radar: An Introduction for Archaeologists, London: AltaMira Press, 1997.

[18] J. Stratton, Electromagnetic Theory, New York and London: McGraw-Hill Book Company Inc., 1941, p. 615.

[19] S. Tulaczyk and N. T. Foley, "The role of electrical conductivity in radar wave reflection," *The Cryosphere,* 2020.

[20] P. Trotman, *BRE Digest 245 - Rising damp in walls - diagnosis and treatment,* Building Research Establishment, 2007.

[21] ASTM C1324, *Standard Test Method for Examination and Analysis of Hardened Masonry Mortar,* American Society for Testing and Materials, 2020.

[22] H. S. Tang and C. W. Wong, "Application of Petrography as A Tool For Assessing Historic Mortars For The Purpose of Restoration," in *InHERIT Conference on International Heritage and Cultural Conservation*, Sarawak, 2018.

[23] C. W. Wong, "Petrography Examination as A Tool in Diagnosis of Building Materials Failure - Singapore Experience," in *8th Euroseminar on Microscopy Applied to Building Materials*, Greece, 2001.

[24] International Association for Science and Technology of Building Maintenance and Monuments Preservation, *WTA, International Association for Science and Technology of Building Maintenance and Monuments Preservation Supplementary Code of Practice No. E-2-6-99/D.*

[25] C. W. Wong and H. S. Tang, "Diagnostic Condition Assessment of a 180 Year Old Church in Singapore for the Purpose of Restoration," in *International Conference on Sustainable Building Restoration and Revitalization*, 2013, 2013.

DEGRADATION OF ANCIENT WALL PAINTINGS BY SALT RECRYSTALLIZATION: THE CASE OF THE UNDERGROUND BURIAL CHAMBERS IN *SAQQARA*, EGYPT

Hiroshi Suita[1], Tadateru Nishiura[2*], Adel Akarish[3], Ashraf Ewais[4], and Mariko Suita[1]

KEYWORDS

Wall Paintings, Underground burial chamber, Ancient Egypt, Degradation, Salts-Recrystallization

ABSTRACT

Salt recrystallization causes deterioration of many materials such as stone, plaster, soil and the like, which is one of the major problems in conservation of cultural heritage. In case of wall paintings on stone, plaster and clay wall, this is a big problem. The extremely valuable wall paintings in underground burial chambers of ancient Egypt, some of which are more than 4000 years old, suffer from this problem to high extent.

Considering the conservation of these wall paintings, the fact that these have been preserved for very long time (more than 4000 years) should be respected. The environment conditions inside the underground burial chambers, especially the temperature and humidity, should be kept as much as before discovery. Otherwise, the wall paintings are threatened from new and rapid salts-recrystallization damages. Some case studies are discussed.

[1] Kansai University, 3-3-35 Yamate-cho Suita-city Osaka, Japan
[2*] <Speaker and Corresponding author> Kokushikan University,
1-1-1 Hirohakama Machida-city Tokyo, Japan, (tadateru.nishiura@gmail.com)
[3] The National Research Centre, Cairo, Egypt
[4] The Supreme Council of Antiquities, Cairo, Egypt

1 INTRODUCTION

Since 2003, Kansai University team has been conducting international projects for the conservation of ancient wall paintings in underground burial chambers, in Saqqara, which is one of the most important archaeological sites in Egypt. Here, a report is made on the damage characteristics, and conservation measures for the ancient wall paintings in *Idout* underground burial chamber and the *Memi* underground burial chamber. In case of *Idout*, the deposition of recrystallized salts on the paintings is limited. However, recrystallization of salts seems to have occurred between the bedrock and the gypsum plaster layer on which wall paintings were drawn. As a result, more than half of the plaster layer had fallen off, and the other was about to fall off. On the other hand, in case of *Memi*, numerous long, thin needle-like crystals have formed on the wall surface. This difference is due to the humidity environment inside the underground burial chambers, which is related to the difference in the water content of their bedrock.

Considering the conservation of these wall paintings, the fact that these wall paintings have been preserved for very long time (more than 4000 years) should be respected. The environment conditions inside the underground burial chambers, especially the temperature and humidity, should be kept as much as before discovery. Otherwise, the paintings are threatened from new and rapid salt-recrystallization damages. Since the conditions are different between *Idout* and *Memi*, both cases are discussed.

2 *IDOUT* UNDERGROUND BURIAL CHAMBER

In the underground burial chamber of *mastaba* of *Idout* (Saqqara archaeological area, Cairo suburbs, Egypt), very precious vividly colored wall paintings remain from the Old Kingdom period (around BC 2360).

The authors of this paper have been engaging in an international cooperative project to conserve them. Judging present-state conservation to be difficult due to the considerable bedrock and setting bed collapse that has accompanied wall decay, we are engaging in restoration work that involves taking off the wall paintings, strengthening their colored layers and setting bed, and returning the wall paintings to their original places. These wall paintings are unique and precious because their colors are still vibrant even after 4400 years.

We measured and analyzed the air temperature and humidity of the underground burial chamber, and found that it is ideal and very stable. While there are many underground burial chambers with wall paintings in Egypt, it is rare to find ones that have an environment that is as close to ideal as this one.

Figure 1: *Idout* underground burial chamber.

In order to check the temperature and humidity environment, measuring instruments were placed and automatic measurement has continued every hour. Fig. 2 and Fig. 3 show the results for the outside (outside air) and the inside of the underground burial chamber (inside air).

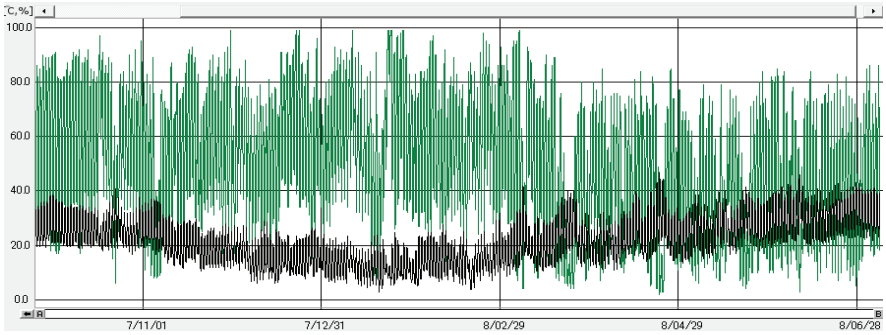

Figure 2: Outside air (black: temperature, green: humidity).

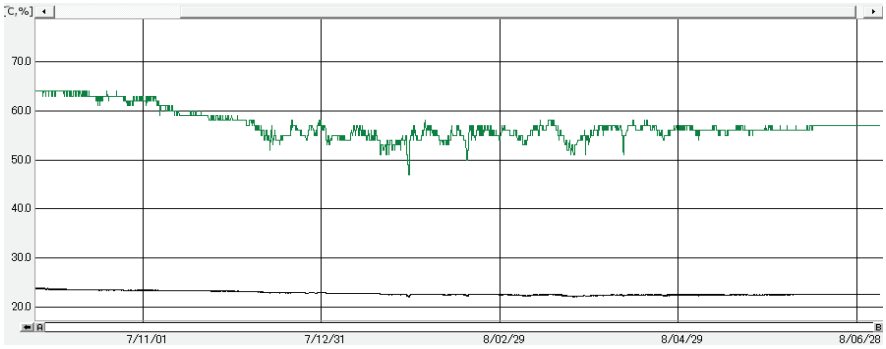

Figure 3: Inside of the chamber (black: temperature, green: humidity).

The Saqqara region is a desert area with extremely large daily temperature and humidity ranges. Outdoors, the difference between the highest and lowest temperatures is close to 20°C. Humidity rises to around 90% in the early morning when the temperature is low, and drops to around 10% during the day when the temperature is high due to strong sunlight (Fig. 2). At night, radiation cooling causes the surface temperature of rocks to fall below the ambient temperature, causing dew condensation to occur early in the morning.

In general, both the diurnal and annual temperature and humidity ranges are small in underground burial chambers, but in the case of *Idout*, this is extremely remarkable, with a temperature of 23±1°C and a humidity of 55±7% throughout the year. This is the ideal environment (Fig. 3). This environment is due factor that has kept the colors of the walls fresh for 4,400 years.

Although the temperature is stable in many underground burial chambers in Egypt, it is common for the humidity to be relatively high, and it is known that there is a mold problem in the tomb of Queen *Neferitari* (Luxor). Even in desert areas, there is a lot of water in the ground and it is normal to be affected by it, but in the case of the underground burial chamber of *Idout*, fortunately, the influence of underground water is extremely less.

3 *MEMI* UNDERGROUND BURIAL CHAMBER

The tomb of *Memi* dates back to around 24 century BC. The underground burial chamber has three beautiful decollated wall covered with awesome paintings. Most of the decollated plaster layers, however, have fallen down off from the bed rock walls. Even at the survived parts, the wall paintings are damaged to high extent.

High humidity in the underground burial chamber and soluble salts in the bed rock are the most important factors for the degradation. Recrystallized salts inside and at the surface of the painted plaster layer, cause the detaching the plaster layers and the painted layers.

Figure 4: Wall Paintings of *Memi* underground burial chamber.

The conditions (temperature and humidity) inside the underground burial chamber were measured as shown in Table 1. The temperature is high and stable, and the humidity is high. This seems to be due to the high water content in the surrounding ground.

In such a condition, if the humidity got down, rapid and massive precipitation of salt crystals would occur. Actually, it is known that the rapid and obvious deterioration by the salt crystallization was noticed during the excavation work.

Table 1: Temperature and humidity inside *Memi* underground burial chamber.

Date	8am	9am	10am	11am	12pm	1pm	2pm
1/8/21	26°/83%	26°/85%	26°/85%	27°/86%	27°/87%	28°/87%	29°/87%
2/8/21	27°/85%	27°/85%	28°/86%	28°/86%	29°/87%	29°/87%	29°/87%
3/8/21	25°/86%	26°/86%	26°/87%	27°/87%	27°/87%	28°/87%	29°/87%
4/8/21	26°/87%	26°/87%	26°/88%	27°/88%	27°/88%	28°/88%	29°/86%
5/8/21	26°/85%	26°/85%	26°/86%	27°/87%	27°/87%	28°/87%	28°/87%
8/8/21	25°/87%	25°/87%	26°/87%	27°/87%	28°/87%	28°/86%	29°/87%
9/8/21	26°/85%	26°/85%	26°/86%	28°/86%	29°/87%	31°/87%	31°/87%
10/8/21	27°/86%	26°/86%	27°/85%	29°/87%	29°/87%	30°/87%	31°/87%
11/8/21	28°/85%	28c/85%	27°/87%	27°/86%	29°/87%	29°/87%	29°/87%
12/8/21	26°/85%	26c/85%	26°/85%	27°/86%	27°/87%	28°/87%	29°/87%
15/8/21	26°/87%	26c/85%	26°/85%	27°/86%	27°/87%	28°/87%	29°/87%
16/8/21	26°/83%	26c/85%	26°/83%	27°/80%	27°/80%	28°/80%	29°/80%
17/8/21	26°/81%	26c/78%	26°/76%	27°/75%	27°/73%	28°/71%	29°/70%
18/8/21	27°/70%	27c/68%	26°/68%	27°/66%	27°/65%	28°/64%	31°/63%
19/8/21	28°/64%	26c/63%	26°/61%	27°/60%	27°/59%	28°/58%	29°/59%
22/8/21	27°/62%	26c/60%	26°/60%	27°/61%	27°/62%	28°/60%	29°/61%
23/8/21	27°/62%	26c/60%	26°/60%	27°/61%	27°/62%	28°/60%	29°/61%
24/8/21	29°/63%	28c/60%	29°/60%	29°/61%	30c/62%	28°/60%	29°/61%
25/8/21	27°/62%	26c/60%	26°/60%	27°/61%	27c/62%	28°/60%	29°/63%
26/8/21	27°/62%	26c/60%	26°/60%	27°/61%	27c/62%	28°/60%	31°/60%
29/8/21	27°/62%	26c/60%	26°/60%	27°/61%	27c/60%	28°/60%	30°/62%
30/8/21	27°/62%	26c/60%	26°/60%	27°/61%	27c/62%	28°/60%	29°/60%
31/8/21	27°/62%	26°/60%	26°/60%	27°/61%	27c/60%	28°/60%	29°/61%
1/9/21	27°/62%	26°/60%	26°/60%	27°/61%	27°/62%	28°/60%	29°/61%
2/9/21	27°/62%	26°/60%	26°/60%	27°/62%	27°/62%	28°/62%	29°/61%
5/9/21	27°/62%	26°/60%	26°/60%	27°/61%	27°/62%	28°/61%	29°/60%

4 WHAT WE SHOULD DO NOW TO CONSERVE

In the case of *Idout*, the condition inside the underground burial chamber is very good. The temperature (23±1°C) and the humidity (55±7%) are ideal and stable. Maintaining this good condition is primal. Therefore, it is fundamentally important to keep the underground burial chamber as airtight as possible, to prevent outside air from entering. When it is necessary to enter the tomb for inspection, conservation work, etc., it is required that the temperature and humidity of the outside air and the inside air be similar to each other in the season and time period. The tomb has been under conservation, and are planned to be opened to the public. In this case, it will be necessary to monitor the environment (temperature, humidity, CO_2 concentration, etc.) and, based on the results, to take measures such as limiting the timing, number of people, and time.

In the case of *Memi*, the condition in the tomb is so different from the case of *Idout,* especially its humidity. The measured values varies between 90% and 60% or lower as shown in Table 1. However, the lower RH value have been measured for the semi-open state during internal investigations, whereas the RH can be considered to be always above 90% when the burial chamber is closed. This high humidity is most probably due to the water contained in the bedrock, and the water containing a large amount of soluble salts which migrate to the surface layer and evaporates, resulting in salt recrystallization.

If the underground burial chamber is kept at a high relative humidity, the equilibrium state is relatively stable. In the case of *Memi*, it has been reported that rapid salt recrystallization occurred during the excavation work. High humidity inside is necessary to minimize rapid salt recrystallization. For this purpose, it would be ideal to completely seal the tomb chamber. However, the monitoring and the conservation measures of the wall paintings are unavoidable. It is necessary, for the time being, to implement artificial humidification and air conditioning while taking measures against microorganisms.

5 CONCLUSION

The greatest cause of deterioration of wall paintings left in the investigated ancient Egyptian tombs is due to recrystallization of soluble salts. After discovery and excavation, how to conserve and utilize these wall paintings is an urgent issue, and many researches are required and are actually being carried out. In this case, the most crucial problems are the recrystallization of soluble salts, the environmental conditions inside the tomb. Even among underground burial chambers from the same region and of the same period, the state of deterioration and environmental conditions are different. Thus, the problems are complex.

Hereby, the participation of many researchers related to salt crystallization is strongly needed.

6 ACKNOWLEDGEMENTS

This work is supported by Grants-in-Aid for Scientific Research of the Japan Society for the Promotion of Science (2022~), and the Grant for Projects for the

Protection, Preservation & Restoration of Cultural Properties & Restoration of Cultural Properties outside Japan of the Sumitomo Foundation (2022~).

REFERENCES

[1] H. Suita, T. Nishiura, et al., "Conprehensive Global Studies for Conservation and Utilization of Cultural Heritage," Center for the Global Study of Cultural Heritage and Culture, Kansai University, 2018.

[2] A. Shoeib, A. Akarish, E. Roznerska, H. Suita, "The State of Conservation for the Wall Paintings of Idout Tomb: Problems and Solutions," in Semawy Menu., Vol. 4, Institute for Conservation and Restoration of Cultural Properties, Kansai University, pp. 9-22, 2013.

[3] A. Shoeib, A. Akarish, H. Suita, "Condition of the Wall Paintings of the South Wall of Idout Tomb and Suggested Treatment (Investigation Report)," in Semawy Menu., Vol. 2, Institute for Conservation and Restoration of Cultural Properties, Kansai University, pp. 17-27, 2010.

[4] A. Shoeib, "Role of Salts in the Deterioration and Collapsing of Ancient Egyptian Stones," in Semawy Menu., Vol. 2, Institute for Conservation and Restoration of Cultural Properties, Kansai University, pp. 29-43, 2010.

[5] Ashraf Ewais et al., "Deterioration Factors that Affect the Mural Paintings at Memi's Burial Chamber in Saqqara, Egypt," in Study of Egyptian Monuments., Vol. 1, Kansai University, pp. 121-146, 2022.

IDENTIFICATION OF CRYSTALLISED DEPOSIT ON OTSU WALLS AND ITS DETERIORATION MECHANISM

Tomoko Uno[1] and Shuichi Hokoi[2]

KEYWORDS

Otsu mud wall, Finishing, Gypsum crystallisation, Structural deformation

ABSTRACT

This study aims to clarify the causes of deterioration on the surface of Otsu walls due to crystallisation. Otsu walls are a type of lime plaster walls fabricated by applying a lime paste mixed with sand to the surface of mud walls, where the surface is repeatedly polished. Although less strong than lime plaster walls (Shikkui-wall), these walls are more durable than normal mud walls. Therefore, they are used for indoor and outdoor finishes, similar to lime plaster finishes. However, deteriorations, such as thin flaking and crystallisation, can be observed on the surface layer of Otsu walls, which are not typically seen on walls finished with normal lime plaster. In particular, deterioration, such as dots with crystallisation, was observed on the surfaces of the interior and exterior Otsu walls of a particular surveyed house. Thus, to identify the causes of deterioration, we conducted (1) a survey of the location and deterioration state of the Otsu wall in the building, (2) a survey of the wall material and layer composition, and (3) an analysis of the crystallised material. The results indicated that deterioration occurred inside the Otsu-finishing layer of the wall due to the crystallisation of gypsum, produced by the reaction of calcium carbonate, a component of the Otsu finishing layer, with sulphides adhering to the surface. Linear and pockmarked deteriorations corresponded to areas where structural cracks were easily promoted. Finally, moisture absorption and desorption occurred preferentially in these parts, resulting in the crystallisation of gypsum.

[1] Mukogawa Women's University, 1-13 Tozaki, Nishinomiya, Hyogo, Japan, uno_tomo@mukogawa-u.ac.jp

[2] Professor Emeritus, Kyoto University, Kyoto, Japan

1. INTRODUCTION

Otsu wall is a type of mud wall, finished using the *Otsu polished finish* (*Otsu miggaki shiage*, 大津磨仕上), in which a lime plaster mixed with sand and strings (*susa*) of paper or hemp is applied to the mud wall surface. The Otsu wall is used for indoor and outdoor finishes in the same way as a lime-plaster wall, even though the polished finish gives a glossy shine to the surface and is not as strong as the finish of the lime-plaster walls (*shikkui*). Depending on the degree of polishing and the type of strings (*susa*) used for the finishing coat, the technique is called *Otsu polished finish* or *ordinary Otsu finish* (*Nami Otsu shiage* 並大津仕上).

The house surveyed in this study is a 120-year-old house with Otsu walls (ordinary Otsu finish), with evident deterioration all over the walls. The linear and pock-marked deteriorations are present, which are quite unique. This deterioration type is not observed on the surface of lime-plaster walls (*Shikkui*). The causes of deterioration might be related to the material and components of the walls and the building structures. Thus, the purpose of this study is to clarify the causes of this deterioration.

To the best of our knowledge, no preceding research has focussed on the deterioration mechanism of Otsu walls. To improve the conservation of these type of walls, the deterioration mechanism should be clarified by evaluating the material components of the wall and building structures.

This study aims to clarify the mechanism of the Otsu wall deterioration based on the evaluation of (1) a survey on the deterioration location and condition of the Otsu wall in the house, (2) a material and layer composition survey of the wall, and (3) an analysis of surface deterioration.

2. SURVEYED HOUSE AND OTSU WALL

2.1 Outline of surveyed house

The surveyed house was the main building of the former Nishio Family House in Suita City, Osaka (Figure 1) [1]. This main building has been undergoing major conservation work since 2022. The house had Otsu walls in many of the interior and exterior walls, and the deterioration of Otsu walls was evident in most of the walls.

2.2 Outline of the Otsu walls

Table 1 lists the finishing coat of two types of Otsu walls. The *Otsu polished finish* (*Otsu migaki shiage*) comprises a ground layer of lime plaster mixed with clay and hempen fibres [Table 1 (2)] and a finishing coat of lime plaster mixed with coloured clay and paper fibres [Table 1 (1)] on the mud wall finished up to the middle layer [2]. The finishing coat was polished using a trowel to obtain a glossy surface.

The degree of the surface gloss depends on the polishing degree. The pressing of the surface and finishing with a rougher degree of polishing than the Otsu polished finish is called the *ordinary Otsu finish* (*Nami Otsu shiage*). The ordinary Otsu

finish differs from the Otsu polished finish in that hemp fibre is used as the finishing layer instead of paper fibre. The lime plaster with sand is sometimes used as the ground layer for ordinary Otsu finish, blending the ground mud layer and the finishing coat.

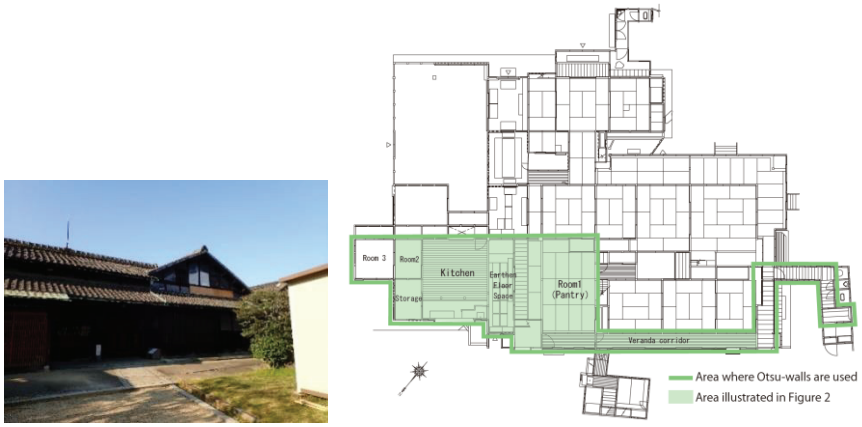

Figure 1 Nishio house (left: outside view, right: plan of the main building [note1]; the area within the solid line frame indicates where the Otsu walls are used. The hatching area shows the area illustrated in Figure 2).

Table 1 Finish layer of the Otsu wall

Finishing coat type		Otsu polished finish (*Otsu migaki shiage* 大津磨仕上)	Ordinary Otsu finish (*Nami Otsu shiage* 並大津仕上)
Material	(1) Finishing coat (*Otsu finish*)	lime plaster, coloured clay, and paper fibres	lime plaster, coloured clay, and hempen fibres
	(2) Ground layer (leveling lime plaster)	lime plaster, clay, and hempen fibres	lime plaster, clay, and hempen fibres / lime plaster, sand, hempen fibres (*Shita kosuri* 下こすり)
Surface polishing		Bright polishing	Not polishing

3. CONDITION OF THE OTSU WALLS

3.1 Location and condition of the Otsu walls

Figure 1 shows the outside view and plan of the house, and Figure 2 shows the photographs of the walls with typical deterioration. The Otsu walls were used for walls in the kitchen, rooms connected to the kitchen, and the veranda corridor. Moreover, Otsu walls were used for exterior finishing; however, we focused on interior walls.

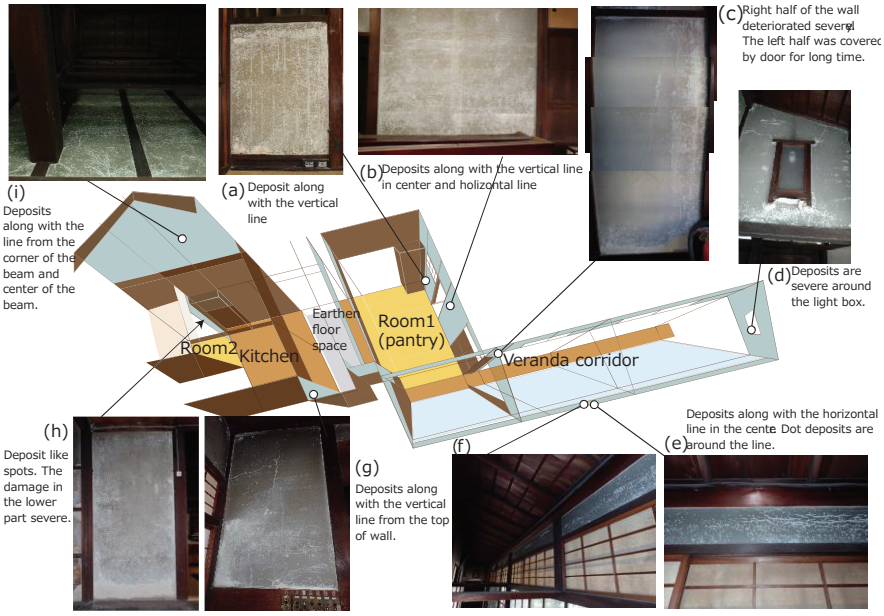

Figure 2 Deterioration conditions of Otsu walls

3.2 Condition survey

Macroscopically, the deterioration can be divided into two types: pockmarked shape deterioration on relatively large surfaces (e.g. Figures 2a, h) and linear deterioration in the middle of the wall (Figures 2e, f, g), the corners, and the middle of the beams (Figures 2d, i). Linear degradation is observed elsewhere also, with longitudinal lines visible in the precipitates, as shown in Figure 2a. It can be observed from Figure 2c that the degradation is concentrated on the right side of the image and less on the left side. In addition, a longitudinal stripe is present in the middle.

Pockmarked deterioration is observed over the entire wide wall (Figures 2a, h) and on the flat areas around the linear deterioration (Figures 2e, f, and Figure 3). In particular, the pockmarked deterioration is worse in the lower part of the wall than in the upper part (Figures 2a and h), where the finishing coat has vanished, and the ground layer has been exposed. Figure 4 shows the enlarged photograph of a wall with pockmarked deterioration. In the area where sediments are found, the finish layer on the surface peels off, as shown in Figure 4 (① and ④), and crystallisation occurs in the interior of the peeled parts (Figure 4②). In addition, crystallisation is not observed in some areas, but the finishing layer exhibits uneven bulges (Figure 4③).

In parts of the linear deterioration of the walls shown in Figures 2a-g, i, and Figure 5, the finishing coat cracks, and crystals are deposited along the cracks. In Figure 2g, deterioration occurs vertically at the centre of the wall, and in Figures 2e and f, deterioration occurs horizontally at the centre of the wall. The walls are flabby. In Figure 5① (Figure 2i), a radial crystallisation is present on the beam in an upward direction. This area is at the centre of the beam and is prone to an upward force from the beam towards the wall and cracks. In addition, as shown in Figure 5② and

in the upper and lower corners of the lighting box (Figure 5③), crystallisation occurs diagonally from the external corner of the beam and lighting box. This area is prone to cracking because of the stress concentration at the corners.

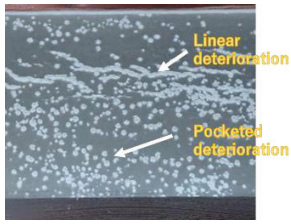

Figure 3 Linear deterioration

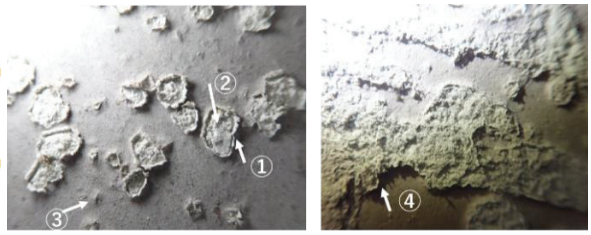

Figure 4 Pocketed deterioration (left Figure 2c, right Figure 2a)

Figure 5 Linear deterioration (left Figure 2i, right Figure 2d)

4. MATERIAL AND LAYER COMPOSITION OF OTSU WALL

The layer composition of the walls at the two locations described in Figures 2a and 2c is shown in Figure 6. Both walls are composed of (1) an Otsu finishing coat, (2) a ground layer, (3) layers of mud plaster, and a rough wall with structural wood. The Otsu finishing appearance comprises two layers: one with fewer fibres on the surface side and the lower layer with more fibres. The crystallisation produced fine crystals. Additionally, the vertical deterioration line of the wall in Figure 2a corresponds to the edges of the wooden support inside the wall.

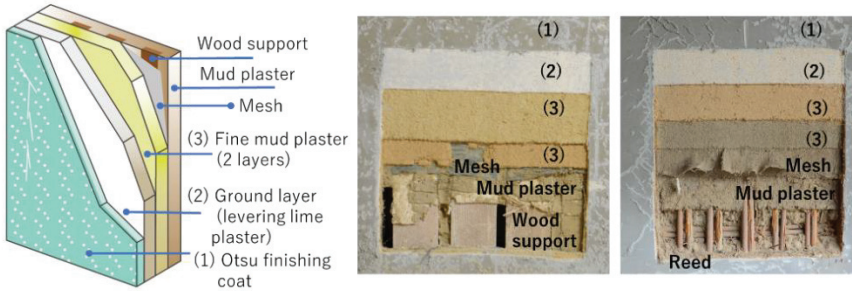

Figure 6 Layer composition of Otsu wall in the walls shown in Figures 2a and 2c

5. ANALYSIS OF CRYSTALLISATION MATERIAL

5.1 Analysis method

X-ray diffraction (XRD) and scanning electron microscopy with energy dispersive X-ray (SEM/EDX) detector were used to analyse the materials deposited on the crystallisation and the constituent materials of each layer of the Otsu wall. [note 2]

Samples for the XRD analysis were obtained from each wall layer, shown in Figures 2a and c, to detect the material on each layer. XRD analysis was performed using Aeris (PANalytical, Netherlands); the X-ray output was set to 40 kV and 80 mA.

Samples for SEM/EDX analysis were obtained from the bottom of the lighting box shown in Figure 2d (Figure 7, left, sample A), where deterioration was significant, and from the sidewall of the veranda corridor shown in Figure 2c (Figure 7, right, sample B), where no crystallisation occurred.

Figure 7 Sample and the collected part (upper-left: the collected part of sample A; bottom left: sample A; upper-right: the collected part of sample B; and bottom right: sample B where the deterioration is not evident)

5.2 Results of analysis

5.2.1 Results of XRD

(1) Detected materials in the wall layer

The analytical results are listed in Table 2. In particular, gypsum ($CaSO_4$ $2H_2O$) and quartz (SiO_2) were detected in the crystallisation on both samples of the wall shown in Figure 6 (middle and right); quartz is the main component of the sand, and gypsum was not found in the materials used for the Otsu wall. Gypsum was detected in the (1) Otsu finishing coat on both walls but was not detected in the (2) ground layer of lime plaster. Quartz (SiO_2) and calcium carbonate ($CaCO_3$) were the components with major contributions detected in the (2) ground layers. SiO_2 and $CaCO_3$ are major components of lime plaster. In particular, SiO_2 was the main component detected in (3) fine mud plaster layers 1 and 2 and rough mud plaster.

(2) Detected materials in sample B that was not deteriorated.

In sample B, where no crystallisation was observed, $CaCO_3$, a component of the finishing layer, was detected, but gypsum was not detected.

Table 2 Materials detected using XRD

	West wall in Figure 2a	Veranda corridor south wall in Figure 2c
Crystals	-	Gypsum, Quartz
(1) Otsu finishing coat	Quartz, Gypsum	Quartz, Gypsum
(2) Ground layer of lime plaster	Calcium carbonate, Quartz	Calcium carbonate, Quartz
(3) Fine mud plaster layer 1	Quartz and others	Quartz and others
(3) Fine mud plaster layer 2	Quartz	Quartz and others

5.2.2 Results of SEM analysis

Figure 8 shows the SEM images and their elemental mapping. The upper images correspond to sample A (Figure 7, left) with deterioration. In contrast, the lower images correspond to sample B (Figure 7, right) without deterioration.

In sample A, the deteriorated areas are evident, and the central area is disrupted. Carbon (C) was present in small quantities in the ground layer, oxygen (O) was uniformly distributed, and silicon (Si) was abundant in the finishing layer. Calcium (Ca) was found in the ground layer and the finishing layer. Sulphur (S) was present in a thin layer on the surface of the finishing layer, as well as inside the finishing layer in deteriorated areas.

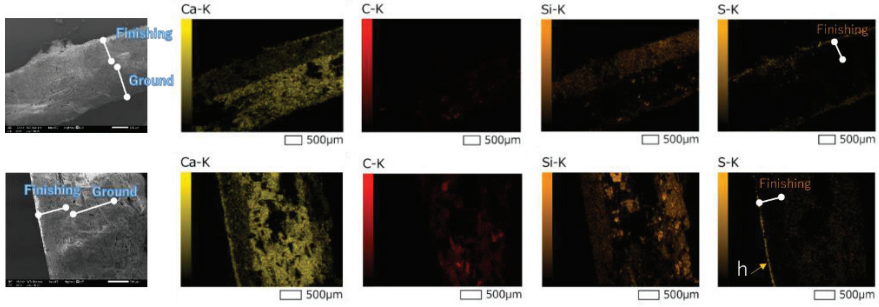

Figure 8 SEM images and elemental mapping (upper: sample A, lower: sample B).

In sample B (Figure 8, bottom left), no crystallisation is observed; the surface is smooth, with no disruption in the finishing or ground layers. C was uniformly present, whereas O and Si were more abundant in the ground layer than in the finishing layer. Ca was more abundant in the surface and ground layers, as well as in the

finishing layer. S was present in thin layers on the surface. The layer of S was approximately 20 μm thick.

5.3 Discussion of Analysis

The results of the XRD analysis indicated that the crystals can be identified as gypsum.

The main components of gypsum, Ca, C, and O were contained in lime, the material of the finishing coat. Because the finishing coat was primarily composed of sand and lime, the ground layer was mainly composed of lime; however, S was not present in the material composition. The SEM observations of sample B that did not show an evident deterioration indicated that the sulphide was deposited on the surface of the finishing coat. Therefore, the results suggested that the sulphide was supplied from the outside and not from the inside of the wall. The analysis suggested that the S deposited on the surface of the finishing coat migrated to the inside of the finishing coat, and gypsum was subsequently formed inside the finishing coat. Because crystallisation occurred inside the finishing layer, it reflected the situation shown in Figure 4, where crystallisation appears to exhibit an unusual distortion from inside the finishing coat.

6. DETERIORATION MECHANISM

Figure 9 illustrates the deterioration process of the Otsu wall. The crystallisation on the Otsu wall was caused by gypsum that might be deposited due to sulphide adhering to the surface in the form of SO_2 or other substances (Figure 9②) and reacting with calcium hydroxide and/or $CaCO_3$ in the finishing coat (Figure 9③). Because gypsum was not detected as a major contributing component in the samples without crystallisation, the gypsum crystallisation reaction might be unlikely to proceed by S adhering to the surface.

Sulphide becomes sulphite in the presence of moisture (Figure 9②), whereas sulphite readily reacts with $CaCO_3$ to form gypsum. Moisture condensation may occur on the wall surface if the relative humidity of the room is high, and the wall is colder than the ambient air temperature. Because the room in which the Otsu wall was present was near the kitchen, the presence of high humidity in the room seemed possible, and the supply of moisture to the wall side was considered sufficient. This implies that the sulphides on the surface received moisture supply and moved with the moisture to the inside of the finishing coat, where they reacted with the $CaCO_3$ and crystallised gypsum.

Otsu walls were fabricated relatively densely by well-polishing the surface; however, where cracks developed on the surface, the more porous inside parts were exposed, thereby accelerating moisture absorption and desorption.

The linear deterioration is mainly present in areas where structural stresses are prone to concentrate, where material edges are present, or both, and at the border inside the wall. In other words, where cracks exist in a linear pattern owing to structural factors, moisture absorption and desorption occur preferentially, and sulphides adhering to the surface crystallise into the interior with moisture, causing reactions in the interior and precipitation in cracked areas.

The pockmarked deterioration observed on a particular wide surface can be explained by the same mechanism. Figure 10 shows the surface of a wet sample [note 3] of a new Otsu wall. Several microcracks are distributed randomly on the surface. The Otsu wall on the site also had multiple cracks on the surface (Figure 9①), which could absorb moisture easily (Figure 9②). Thus, these observations explain that the crystallisation can occur on the surface at random due to the microcracks in the structure cracks (Figure 9③, ④).

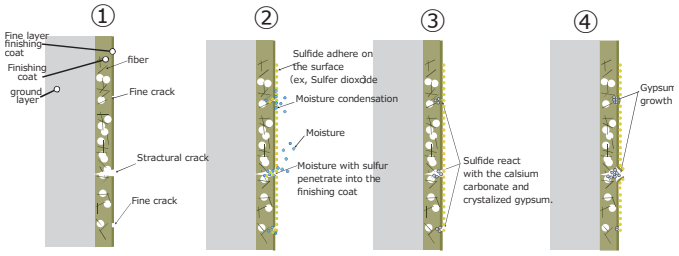

Figure 9 Deterioration mechanism

Figure 10 Surface of a sample

7. CONCLUSION

In this study, the deterioration with crystallisation observed in the Otsu wall was investigated based on the surveys of the material and layer composition of the wall and surface deterioration. The following conclusions were drawn.

(i) Deterioration observed in the Otsu wall was due to gypsum crystallisation.

(ii) Of the gypsum components, sulphur (S) could have been supplied from the outside (ambient air), not from inside, of the wall materials.

(iii) S compounds adsorbed on the surface moved inside with the moisture movement and reacted with $CaCO_3$, the main component of the finishing layer, resulting in the crystallisation of gypsum inside the finishing layer.

(iv) Linear and pockmarked degradation were observed. Linear degradation corresponded to wall areas where surface cracks might occur owing to structural stress. This observation suggests that moisture absorption and desorption occurred preferentially in these areas, developing gypsum.

Elucidating the mechanism of the pockmarked deterioration is a future task.

NOTE

1 The plan provided by the Architectural Research Association was included.

2 For the analysis by XRD and SEM/EDX, cooperation was provided by Prof Chie Sawatari, Faculty of Life and Environment, Mukogawa Women's University.

3 The sample made by the way of ordinally Otsu finishing same as the finishing of the surveyed house. The sample size is 30 cm square.

ACKNOWLEDGEMENTS

Part of this research was funded by the Matsuikadohira Memorial Foundation under grant 2022 (7th). We also acknowledge the cooperation of Mr Kakimoto and Ms Kawai of Suita City, Ms Nonobe and Mr Tsuji of the Architectural Research Association, Mr Sato of Sato Plastering Works, and Prof. Sawatari of the Faculty of Life and Environment at Mukogawa Women's University. We express our gratitude to the reviewers.

REFERENCES

[1] Suita Museum “Former Nishio Family House” website, https://www.suita.ed.jp/hak/Kyunishioke/kyunishioke.html, accessed June 20, 2023.

[2] K. Sato and S. Sato (2001) *The work and techniques of clay walls and plasterers* (土壁・左官の仕事と技術), Gakugei pub. *(in Japanese)*

[3] The Society of Inorganic Materials, Japan (1986), *Basics of gypsum, handbook of gypsum and lime*. *(in Japanese)*

LONG-TERM MONITORING OF MICROENVIRONMENT AND WALL PAINTINGS INFLUENCED BY SOLUBLE SALTS AT MOGAO GROTTOES, CHINA

Hailing Chen[1], Gangquan Chen[1], Neville Agnew[2], Martha Demas[2], Bomin Su[1], and Qinglin Guo[1]

KEYWORDS

Mogao Grottoes, Wall painting, Salt damage, Tourist rush season, Microenvironment

ABSTRACT

The Mogao Grottoes, consisting of 45000 m^2 of wall paintings and 2415 Buddhist sculptures dating from the 4th to the 14th century A.D., are located in arid region of northwest China. Severe deterioration caused by salt activity has been observed on numerous wall paintings at the Mogao Grottoes. To evaluate the effect of microenvironmental changes in caves induced by mass tourism on salt damage of wall paintings, climatic condition, microenvironment in two test caves, visitors and wall paintings showing salt-related deterioration were monitored from 2006 to 2013. Soluble salts accumulated in earthen plasters were investigated by the methods of IC and CCSEM. Moreover, the phase diagram of potential dominant salt was used to link the environmental condition with salt damage of wall paintings. During the 8-year monitoring period, the visitation strategies for two test caves were designed to be opposite. Results showed that plaster disruption of wall paintings worsened mainly in tourist rush season, when high relative humidity appeared in visited and non-visited caves. Sodium chloride was inferred to be the potential predominant salt causing continuous damage to wall paintings. Deliquescence and crystallization cycles of salt mixtures driven by microenvironmental fluctuations were considered to be responsible for the weathering of wall paintings. This research work developed a cost-effective methodology for long-term monitoring of salt weathering process of wall paintings, meanwhile, it could guide the visitor management and preventive conservation of wall paintings in cultural heritage sites of arid regions.

[1] Monitoring Center of Dunhuang Grottoes, Dunhuang Academy, Dunhuang, Gansu, China, chenhl_131@163.com

[2] The Getty Conservation Institute, Los Angeles, USA

1 INTRODUCTION

The Mogao Grottoes, a famous World Heritage Site, is about 25 km to the southeast of Dunhuang oasis city along the ancient Silk Road. Situated in a desert landscape, the grottoes lie at the eastern foothills of the Mingsha Mountains, southern margin of the Gobi Desert. Near the west bank of Daquan River, the caves of varying size were excavated into the cliff face (10-40 m in height and 1680 m in length) in four or five levels. In the site, 45000 m^2 of wall paintings, 2415 painted sculptures,and 5 wooden-structure eaves dating from the 4th to the 14th century A.D. are preserved. Salt damage is one of the most widespread threats to the long-term existence of wall paintings at the Mogao Grottoes. There are several forms of deterioration induced by salts such as flaking, crater eruption, salt efflorescence and plaster disruption (Figure 1). In all these deterioration phenomena, plaster disruption is recognized as the most harmful damage owing to the lack of effective treatment measures [1, 2]. Plaster disruption is a weathering phenomenon of wall paintings which refers to the loss of cohesion in earthen plaster resulting from salt activities. It can lead to continuous powdering of plaster and therefore the resulting paint loss.

Figure 1: Salt damage of wall paintings at Mogao Grottoes; (a) plaster disruption; (b) crater eruption; (c) salt efflorescence.

The degree of salt damage occurring in porous building materials depends on material characteristic, salt species, salt concentration and environmental condition. The porous networks of materials can influence the location of salt crystals (i.e., subflorescence and efflorescence of salts) and crystallization pressure significantly. Materials with small pores tend to suffer more severe damage caused by salt crystallization [3, 4, 5, 6]. Sodium sulfate is more destructive for building materials than sodium chloride due to its stronger ability to supersaturate, which provides the driving force for the generation of stress [3, 7, 8]. Weathering pattern of stone caused by sodium sulphate is affected obviously by salt concentration, temperature and relative humidity because of the change in evaporation rate [9, 10].

Wall painting at the Mogao Grottoes is a multi-layered architectural structure. Base layer is the conglomerate rock that serve as the substrate for wall paintings. Earthen plaster including the lower coarse plaster (5-30 mm in thickness) and the upper fine plaster (4-5 mm) is intermediate layer, which is composed of mud plaster, sand and straw and act as a preparing layer for painting. On the outermost layer, a white ground (20-300 μm) is applied directly on the surface of fine plaster and then mineral pigments mixed with bonding media are painted onto the ground [11, 12]. Among them, earthen plaster layer is the most key structure because it connects the rock body to the paint layer. Earthen plasters with a porosity between 25-33% are very porous and sensitive to moist air. They favor the migration of soluble salt

originating in the conglomerate rock through themselves under a humidity differential [1, 13, 14, 15]. Since Mogao Grottoes was officially opened to visitors in 1979, visitor numbers have showed a significant increase trend, especially in recent two decades. For example, visitor numbers increased from 537 thousand in 2006 to 778 thousand in 2013, which even reached a high of 2.2 million in 2019. This paper aims to evaluate the impact of microenvironmental variations in caves induced by visitors on the continuous salt-related deterioration of wall paintings at Mogao Grottoes, as well as to develop a cost-effective method for long-term monitoring of salt weathering process of wall paintings.

2 MATERIALS AND METHODS

2.1 Description of the Test Caves

Cave 25 (960-1127 AD) and Cave 26 (705-781 AD) exhibiting severe salt-related deterioration phenomena (disruption of plaster) were selected as the test caves. These two caves are adjacent and similar in architectural form (Figure 2). Cave 25, a medium-sized cave with a main chamber of about 128.6 m^3, is fitted with an outside aluminum door and an inside wooden door. Distinct from Cave 25, Cave 26 just with an aluminum door is a quite smaller cave and the volume of its main chamber is 43.6 m^3. There are shutter-type windows on upper and lower parts of aluminum doors of caves, which permit air exchange between the outside and the inside of caves. The series of tests were carried out from 2006 to 2013. Cave 26 was open to routine visitation, while Cave 25 was closed between January 2006 and April 2008. Due to the heterogenity of wall paintings, the conditions of deterioration induced by salts were different in two test caves, which make the comparison of deterioration rate in Cave 25 and Cave 26 difficult. To understand how the deterioration phenomena in same cave respond to microenvironmental changes, reversed management strategy therefore was conducted from May 2008 until December 2013. In other word, Cave 26 was switched to be a non-visited cave and Cave 25 became a visited cave.

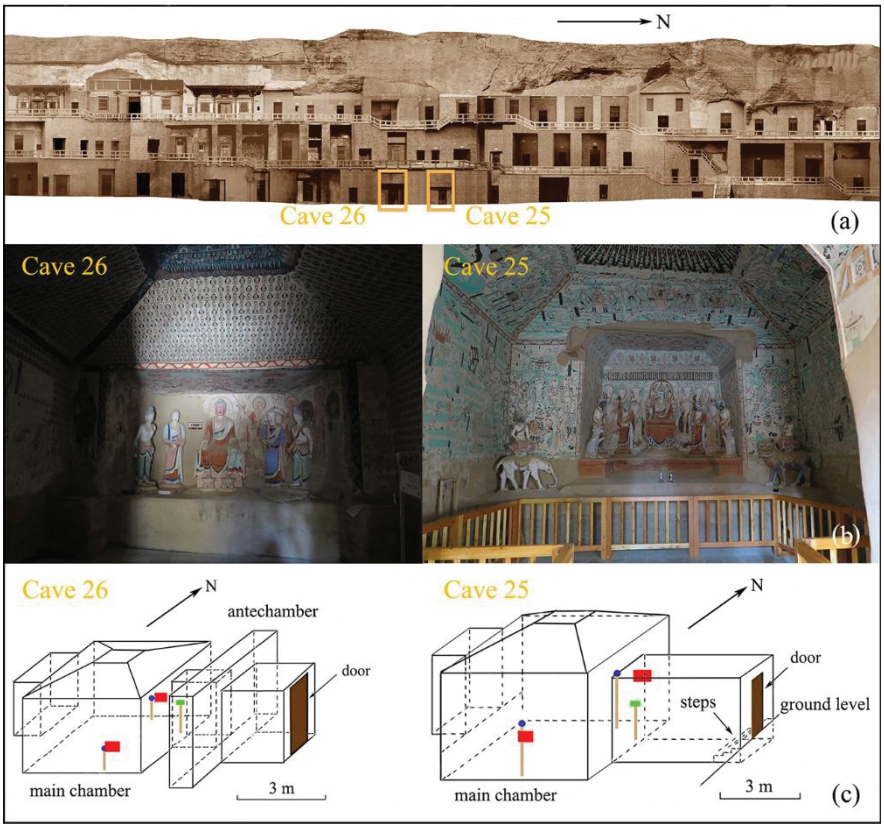

Figure 2: Overview of the study site; (a) partial elevation of Mogao Grottoes; (b) interior of main chamber of Cave 25/ 26; (c) monitoring areas of wall paintings (red filled squares) and the position of sensors for temperature and humidity (blue filled circles) and visitor numbers (green filled squares).

2.2 Methods

In order to estimate the rate of deterioration quantitatively, representative areas of wall paintings influenced by salts (exhibiting severe plaster disruption combined with flaking phenomena) were documented periodically by the methods of taking photos and weighing. Between 2006 and 2013, selected areas of wall paintings were photographed under same raking light and direct light twice a year (Figure 3). One was conducted at the beginning of tourist rush season (the end of April or the beginning of May) and the other at the beginning of tourist off-season (the end of October or the beginning of November). The photos taken at the same location at different times were compared under naked eyes and the changes of wall paintings (i.e. paint layer loss) were quantified through an image processing software (AutoCAD). At the same time, materials falling from the corresponding monitoring areas of wall paintings (mainly powdery plaster, few flakes of paint) were collected by papers placed at the base of walls and then weighed.

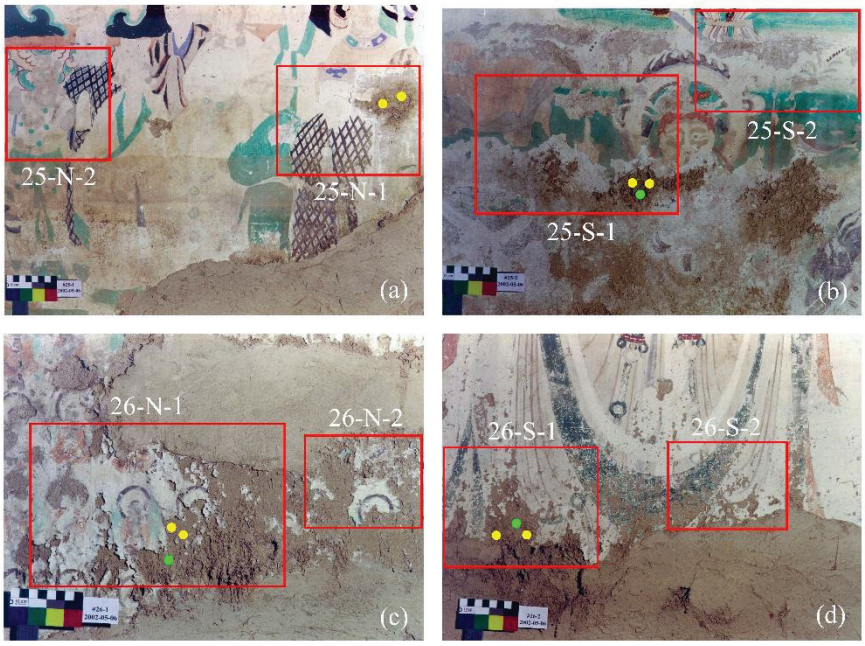

Figure 3: Location of photographic monitoring (red unfilled squares) and sampling points for IC analysis (yellow filled circles) and CCSEM analysis (green filled circles) in detail; (a) north wall of main chamber in Cave25; (b) south wall of main chamber in Cave25; (c) north wall of main chamber in Cave26; (d) south wall of main chamber in Cave26; monitoring areas of wall paintings and samples for salt analysis share the same numbers marked next to the red unfilled squares.

Eleven samples of fine weathered particles were taken from loose earthen plaster layers in corresponding zones of photographic monitoring, where relatively severe deterioration phenomena occurred, by using a scalpel and weighing papers. Subsequently, they were analyzed by two types of methods at the laboratory. A Dionex ion chromatography system (IC) was employed following the procedure reported previously to recognize the species and contents of water-soluble ions in samples [2]. The images and elemental compositions of sample particles were obtained by using a computer-controlled scanning electron microscopy system (CCSEM). The detailed information of sampling points for salts analysis were illustrated in Figure 3.

The monitoring of climate, microenvironment and visitor numbers were performed from 2006 to 2013. The data of temperature, relative humidity, rainfall, wind speed and direction outside caves were collected every 15 min by a weather station located on the top of the cliff near the famous nine-storied temple. In the main chamber of each test cave, two miniaturized data loggers for acquiring temperature and relative humidity data were mounted on wooden supports, which were placed against the wall exhibiting salt weathering phenomena, and infrared photosensors for gathering data of visitors were positioned at the entrance of caves (Figure 2). During the day, the visitors and conservators were allowed to enter the caves and

a two-minute interval was therefore chosen to monitor microenvironmental conditions and visitor numbers from 7 am to 7 pm. At night when caves were closed, the interval was prolonged to 15 min.

3 RESULTS AND DISCUSSION

3.1 Deterioration Processes of Wall Paintings

The rate of paint layer loss are used to evaluate the deterioration rate of wall paintings in long term. Figure 4 (a-c) displays the proportion of paint loss area to the total area of monitoring zones on each wall marked by red unfilled squares in Figure 3 from 2006 to 2013. Wall paintings presented various deterioration processes from one wall to another. Except for monitoring area on the north wall of main chamber in Cave 25, different degree of paint layer loss was observed to occur in monitored zones of remaining walls. The wall paintings on the north wall of Cave 26 deteriorated most rapidly with a paint loss of about 9.40% during the 8-year monitoring period, followed by that on the south wall of Cave 25 (4.18%). The south wall of Cave 26 showed the least paint loss (1.21%).

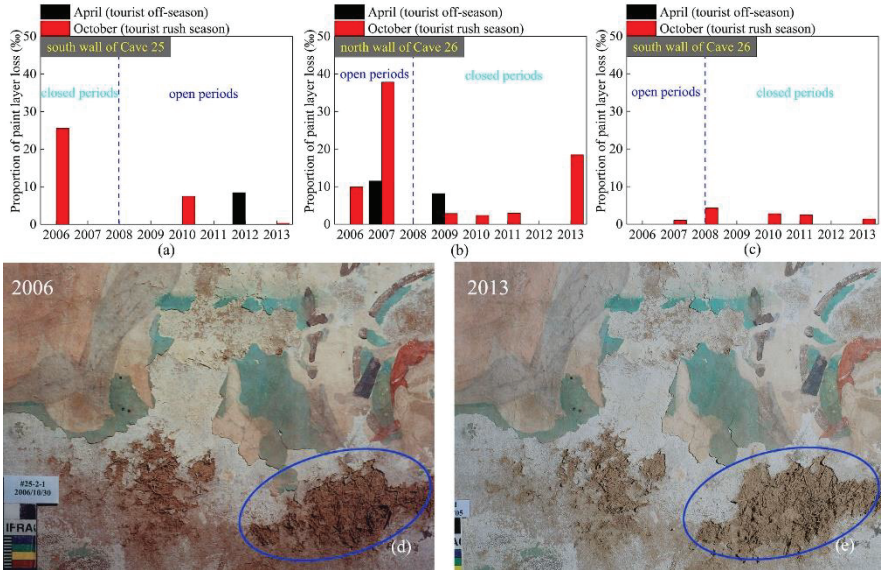

Figure 4: (a)-(c) The proportion of paint loss area to the total area of monitoring zones on each wall from 2006 to 2013; (d) monitoring area 25-S-1 on October 30, 2006, showing severe deterioration (plaster disruption occurring in the lower zone); (e) the same area on November 5, 2013, displaying an increase in loss of paint layer.

Meanwhile, the weathering behaviors of wall paintings exhibited an obvious seasonal characteristics (Figure 4 (a-c)). The phenomena of paint layer loss commonly appeared in the tourist rush season (from May to October), while that occasionally happened in the tourist off-season (from November to next April). It seems that there is a correlation between visitation and paint loss. In April 2008, management

strategies for Cave 25 and Cave 26 were reversed, which meant Cave 26 was closed to visitation while Cave 25 was open to visitation after that. As shown in Figure 4 (b), the rate of paint layer loss on the north wall of Cave 26 declined clearly after 2008. The maximum rate of paint loss on the north wall of Cave 26 before 2008 was as high as 3.78%, which was reduced to 1.85% after 2008. It indicates that the weathering process of wall paintings on the north wall of Cave 26 was slowed down after Cave 26 was closed. The deterioration rate of wall paintings showed a positive relationship with the visitation. However, the weathering behaviors of wall paintings on the south wall of Cave 26 was not in correspondence with this conclusion. No evident decrease in rate of paint loss was found on the south wall of Cave 26 after 2008 (Figure 4 (c)). This is likely because the rate of paint loss on the south wall of Cave 26 was too low to reflect the effect of visitation on it. Over the 8-year test period, the maximum deterioration rate of wall paintings on the south wall of Cave 26 was only 4.33‰. Similarly, a significant increase in the rate of paint loss didn't happen on the south wall of Cave 25 after 2008 as expected. As shown in Figure 4 (a), the phenomenon of paint layer loss on the south wall of Cave 25 only occurred discontinuously for three times. Owing to this reason, no trend of deterioration rate of wall paintings could be found. Nevertheless, what is certain is that the diseases of wall paintings related to salts in test caves were active and developed slowly. This can be illustrated by the example shown in Figure 4 (d and e). Through comparing the plaster disruption in zone 25-S-1 marked by blue ellipses between 2006 and 2013, it can be found that the deterioration slightly spread to adjacent zones and as a consequence the extent of paint layer loss expanded.

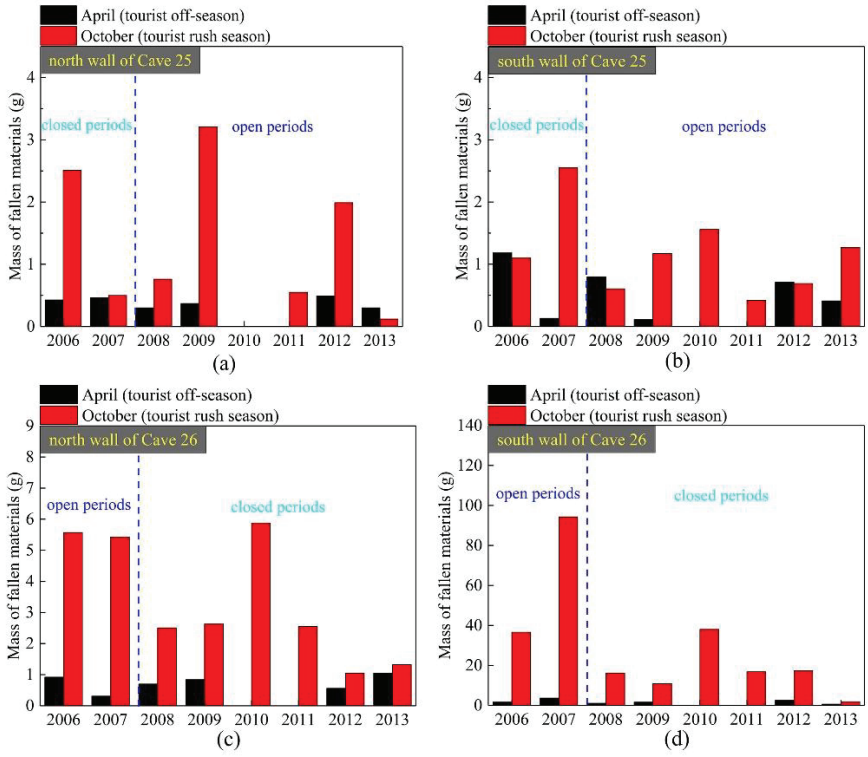

Figure 5: Mass of fallen materials from 2006 to 2013.

Figure 5 illustrates the mass of materials falling from areas of photographic monitoring on four walls. The amount of fallen materials from south wall in Cave 26, which consisted mainly of earthen plasters, but also minor paint flakes, was largest (Figure 5 (d)). It had a maximum value of 94.27g in October 2007. The north wall of Cave 26 had the second largest mass of fallen materials with earthen plasters, wheat straw and paint flakes as main component. Its maximum mass was just 5.88 g, which was far below that of south wall in Cave 26. The south wall of Cave 25 and the north wall of Cave 25 had comparable mass of fallen materials, which were slightly lower than that from north wall of Cave 26 (Figure 5 (a-b)). Unlike Cave 26, the fallen materials collected in Cave 25 comprised a large proportion of dust except for earthen plasters and paint flakes.

In addition, much more fallen materials were collected in October than in April, which was consistent with the variation features of paint loss (Figure 5 (a-d)). In tourist off-season from 2006 to 2013, the total mass of fallen materials gathered at the base of north wall in Cave 25, south wall in Cave 25, north wall in Cave 26 and south wall in Cave 26 was 2.35g, 3.34g, 4.38g and 11.30g respectively. While, the corresponding mass of fallen materials in tourist rush season reached 9.64g, 9.37g, 26.94g and 231.95g. Simultaneously, an obvious mass reduction of fallen materials happened on the north wall and south wall of Cave 26 after 2008. But the north wall and south wall of Cave 25 didn't show an evident increase in mass of fallen materials with the opening of Cave 25 in 2008. Furthermore, it must be noted that not all the materials gathered were from the zones of photographic monitoring. The fallen materials might be from the neighboring area which were beyond the monitoring area, or even come directly from outdoor. For instance, abundant weathered plasters collected at the base of south wall of Cave 26 actually fell from the part below monitored zone, where restoration had been performed and the new plasters deteriorated severely (Figure 3 (d)). For this reason, the mass of fallen materials could merely serve as a reference index for the estimate of damage degree of wall paintings.

According to the above analysis, it can be concluded that the weathering of wall paintings mainly happened in tourist rush season regardless of whether the cave was open or closed. The deterioration rate of wall paintings varied from wall to wall and from year to year. A positive correlation between the deterioration rate of wall paintings and visitation is demonstrated by the weathering behavior of monitored wall paintings in Cave 26.

3.2 Salt in Earthen Plasters

The soluble ion contents in weathered earthen plasters were determined by means of ion chromatographic analysis and were expressed as the weight percent of plasters. The total soluble ion content in the samples varied from 2.71 % to 10.04 % (Table 1). Among all four monitored walls, the north wall of Cave 26 has the highest salt ion content with an average value of 8.94 %, while a lower salt ion content is found in the south wall of Cave 25, with an average value of 4.89 %. The north wall of Cave 25 shows the lowest salt ion content, the average value of which is 2.81%. Overall, the distribution trend of salt ion content matches the deterioration

rate of wall paintings observed, which seems to imply that the higher the ion content is, the greater the paint loss is.

On the aspect of the types of salt ions, chlorine ion and sodium ion are the most abundant ions. It is especially evident in the north wall of Cave 26, where the contents of chlorine ion and sodium ion, with the mean of 4.25% and 2.94% respectively, greatly exceed that of other salt ions. In four kinds of cations, calcium ion is the second most ion, followed by magnesium ion and potassium ion. The second most anion is nitrate ion and the amount of sulfate ion is least. Moreover, the content of sulfate ion in south wall of Cave 25 and north wall of Cave 26 is very close to that of nitrate ion, while the north wall of Cave 25 and south wall of Cave 26 have an obviously lower sulfate ion content.

Table 1: The soluble ion content in samples of earthen plasters.

Sample #	Soluble ion content (weight %)							Total content of soluble ions (weight %)
	Cl^-	NO_3^-	SO_4^{2-}	Na^+	K^+	Mg^{2+}	Ca^{2+}	
25-N-1	0.7833	0.8726	0.2571	0.4213	0.0300	0.1463	0.3923	2.9029
	0.9255	0.8124	0.1801	0.4323	0.0240	0.0543	0.2827	2.7112
25-S-1	1.5292	0.9721	0.7547	0.9003	0.0288	0.1159	0.4104	4.7113
	1.6059	1.0005	0.9069	0.9724	0.0271	0.0617	0.4874	5.0618
26-N-1	4.9302	0.6590	0.5738	3.4830	0.0292	0.0857	0.2840	10.0449
	3.5656	0.8302	0.7562	2.4034	0.0321	0.0484	0.2039	7.8398
26-S-1	1.4997	0.7053	0.2835	0.9495	0.0344	0.2196	0.2324	3.9244
	1.2932	0.8412	0.2766	0.7009	0.0320	0.1172	0.1565	3.4176

In order to infer the types of salts accumulated in the weathered earthen plasters, CCSEM technology was used to analyze the powdered plasters. Figure 6 displays some of the micrographs of salt particles, in which the morphology and size of salt particles can be seen clearly. Besides, elemental distribution of salt particles is also shown in the far right column of each micrographs, from which potential salts can be speculated. For example, in the first micrograph of Figure 6 (a), the distribution rang of sodium extremely matches that of chlorine. Meanwhile, they exactly coincide with the profile of salt particle. Based on this and combining with the analysis results of soluble ions, sodium chloride (NaCl) is considered to be the potential salt present in the plasters of south wall of Cave 25. Similarly, other species of salts could be inferred. And sodium chloride (NaCl), magnesium chloride ($MgCl_2$), calcium chloride ($CaCl_2$), potassium chloride (KCl) and calcium sulfate ($CaSO_4$) are deduced to be the potential salts existing in all three samples. Moreover, there is probably sodium sulfate (Na_2SO_4) in the north wall of Cave 26 and south wall of Cave 25 according to the elemental distribution shown in the middle micrographs of Figure 6 (a and b). While, same elemental distribution doesn't appear in the sample from south wall of Cave 26. This corresponds with the analysis results for sulfate ion in the plasters of four walls (Table 1).

It must be pointed out that CCSEM technology can't be used to speculate about the presence or absence of nitrate owing to its technical defects. But according to the

good correlation between soluble ion content and elemental distribution, it is presumed that nitrate is likely to exist in the plasters of four monitored walls. There is no doubt that salt mixtures cause damage to the wall paintings and sodium chloride (NaCl) is the predominant potential salt. Nitrate is probably another potential salt but its species are still unclear. Sodium sulfate (Na_2SO_4) is a potential hazardous salt to the wall paintings of south wall in Cave 25 and north wall of Cave 26. Additionally, magnesium chloride ($MgCl_2$), calcium chloride ($CaCl_2$), potassium chloride (KCl) and calcium sulfate ($CaSO_4$) are identified to be the potential salts existing in weathered plasters as well, but they are not the main potential salts owing to their low contents. By the comparison of salt analysis results and deterioration processes on four monitored walls, it can be found that the rate of deterioration of wall paintings is positively related to the total content of soluble ions. These investigation results basically coincide with the conclusions of previous studies on the salt damages of wall paintings at Mogao Grottoes [1, 2, 11, 15, 16], with the exception of high content of nitrate ion being found in the samples. And this exception might be explained by the difference between caves.

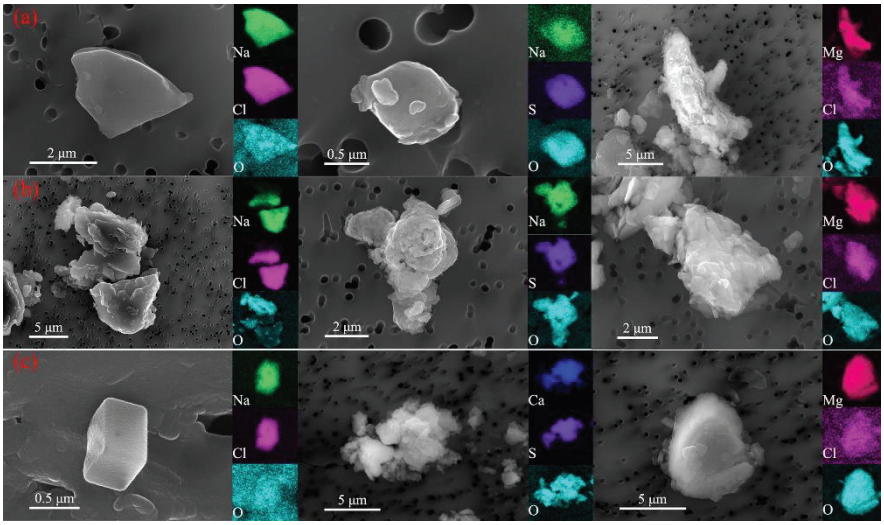

Figure 6: Micrographs of salt particles with their EDX mapping of elemental distribution; (a) from left to right: NaCl, Na_2SO_4 and $MgCl_2$ in sample 25-S-1; (b) from left to right: NaCl, Na_2SO_4 and $MgCl_2$ in sample 26-N-1; (c) from left to right: NaCl, $CaSO_4$ and $MgCl_2$ in sample 26-S-1.

3.3 Characteristics of Microenvironment in Visited Cave and Non-visited Cave

The microenvironment in test caves and its relationship with external climatic conditions and visitor numbers from July 16, 2006 to July 19, 2006 are shown in Figure 7 (a and b). Visitation has a remarkable effect on the thermo-hygrometric conditions of the caves. During opening hours of caves (from 8 am to 5 pm), the temperature and relative humidity in visited cave (Cave 26) spiked with the entry of visitors, and decreased sharply with the leaving of visitors. The degree of fluctuations in temperature and relative humidity highly depended on the frequency of visitation.

In contrast, the temperature and relative humidity in non-visited cave (Cave 25) were quite stable, even during rainy days. During closed hours, microenvironmental parameters in both visited and non-visited caves kept relatively stable. In general, the change trend of temperature and relative humidity in visited cave tended to be in coincidence with external climate within opening hours, although with a delay and smooth variation.

Figure 7 (c and d) exhibit the long-term changes of monthly maximum relative humidity, its corresponding temperature and monthly mean diurnal variation in relative humidity from 2006 to 2013. Before April of 2008, the monthly maximum relative humidity in Cave 26 fluctuated more sharply during annual cycle than that in Cave 25, with a maximum range from 16.2 % (January 2007) to 80.6% (July 2006). Its corresponding temperature behaved similarly, with a maximum range between 5.9 ℃ (February 2008) and 22.2 ℃ (October 2007). After visitation strategy for these two caves was switched (from April 2008 to December 2013), the monthly maximum relative humidity of Cave 25 during tourist rush season, when the precipitation was relatively large, exceeded that in Cave 26 gradually. And an increase in its corresponding temperature was also observed, which rose to the same level with that of Cave 26. Figure 7 (d) reveals the correlation between visitation and the daily fluctuation of humidity clearly. Cave 26 had an obviously higher monthly mean diurnal variation in relative humidity ranging from 4 % to 14% during tourist rush season before 2008 than Cave 25. Thereafter, this pattern was reversed. It is important to mention that the relationship between relative humidity in Cave 25 and that in Cave 26 during tourist off-season didn't change as the changing of visitation strategy. Analogous behavior was found in temperature. Therefore, we can conclude that the more intense fluctuations of thermos-hygrometric parameters in visited cave during tourist rush season should be attributed to the increased air exchange between inside and outside cave caused by visitation.

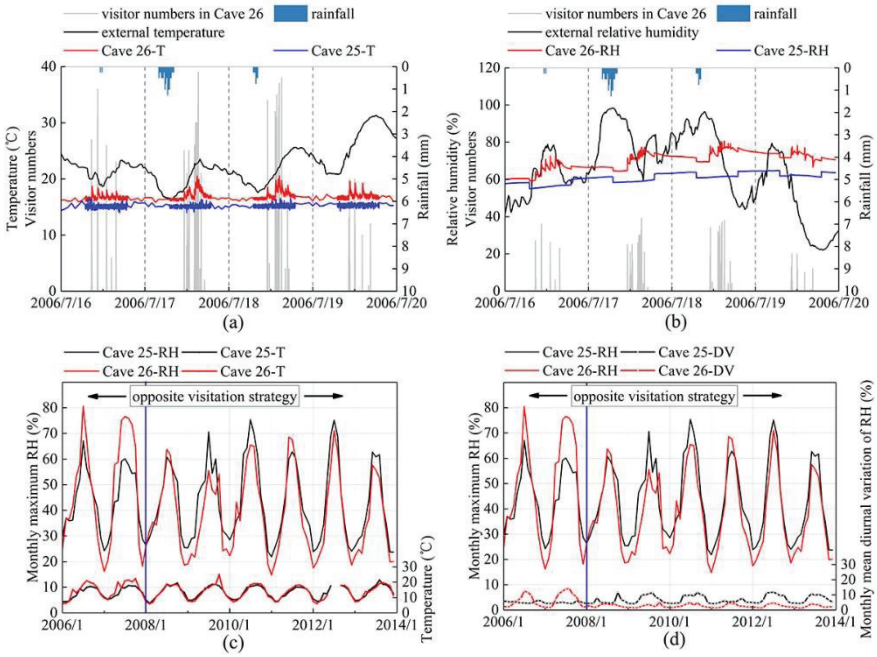

Figure 7: Temperature (a) and relative humidity (b) in visited cave and non-visited cave during rainy days (from 16 July 2006 o 19 July 2006). The changes of monthly maximum relative humidity, corresponding temperature (c) and monthly mean diurnal variation of relative humidity (d) between 2006 and 2013.

3.4 Deliquescence and Crystallization Cycles of Potential Salts

It is well known that the mutual deliquescence relative humidity (MDRH) of salt mixtures is usually significantly lower than that of any of its component pure salt [17]. We attempt to explain the weathering phenomenon observed in test caves by combining the phase diagram of potential dominant salt with the microenvironmental parameters. Annual maximum relative humidity and its corresponding temperature of two test caves from 2006 to 2013 were plotted in the phase diagram of sodium chloride (NaCl), which dominates quantitatively in salt mixtures. As shown in Figure 8, the annual maximum relative humidity in Cave 25 before 2008 never crossed the equilibrium curve of sodium chloride. Whereas, after Cave 25 was open, the annual maximum relative humidity of the cave reached the DRH in some years (2010 and 2012). Similarly, Cave 26 had an annual maximum relative humidity obviously higher than DRH of sodium chloride when it was open. After 2008, the annual maximum relative humidity in Cave 26 decreased to the level which was far below the equilibrium curve.

It can be speculated that the MDRH of salt mixtures present in wall paintings was probably lower than the DRH of sodium chloride (NaCl) [15], which allows the occurrence of deliquescence under relatively low humidity. Moreover, the surface temperature of wall paintings is lower than that of surrounding air during summer [18], as a consequence, the surface of wall paintings would have a higher relative humidity. Thus, the relative humidity in open Cave 25 probably surpassed the

MDRH of salt mixtures during some days of summer and thereby caused deliquescence and crystallization cycles. The fact that there was no dramatic difference in the deterioration rate of wall paintings in Cave 25 between before and after 2008 might be attributed to minor variation in relative humidity and low salt contents in plasters of Cave 25. As for Cave 26, a comparatively reliable deduction is that its relative humidity in some days of summer months greatly exceeded the MDRH of salt mixtures when it was open and harmful deliquescence and crystallization cycles happened frequently. After 2008, the relative humidity in Cave 26 declined considerably, which result in the reduction of deliquescence and crystallization cycles occurring within the structure of wall paintings and consequently the slowing down of deterioration rate. This is particularly evident in the weathering behavior of wall paintings on the north wall of Cave 26 with extremely high level of salts (Figure 4 (b) and Figure 5 (c)).

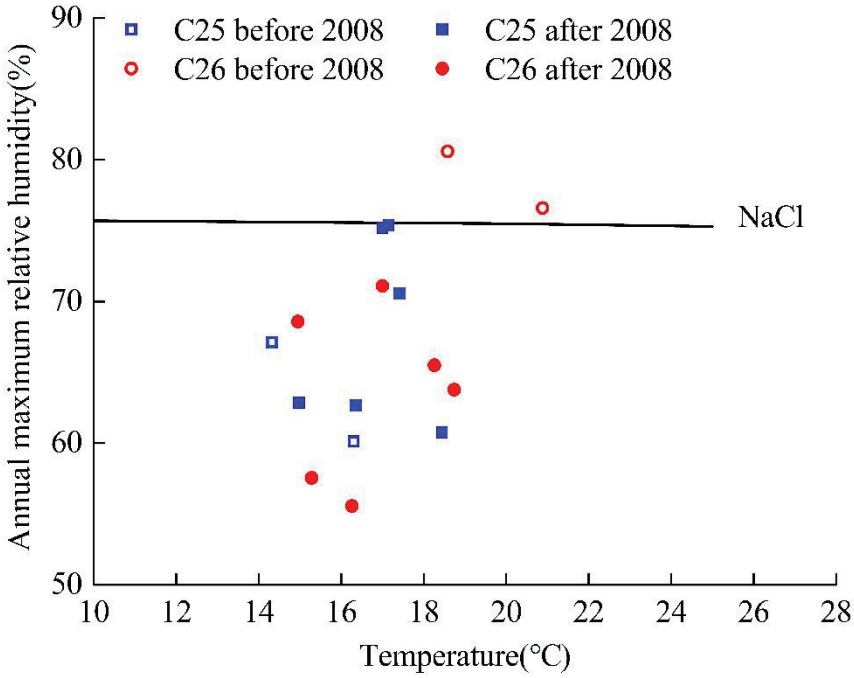

Figure 8: Phase diagram for sodium chloride (after Arnold and Zehnder 1991[19]); symbols represent annual maximum RH and corresponding temperature of two test caves during different monitoring periods and have the following meanings: (□) data in closed Cave 25 from 2006 to 2007; (■) data in open Cave 25 from 2008 to 2013; (○) data in open Cave 26 from 2006 to 2007; (●) data in closed Cave 26 from 2008 to 2013.

4 CONCLUSIONS AND RECOMMENDATIONS

During the 8-year monitoring period, the deterioration of wall paintings caused by salt activities mainly happened in tourist rush season when the relative humidity in

both visited and non-visited caves was relatively high. Sodium chloride was inferred to be the potential dominant salt. Continuous deterioration of wall paintings was attributed to the deliquescence and crystallization cycles of salt mixtures triggered by the variation of thermo-hygrometric conditions, which can be strongly influenced by the visitation strategy of caves. The salt weathering of wall paintings with high salt content can be accelerated evidently due to the opening of cave. On the contrary, when cave was closed, the deterioration tended to slow down. The degree of salt damage in porous wall paintings is influenced by the species and contents of salts, environmental conditions and consequently the visitation strategy of caves. For all these reasons, the conditions of wall paintings and microenvironment in both visited and non-visited caves should be evaluated periodically and effective interventions for the preventive conservation of wall paintings such as microenvironment control and removal of salts from weathered materials should be conducted.

REFERENCES

[1] Q. L. Guo, "Origin of water and salts responsible for wall paintings disease at Dunhuang Mogao Grottoes," PhD thesis, Lanzhou University, 2009.

[2] G. Q. Chen, "Study on salting damage analysis and treatment of wall paintings at Mogao Grottoes, Dunhuang," PhD thesis, Lanzhou University, 2016.

[3] R. M. Espinosa Marzal, L. Franke, and G. Deckelmann, "Predicting efflorescence and subflorescences of salts," In Proc. MRS Sprign Meeting: Symposium Y - Materials Issues in Art and Archaeology, 2007, pp. 105-114.

[4] M. Angeli, J. Bigas, D. Benavente, B. Menéndez, R. Hébert, and C. David, "Salt crystallization in pores: quantification and estimation of damage," *Environmental Geology*, vol. 52, no. 2, pp. 205-213, 2007.

[5] G. W. Scherer, "Stress from crystallization of salt," *Cement and Concrete Research*, vol. 34, no. 9, pp. 1613-1624, 2004.

[6] D. Benavente, M.A. García del Cura, J. García-Guinea, S. Sánchez-Moral, and S. Ordóñez, "Role of pore structure in salt crystallisation in unsaturated porous stone," *Journal of Crystal Growth*, vol. 260, pp. 532-544, 2004.

[7] R. J. Flatt, "Salt damage in porous materials: how high supersaturations are generated," *Journal of Crystal Growth*, vol. 242, pp. 435-454, 2002.

[8] M. Steiger and S. Asmussen, "Crystallization of sodium sulfate phases in porous materials: the phase diagram Na_2SO_4-H_2O and the generation of stress," *Geochimica et Cosmochimica Acta*, vol. 72, no. 17, pp. 4291-4306, 2008.

[9] M. Angeli, R. Hébert, B. Menéndez, C. David, and J. Bigas, "Influence of temperature and salt concentration on the salt weathering of a sedimentary stone with sodium sulphate," *Engineering Geology*, vol. 115, pp. 193-199, 2010.

[10] C. Rodriguez-navarro and E. Doehne, "Salt weathering: influence of evaporation rate, supersaturation and crystallization pattern," *Earth Surface Processes and Landforms*, vol. 24, pp. 191-209, 1999.

[11] L. Wong and N. Agnew, Eds., *The Conservation of Cave 85 at the Mogao Grottoes, Dunhuang: A Collaborative Project of the Getty Conservation Institute and the Dunhuang Academy*. Los Angeles: Getty Conservation Institute, 2014.

[12] B. M. Su, "Wall painting materials and techniques of the Mogao Grottoes," in *Conservation and Painting Techniques of Wall paintings on the Ancient Silk Road*, S. Aoki, Y. Taniguchi, S. Rickerby, M. Mori, T. Kijima, B.M. Su, and F. Kirino, Eds. Singapore: Springer, 2021, pp. 253-263.

[13] W. B. Bi, Z. F. Yan, H. Zhao, L. Sun, X. D. Wang, and Z. M. Zhang, "The influence of two natural reinforcement fibers on the hygrothermal properties of earthen plasters in Mogao Grottoes of China," *Journal of Renewable Materials*, vol. 8, no. 12, pp. 1691-1710, 2020.

[14] F. J. Li, X. D. Wang, Q. L. Guo, B. Zhang, Q. Q. Pei, and S. L. Yang, "Moisture absorption mechanism of earthen plaster containing soluble salts in the Mogao Grottoes of China," *Studies in Conservation*, vol. 64, no. 3, pp. 159-173, 2019.

[15] N. Agnew. S. Maekawa, and S.Y. Wei, "Causes and mechanisms of deterioration and damage in cave 85," In Proc.The Second International Conference on the Conservation of Grotto Sites, Mogao Grottoes, Dunhuang, People's Republic of China, 2004, pp. 412-420.

[16] G. Q. Chen. B. M. Su, L. Y. Zhao. Z. R. Yu, Z. X. Li, and N. Agnew, "Simulating test of efflorescence of earthen plasters in Mogao Cave 85," *Dunhuang Research*, no. 4, pp. 62-66, 2005.

[17] L. Yang, R. Pabalan, and L. Browning, "Experimental determination of the deliquescence relative humidity and conductivity of multicomponent salt mixtures," *MRS Online Proceedings Library (OPL)*, vol. 713, pp. JJ11.4.1-JJ11.4.8, 2002.

[18] G. Liu, P. Xue, W. F. Hou, and S. Maekawa, "A study on the microclimate of the Mogao Cave 85," *Dunhuang Research*, no. 1, pp. 36-41, 2000.

[19] A. Arnold and K. Zehnder, "Monitoring wall paintings affected by soluble salts," in *The Consevation of Wall Paintings: Proceedings of a Symposium Organized by the Courtauld Institute of Art and the Getty Conservation Institute*, S. Cather , Eds. London: Getty Publications, 1991, pp. 103-136.

MEASUREMENT OF SALINITY IN INDOOR AIR AND ESTIMATION OF SALT SOURCES IN AQUARIUMS IN COASTAL AREAS

Taiki Iwashima[1], Satoru Takada[1], Kentaro Amano[2], Hideaki Tani[2], Kaori Nomura[2], and Tatsunori Maeda [3]

KEYWORDS

Salt source, Indoor air, Aquarium, Ion chromatography, Impinger method

ABSTRACT

In this study, the salt concentration in indoor air was measured in several rooms of two aquariums in coastal areas, by trapping salt present in the air into water (impinger method) and detecting the ionic component concentration of the aqueous solution using ion chromatography. The results revealed that the salt concentration in the indoor air of aquariums located in coastal areas ranged from 1 to 200 ppb. The airborne salinity was higher in several rooms than that in the outdoor air, indicating that salt in the indoor air was generated from seawater surface of the aquarium tank. Moreover, the airborne salinity was greater when the seawater surface area was larger based on the room size and when less volumes of outdoor air were introduced in that room. This suggested that the difference in salt concentration between the rooms might be explained by the balance between salt generation from the indoor seawater tanks and ventilation. Consequently, salt generation in indoor tanks may contribute more to the presence of salt in the indoor air of aquariums in coastal areas than to the introduction of outside air.

[1] Kobe University, Hyogo, Japan, satoruta@kobe-u.ac.jp
[2] Takenaka R&D Institute, Chiba, Japan
[3] Takenaka Corporation, Osaka, Japan

1 INTRODUCTION

In coastal areas, reinforced concrete on the exterior walls of buildings may crack and peel and metal parts may rust [1]. Rust is caused by chloride [2], and this damage is known as salt damage as it is caused by sea salt [3]. Contrastingly, airborne salinity of outdoor air in coastal areas has been measured in several studies [4-8], but indoor measurements have rarely been conducted; additionally, the presence of salt in indoor air is not well-studied. Aquariums, which are often built in coastal areas, have seawater tanks installed in viewing areas and keeper's spaces, which are considered possible sources of indoor salt; therefore, if salt is present in indoor air, it can originate from both tanks and the sea.

This study aimed to measure airborne salinity in several rooms of two aquariums located in coastal areas, explain the differences in airborne salinity in the different rooms, estimate its origin, and gain insights to design countermeasures against salt damage, such as rusting of metal parts in rooms.

2 MEASUREMENT METHOD

The impinger method [8, 9] (Figure 1) was used to collect ambient air samples and trap atmospheric airborne components in water. Ion chromatography was used to analyze the aqueous solution. Moreover, an air pump (Shibata Kagaku, MP-Σ300NII) was used to collect air and impinge it into ultrapure water in a glass bottle called "impinger" at a flow rate of 1.0 L/min for 2 h. The instruments were placed approximately 1000 mm above the ground. The water in the impinger was used as the sample of ion chromatography, and water-soluble cations, namely, Na^+, NH_4^+, K^+, Mg^{2+}, and Ca^{2+}, and water-soluble anions, namely, Cl^-, NO_2^-, NO_3^-, PO_4^{3-}, and SO_4^{2-}, were detected by ion chromatography. Moreover, air temperature and relative humidity were measured simultaneously at each measurement point.

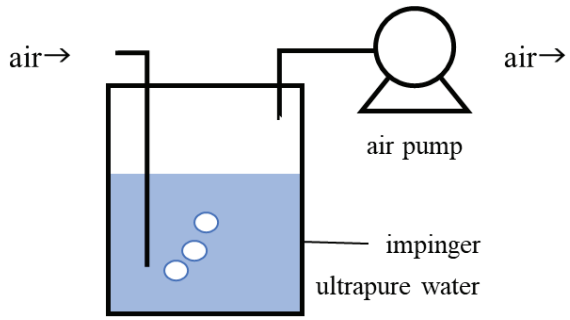

Figure 1: Conceptual diagram of the impinger method.

The concentration of ionic components in the air was calculated using temperature and atomic or molecular weight by dividing the number of ionic components in all sample solutions obtained by ion chromatographic by the total suctioned air volume. The salt concentration in the air was estimated from the concentrations of sodium and chloride ions using Equation (1). Concentrations below the detection limit were assumed to be 0 ppb. The symbols in Equation (1) were defined as C_{NaCl}: airborne salinity [ppb], C_{Na}: airborne sodium ion concentration [ppb], C_{Cl}:

airborne chloride ion concentration [ppb], M_{Na}: molecular mass of sodium (=22.99) [-], and M_{Cl}: molecular mass of chlorine (=35.45) [-].

$$C_{NaCl} = \min\left(\frac{M_{Na} + M_{Cl}}{M_{Na}} C_{Na}, \frac{M_{Na} + M_{Cl}}{M_{Cl}} C_{Cl}\right) \quad (1)$$

Salt concentrations were measured in two aquariums located in the coastal areas of Japan. Aquarium X faced the Pacific Ocean and Aquarium Y faced the Seto Inland Sea. Table 1 describes the measurement locations in the two aquariums. In Aquarium X, four points ("keeper's spaces A and B", "machine room", and "well water receiver tank room") were measured indoors and one point was measured outdoors during the first round, whereas one more point ("viewing room") was additionally measured indoors and one more point ("service entrance") was additionally measured outdoors during the second round. In Aquarium Y, four points ("keeper's spaces C and D", "freshwater tank room", and "seawater storage room") were measured indoors and two points were measured outdoors during both rounds of measurements. In the keeper's spaces, the viewing room, and the seawater storage room, there were seawater tanks and the room air was in contact with the seawater. In these rooms, the keeper's spaces and the viewing room, most seawater tanks for aquatic organisms had bubbling water surfaces, whereas the seawater storage room contained tanks for storing filtered seawater without bubbling water surfaces.

The values of the contact area between the indoor air and seawater (seawater surface area) and the room area were determined based on the observations of the venue, design specifications, drawings, or interviews with the aquarium administrators. For the fixed tanks, the seawater surface area was calculated using the dimensions specified in the drawings and specifications. For the tanks not shown in the drawings, it was estimated based on site inspections. The ventilation capacity of the fans, operation of each fan, and whether a desalination filter was installed on the ventilation fan were determined similarly. These details are summarized in Table 1.

Table 1: Locations of airborne salinity measurement.

	Name of the measurement point	Times of measurements performed	Seawater surface area[m^2]	Volume of measured room [m^3]	Amount of outside air introduced [m^3/h]	With or without desalination filter	Remarks
Aquarium X	Keeper's space A	1st/2nd	198.8	563	3000 (all day)	Not installed	Some tanks had wave-making devices. Waves and spray were observed on the seawater surface.
	Keeper's space B	1st/2nd	52.1	608	6000 (7 h/d)	Installed	There was an opening for loading, which was fully open during business hours in summer and partially open in winter.
	Machine room	1st/2nd	0	3253	13300 (all day)	Installed	
	Well water receiver tank room	1st/2nd	0	147	300 (20 m/d)	Not installed	
	Viewing room	2nd	291.5	10283	22900 (7 h/d)	Installed	This room was connected to Keeper's space B.
	Service entrance	2nd	–	–	–	–	The air was introduced to Keeper's space A from this space.
	Outdoors	1st/2nd	–	–	–	–	The salinity was measured at ground level.
Aquarium Y	Keeper's space C	1st/2nd	58.4	691	2150 (20 m/d)	Not installed	The air in the viewing room was introduced at a rate of 2150 m^3/h. (Air conditioning was operated for 8 h/d, during business hours)
	Keeper's space D	1st/2nd	30	796	1000 (20 m/d)	Not installed	The air in the viewing room was introduced at a rate of 2000 m^3/h. (Air conditioning was operated for 8 h/d, during business hours)
	Freshwater tank room	1st/2nd	0	310	600 (all day)	Not installed	The ventilation system was not operational during winter.
	Seawater storage room	1st/2nd	393	1686	–	Not installed	No ventilation facilities.
	Outdoors 1	1st/2nd	–	–	–	–	The salinity was measured at ground level.
	Outdoors 2	1st/2nd	–	–	–	–	The salinity was measured at the height of 3rd floor

3 RESULTS

Figure 2 shows the airborne salinity results at each measurement point. In both aquariums, airborne salinity was higher in rooms with seawater tanks than in rooms without seawater tank. In Aquarium X, the measured airborne salinity of the second-round measurements was higher than that of the first-round measurements in a room with seawater tanks. High salinity was detected in the first-round measurement in the "outdoors", but not in the second-round measurement. In Aquarium Y, the results of the first-and second-round measurements were similar.

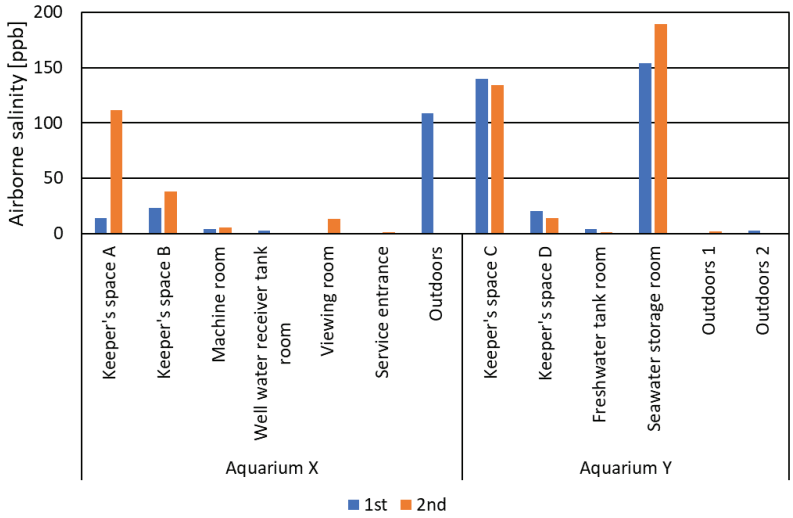

Figure 2: Airborne salinity at each measurement point (measured results).

The measured airborne salinities ranged from 1 to 200 ppb, demonstrating the presence of salt in the indoor air, since these results were mostly included in the range of measured values of airborne salinity in the outdoor air near the coast in previous studies [4-7]. The measured values were obtained by subtracting the number of ions in the blank sample from the number of ions in the collected sample. Most of the sodium and chloride ions were detectable because they exceeded the number of ions in the blank sample.

In both aquariums, the airborne salinity in the room with the seawater tank was higher than that in the room without the tank. On the seawater surface in the tanks, bubbles were produced along with the aeration for the aquatic organism. Additionally, the seawater tank in Keeper's space A had an operational wave generator, that produced bubbles in the other way. The bursting of bubbles and breaking of waves on the surface might have diffused seawater droplets [11, 12] that remain in the air. Therefore, the seawater surface can be a source of salt in indoor spaces.

Figure 3 shows the relationship between the ratio of seawater surface area to floor area in each room and the airborne salinity.

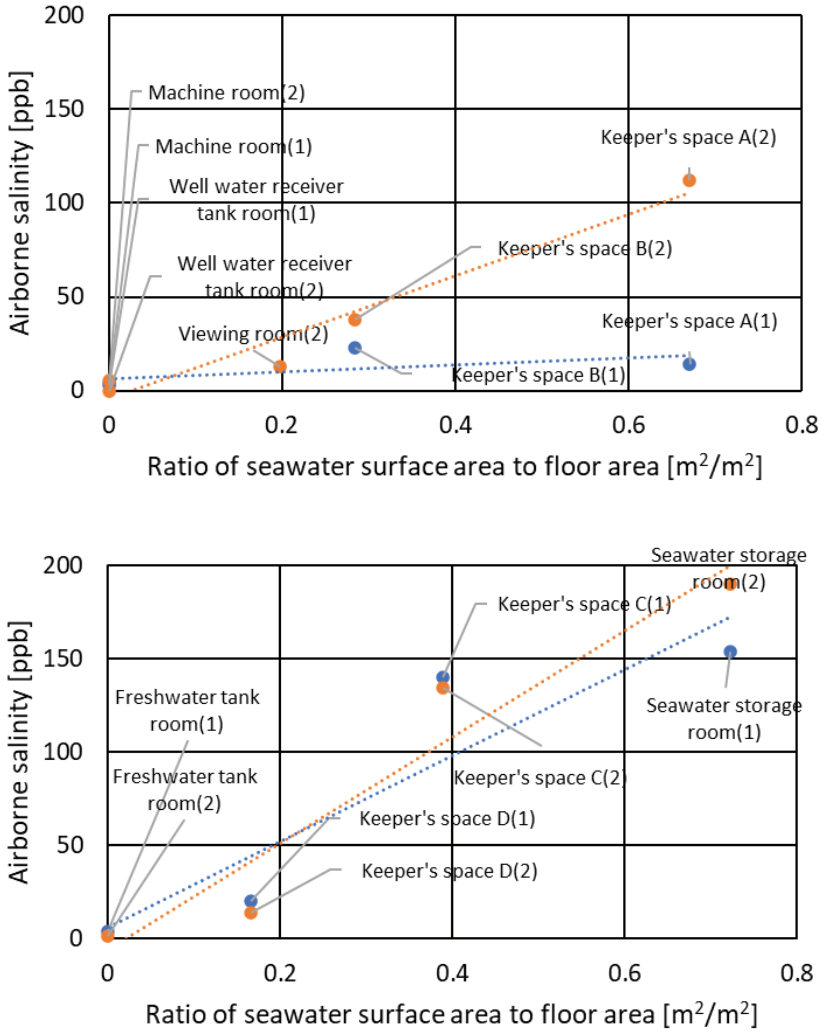

Figure 3: Relationship between the ratio of seawater surface area to floor area and airborne salinity (Top: Aquarium X, Bottom: Aquarium Y).

For each aquarium, the airborne salinity was higher when the seawater surface area in contact with the Keeper's space was larger. However, the higher airborne salinity in Aquarium Y than that in Aquarium X cannot be explained only by the seawater surface area. Dilution by the outside air introduced by the ventilation fan could be another contributory factor.

According to the survey, the ventilation rate was higher in Aquarium X than in Aquarium Y (Table 1); In Aquarium Y, the ventilation system was operational for a shorter period and the net ventilation rate was relatively lower, suggesting that

high airborne salinity was measured in Aquarium Y because the salinity generated in the room remained in the room air.

Despite the high airborne salinity in outdoor air in the first-round measurement and the large-scale introduction of outdoor air, the indoor airborne salinity was lower than the outdoor airborne salinity in Aquarium X. Although the outdoor air was introduced directly to "Keeper's space A", the opening was on the opposite side of the building, that is, from the seaside of the building and on a loading dock behind the building's exterior wall line, and therefore, the airborne salinity could have been low. The air supply fan of "Keeper's space B" had a desalination filter, and salt in the air introduced into this room could have been low. The airborne salinity in the second-round measurement of "Keeper's space B" was higher than in the first-round measurement because the ventilation fan in this room was intermittently operational and the operating time was shorter when the room air was sampled in the second-round measurement.

4 DISCUSSION

The airborne salinity in both aquariums was higher than that in rooms without seawater tanks and was proportional to the seawater surface area. The outdoor airborne salinity in Aquarium Y was low while the airborne salinity in the room with the seawater tank was high, suggesting that salt detected in the indoor air was generated indoors. Although the airborne salinity of the outdoor air in the first-round measurements in Aquarium X was high, the salinity of the air introduced into the indoor space was low as described in Section 3. The low ventilation rate in Aquarium Y may have caused salt particles to remain in the air, resulting in higher salinity than in Aquarium X. Therefore, the airborne salinity in both aquariums was determined by the balance between salt generation from the seawater tank in the room and salt dilution by the introduced air at a low concentration. Thus, the salt present in the indoor air might be generated from the seawater tanks in the room and, not from salt transferred from the ocean.

In the two aquariums, metal parts, such as pipes, ducts, and railings, were rusted. Rust was particularly severe on the top surfaces of the metal parts, suggesting that the rust in the two aquariums was mainly caused by accumulation of salt on top of the metal parts carried by the indoor air flow. If the salt in the indoor air originates from seawater tank, the metal parts are always exposed to corrosive substances. Unlike outdoors, rainwater is not expected to clean the salt, which is likely to progress corrosion.

5 CONCLUSIONS

Herein, airborne salinity was measured in several rooms of two coastal aquariums by collecting indoor air samples into the water using the impinger method and analyzing the water using ion chromatography. The results revealed that salt was present in the indoor air of aquariums located in coastal areas at concentrations ranging from 1 to 200 ppb. The higher airborne salinity than the outdoor air salinity, even though the outdoor airborne salinity was lower, indicated that salt was generated from the surface of seawater in the indoor aquarium and that the salt was present in the indoor air. Airborne salinity was higher in rooms with a larger contact surface

area between the air and seawater and lower ventilation rate. Further, the airborne salinity in each room could be explained by the balance between salinity generation in the room and its dilution by ventilation. These results suggested that the salt in the air in the two aquariums originated from salt generation from the seawater tanks in the rooms, and not from salt flowing in from the sea.

ACKNOWLEDGEMENTS

We thank the aquariums staffs for their cooperation during the survey.

REFERENCES

[1] H. Yoda, "Investigation of damage from salty breezes and sea water aerosol concentration at seaside area," *Journal of. Archit. Plann. Environ., Eng, AIJ*, No.522, pp. 115-121, 1999.

[2] S. Hara, "Influence of deicing salt on the characteristics of the rust formed on weathering steels," *Zairyo-to-Kankyo*, vol. 54, pp. 337-343, 2005.

[3] Architectural Institute of Japan, Environmental Standards AIJES-H0003-2013 (English Version), Standard for diagnosing moisture damage in buildings and implementing countermeasures, p. 7, p. 14, 2019. https://www.aij.or.jp/eng/publish/index.htm

[4] K. Hotta, "A study on the incidence of sea-salt particles from sand beach," *Journal of Struct. Constr. Eng, AIJ*, No. 444, pp. 145-152, 1993.

[5] K. Hotta, "Generation of the sea-salt particle in the coastal area Generation characteristics at the natural sandy beach and artificial beach," *Journal of Struct. Constr. Eng, AIJ*, No. 441, pp. 101-106, 1992.

[6] K. Hotta and M. Hirano, "Generation of the sea-salt particle in the coastal area, Generation characteristics at the sandy beach and artificial beach," *Journal of Struct. Constr. Eng, AIJ*, No. 455, pp. 207-213, 1994.

[7] M. Katayama, "Field measurement of the aerial distribution of sea-salt particles in the northern Kyushu region," *Proceedings of Civil Engineering in the Ocean*, Vol. 12, pp. 115-120, 1996.

[8] Y. Atsumi, Y, Wakayama, A. Kunita, S. Sekiguchi, K. Sato and J. Miyakawa, "Field measurement and numerical simulation of distribution of sea salt particles in the open coastal region," *Proceedings of Civil Engineering in the Ocean*, Vol. 13, pp. 723-728, 1997.

[9] Japan Air Cleaning Association, "Standard for evaluation of airborne molecular contaminants emitted from construction/composition materials for cleanroom," No.34-1999, pp. 25-26, 1999.

[10] Japan Air Cleaning Association, "Classification of air cleanliness for airborne molecular contaminants (AMC) level in cleanrooms and associated controlled Environments and its measurement methods," No.35A-2003, pp. 7-9, 2003.

[11] Y. Toba, “Drop production by bursting of air bubbles on the sea surface. III study by use of a wind flume,” *The Journal of the Oceanographical Society of Japan* Vol. 17, No. 4 pp. 169-178, 1961.

[12] K. Miura, “Production, and chemical and physical properties of sea salt particle,” *Bulletin of the Society of Sea Water Science, Japan*, Vol. 61, No. 2, pp. 102-109, 2007.

MONITORING AS A BASIC TOOL FOR UNDERSTANDING SALT CRYSTALLIZATION PROCESSES ON MONUMENTS – CASE STUDY OF THE BAROQUE TOMB IN ST. MARIEN IN FRANKFURT/ODER

S. Laue[1]

KEYWORDS

Monitoring, cyclic salt crystallization, climate, niter, ECOS/RUNSALT

ABSTRACT

Monitoring of monuments together with climate measurements and salt analyses is a recognized method to gain knowledge about the complex interaction between all relevant factors within a building, e.g., materials and their properties, temperature and humidity changes, salts, and anthropogenic influences.

The paper starts with a general introduction to the monitoring method and describes the requirements for a successful monitoring of salt damages on a monument. The monitoring method is then applied to a case study: The baroque tomb in the church of St. Marien in Frankfurt/Oder (Germany).

Monitoring together with climate measurements, salt analyses and calculations with the computer model ECOS/RUNSALT were able to clarify the preliminary processes of the deterioration at the tomb by salts resulted in a sustainable conservation concept. In the winter months, cyclic potassium nitrate crystals occur at low temperatures, which damage the surfaces, especially in the height between 50cm and 150cm. The salinity of the tomb in the lower parts is as high that no salt reduction measure would be successfully possible.

Salt reduction without major interventions on the monument is not possible. The conservation approach is, in general, to live with the salts, to carry out regular monitoring, and to replace the front areas of the stucco applications (reconstructions from 1985), with a sacrificial plaster material (lime-gypsum mixture). In this way, as much of the original substance as possible will be preserved, and the tomb can be appreciated by the general public for its beauty and authenticity.

[1] University of Applied Sciences Potsdam, steffen.laue@fh-potsdam.de

1 INTRODUCTION

The term monitoring describes the systematic study and recording of processes with the help of technical instruments or other surveillance systems. Within conservation and restoration of art and cultural property, monitoring is commonly used on two different issues:

1. To understand the damage process and intensity: when does damage to an object increase (or decrease), under which framework conditions and influences.

2. To detect changes to a surface after a conservation/restoration/renovation treatment.

Applying the term monitoring to salts in masonry and wall paintings, monitoring entails the systematic recording, observation and documentation of salts and/or salt decay as well as environmental parameters like climate or humidity changes. Monitoring is the only method to gain knowledge about the complex interaction between all relevant factors within a building [1].

Several examples have already shown how useful well-planned monitoring of salt damage is with regard to sustainable conservation strategies [2], [3], [4].

First, this paper describes the conceptual procedure and planning of a monitoring and names the requirements and measures for successful implementation. Second, a case study from a current research project is presented, in which the monitoring approach was successfully applied resulting in a conservation concept.

2 REQUIREMENTS FOR A SUCCESSFUL MONITORING OF SALT DAMAGES

Requirements for Monitoring of salt-loaded walls are described in detail by [1], [5]. Some key aspects are summarized here.

Depending on its objectives, monitoring of salts and salt decay can be carried out to varying degrees of detail. Prior to beginning the actual monitoring and depending on the object and decay scenario, the aim of the monitoring needs to be defined. The aim of monitoring can, for example, serve to answer the following questions:

- What is the activation mechanism for the crystallization of the salts present?
- When and in which climatic conditions will the salts cause active damage?
- What kinetics does the process involve?
- When is the best time for salt reduction or other intervention measures?
- What preventive measures are required?

Additionally, it is necessary to consider if monitoring of clearly defined reference surfaces is preferable to monitoring the whole situation. The duration of possible preliminary investigations and subsequent monitoring also needs to be agreed on at the beginning of the project unless its sole purpose is research based.

Prior to undertaking monitoring (which, depending on the nature of the problem, can be carried out before, during or after an intervention) the following points should be determined:

What is to be observed/measured? Examples: Efflorescence, quantitative amount of salt ions, decay (type and form), climate (air temperature, relative humidity, surface temperature), dampness horizons.

Which area is to be observed and measured? To answer this question, in addition to the already mentioned condition survey, it is necessary to consider whether the determination of monitoring locations would require additional preliminary investigations and if so, what are the properties of the object surface and substrate?

How long and at which intervals is monitoring to be carried out? The duration and cycles of observation need to be determined.

What is to be used for monitoring? Which methods and equipment are likely to obtain optimal results? Which methods and equipment are available? Is a macroscopic observation and documentation of the processes sufficient or should recording equipment to measure climatic or surface conditions be used?

How detailed and precise should the recorded data be? How is the monitoring going to be documented? At what intervals should the observations/measurements be carried out?

Who carries out the monitoring and who evaluates the results? Primarily this concerns the qualifications of the practitioner or commissioning person: Is specialist training/guidance required? Are there objects/situations which require special training? Who interprets the results and who draws up the conclusions in relation to treatment recommendations?

Monitoring is not the final objective in itself but merely a critical step in the process that needs to be followed to finally arrive at a solution to a problem. The results will be more meaningful if the relevant questions can be answered and if the procedure to be followed is precisely defined. Monitoring is an adaptable process that requires open minded operators.

If the object to be examined allows minor-destructive sampling, height and depth profiles of the salt ion distribution should also be obtained. From this, salt reduction measures can be considered, which can be optimized together with the findings from the monitoring results: when is the best time for a salt reduction and where.

The approach of a suitable monitoring in combination with salt ion concentrations at different heights and depths is described in the following example. Prerequisite for this is a condition survey of the relevant object together with qualitative and, if necessary, also quantitative analysis of the salt content of the walls.

3 THE BAROQUE TOMB COMPLEX OF ST. MARIEN

The baroque tomb is located within the church of St. Marien in Frankfurt/Oder, which is an imposing brick building with a five-aisled nave with a transept, ambulatory choir and western double-tower façade [6]. The core of today's building contains the founding structure of the 13th century.

The tomb is on the east side of the south tower in a round arched niche inside the church with a height of almost 4m (fig.1, fig.2). Two by two metal tablets are the central focus of the epitaph (fig.2). It's probably about a larger family funeral [7].

The inscriptions are framed by richly ornamented stucco. On both sides will be the plant framed by pilasters, each topped by a Corinthian capital. In the area below the tablets between the stucco pilasters there are vanitas symbols such as skulls and crossbones. The lower part of the epitaph is crowned by a multiple cranked architrave cornice. Above the central pilaster is a very plastic stucco ornament with putti, snakes and an hourglass and skull attached. A flat calotte arches over the architrave cornice like an apse with a wall painting.

Figure 1: Baroque tomb within the church St. Marien

The epitaph niche was walled up around 1830 when extensive security measures were taken on the north tower after the south tower collapsed in 1826 [7]. The epitaph, which remained largely intact behind the wall, fell into oblivion over time. In the spring of 1945, during World War II, the church caught fire and the roof collapsed along with the vaults of the nave. The fact that the epitaph was walled up probably saved it from destruction.

After the 2nd World War the church St. Marien was long a ruin. Biogenic growth, rain and other environmental influences further contributed to the decay of the

church at. It was not until 1980 that piecemeal reconstruction began. Between 1995 and 1997 the nave and choir received again a wooden roof trusses.

In the course of the reconstruction of the church in the 1980s, the wall niche was opened and the forgotten baroque epitaph came to light again. The condition of the epitaph deteriorated rapidly after opening, so that a restoration became necessary. The work began 1983 and were completed in 1988. In addition to inorganic materials for e.g. plasters and stucco, synthetic binders such as acrylates were also used for restoration.

Today, considerable damage can be seen, especially in the lower part of the tomb up to 150cm (fig.2), caused mainly by salt crystallization and moisture. The surfaces of the monument shows typical damage phenomena by salt deterioration like disintegration of stucco and plaster, formation of alveolus as well as partial loss of substance.

The research questions were: Which salts crystallize under which conditions and produce damage? How high is the salt ion concentration also in deeper areas of the masonry? Which sustainable conservation concept can be recommended?

Figure 2: Baroque tomb, moisture and salt damage (highlighted in yellowish) in the lower area of the tomb, on the left are marked the drill powder extraction points for the quantitative analyzes in one height and three depth profiles

4 METHODOLOGY

To investigate the question under which climate conditions new salt crystallizations take place and what kind of damage they are producing, an adapted monitoring were developed for the tomb in St. Marien. Permanent climate measurements of room temperature, surface temperature and relative humidity were executed using data logger. Since January 2021, the climate measurements were combined with regular observations (monitoring) of selected reference areas on the tomb complex where newly crystallizing salts are to be expected. The reference areas were inspected once a month on average, shorter interval times were not possible due to logistical reasons. In the case of new crystal formations, the salts were removed and analysed by polarizing microscopy and XRD. Thus, it was possible to determine in which month which crystals were newly crystallized under which climatic conditions.

Additionally, drill powder samples were taken at the left pilaster of the tomb to investigate the distribution of salt ions concentrations in one vertical profile in the heights of 45, 114 and 155 cm and in four depths respectively (0-5, 5-15, 15-25 and 25-40cm) (see fig.2, fig.3). The left pilaster was chosen because this area is representative and most of other areas were too fragile for sampling without risking major damage. In the laboratory, 1 g of sample were mixed with 50 ml distilled water around 24 hours, then filtered before the analyses of Na^+, K^+, Ca^{2+}, Mg^{2+}, Cl^-, NO_3^- and SO_4^{2-} were executed by ion chromatography (IC - Thermo, Dionex, IC90). The data have been converted to units of equivalent concentrations [mEq/kg].

ECOS/RUNSALT

The observations by monitoring were compared with calculation by the computer program ECOS/RUNSALT to get a vision under which climate condition which salts are crystallizing at the tomb [8], [9]. In order to use the program, the IC data set must be simplified. The ion balance is compensated by the reduction of calcium. Calcium and sulfate are then reduced (elimination of gypsum) until one of the two ions is no longer present in the data set. This is necessary because ECOS/RUNSALT cannot calculate with 7 different ions.

5 RESULTS AND DISCUSSION

The documentation of the damage to the tomb revealed an active crystallization zone up to a height of approximately 150cm. Many salts crystallize at a height between 50 and 150cm which consist predominately of niter [KNO_3] and gypsum [$CaSO_4 \bullet 2H_2O$], only during winter 2022/23 syngenite [$K_2Ca(SO_4)2 \bullet H_2O$] could be analyzed too, but in a much lower degree.

Quantitative salt analyses demonstrate the distribution of ions in the heights of 45, 114 and 155 cm and in depth (fig. 3). Of course, the analyses contain a lot of calcium and sulfate because the soluble components have been eluted from the stucco in the front area. It is interesting to look at the other ions that - seen relatively - occur in high concentrations, especially nitrate and potassium and, to a lower degree, sodium and chloride. These ions most likely originate from more easily soluble salts and actively produce the main damage between 50 and 150cm height at the tomb. Nitrates probably originate from metabolic reactions of organic materials

and are often concentrated at burial sites and in and around churches. Potassium and sodium probably derived from alkaline building materials used in the church's reconstruction.

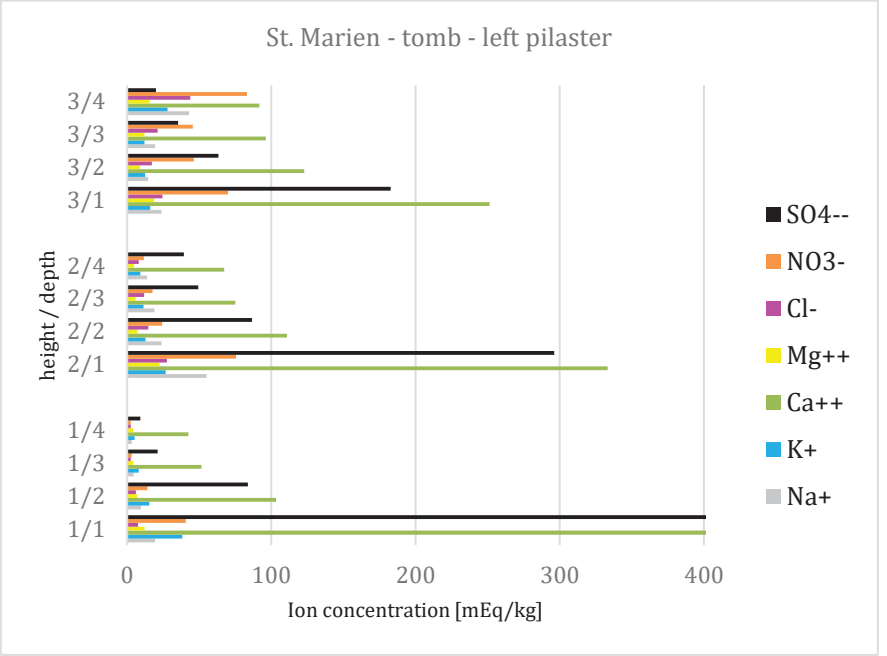

Figure 3: Salt ion concentrations in [mEq/kg] within the left pilaster in three heights and four depths each

The result of monitoring in relation to the climate in St. Marien is shown in fig.4. New efflorescences of predominately niter (KNO_3) only take place in the winter months when the temperature is below 10°C. No crystallization can be observed in summer months when the temperature is higher. The reason for this is the relatively strongly temperature-dependent solubility of niter [10]. At cold temperatures below 10°C the solubility of niter is by half in contrast to temperatures around 20°C. Consequently, at low temperatures a solution containing potassium and nitrate ions reaches the saturation much earlier than at higher ones. This knowledge, transferred to the salt load in St. Marien, suggests that the salt ion solution in the lower parts of the tomb is supersaturated with regard to nitrate and potassium resulting in the crystallization of niter at low temperatures at the tomb.

Fig.5 shows the crystallization sequence of salts according to the analysis from the foremost centimeter of the lower level on the pilaster after calculation with the ECOS/RUNSALT program. Using the IC data from P1/1 and after the necessary corrections (see methodology), it can be seen in Figure 5 that at 6°C in the church below 90% relative humidity, niter begins to crystallize and below 83% relative humidity further sulfate salts and below 65% even NaCl would crystallize. Despite the strong simplification of the data set, which reduces a large part of ions and

which excludes the representation of gypsum, the same trends can be taken from the calculations as were obtained from the monitoring: Niter is the particularly damage-relevant salt on the grave site. In combination with the climate measurements and the knowledge that the solubility of potassium nitrate is strongly temperature-dependent, the observations of the monitoring and the calculations can be explained.

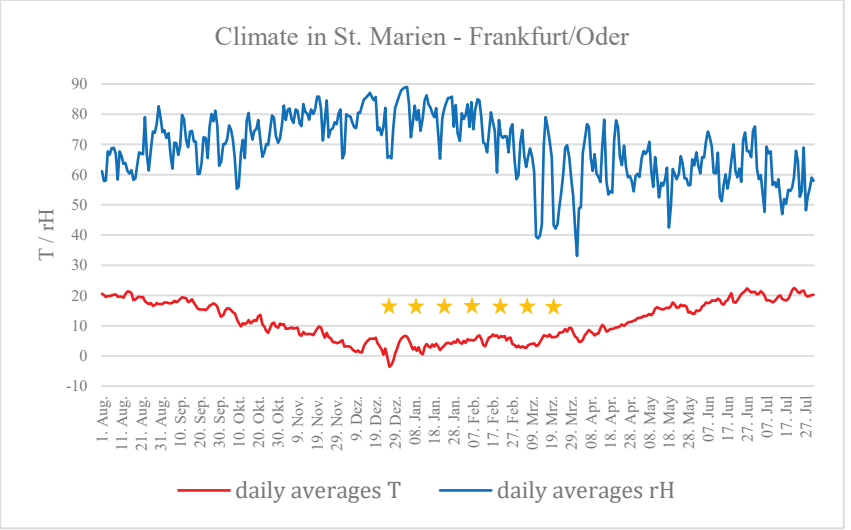

Figure 4: Daily averages temperature (T) and relative humidity (rH) from 01.08.2021 until 31.07.2022 measured close to the tomb, yellow stars represent the crystallization times of predominantly niter.

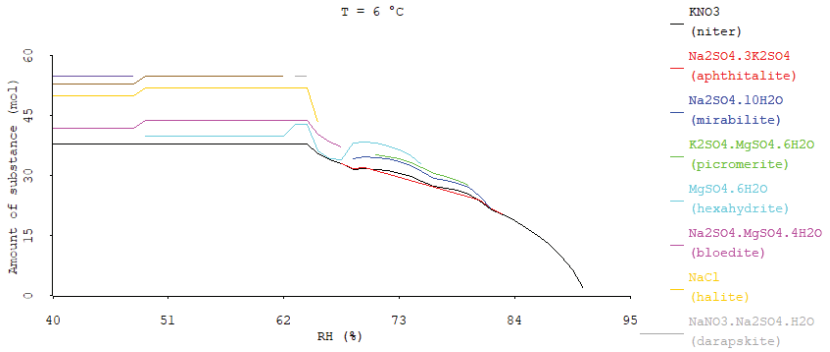

Figure 5: Crystallization sequence (excluding gypsum) calculated with ECOS/RUNSALT using IC-data from sample 1/1 after the necessary corrections (further explanation see text)

6 CONSERVATION MEASURES

The depth profiles of the quantitative salt analyzes (fig.3) have shown that even higher salt ion concentrations exist in rear wall areas. For this reason, salt reduction measures do not make sense, especially since further losses of the fragile surface are to be expected in the case of treatment by poultices (due to the application and removal of it). There is no promising solution to get most of the salts out of the masonry without destroying original substance.

The tomb complex is again an example where you have to live with a high salt load which only leads to damage in the lower areas of the wall.

An attempt should be made to reduce the supply of moisture, for example by creating better evaporation opportunities for moisture through openings on the side and behind the grave. But it is also clear that with less moisture supply, more salts could crystallize.

Since many of the lower stucco parts were re-applications of a restoration from 1985, an interdisciplinary team of monument conservators, restorers and natural scientists decided to remove the badly damaged and salty surface areas and to redesign the stucco elements with a new gypsum-lime plaster mixture designed as sacrificial plaster. The sacrificial plaster system has the task of absorbing salt ions from the rear areas of the wall that have been mobilized to the front. Regular monitoring with possible renewal of the surfaces or other interventions should help ensure that future generations can also admire the baroque tomb complex.

7 CONCLUSION

Monitoring together with climate measurements and salt analyzes were able to clarify the preliminary processes of destruction caused by salts at the baroque tomb in the church St. Marien in Frankfurt/Oder resulting in an affordable conservation concept.

In the winter months, cyclic potassium nitrate crystallizations occur at low temperatures, which damage the surfaces, especially in heights between 50cm and 150cm.

Everyone involved is aware that there can be no ideal solution through successful salt reduction on this structure. A way had to be found that would make it possible to live with the salt contamination in the long term, while still being able to present the monument to the general public.

The desired solution is continuous maintenance with further monitoring of the tomb with minimal repair interventions.

REFERENCES

[1] https://www.saltwiki.net/index.php/Monitoring

[2] A. Arnold, K. Zehnder, "Monitoring wall paintings affected by soluble salts", The Conservation of Wall Paintings, Sympos. by Courtauld Inst. of Art at the Getty Conserv. Inst., London, July 13-16, 1987, 103-135, 1991.

[3] S. Laue, "Salt Weathering of Porous Structures Related to Climate Changes", *Restoration of Buildings and Monuments*, vol. 11, No. 6, pp. 381-390, 2005.

[4] K. Zehnder, "Long-term monitoring of wall paintings affected by soluble salts", *Environ. Geol,* vol.52, pp. 353-367, 2007, https://doi.org/10.1007/s00254-006-0463-2.

[5] S. Laue, E. Stadlbauer, & C. Bläuer C., "Monitoring", in: H.-J. Schwarz, M. Steiger (eds), "Salzschäden an Kulturgüter – Stand des Wissens und Forschungsdefizite, Ergebnisse des DBU-Workshops im Februar 2008 in Osnabrück", 59-64, Hannover, 2009.

[6] G. Dehio, "Handbuch der Deutschen Kunstdenkmäler - Brandenburg", Deutscher Kunstverlag GmbH München, 2000.

[7] L. Böwe, "Barockes Erbbegräbnis, St. Marienkirche, Frankfurt/Oder - Restauratorische Erstbegutachtung", unpublished report, 40 p., 2019.

[8] D. Bionda, "Modelling indoor climate and salt behaviour in historical buildings: A case study", PhD thesis, Diss. Nr. 16567, ETH Zürich, 2006.

[9] C. Price, Ed., "An expert chemical model for determining the environmental conditions needed to prevent salt damage in porous materials", European Commission Research Report No 11, Protection and Conservation of European Cultural Heritage, London, Archetype Publications, 2000.

[10] H. Stephen, T. Stephen, "Solubilities of inorganic and organic compounds", Pergamon Press, Oxford, p. 116, p S.180, 1963.

NOTE OF THANKS

This research has been supported by Deutsche Bundesstiftung Umwelt (DBU), AZ36080-1. I am very grateful to Ellen Egel and Mechthild Noll-Minor from the Brandenburgisches Landesamt für Denkmalpflege und Archäologisches Landesmuseum for climate measurements and constant support. For fruitful discussions and support to get drill powder samples and quantitative salt analyses I am very thankful to Ellen Egel, Lis Mette Eggers, Christine Fuchs, Hans-Christian Klein and Margarete Piehl.

RESEARCH ON SALT DETERIORATION MECHANISM OF BRICK MASONRY BASE OF THE XI'AN BELL TOWER AND THE CONSERVATION SUGGESTION

Wei Liu[1], Weiqiang Zhou[2], Qianqiao Zhao[3],Jing He[4], and Jiawei Zheng[5]

KEYWORDS

Xi’an Bell Tower; Desalinization; Soluble salt; Deterioration Mechanism

EXTENDED ABSTRACT

1 INTRODUCTION

The Xi'an Bell Tower was built in the 17th year of the Hongwu Ming Dynasty (1384), and moved eastward to the current site in the 10th year of the Wanli Ming Dynasty (1582). It was repaired during the Kangxi and Qianlong’s dynasties of the Qing dynasty, but the basic structure and style still maintained the characteristics of the early Ming Dynasty.[1] The bell tower is composed of two parts, wooden pavilion and brick base. The building is square with a total area of 1377.4 square meters. The Xi'an Bell Tower is an important example of the official architecture when the capital was built in the early Ming Dynasty in Nanjing[3], and the research of The Xi'an Bell Tower is also an significant link in the study of the inheritance and traceability of architecture in various periods of the Ming Dynasty.

In the tenth year of the Wanli Ming Dynasty (1582), the bell tower was moved eastward to the current site to accommodate the development of the city.[4]Meanwhile the base was added. Now the base is a square, brick-clad structure, which is 35.5 meters long and 8.5 meters high.The bricks were arranged in accordance with the principle of "Flemish garden wall bond". The transverse brick is 46cm long and

[1] Xi' An Bell And Drum Towers Museum, Xi’an’, China, qiao9901@foxmail.com
[2] Northwest University,Xi’an’, China
[3] Northwest University,Xi’an’, China
[4] Shaanxi University of Science & Technology,Xi’an’, China
[5] Northwest University,Xi’an’, China

10cm high, and the vertical brick is 22cm long and 10cm high. The distance between the bricks is 1.5cm, and the interval between the bricks of each layer is 2cm.

The base of the bell tower has always had the problem of soluble salt, affecting the appearance. In order to ameliorate the appearance, in the 90s of the 20th century, acrylic paint began to be painted on the surface of brick masonry of the base. After several years, there were problems such as thick exfoliation about 1-2 cm on the surface of the base, and large areas of hollowing, which seriously affected the safety of cultural relics.Based on site investigation and literature review [6,7], it can be inferred that the base structure of Xi 'an bell Tower consists of internal rammed earth, external black bricks, and surface covering mixed by polystyrene acrylic resin and brick powder.Its schematic diagram is shown in Figure 2.

In this study, microscopic analysis, XRD analysis and infrared spectroscopy were used to analyze the structure and phase composition of bricks, mortar and surface coating; the types and contents of soluble salts were analyzed by ion chromatography; infrared thermal imaging and microwave humidity analysis were used to analyze the water distribution at different depths of the base of the bell tower and to interpret the water and salt transport regularity. And the development trend of disease was determined by regular three-dimensional scanning of fixed disease area. The relationship between surface coating and water,salt transport and disease development of the base was explored through the above comprehensive analysis,which provide support and reference for the later protection and treatment of the base of the bell tower.

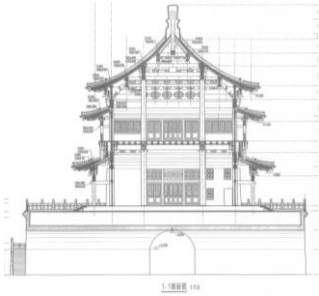

Fig 1. The cross-section of the Bell Tower

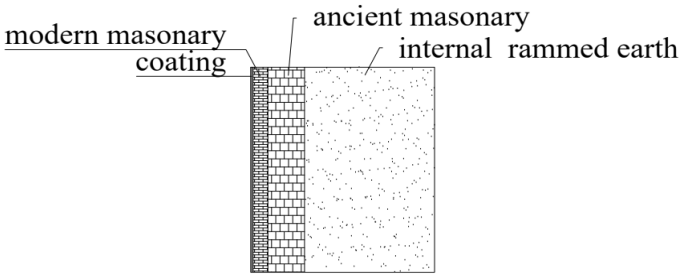

Fig.2 Schematic diagram of the facade of the Bell Tower base

2 ANALYSIS AND RESULTS

2.1 Detection and analysis of Brick

Take a square brick of the Bell Tower base. The size of brick is measured as 46cm in length, 22cm in width and 10cm in height. The color of brick is blue-gray, which means it is the commonly used standard green brick in ancient buildings. Porosity, phase composition, mechanical strength, XRD and other analyses are finished, and the physical performance test results are shown in Table 1.

Table 1 Analysis results of physical properties of bricks of the Bell Tower base

Number	Porosity %	Density g/cm3			Water content%	Compressive strength	Shearing strength	
		natural	dry	saturate			C	Φ
Y113	31.19	1.63	1.55	1.87	20.01	4.47	1.3	34.3
Y114	29.78	1.64	1.56	1.86	19.05	6.05		

It can be seen from the results that the average compressive strength of brick from the Bell Tower base is 5.26MPa, while the compressive strength of the traditional green brick stipulated in the "Traditional Green Brick Green Tile Quality Inspection Reference Standard" is 5MPa, indicating that the brick of the bell tower base has good strength.

XRD test results: The main components of the brick are quartz: 54.7%, plagioclase feldspar: 14.5%, potassium feldspar: 18.5%, calcite: 0.6%, dolomite: 1.3%, pyroxene: 10.4%. The specific analysis spectrogram is shown as Figure 3.

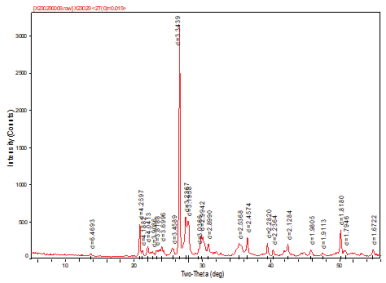

Fig 3. X-ray diffraction spectrogram of brick

2.2 Surface coating analysis

There is a clear layer of coating on the surface of the Bell Tower base. Take coating samples from west, south and east sides of the base respectively. The components are analyzed by infrared spectrum, while the surface bonding condition is observed by microscope (seen in Figure 4). It is observed by microscope that the surface has been painted with multiple coatings.

Fig 4. Photomicrograph of the surface coating

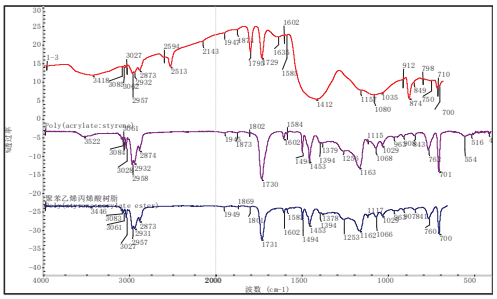

Fig 5. Copolymer of butyl acrylate and styrene

The results of infrared spectrum analysis are shown as follows:

There are obvious organic matters in the coating samples from three sides of the base wall. The main component of the organic matter is polystyrene acrylic resin, in which the main ingredient is a copolymer of butyl acrylate and styrene (Figure 5). Meanwhile, there are calcium carbonate, calcium sulfate and silicate substances in the sample, and the sample may contain quartz sand.

2.3 Analysis of soluble salts

In the investigation, it was found that soluble salts are concentrated on the surface of bricks, hollowing layers or peeled warping parts. The microscopic results showed that the salt is covered on the surface of the brick or inside the brick structure, and is crystalline(Figure 6).

Ion chromatography analysis results: through analysis, the cations in the surface of the brick wall of Xi'an Bell Tower base mainly contain Na^+ and Ca^{2+}, next is K^+, and a little Mg^{2+}, while in anions, the NO^{3-} content is relatively larger, the content of Cl- and SO_4^{2-} is smaller. This shows that the main soluble salt component of the brick wall of the Bell Tower base should be $NaNO_3$, seen in Table 2. From the analysis results, it can be seen that in the external salt, the nitrate ion content percentage is 13.43%, the nitrate ion content of internal salt is reduced to 2.5%, while the nitrate ion content in the unweathered brick is only 0.54%, and the sulfate ion content and chloride ion content in external salt are higher than that in internal salt, which shows that the soluble salt has a process of transport from inside soil mass to the outside brick wall.

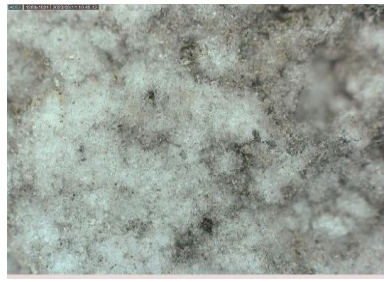

Fig 6. Weathering products

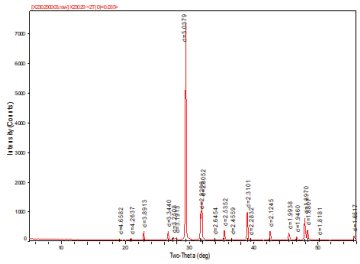

Fig 7. XRD pattern of weathering products

Table 2 Ion chromatography test results

Position	Atomic percentage of chemical elements %						
	Na	K	Mg	Ca	Cl	NO_3	SO_4
external salt	5.44	0.09	0.06	0.91	0.80	13.43	0.37
Internal salt	0.46	0.04	0.03	0.51	0.16	2.50	0.10
Unweathered brick	0.31	0.04	0.00	0.13	0.38	0.54	0.06

3 DISEASE ASSESSMENT

In order to further understand the development trend of brick detachment, flaking and peeling deterioration caused by water and salt damage, full-frame high-pixel digital camera (Nikon D850) and three-dimensional scanner were used to monitor the displacement and deformation of typical deterioration areas of the Bell Tower in February, May and August 2022. The detailed analysis results are shown in the table 3.

Table 3.Deterioration development trend of the Bell Tower

location	Brick detachment	Brick disruption	Thick flaking	other
east	gradual bulge trend, the bulge in the second quarter is about 0.2-0.5mm	Soluble salt increase	Flake loss, 10-15mm thick	About 40% of the monitored areas showed no significant deformation, Cement mortar has gradual bulge trend
west	Mass loss, 15--25mm thick	Flaking loss, 1.1--4.8mm thick	New loss appears	About 41% of the monitored areas showed no significant deformation
south	Flaking loss, 3.4-3.9mm thick		Flaking loss 1.0--1.3mm thick in the second quarter，1.6--2.0mm thick in the third quarter	About 30% of the monitored areas showed no significant deformation, Cement mortar has gradual bulge trend, 8--11mm thick
north	gradual bulge trend, the bulge in the second quarter is about 1.0-2.2mm		Some parts showed significant performance, 6--8.5mm thick	Cement mortar has gradual bulge trend, 1.0-1.6mm

It is found that the deterioration area of the east and west wall of the Bell Tower changes obviously. In half a year, the brick detachment on the surface of the brick body gradually flakes off, and the mortar has a tendency to gradually bulge. Although the depth is not deep, the long-term development will be very unfavorable to the conservation of the brick wall of the Bell Tower.

SALT ANALYSES AND THERMODYNAMIC MODELLING TO PRESERVE BUILT HERITAGE: THE CASE OF CORDOUAN LIGHTHOUSE

J. Desarnaud[1], S. Godts[1], V. Crevals[1], S. Dubois[2], M. de Bouw[2], and Y.Vanhellemont[2]

KEYWORDS

Built Heritage, Conservation, Salt weathering, salt mixtures, porous media, stone decay

ABSTRACT

The lighthouse of Cordouan is a world heritage site located off the coast of Verdon-sur-Mer in the middle of the ocean. Built during the XVII century it is the oldest lighthouse in France which has also a chapel. The circular chapel follows the shape of the tower. The vaulted ceiling with an oculus allows light and air to pass through. Salt weathering is observed inside the chapel but regarding the location of the building, the conservation of stone with durable treatments is difficult. In this study, the optimization of climatic conditions in the chapel are investigated to establish a conservation treatment through the identification and quantification of soluble salts in the limestone (*pierre blanche de Saintonge*) and the understanding of the crystallization behaviour of the salt mixture identified. A salt mixture was found including halite, gypsum, sylvite, carnallite, picromerite, aphtitalite, niter, nitratine, antarticite, calcium nitrate, magnesium sulfate and sodium carbonate. In spite of a relatively low salt content, the stone decay in the chapel is important. Due to the constructive system, the oculi crossing the lighthouse from top to bottom generate variations in temperature and relative humidity that are particularly intense within the chapel, leading to the repetition of the cycles of crystallization and dissolution.

Crystallization experiments of salt mixtures found in the chapel have been performed with a RH generator coupled to a windowed climate chamber and a 3D microscope. The phase transitions observed matches the modelled crystallization behaviour with ECOS/RUNSALT, with expected deviations considering gypsum and carbonates. The results established an optimal indoor climate for the stone conservation in the chapel without invasive interventions. They also demonstrate the

[1] Royal Institute of Cultural Heritage, 1 Parc du Cinquantenaire 1000 Brussels, Belgium

[2] BuildWise, Kleine Kloosterstraat 23, 1932 Zaventem, Belgium

strength of the combined techniques of salt analyses, thermodynamic modelling, and experimental observations as tools for the conservation of Built Heritage.

1 INTRODUCTION

Stone degradation by salt crystallization is one of the major causes of mechanical and physical damage of built heritage (1-3). Salts can be naturally present in the materials used for construction (such as mortars and bricks) or can derive from external sources (rising damp, sea brine, atmospheric pollution, etc…). Salt weathering occurs when salts, accumulated at the first millimeters or centimeter over years, fill a porous material and are submitted to crystallization/dissolution cycles due to variations in environmental conditions. There is compelling evidence that its influence will increase due to global climate change (4,5). The risk factors related to such a change include sea level rise, intense rainfall, flooding and changes in humidity cycles which can considerably amplify phase changes in salt crystallization. In the case of sodium chloride contaminated stones, it has been shown how humidity fluctuations (i.e. deliquescence followed by drying) induce the recrystallization of large NaCl crystals in the pores at the subsurface of the porous material leading to damage after several cycles (6). However, in buildings not a single salt, but salt mixtures contaminate porous materials. Individual mixture composition determine the crystallization behaviour of each possible salt that can precipitate (7,8). Understanding this behavior is essential to prevent salt decay and the overall for conservation strategy.

This is illustrated through a case study. The lighthouse of Cordouan is a listed building located in Verdon-sur-Mer in the Bay of Biscay at the entrance of Gironde Estuary. Strong salt weathering is observed inside the chapel and finding a durable conservation treatment is difficult considering its location. In this study, several strategies to optimize the climatic conditions in the chapel are investigated, through the identification and quantification of soluble salts in the limestone of the masonry and the understanding of the crystallization behaviour of salt mixtures.

2 MATERIALS AND METHODOLOGY

Previously known as the 'Lighthouse of the King', the Cordouan Lighthouse stands as a historic beacon of maritime navigation. Because shipwrecks in the estuary of Gironde became very frequent, Henry III decided to rebuild the lighthouse in the place of an English fire tower and confided the project to the architect and engineer Louis de Foix in 1582. He wanted to make the lighthouse a royal project worthy of the ancient wonders, such as, the Alexandria lighthouse. The period of Wars of Religions made the construction very slow and tremendously expensive. At the death of Henri III, Henri IV gave in 1593 his approval for a new and much more sumptuous project to be a symbol of the royal power, adding sculptures, woodworks and a chapel. The construction ended in 1611 with a 37m high tower, round with three floors. In the 1780's the lighthouse was risen by 20m in order to improve the visibility to sailors. The well-proportioned circular chapel with its remarkable massive dome is the central element of the tower, design by Louis de Foix [9]. It symbolized the monarchy and, furnished in the historical context, proof that the recently converted Henri IV was a 'good Catholic'. The decorations of the chapel are elaborated and meticulous paying tribute to the two kings (Henri's). There are

two oculi in the room, one at the peak of the ceiling providing a glimpse of a fleur-de-lis crown on the upper floor (Figure 1a) and one on the floor of the chapel (Figure 1b). The oculi bring light in the chapel and allow an air flow.

Figure 1: Interior of the chapel (a) view of the overhead dome, the arrow (A) indicates the oculus at the peak. (b): southern part of the chapel, the arrow (B) indicates the oculus on the floor of the chapel. (c): details of natural stone decay, granular disintegration, powdering and scaling are seen in the chapel. (Picture ECMH)

The lighthouse is a massive construction in Saintonge stones, limestones with a very fine porosity and some shells. It is located at the entrance of the Gironde Estuary at 7km from the coast.

The interior shows extensive degradation, such as powdering, granular disintegrations, detachment of the polychromies and preparation layer, all typical symptoms of moisture and of salt weathering (Figure 1c). To determine the ion content and identify the salts present, eleven samples (cores of 3 cm in depth and 1cm in diameter) of stone were taken by the Hory-Chauvin Saintonge firm (ECMH) in several locations of the chapel:

Samples 1 (at the lower section of the wall) and 2 (above the shoulder of the sculpted bust of Louis de Foix), western part of the chapel (Figure 2a). Samples 3 (at the base), 6 (at the bottom of the cornice of the spherical vault) and 8 (in a stone coffer of the dome-shaped vault), northern part of the chapel (Figure 2b). Samples 4 (in the niche above the altar), 7 (at the bottom of the cornice of the vault) and 9 (in a stone coffer of the dome-shaped vault) eastern part of the chapel (Figure 2c). Samples 5 (at the lower section of the wall), 8 (at the bottom of the cornice of the vault) and 11 (in a stone coffer of the dome-shaped vault), were taken from the southern part of the chapel.

The determination of the ion content of each sample was carried out as followed: the dried sample was placed in a bottle containing ultra-pure water in order to extract the solubilised salts. The concentrations of anions (Cl^-, NO_3^- and SO_4^{2-}) and cations (Na^+, K^+, Ca^{2+} and Mg^{2+}) are then measured by ion chromatography (Metrohm apparatus). The results are expressed as a percentage by weight of the dry sample. From the excess of cations , the soluble carbonates content was calculated. The results were used to determine for which samples modelling of the salt behaviour was deemed relevant.

Figure 2: Location of the stone samples for analysis in the lower section of the wall and cornice of the spherical vault (Picture ECMH)

Figure 3: Location of the stone samples for analysis in the base and interior of the caissons of the spherical vault (Picture ECMH)

The thermodynamic model ECOS/RUNSALT has been used to determine the crystallization behavior of the mixed salt solutions as a function of indoor climate conditions (i.e., relative humidity and temperature), excluding factors such as the internal pore structure. It is currently the only model that includes the most relevant salt phases found in built heritage (8). However, as several limitations and pitfalls exist when using the model, possible incorrect interpretations of the derived outputs can occur. In order to verify the RUNSALTS outputs, the dissolution and crystallization properties of the salt mixtures were observed under changing RH. For this purpose, the first three millimeters of the cores were grounded and mixed with 4 ml of ultra-pure water for 24 hours to dissolve the salts. The mixtures were then filtered to extract only a solution containing the dissolved salts. A 0.5µl drop of the salt mixture was then placed in a micro climatic chamber (GenRH/Mcell) with a constant gas flow (H2O and N2) at 200 sccm (standard cubic centimeters per minute) and observed with 3D-digital microscopy, (HIROXKH-8700). The solution containing the salt mixture was exposed to a relative humidity ranging from 100% to 20% in 5% reductions with 20 min intervals. The temperature was set at 20°C.

By recording an image every 5 seconds, the time of phase change (crystallization/dissolution) was accurately determined. The humidity changes are recorded every 5 seconds, which allowed the identification of the relative humidity during the phase changes (i.e. crystallization).

3 RESULTS AND DISCUSSION

3.1 Determination of ions content

The ions content from the first centimeter of the 11 samples are given in the table 1.

In general, the samples show low content of soluble salts (Table 1). The concentrations of sodium chloride (NaCl) in samples 3, 4, 6, 7 and 8 are above the critical threshold of 0.1% (10). However, the total soluble salt content (excluding $CaSO_4$ and including CO_3) of samples 3 and 4 remains low. The highest amount of soluble salts are found in samples 6, 7 and 8, all of them were taken from the lower parts of the cornice of the spherical vault. Sample 9, which was taken from a coffer of the spherical vault, also has a higher total soluble salt content. Thus these 4 samples (i.e. 6, 7, 8, 9) are the most relevant for the tests to determine the crystallization behavior of the salt mixtures. It should be noted that compared to the stoichiometric equilibrium, samples 6, 7, 8 and 9 show excesses of Na^+ and sample 8 shows a strong excess of CO_3, which will have to be taken into account during the thermodynamic modelling with the ECOS-Runsalt software.

Table 1: Ions content obtained by Ionic Chromatography for the stone samples from Cordouan Lighthouse. Samples with more than 0.1% chloride are marked green.

(*): total excluding equimolar Ca+SO4 content (anhydrite is considered as the gypsum content). Values are shown in % by mass calculated on the basis of the IC values in ppm .

(**) Samples with a total salt content of more than 1% by weight (after subtraction of calcium sulphate, Ca+SO4, but including the theoretical carbonate are highlighted in red).

	Anions			cations				$Ca+SO_4$	Wt% CO_3	Total excl*	Total incl**
	Cl^-	NO_3^-	SO_4^{2-}	Na^+	K^+	Ca^{2+}	Mg^{2+}				
PC1	0.05	0.0005	0.02	0.05	0.004	0.12	0.003	0.03	0.21	0.21	0.42
PC2	0.02	0.0001	0.01	0.03	0.02	0.12	0.003	0.02	0.22	0.18	0.40
PC3	0.13	0.0002	0.01	0.13	0.02	0.13	0.005	0.02	0.28	0.40	0.69
PC4	0.13	0.0001	0.02	0.13	0.02	0.27	0.001	0.02	0.24	0.37	0.62
PC5	0.08	0.0006	0.08	0.07	0.01	0.16	0.003	0.12	0.23	0.29	0.52
PC6	**0.20**	**0.0002**	**0.03**	**0.20**	**0.02**	**0.10**	**0.01**	**0.04**	**0.28**	**0.53**	**0.81**
PC7	**0.26**	**0.0002**	**0.02**	**0.27**	**0.03**	**0.12**	**0.004**	**0.03**	**0.35**	**0.67**	**1.02**
PC8	**0.23**	**0.0004**	**0.12**	**0.13**	**0.02**	**0.20**	**0.010**	**0.17**	**0.24**	**0.53**	**0.78**
PC9	**0.09**	**0.0003**	**0.02**	**0.21**	**0.01**	**0.10**	**0.003**	**0.02**	**0.35**	**0.40**	**0.76**
PC10	0.08	0.0004	0.02	0.10	0.01	0.12	0.01	0.03	**0.27**	**0.32**	0.59
PC11	0.08	0.0004	0.01	0.15	0.02	0.010	0.002	0.02	**0.29**	**0.34**	0.63

3.2 Thermodynamic modelling with ECOS/RUNSALT of the crystallization behavior of salt mixture

The IC identifies the ions composition of mixture; These results are used as input for the ECOS/RUNSALT model to determine the crystallization behavior of the mixture under changing relative humidity and temperature. The result obtained for sample 6 and sample 7 are similar it is why only results from sample 7 will be presented.

Eastern Part of the Chapel, cornice of the vaulted ceiling : Sample 7

The observations under the microscope show that phase transition of the salt mixture solution (liquid) of sample 7 appears at a relative humidity (RH) of 50%. The first crystals of halite (sodium chloride) precipitate at 50% RH with a dendritical habits and at 45% RH all the salts have crystallised (images in Figure 4) the whole solution has evaporated. The crystallisation behaviour determined by the ECOS/RUNSALT model (graph in Figure 4) shows that repeated dissolution-crystallisation cycles of the salts present can occur within a restricted relative humidity (RH) range, with significant changes around 57% and 49% RH. Antarticite, a very

hygroscopic salt crystallizes theoretically at a relative humidity lower than 30%. At a relative humidity higher than 60% all the salt are dissolved in solution. The results obtained by microscopic observations and by modelling are in general agreement but reveal some discrepancies. They can be caused by the rapid lowering of the relative humidity in the micro climatic chamber with 5% steps each 20 minutes. Moreover, it was expected from theory that remaining solution would be visible at 45% due to the high content of extreme hygroscopic salts. Calcium nitrate should theoretically precipitates in this mixture at very low RH : 20% but as tetrahydrate crystals. This is not observed and it could be likely caused by the excess cations (especially sodium) most likely related to carbonates, thus changing the mixture composition, crystallization pathway and possible solids that precipitate.

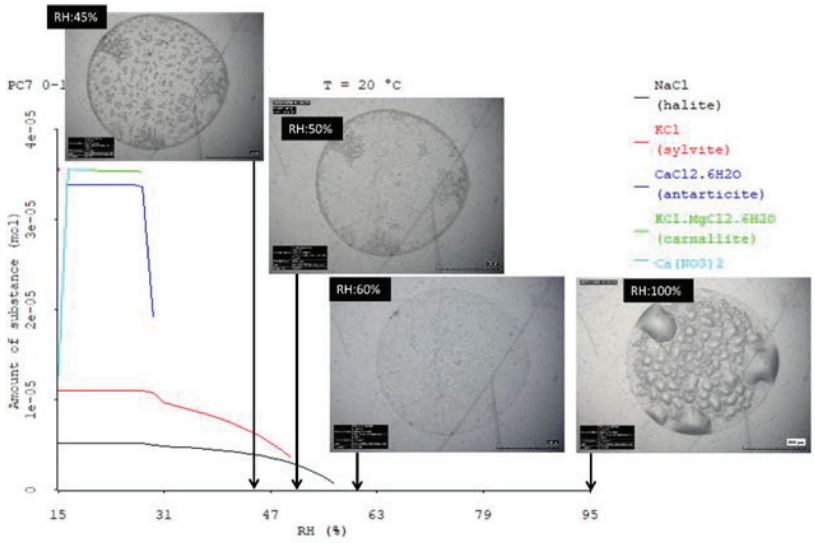

Figure 4: Crystallization behavior for variable relative humidity at a temperature of 20°C of the mixture of ions detected in sample 7 taken from the first centimeter of the stone core (subtraction made from an equimolar content of sodium and calcium ions) generated with the ECOS-Runsalt model.

Southern part of the chapel, cornice of the vaulted ceiling : Sample 8

The phase change observed under the microscope of the salt mixture solution in sample 8 starts at 75% (Figure 5). The first crystallisations appear at a humidity of 75% at 20°C in cubic habits and they grow rapidly. As salt concentrations are not high, the quantity of crystals is low. At relative humidity of 55% a second type of crystal precipitates and all crystals have precipitated at 50%RH.

The crystallization behaviour determined by the ECOS-Runsalt model (Figure 5) shows that repeated dissolution-crystallisation cycles of the salts present in the mixture can occur within a narrow relative humidity (RH) range, with significant changes between 71% and 60% RH. The majority of salt in this mixture is halite (sodium chloride). At a relative humidity higher than 71% all the salt are dissolved

in solution and will not crystallize. This mixture does not present an excess of cations. The crystallization observed under the microscope occur with slightly discrepancies with the modelled one likely caused by the fast rate of lowering relative humidity.

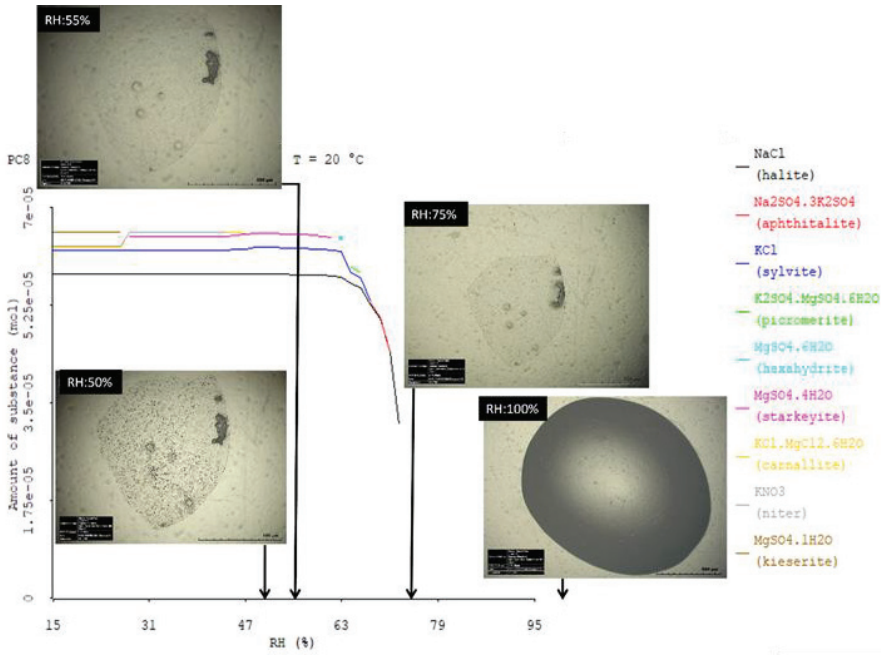

Figure 5 : Crystallization behavior for variable relative humidity at a temperature of 20°C of the mixture of ions detected in sample 8 taken from the first centimeter of the stone core (subtraction made from an equimolar content of sodium and calcium ions) generated with the ECOS-Runsalt model.

Southern part of the chapel, inside vaulted ceiling : Sample 9

The phase change of the salt mixture solution in sample 9 was observed at 20°C under the microscope. At a relative humidity of 70%, cubic crystals precipitated and grew rapidly to reach a mean size of 350µm. Almost no precipitation was observed between 70% and 50%, and at 50%RH a new batch of small cubic crystals (with a size of max 150µm) precipitated (Figure 6). From 45% no more crystallization is observed.

The crystallisation behaviour determined by the ECOS-Runsalt model (Figure 6) shows that repeated dissolution-crystallisation cycles of the salts present can initially occur around 70% RH for the niter and bloedite. It should be noted that this last one is in very small quantities in the salt mixture. At 59% RH there are significant changes with the crystallization of halite (sodium chloride), nitratine (sodium nitrate) and starkeyite (hydrated magnesium sulfate). Above 70%RH all the salts are dissolved in solution.

The precipitation of cubic crystals at 70%RH is observed under the microscope and modeled by ECOS/RUNSALT. The 59% crystallization modelled are likely the ones that correspond to the observation under the microscope when the second batch of tiny crystals precipitations at 50% RH, again due to the rate of RH change in the climate chamber.

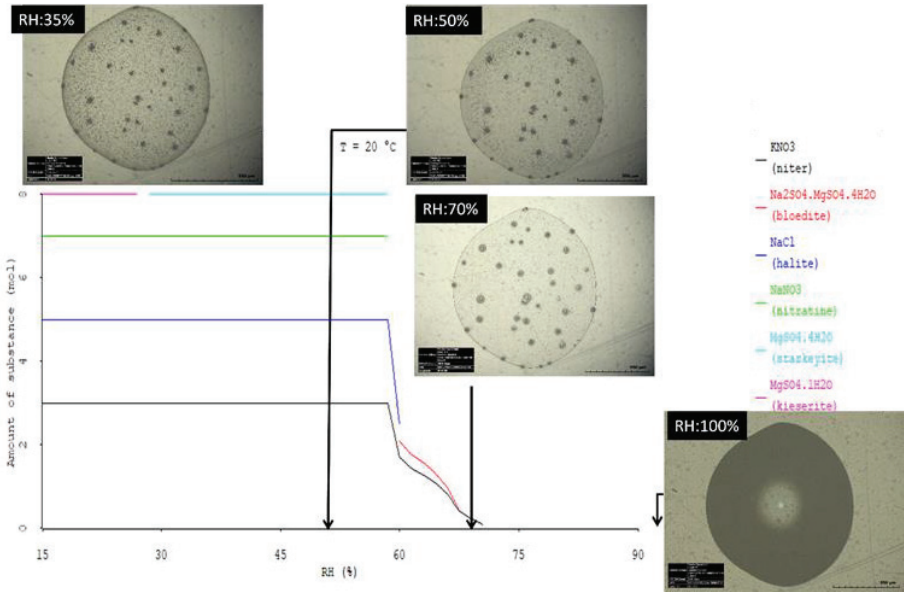

Figure 6: Crystallization behavior for variable relative humidity and at a temperature of 20°C of the mixture of ions detected in sample 9 taken from the first centimeter of the stone core (subtraction made from an equimolar content of sodium and calcium ions) generated with the ECOS-Runsalt model

For all the salt mixtures analyzed, crystallization and dissolution can occur within short time spans of changing relative humidity, that is, over the course of a single day and even several times a day, resulting in a large number of dissolution/crystallization cycles. The results can explain the observed degradations of the stones even if the amount of salt measured is low.

For samples 6 and 7, observations under the microscope and the outputs of ECOS/RUNSALT model showed that if the relative humidity inside the chapel is maintained above 63%, the salts will remain dissolved, limiting the number of dissolution/crystallization cycles and therefore the degradation of the stone in these parts of the chapel. The excess in sodium in those samples and the highly hygroscopic salt mixtures could lead to discrepancies with the observed crystallization under the microscope, especially at very low relative humidity.

Microscopic observations crystallization behavior under changing relative humidity of the salt mixture in sample 8 show initial crystallisation at 75% RH, which is confirmed by the modelling software at 71% RH. However, the amount of salt (NaCl) that crystallizes at this relative humidity appears to be very low. According to the microscope observations, most of the salts will only crystallize when the

humidity reaches a value of 55% and 50% RH. In order to reduce the number of dissolution and crystallisation cycles, the humidity could be kept higher than 63%, as most of the salts would be dissolved in solution. It is important to follow the evolution and monitor the degradations of this specific area because at this relative humidity a small quantity of salt (NaCl) can still precipitate.

The observations show that for sample 9 the first crystals appear and grow from 70% RH. From 70% to 50% there is no precipitation. It is only from 50% RH that new crystals appear until the total precipitation of all the salt crystals at 45% RH. In order to avoid any crystallization, the humidity should be kept higher than 70% but this humidity value can be considered too high and biological development can occur. Consequently, to reduce the number of dissolution/crystallization cycles should be at least above 60% where most of the salts are dissolved in solution.

In the sample 8 ant 9, the salt mixtures do not present an excess in cations. The microscopic observations revealed discrepancies with theoretical ECOS output which is caused by the rate of RH change in the climatic chamber which is very with 5% steps each 20 minutes.

4 CONCLUSION

The deteriorating stone of the chapel of Cordouan have been analyzed to identify and determine the ion content and salt behavior with Ion chromatography (IC) and the thermodynamic model ECOS/RUNSALT. Four samples (6, 7, 8, and 9) were selected on the basis of the IC results, as they showed the highest contents (mean 0.8 wt.%). Almost half of the total salt content was related to an excess of sodium ions, likely related to carbonates.

The first 3 samples were taken from the cornice of the spherical vault and sample 9 was taken from a coffer in the spherical vault. Only sample 7, taken from the stone at the cornice of the spherical vault, contains a total salt content of over 1 wt.%. Regarding the intensity of the damage in the chapel and the low amount of salt measured within the first centimeters of the stone inside the chapel, it is clear that the number of dissolution/crystallisation cycles for the salts present in the masonry is very high. The possible impact of potential ancient treatments and to a lesser extend freeze-thaw cycle to damage has not be studied in this research. Keeping the humidity higher than 63% would prevent most of the salts from crystallising and would keep them dissolved in solution. On the other hand, dissolution/crystallisation cycles can still occur, which may cause damage. For this reason, in the area of sample 9 and 8, the evolution of degradation should be monitored.

The relative humidity and the temperature are currently not controlled in the chapel. The chapel's oculi allows the air flow from the floor to the bottom that leads to large variations in climatic conditions. Closing them will reduce the variation of climatic conditions in the chapel and consequently the dissolution/crystallisation cycles and therefore limit salt weathering. The relative humidity and temperature inside should be monitored and controlled by installing sensorsin order to measure gradients in the chapel and its impact on the degradation.

It should be noted that above 70% humidity there is a risk of biological development. The likelihood of mould growth is low because there is little organic matter

(such as wood) in the chapel In addition, in order to reduce this growth, the chapel should be heated as little as possible, taking care to maintain the temperature gradient between the lower level and within the vault.

Because of its location in the middle of the estuary, the type of construction, presence of polychrome, a sustainable desalination of the lighthouse is complicated, yet a possibly to be further explored. Additionally, it would be advised to continue investigations concerning possible water infiltrations, frost damage, and previous treatments that might have been carried out.

The combination of salts analyses, thermodynamic modelling and microscopy allowed to set optimal climatic conditions to reduce salt decays on the stone inside the chapel. The comparison of results showed that the use of ECOS/RUNSALT should be carefully evaluated when an excess sodium is significant. An important obstacle in the calculations is caused when there are extremely high concentrations in hygroscopic mixtures, including calcium nitrate and calcium chloride, resulting in water activities higher than expected from thermodynamics as Godts et al. 2022 have demonstrated. But when the presented issues and solutions are taken into consideration, the RUNSALT outputs can be considered highly accurate.

5 ACKNOWLEDGEMENT

The authors want to thank ECMH the engineering consultants firm specializing in the conservation of built heritage in France which gave the opportunity to work on the project and provided all the pictures used in the article.

6 REFERENCES

[1] Goudie, A.; Viles, H. Salt Weathering Hazards; John Wiley & Sons: Chichester, UK, 1997; ISBN 0-471-95842-5

[2] Oguchi, C.T.; Yu, S. A Review of Theoretical Salt Weathering Studies for Stone Heritage. Prog. Earth Planet. Sci. 2021, 8, 1–23

[3] Godts, S.; Steiger, M.; Orr, S.A.; De Kock, T.; Desarnaud, J.; De Clercq, H.; Cnudde, V. Charge Balance Calculations for Mixed Salt Systems Applied to a Large Dataset from the Built Environment. Sci. Data 2022, 9, 324

[4] Augustin, C. Climate Change and World Heritage: Report on Predicting and Managing the Impacts of Climate Change on World Heritage and Strategy to Assist States Parties to Implement Appropriate Management Responses (Ed. UNESCO World Heritage Centre, Paris 2007).

[5] Sabionni, C., Cassar, M., Brimblecome, P. & Lefevre, R. A. Vulnerability of cultural heritage to climate change, EUR-OPA major hazards agreement, Council of Europe November (2008).)

[6] Desarnaud, J., Derlyun, H., Molari, L., de Miranda, S., Cnudde, V. & Shahidzadeh, N. Drying of Salt contaminated porous media; Effect of primary and secondary nucleation. J. App. Phys. 118, 114901 (2015).

[7] Price, C., Brimblecombe, P. Preventing Salt Damage in Porous Materials. Stud. Conserv. 1994, 39, 90–93.

[8]- S. Godts et al., Modeling Salt Behavior with ECOS/RUNSALT: Terminology, Methodology, Limitations, and Solutions, Heritage, vol. 5, no. 4, pp. 3648–3663, Nov. 2022, doi: 10.3390/heritage5040190.

[9] Munoz, E., C. L'exhaussement du phare de Cordouan. Un chantier des Lumières (1786, 1789). Bull. 2006. V164-2, pp187-194.

[10] Philippon, J., Mourlon-Druol, E., Tetart, F., Bromblet, P., Verges-Belmin, V. Marie-Victoire., E, Bottineau, C., Babics, F., Desmarquest, J., Morot-sir, P., Decousu, A., Molard, A., Patrouilleau C., Coquillat, A. Ouvrages de maçonnerie. Ministère de la culture et de la communication, direction de l'architecture et du patrimoine, Sous-direction des monuments historiques et des espaces protégés (France). 2006 p40;

SANDSTONE PORE CHARACTERISTICS AND DISTRIBUTION OF SALT CRYSTALS IN CAVE NO.4 OF THE YUNGANG GROTTOES

Xiaotong Huo [1,2], Zhiyan Du[1], Hongbin Yan[3], Yamin Xiong[1], and Jinhua Wang[1*]

KEYWORDS

Chemical weathering, magnesium sulphate, pore distribution, pore categories, salt weathering,

ABSTRACT

The Yungang Grottoes, one of China's most representative sand-stone grottoes, currently face various types of damage, including severe salt weathering. Magnesium sulphate has been identified as one of the major contributors to weathering and tends to occur most intensively in areas with long-term water infiltration. In this study, the MIP method was employed to evaluate the porosity and pore diameter distribution characteristics of Yungang sandstone samples under various conditions. The pores were classified into four types based on their size. The findings revealed distinct differences in salt crystallisation behaviour and the resulting pore damage be-tween the simulated samples of $MgSO_4$ and Na_2SO_4: the former tended to form crystals across all pore categories, whereas the latter predominantly formed crystals in larger pores and mesopores. These findings emphasise the critical role of microstructural characteristics, specifically pore size distribution, in the salt damage observed in Cave No. 4 in the Yungang Grottoes.

[1] Department of Cultural Heritage and Museology at Fudan University, 220 Handan Road, Shanghai, 200433, China, 20110540002@ fudan.edu.cn

[2] Shaanxi History Museum, 91 Xiaozhai East Road , Xi an, 710061, China

[3] Yungang Grottoes, Yungang Tourist Area, Datong City, Shanxi Province, China

1 INTRODUCTION

The Yungang Grottoes, constructed 1500 years ago, are prime examples of ancient Chinese sandstone grooves. Cave No. 4 exhibited blistering, scaling, crumbling, and subflorescence deterioration (Figure 1). This study specifically investigated Cave No. 4, where the subflorescence is composed of magnesium sulphate salts ($MgSO_4 \cdot 6H_2O$ and $MgSO_4 \cdot 4H_2O$). Salt weathering has been considered as the primary abiotic factor contributing to cave deterioration.

Previous studies have shown that the size and distribution of pores within sandstone play a crucial role in the migration of salt solutions, salt crystallisation, and the resulting damage to the pores[1]. Therefore, analysing the pore properties of sandstone in the Yungang Grottoes is essential for exploring the salt weathering mechanisms. The MIP method was used to assess the pore characteristics of the fresh, weathered, and simulated $MgSO_4$ and Na_2SO_4 samples.

2 INVESTIGATION AND EXPERIMENTS

A non-differential grid-based sampling strategy was utilised to cover all of the wall surfaces of the grottoes. Areas exhibiting visible signs of salt damage, such as cracks with water seepage and peeling surfaces, were specifically targeted to obtain focused samples (Figure 2). X-ray diffraction was employed to compare the chemical and mineralogical compositions of the fresh and weathered specimens, leading to the selection of $MgSO_4$ and Na_2SO_4 as target salts for further experimentation.

Fresh sandstone samples of Cave No. 4 and shaped into cylinders. Salt crystallisation was induced in the sandstone cylinder pores by capillary action. Two samples were individually soaked in 0.2 mol/L solutions of $MgSO_4$ and Na_2SO_4. The lower half of each sample was immersed in the salt solution and placed in a sealed container, whereas the upper half was exposed to lab environmental conditions (Figure 3). Subsequently, MIP intrusion was employed to assess the porosity and pore size distribution of the samples. Prior to porosimetric characterisation, the precipitated salts were removed through three cycles（one cycle for three days） of washing with deionised water.

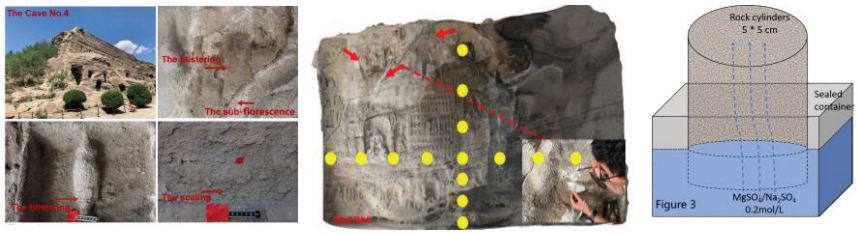

Figure 1: The weathering diseases in Cave No. 4
Figure 2: Salt sample collection on site
Figure 3: Experimental setup diagram

3 RESULTS

3.1 Mineral characterization

The XRD semi-quantitative comparison of the compositions (Figure 4a) indicates that the quartz content remained relatively unchanged between the fresh and weathered samples. However, the weathered samples exhibited a notable decrease in the potassium feldspar and siderite contents, while the calcite, illite and kaolinite contents increased. The XRD analysis confirmed the presence of hexahydrite and starkeyite in the salt-damaged areas (Figure 4b). The coal mining and combustion activities near the Yungang Grottoes maybe an external source of sulfur in the salt weathering products.

Blister-like aggregates were observed in the upper part, causing convex deformation of the stone surface layers through MgSO4 crystallization. whereas the surface of the Na2SO4 sample was covered with white flocculent crystals that precipitated from the rock surface (Figure 5).

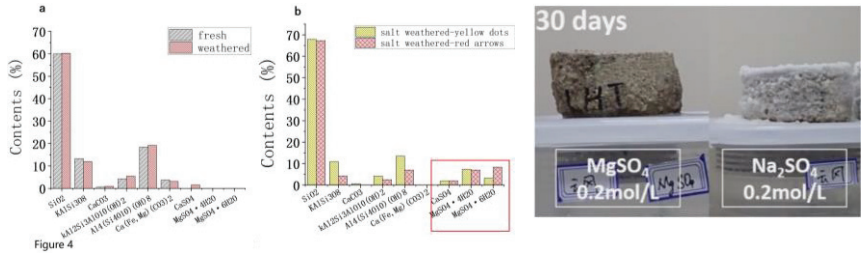

Figure 4: The column chart of semi-quantitative composition of XRD.

Figure 5. Photos comparing the experimental sandstone samples after 30 days

3.2 Microscale pore characteristic

The MIP analysis of the open-pore access diameter distribution in fresh and weathered sandstone samples displayed distinct characteristics. The fresh sample exhibited a monomodal distribution with a peak centred at 500 nm. In contrast, the weathered sample exhibited a polydisperse distribution with an additional peak at 9000 nm and a smaller peak at 500 nm (Figure 6). The pore access diameter distributions of the $MgSO_4$ and Na_2SO_4 salt-simulated weathered samples exhibited significant differences. In Figure 7a, the green areas indicate pore expansion with $MgSO_4$, while the blue areas indicate pore expansion within. Figure 7b shows pore expansion with Na_2SO_4. The grey areas in Figure 7 represent pores that were filled or blocked; in the pore diameter range of 100–1000 nm, the $MgSO_4$ crystals filled less pore space than the Na_2SO_4 crystals.

4 DISCUSSION

This study, which classified the pore-size distribution based on the water behaviour in rock pores using Kelvin's equation, was appropriate [2]. The MIP analysis

revealed that both naturally weathered samples and salt-simulated weathered samples exhibited significant effects on pores within the diameter range of 100 nm to 1000 nm (Figure 6 and 7). The sandstone pores in Cave No. 4 were classified into four categories: micropores (<50 nm), small pores (50–100 nm), mesopores (100–1000 nm), and large pores (>1000 nm). Figure 8 illustrates the pore volume percentage for each category, highlighting the differential impacts of the two salts on the pore size. $MgSO_4$ exhibited a tendency to crystallise across all pore sizes, whereas Na_2SO_4 primarily crystallised in larger mesopores. The disparity in crystallisation patterns between these two salts can be attributed to variations in the evaporation rates caused by differences in capillary flow within the stone [3]. The slower flow of the $MgSO_4$ solution resulted in faster evaporation and crystallisation beneath the stone surface, as the solution replenishment from within the stone through capillary migration was insufficient. In contrast, the faster flow of the Na_2SO_4 solution led to crystallisation primarily on the surface of the stone in the larger mesopores.

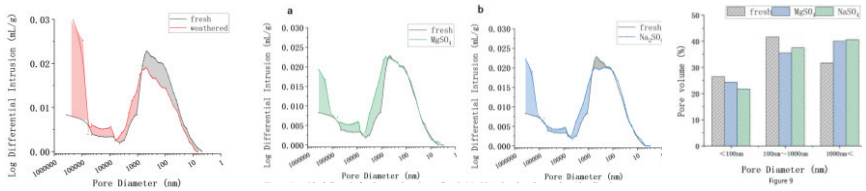

Figure 6: MIP plots of pore diameter distribution: fresh and weathered sample
Figure 7: MIP plots of pore diameter distribution: fresh and simulated samples
Figure 8: The column of pore volume percentage

5 CONCLUSIONS

This study proposes a pore classification scheme for sandstone from the Yungang Grottoes, the $MgSO_4$ was found to have a propensity to form crystals in all pore categories.

REFERENCES

[1] Swe Yu and Chiaki T. Oguchi, 'Role of pore size distribution in salt uptake, damage, and predicting salt susceptibility of eight types of Japanese building stones', *Engineering Geology*, vol. 115, no. 3, pp. 226–236, Oct. 2010, doi: 10.1016/j.enggeo.2009.05.007.

[2] Martin Ondrášik and Miloslav Kopecký, 'Rock Pore Structure as Main Reason of Rock Deterioration', *Studia Geotechnica et Mechanica*, vol. 36, no. 1, pp. 79–88, Mar. 2014, doi: 10.2478/sgem-2014-0010.

[3] E. Ruiz-Agudo, F. Mees, P. Jacobs, and C. Rodriguez-Navarro, 'The role of saline solution properties on porous limestone salt weathering by magnesium and sodium sulfates', *Environ Geol*, vol. 52, no. 2, pp. 269–281, Mar. 2007, doi: 10.1007/s00254-006-0476-x.

STUDY AND EVALUATION OF EFFLORESCENCE IN CAVE 4 OF THE YUNGANG GROTTOES

ZhiYan Du[1], HongBin Yan[2], YanMin Xiong[1], XiaoTong Huo[3,1], Jia Jia[1], and JinHua Wang[1]*

KEYWORDS

Field survey, sandstone, magnesium sulfate, gypsum, Yungang Grottoes

ABSTRACT

Cave 4 of the Yungang Grottoes is a central-pillar cave that has been exposed to open air for over 1500 years. The sandstone carvings in Cave 4 suffer from deterioration, delamination, exfoliation, and especially efflorescence on all carved walls.

To find effective methods to preserve Cave 4, a field survey was conducted to clarify the composition and distribution characteristics of efflorescence on the carved walls and central pillar. White precipitates and weathered sandstone powder-samples were collected from all cave walls and central pillar surfaces, then examined by X-ray diffraction (XRD). Further, a drilled sandstone core was examined by a micro-X-ray fluorescence scanner (XRF). Drilled sandstone powder produced during the drilling process was also collected.

The white precipitates gathered near the fissures in Cave 4 are considered imprints that seep in from rainfall. Sample testing showed both white precipitates and weathered sandstone powder containing magnesium sulfate and gypsum. Furthermore, the XRF scanning results showed that the content of magnesium and calcium in the exterior layer of the drilled sandstone core is higher than in its interior. Through a field survey and laboratory study, the distribution characteristics of efflorescence in Cave 4 of the Yungang Grottoes were mapped for discussion.

1 INTRODUCTION

The UNESCO World Heritage site Yungang Grottoes is located in Wuzhou Mountain, in Datong City. Cave 4 is a central-pillar cave with exquisite Buddhist art

[1] Department of Cultural Heritage and Museology at Fudan University, 220 Han-dan Road, Shanghai, 200433, China, dzy619@hotmail.com.
[2] Yungang Research Institute, Datong, China
[3] Shaanxi History Museum, Xi an, China

carvings on all vertical walls and central-pillar surfaces (Fig.1). The carvings, exposed for 1500 years, show deterioration from delamination and efflorescence.

To preserve Cave 4, it is important to clarify the efflorescence composition and distribution. A field survey was carried out by a research team from Fudan University and the Yungang Research Institute.

Figure 1: a. View of Cave 4 from outside. b. Central pillar.

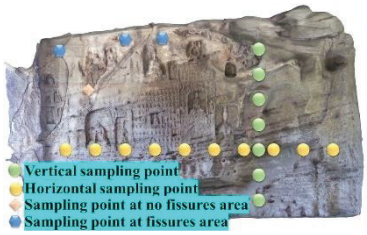

Figure 2: Sampling diagram on west wall.

2 METHODOLOGY

2.1 Field Survey

The preservation status, weathering pattern, and efflorescence distribution of all surfaces in Cave 4 were noted. Weathered sandstone powder was collected from the surfaces of each wall, including central-pillar surfaces (Fig.2). Horizontal sampling positions were 1.5 m from the ground, and vertical sampling positions were in the middle of the wall. Precipitate samples from fissure and non-fissure areas were also collected.

Holes with a diameter of 2cm and 90cm deep were drilled horizontally into the north wall for gradient temperature sensors by another team. The drilling took place over 14 phases. All sandstone cores and powder were collected before the next drilling phase was started. Dry-bit drilling was done to preserve the water-soluble minerals in the sandstone cores and powder. All drilled sandstone powder and sandstone core were collected for further examination.

2.2 Laboratory Study

First, thin rock section observation was carried out on unweathered sandstone collected near Cave 4. Then, the permeability of three of the cylinder specimens (Φ5cm × 5cm), was measured using a customized machine with test conditions of an applied pressure difference $\Delta P = 3.5$MPa and a confining pressure $P_{conf} = 7$MPa. All collected samples were examined using the XRD method (Rigaku, D/max-2600). The 0-2cm drilled sandstone cores were scanned using a micro-XRF Scanner (Bruker, M4 Tornado Plus).

3 RESULTS AND DISCUSSION

3.1 Results of the Field Survey and Laboratory Study

FIELD OBSERVATION: Serious deterioration, including exfoliation, delamination, and efflorescence, was observed on all walls, the central pillar, and roof (Fig.

3). Some parts of the walls were in a worse state of preservation, such as the carvings on the north wall that were weathered to tafoni (Fig. 3c). There was seepage near a fissure on the roof (Fig. 3a) and efflorescence around fissures on each wall. Figure 3b shows typical efflorescence in the area without fissures with large amounts of white precipitates appearing a few millimeters beneath the surface.

THIN SECTION OBSERVATION: Thin section observations show that the rock is medium-coarse lithic sandstone (Fig. 4). Some feldspar is replaced by calcite and dolomite.

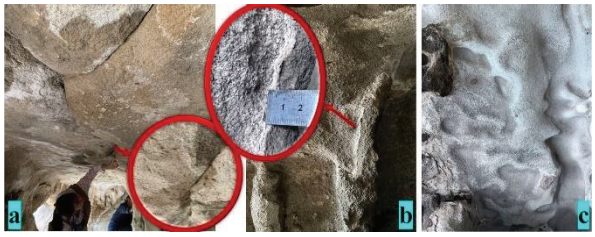

Figure 3: a. Seepage is seen near a fissure in the roof, b. Typical deterioration pattern on no fissures area, c. North wall in Cave 4 has been weathered to tafoni

Figure 4: Thin section image of unweathered sandstone.

STONE PERMEABILITY: Measurements of the liquid water permeability of the stone in the three cylinder specimens are 8.3×10^{-10} m^2, 8.3×10^{-9} m^2, and 3.3×10^{-9} m^2, which vary greatly.

XRD DETECTION: Result of XRD of the white precipitate samples collected at fissure and non-fissure areas shows precipitates containing hexahydrite, gypsum, and kaolinite. Table 1 shows the XRD result of weathered sandstone powder-samples collected from horizontal and vertical walls, which shows gypsum and MgSO4•nH2O precipitated on some surfaces. The XRD semi-quantitative analysis of drilled sandstone powder showed little difference in mineral or weathered product content from the 14 phases except for calcite (Fig. 5). Calcite at 0–2 cm is much higher than other phases, which means that calcite tends to be enriched on the surface of the wall.

XRF SCANNING: An exterior area near the surface and two interior areas near the 1cm- and 2 cm-depths of the drilled sandstone core were scanned using a micro-XRF scanner. Results indicated levels of magnesium (Mg) and calcium (Ca) in the exterior area were higher than in interior areas, while almost no difference in the levels of silicon (Si) could be distinguished in the three areas (Fig. 6).

Table 1: XRD result of samples collected from horizontal and vertical walls

Wall/surface	Sample quantity	Quantity of the following minerals present in all samples					
		Quartz	Gypsum	Kaolinite	Hexahydrite	Epsomite	Calcite
Vertical walls	68	68	28	65	4	1	1
Pillar	42	42	23	42	1	0	0

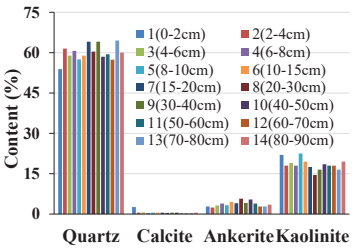

Figure 5: Semi-quantitative XRD analysis of drilled sandstone powder over 14 phases

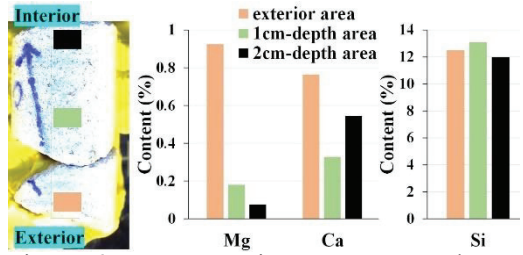

Figure 6: XRF Scanning areas on sandstone core, and XRF semi-quantitative analysis of Mg, Ca and Si.

3.2 Distribution Characteristics of Efflorescence

Efflorescence in Cave 4 could be divided into two types: One is distributed around the fissures and is considered to be imprints from rainfall seepage. The other type occurs in the area without fractures (Fig. 3b) and could be caused by the crystallization of the moisture in the sandstone's unsaturated exterior with the continuous evaporation of moisture in the mountain. This consideration is supported by the presence of calcite, Mg, and Ca on the surfaces (Figs. 5, 6). Furthermore, both types of efflorescence contain magnesium sulfate and gypsum. In areas without fissures, since the deliquescence relative humidity of gypsum is higher than that of magnesium sulfate, gypsum should precipitate closer to the surface [1]. The appearance of magnesium sulfate on surfaces (Table 1) shows the result of exfoliation. Measurements show that the permeability of the sandstone in Cave 4 varies greatly, which would lead to different evaporation rates at different surface areas. As a result, the level and depth of exfoliation would also vary at different surface areas. This is considered the reason for the appearance of tafoni in Cave 4 [2].

4 CONCLUSIONS

Two types of efflorescence, both consisting of magnesium sulfate and gypsum, occur in Cave 4. One is caused by seepage in fissures, and the other by continuous evaporation. Efflorescence occurring on areas with no fissures could lead to exfoliation and tafoni on the sandstone walls.

REFERENCES

[1] A. E. Charola, J. Pühringer, and M. Steiger, "Gypsum: a review of its role in the deterioration of building materials," *Environ Geol*, vol. 52, no. 2, pp. 339–352, 2007.

[2] A. V. Turkington and T. R. Paradise, "Sandstone weathering: a century of research and innovation," *Geomorphology*, vol. 67, no. 1–2, pp. 229–253, 2005.

A PERSPECTIVE VIEW OF SALT CRYSTALLIZATION FROM SOLUTION IN POROUS MEDIA: MORPHOLOGY, MECHANISM, AND SALT EFFLORESCENCE

Hongjie Luo[1,2], Qiang Li[1,2,3], Jing Zhao[3], and Xiao Huang[2*]

KEYWORDS

salt crystallization; porous media; morphology; mechanism; salt efflorescence

ABSTRACT

Salt efflorescence is one of the major hazards to cultural heritages, masonries and highways etc. It is now generally accepted that damages caused by salt efflorescence are mainly due to continuous cycles of salt crystallization/dissolution or hydration/dehydration in confined spaces. The position where salt efflorescence occurs and its type are closely related to the degree of damages caused by salt efflorescence. But the environmental factors that control the position and development of different salt efflorescence via nucleation and crystal growth still remain poorly understood. In this work, a set of experiments are designed to investigate salt efflorescence in porous matrix. It is found that the types and positions of salt efflorescence have little to do with nucleation, but are mainly governed by crystal growth, which is controlled by the rates of water evaporation, water and salt supply, capillary forces and surface properties of the porous matrices.

[1] School of Materials Science and Engineering, Shanghai University, Shanghai, China
[2] Institute for the Conservation of Cultural Heritage, Shanghai University, Shanghai, China
[3] Ancient Ceramics Research Center, Shanghai Institute of Ceramics, Chinese Academy of Sciences, Shanghai, China,
[*] Corresponding author, e-mail: xhuang@shu.edu.cn

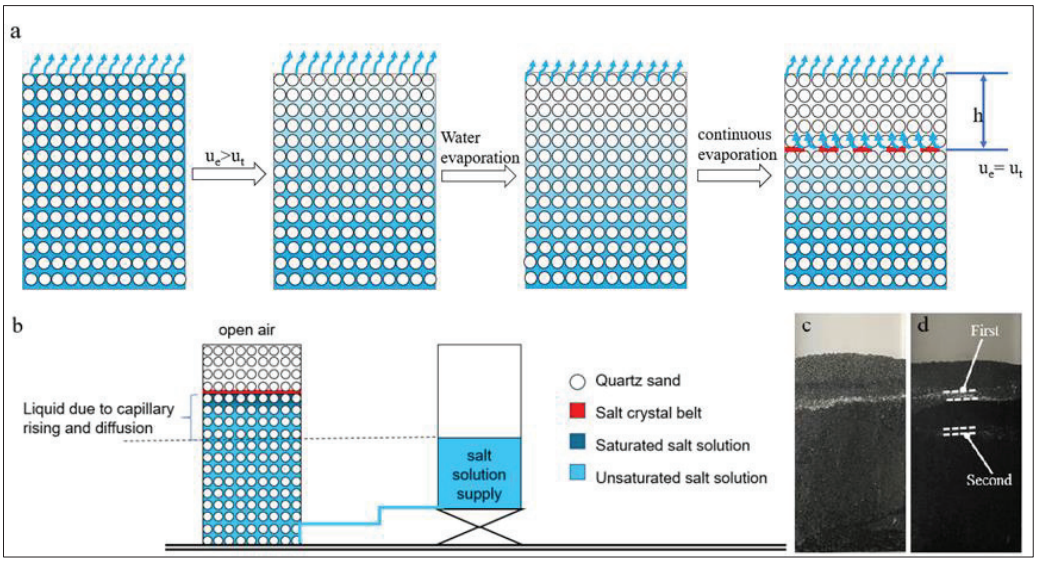

Figure 1. a) An illustration of water equilibrium between evaporation and migration in porous matrix. The lattice constructed by circles represents porous matrix; blue color represents liquid water (the bluer, the higher water content); red represents salt crystals; arrows indicate water evaporation. b) experimental set-up of water supply control; pictures of results: c) one salt line formed; d) multiple salt lines formed. Environmental condition: 35°C, 30% RH.

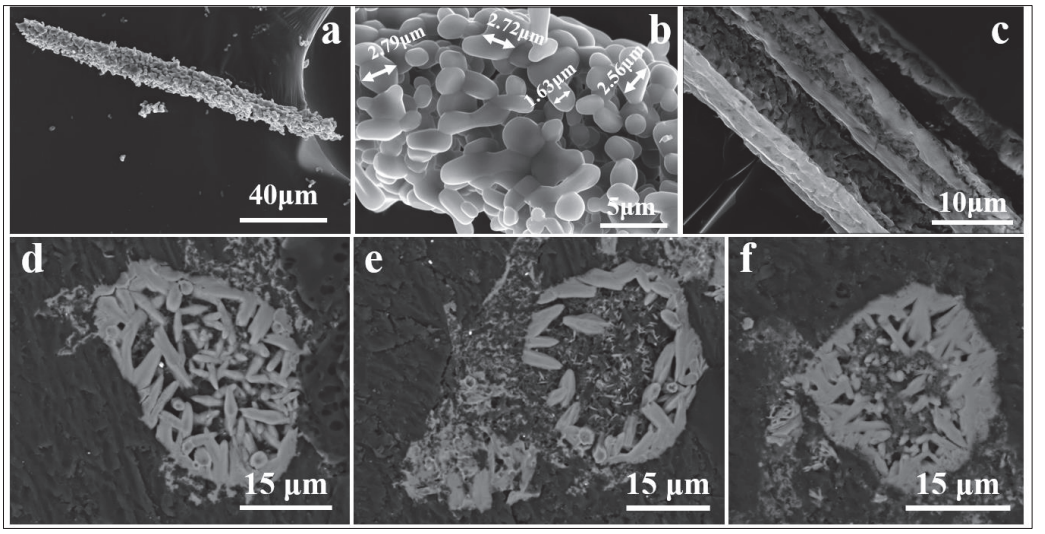

Figure 2. a) a SEM picture of one single sodium sulfate fibril; b) SEM picture of the sodium sulfate fibril in a) at higher magnification; c) SEM picture of hollow sodium sulfate fibril. Sample prepared at 25ºC, 90%RH on a brick in a closed vessel. SEM pictures of sodium sulfate fibrils. d) top e) middle and f) bottom

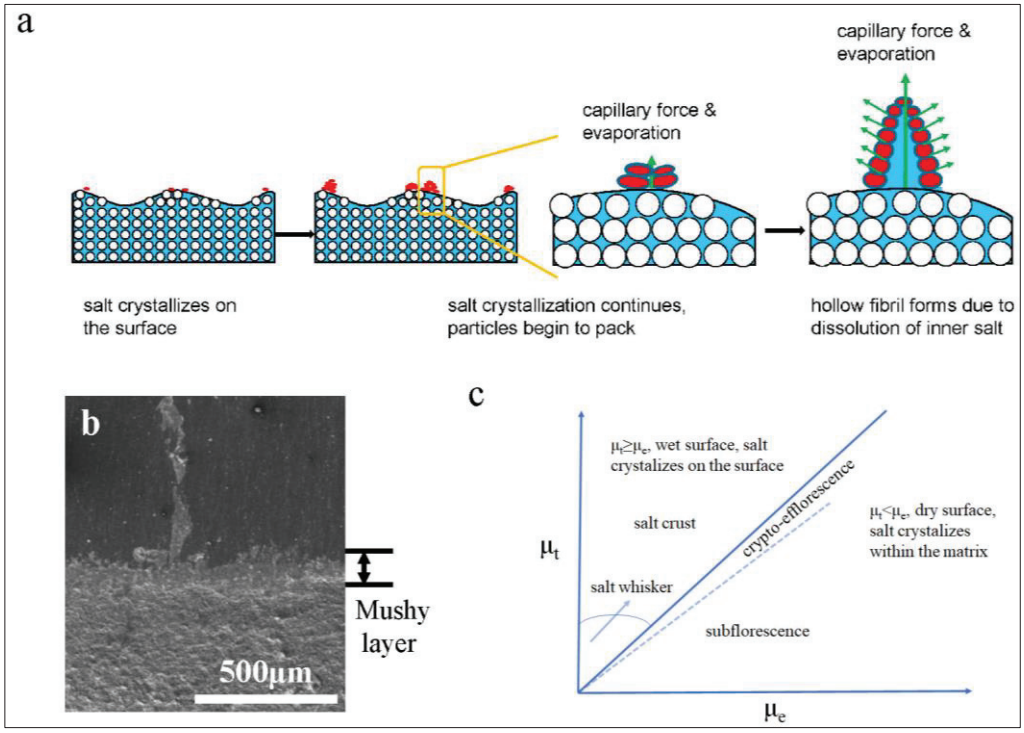

Figure 3. a) Proposed mechanism for the formation of hollow fibril structure; b) fibrils growing on sol-called mushy layer; c) Overall description of salt efflorescence in porous matrix.

A perspective view of salt crystallization from solution in porous media: morphology, mechanism, and salt efflorescence

ACCURATE IDENTIFICATION OF COMMON SOLUBLE SALTS IN CULTURAL RELICS BASED ON MODERN ANALYTICAL TECHNIQUES

Wenhua Zhao[1] **and Xiangna Han**[2]

KEYWORDS

Cultural heritage conservation, Salt damage, Soluble salts, Analysis and identification

ABSTRACT

Salt damage is a common and serious disease in porous cultural relics. Complex water and salt activities make the salt continuously destroy the cultural relics. Accurate identification of soluble salts in cultural relics is an essential prerequisite for the study of the salt damage mechanism and management, the design and development of appropriate protection materials for cultural relics as well. In this study, an operational procedure for the extraction and identification of soluble salts in cultural relics was established. Through the optimization of ion chromatography (IC), optical microscopy, infrared spectroscopy (FTIR), Raman spectroscopy (Raman), scanning electron microscopy (SEM-EDS), accurate identification of common soluble salts in cultural relics has been achieved. The research shows that for NaCl, Na_2SO_4, and $CaSO_4$ with obvious morphological features, they can be directly identified through microscopic morphological characteristics, without even requiring costly ion chromatography detection; NaCl and $CaCl_2$ can be identified through ion chromatography and energy spectrum analysis; Na_2SO_4, $CaSO_4$, $NaNO_3$, $Ca(NO_3)_2$-$4H_2O$ can be identified through ion chromatography, spectral analysis, and energy dispersive analysis.This identification technology combined common instruments, has relatively low cost, simple and easy to operate, with reliable results. It can be used for accurate identification of soluble salts in cultural relics of different materials, with good prospects for application and promotion.

[1] Chongqing Culture Relics and Archaeology Research Institute (Chongqing Cultural Heritage Protection Center), Chongqing 400013, China, 18811700358@163.com

[2] Institute of Cultural Heritage and History of Science & Technology, University of Science and Technology Beijing, Beijing 100083, China

1 INTRODUCTION

There are various diseases in cultural relics, and salt damage is a very common and serious type of disease. The occurrence of salt damage to cultural relics is related to various factors, including the loose and porous internal structure of cultural relics, the crystallization pressure and hydration pressure caused by the dissolution and crystallization of soluble salts, and changes in external environment such as temperature and humidity. These factors together lead to complex water and salt activities inside cultural relics, continuously damaging the cultural relics themselves, and accelerating the weathering and damage of cultural relics. Common soluble salts in cultural relics include NaCl, $CaCl_2$, Na_2SO_4, $CaSO_4$, $NaNO_3$, $Ca(NO_3)_2$-$4H_2O$, etc[1]–[4], with significant differences in physical and chemical properties. The synergistic destruction mechanism of multiple salts is even more complex.

At present, the common methods for the detection of soluble salts in cultural relics are: ion chromatography (IC) [5]–[7], chemical analysis methods [8], capillary electrophoresis [9], Merckoquant semi-qualitative test strips [10]. These methods are based on the content of each ion detected, pairing and combining anion and cation with high content, and then inferring the main types of soluble salts. But the accurate identification of all soluble salt types in cultural relics cannot be achieved solely through the combination of anions and cations, and other analytical techniques need to be used for auxiliary verification. Common auxiliary verification methods include X-ray fluorescence analysis (XRF) [11], [12], X-ray diffraction analysis (XRD) [11]–[13], X-ray photoelectron spectroscopy (XPS) [12], scanning electron microscopy spectroscopy (SEM-EDS) [11], [14]–[16] Infrared spectroscopy analysis (IR) [4], [14]–[16], etc. XRD determines the types of soluble salts present in the sample by comparing the lattice plane spacing and diffraction intensity measured by the sample with the diffraction data of the standard salt, but the effect is poor for complex mixed salts and amorphous salts. XPS can calculate the element composition and chemical state information in the sample according to the different binding energy, and then identify the type of crystalline salt, but it is still difficult to identify mixed salt, and the cost is high. XRF and SEM-EDS can test the chemical elements of crystalline salts; FTIR can provide the characteristic information of functional groups or chemical bond of soluble salts. It is a low-cost identification method, but it cannot identify chlorine salts. Different identification methods will be affected by the salt crystal state and the amount of water of crystallization. In addition, the soluble salt composition in cultural relics is usually complex, and a single method cannot obtain complete and accurate analysis results. Therefore, it is necessary to establish a combination method that can accurately identify the types of soluble salts in cultural relics.

This study established a set of operational procedures for extracting and identifying soluble salts, including testing conditions for analytical methods, salt crystallization extraction methods, and identification methods for different soluble salts. This combination technology uses low-cost common detection instruments, which are simple and easy to operate. The results of using this method to identify common soluble salts in cultural relics are accurate and reliable.

2 EXPERIMENTAL METHODS AND TESTING CONDITIONS

1) Ion chromatography (IC) is an ion analysis liquid chromatography technology. When analyzing salt damage samples of cultural relics, seven soluble ions (Na^+, K^+, Mg^{2+}, Ca^{2+}, Cl^-, SO_4^{2-}, NO_3^-) are usually quantitatively detected. Test steps: After drying and grinding the sample, weigh 0.3 g to 0.5 g of the sample and place it in a centrifuge tube. Add 10 ml of secondary deionized water, sonicate for 5 minutes, and centrifuge at a speed of not less than 4 000 r/min and a separation time of 10 minutes. The upper clear liquid is filtered with a 0.22 μm microporous filter membrane and tested to determine the soluble ion content in the sample.

2) Extracting salt crystals: Using evaporation method to extract soluble salt crystals. Weigh a certain amount of samples separately and add high-purity water. Shake them with ultrasound for 30 minutes and let them stand for 24 hours. Take the upper clear liquid, filter it through qualitative filter paper, and dry to obtain the salt crystals of the samples. Perform optical microscopy, FTIR, Raman, and SEM-EDS analysis on the extracted salt crystals, and identify the specific salt types based on the IC analysis results.

3) Optical microscopy observation: Identify salt crystals with obvious morphology.

4) Fourier transform infrared spectroscopy (FTIR): The infrared spectrum of the sample is tested using the potassium bromide compression method, and sulfate and nitrate can be identified by analyzing the spectrum. Test steps: Mix salt crystals and potassium bromide (spectroscopically pure) evenly in a ratio of 1:150-200, press them into thin sheets, and place them in an infrared spectrometer for testing. Instrument setting conditions: scanning range: 4 000~ 400 cm^{-1}, scanning times: 16, Spectral resolution: 4 cm^{-1}, acquisition time: 32 s.

5) Raman spectrum analysis (Raman): Sulfates and nitrates can be identified. Test conditions: Laser wavelength is 785 nm; Laser power is 100%; The laser grating is 1 200 gr/mm; The scanning range is 2 000~50 cm^{-1}; Scan 3 times for 60 seconds each time.

6) Scanning electron microscopy energy dispersive spectroscopy (SEM-EDS) : Observing the morphology of soluble salt crystals through SEM, combined with EDS, common soluble salts can be identified, and the results of the above spectral tests can be verified. Test steps: Paste the salt crystal sample directly onto the conductive adhesive, use an air compression tank to blow the sample to ensure that there are no loose samples on the conductive adhesive, and place the processed sample in the sample compartment for testing.

3 COMMON IDENTIFICATION METHODS FOR SOLUBLE SALTS

3.1 Sodium chloride

The solid phase of sodium chloride is colorless cubic crystal, which belongs to ionic crystal and is easily soluble in water. In sodium chloride crystals, chloride ions are connected to six surrounding sodium ions, and sodium ions are connected

to six surrounding chloride ions. Sodium ions and chloride ions extend in this arrangement in various directions of space, forming a sodium chloride crystal. The microstructure and SEM-EDS test results of sodium chloride crystalline salt are shown in Figure 1. Sodium chloride crystal salts always exhibit a cubic morphology under the microscope, making them easier to identify. By combining analysis results such as ion chromatography (Na^+, Cl^-), microscopic observation (cubic crystal), and scanning electron microscopy (cubic crystal) energy spectrum (mainly containing Na and Cl elements), sodium chloride can be identified.

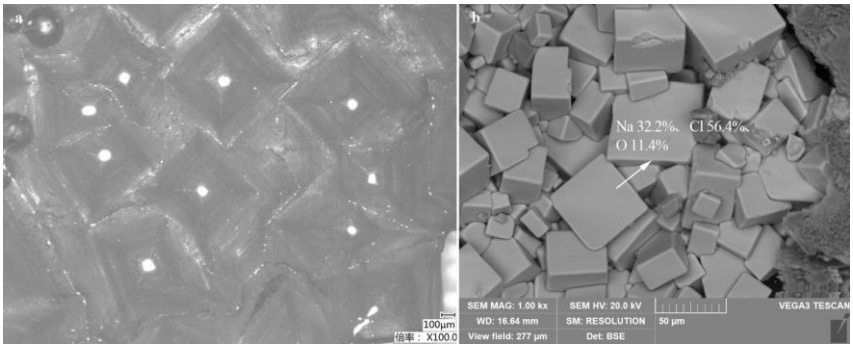

Figure 1: Micromorphology(a) and SEM-EDS(b) of sodium chloride crystal.

3.2 Calcium chloride

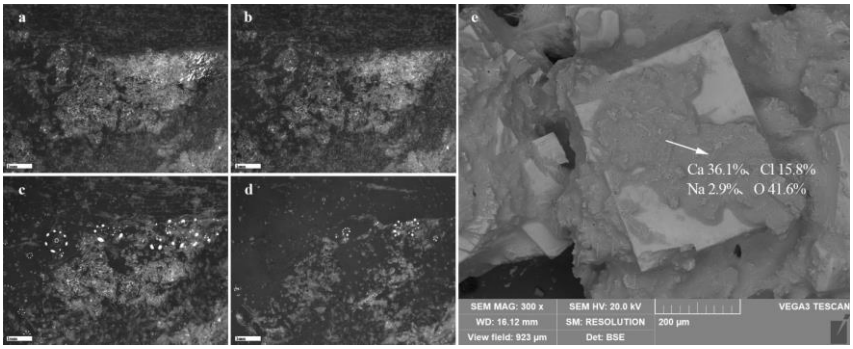

Figure 2: Deliquescence phenomena (a~d) and SEM-EDS (e) of calcium chloride crystal. (a~d are the micrographs of $CaCl_2$ exposed to room temperature at 0, 5, 15 and 20 minutes respectively).

Anhydrous calcium chloride is a white cubic crystal with strong hygroscopicity. It can form monohydrate, dihydrate, tetrahydrate, and hexahydrate with water. Among them, calcium chloride hexahydrate ($CaCl_2$-$6H_2O$) is a colorless hexagonal crystal; Calcium chloride dihydrate ($CaCl_2$-$2H_2O$) is a white, porous, and hygroscopic substance. The precipitates from aqueous solution crystallization at normal temperature are usually hexahydrates. When heated to 30 ℃ gradually, they will dissolve in their own crystal water. When heated continuously, they will gradually lose water. When heated to 200 ℃, they will become dihydrates. When heated to 260 ℃, they will become white porous anhydrous calcium chloride. Expose the dried crystalline salt to the air, and calcium chloride will quickly absorb moisture

and deliquescence (Figure 2a~d), which can be used to determine whether there is calcium chloride that is easily deliquescent. However, this also makes it difficult to distinguish calcium chloride through optical microscopy. The SEM-EDS test results of calcium chloride crystal salts are shown in Figure 2e, which are usually amorphous. Combining analysis results such as ion chromatography (Ca^{2+}, Cl^-) and scanning electron microscopy energy spectrum (mainly containing Ca and Cl elements), calcium chloride can be identified.

3.3 Sodium chloride

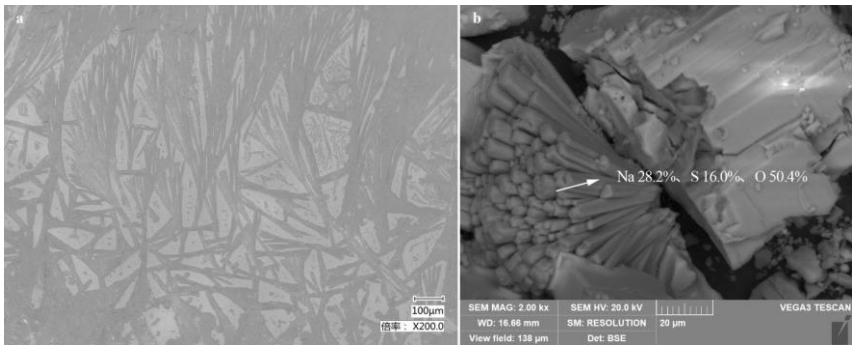

Figure 3: Micromorphology (a) and SEM-EDS (b) of sodium sulfate crystal.

Table 1: Infrared vibration and Raman shift frequency of common sulfates (SO_4^{2-}) and nitrates (NO_3^-).

Soluble salts	Light spectrum	Anti-symmetric stretching	Symmetric stretching	Asymmetrical deformation vibration	Symmetrical deformation vibration	Out of plane bending	In-plane bending
Na_2SO_4	IR[17]	1134		637,615		-	-
	Raman[18]	1153,1132,1101	993	647,632,620	449	-	-
$CaSO_4$	IR[19]	1144	-	668,603	-	-	-
	Raman[18]	1160,1129,1111	1017	675,628,609	499,417	-	-
$NaNO_3$[20]	IR	1379,1353	-	-	-	837	-
	Raman	1388	1071	-	-	-	729
$Ca(NO_3)_2 \cdot 4H_2O$[20]	IR	1437,1367	1047	-	-	815	748
	Raman	1419	1059	-	-	-	744

Sodium sulfate is white monoclinic crystal system fine crystal or powder, hygroscopic, and is the most harmful soluble salt among cultural relics. There are two kinds of crystal hydrates of sodium sulfate: one is sodium sulfate heptahydrate (Na_2SO_4-$7H_2O$), a white hexagonal or tetragonal crystal, and the other is sodium sulfate decahydrate (Na_2SO_4-$10H_2O$), commonly known as mirabilite, a colorless monoclinic crystal. Sodium sulfate decahydrate crystals are in needle, cluster or cluster shape, and become powder after losing water of crystallization [21], [22]. When the sodium sulfate aqueous solution is below 32.38 ℃, it crystallizes as a

decahydrate, and when it is above 32.38 ℃, it crystallizes as anhydrous sodium sulfate. The microstructure and SEM-EDS test results of sodium sulfate crystals are shown in Figure 3, often exhibiting cluster like, cluster like, and thin sheet like morphology characteristics. The infrared vibration frequency and Raman shift frequency of sodium sulfate are shown in Table 1. Combining analysis results such as ion chromatography (Na^+, SO_4^{2-}), microscopic observation (clustered crystals), infrared spectroscopy (Figure 4a), Raman spectroscopy (Figure 4b), and scanning electron microscopy (clustered crystals) energy spectrum (mainly containing Na, S, O elements), sodium sulfate can be identified.

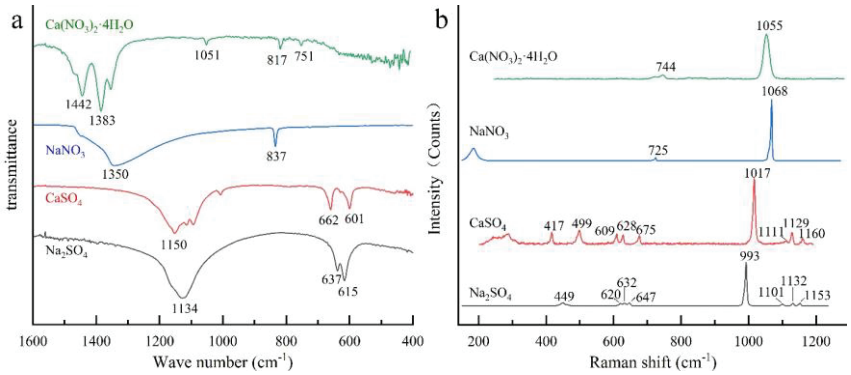

Figure 4: Infrared spectra (a) and Raman spectra (b) of common sulfates and nitrates[23].

3.4 Calcium sulfate

Calcium sulfate crystals include calcium sulfate dihydrate ($CaSO_4$-$2H_2O$), calcium sulfate hemihydrate ($CaSO_4$-$0.5H_2O$), and anhydrous calcium sulfate ($CaSO_4$). The calcium sulfate dihydrate crystal belongs to the monoclinic crystal system, which is connected by SO_4^{2-} with tetrahedron and CaO_8 with octahedron to form the axial direction of calcium sulfate dihydrate whisker. After the formation of crystal nuclei, the high surface energy crystal planes along the axis grow at a high speed, and the crystal planes gradually decrease until they disappear; The crystal surface with low surface energy continuously elongates and expands with the progress of growth, and the degree of crystallization is intact, finally forming the morphology characteristics of needle like or rod-shaped whiskers [24]; The crystal structures of semi water and anhydrous calcium sulfate whiskers belong to the hexagonal crystal system. Calcium sulfate hemihydrate is divided into two variants: type α and type β, α- $CaSO_4$-$0.5H_2O$ has a good degree of crystallization and appears as short hexagonal prism shaped whiskers [25]; The crystallinity of β-$CaSO_4$-$0.5H_2O$ is poor, with flake like whiskers [24]; Anhydrous calcium sulfate is a fibrous single crystal, slightly soluble in water, and neutral in aqueous solution [26]. The microstructure and SEM-EDS test results of calcium sulfate crystals are shown in Figure 5, showing hexagonal, needle like, or rod-shaped crystal morphology characteristics. Combining analysis results such as ion chromatography (Ca^{2+}, SO_4^{2-}), microscopic observation (hexagonal prismatic, needle like or rod-shaped crystals), infrared spectroscopy (Table 1 and Figure 4a), Raman spectroscopy (Table 1 and Figure 4b), and scanning electron microscopy (hexagonal prismatic, needle like or rod-shaped

crystals) energy spectrum (mainly containing Ca, S, O elements), calcium sulfate can be identified.

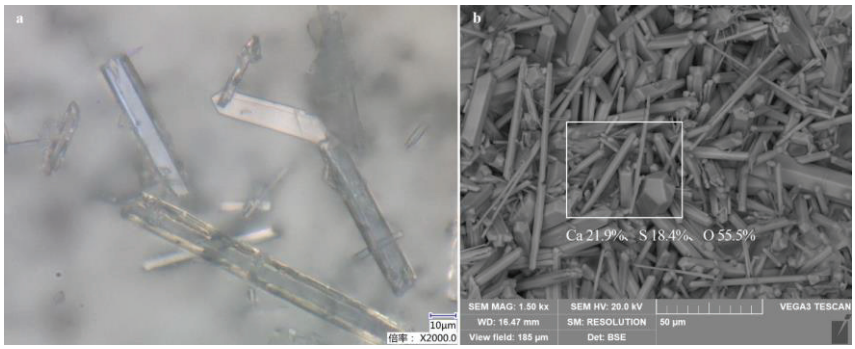

Figure 5: Micromorphology (a) and SEM-EDS (b) of calcium sulfate crystal.

3.5 Sodium nitrate

Sodium nitrate is a colorless transparent or white slightly yellow diamond shaped crystal that is prone to deliquescence and cannot be identified through optical microscopy. The SEM-EDS test results of sodium nitrate crystals are shown in Figure 6a, showing irregular granular morphology characteristics. Combining analysis results such as ion chromatography (Na^+, NO_3^-), infrared spectroscopy (Table 1 and Figure 4a), Raman spectroscopy (Table 1 and Figure 4b), and scanning electron microscopy energy spectrum (mainly containing Na, N, O elements), sodium nitrate can be identified.

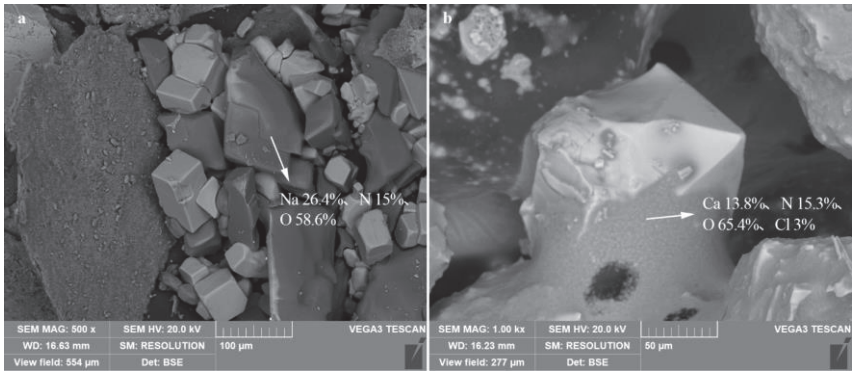

Figure 6: SEM-EDS of sodium nitrate (a) and calcium nitrate (b).

3.6 Calcium nitrate

The crystallization of calcium nitrate has the following hydrate crystal forms: α，β-Tetrahydrate $Ca(NO_3)_2$-$4H_2O$, trihydrate $Ca(NO_3)_2$-$3H_2O$, and dihydrate $Ca(NO_3)_2$-$2H_2O$. At saturation temperature, calcium nitrate can become a solid phase in the form of anhydrous salts. Whether it is anhydrous salt or crystalline hydrate, calcium nitrate is hygroscopic, so it is difficult to identify calcium nitrate by microscopic morphology. The SEM-EDS analysis results of calcium nitrate

crystals are shown in Figure 6b, mainly in amorphous form. Combining analysis results such as ion chromatography (Ca^{2+}, NO_3^-), infrared spectroscopy (Table 1 and Figure 4a), Raman spectroscopy (Table 1 and Figure 4b), and scanning electron microscopy energy spectrum (mainly containing Ca, N, O elements), calcium nitrate can be identified.

4 CONCLUSIONS

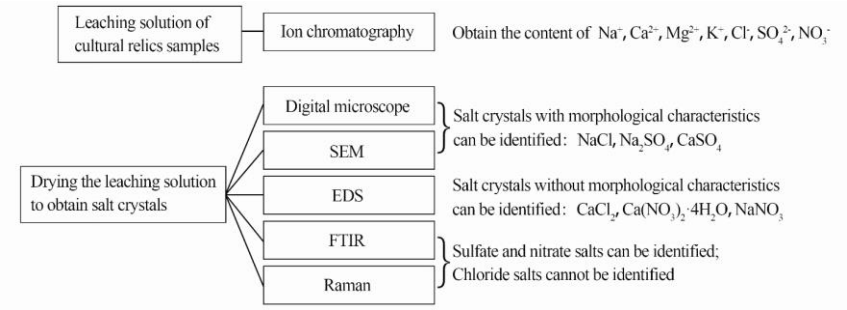

Figure 7: Summary of accurate identification techniques of soluble salts in cultural relics.

After summarizing previous literature and conducting identification experiments on a large number of cultural relics, this study established a set of operational procedures and technical methods for precise identification of soluble salts in cultural relics, as shown in Figure 7. Firstly, ion chromatography was performed on the leaching solution of cultural relics samples to obtain the main types and relative content of anions and cations. Then, spectral and energy dispersive analysis was performed on the crystalline salt obtained after drying the leaching solution, and the soluble salt types in the cultural relics samples were obtained by combining multiple test results. The research shows that NaCl can be identified by IC (Na^+ and Cl^- in leachate), microscopic observation (cubic crystal) and SEM-EDS (mainly containing Na and Cl elements); $CaCl_2$ can be identified by IC (Ca^{2+}, Cl^-) and SEM-EDS (Ca, Cl elements); Na_2SO_4 can be identified by IC (Na^+, SO_4^{2-}), microscopic observation (clumped or cluster crystal), FTIR (main peaks 1 134 cm^{-1}, 637 cm^{-1}, 615 cm^{-1}), Raman (main peak 993 cm^{-1}) and SEM-EDS (Na, S, O elements); $CaSO_4$ can be identified by IC (Ca^{2+}, SO_4^{2-}), microscopic observation (hexagonal prism, needle or rod-shaped crystal), FTIR (1 144 cm^{-1}, 668 cm^{-1}, 603 cm^{-1}), Raman (1 017 cm^{-1}) and SEM-EDS (Ca, S, O elements); $NaNO_3$ can be identified by IC (Na^+, NO_3^-), FTIR (1 379 cm^{-1}, 1 353 cm^{-1}, 837 cm^{-1}), Raman (1 071 cm^{-1}) and SEM-EDS (Na, N, O elements); $Ca(NO_3)_2 \cdot 4H_2O$ can be identified by IC (Ca^{2+}, NO_3^-), FTIR (1 437 cm^{-1}, 1 367 cm^{-1}, 1 047 cm^{-1}), Raman (1 059 cm^{-1}) and SEM-EDS (Ca, N, O elements). In addition, cubic NaCl, clumped, cluster or flake Na_2SO_4, and hexagonal prism, needle or rod-shaped $CaSO_4$ can be directly identified through microscopic morphology observation. $CaCl_2$, $NaNO_3$ and $Ca(NO_3)_2 \cdot 4H_2O$ have strong hygroscopicity, and have rapid deliquescence when exposed to room temperature, according to which it can be determined. This technology combines conventional and common detection instruments to achieve rapid

identification of common soluble salt types in cultural relics. It has strong operability, reliable identification results, and good potential for application and promotion.

REFERENCES

[1] K. Zehnder, "Long-term monitoring of wall paintings affected by soluble salts," Environ. Geol., vol. 02, pp. 52, 2007.

[2] S. Yang, Q. Guo, and X. Wang, "Application of non-destructive testing analysis technology in surveying salt distribution in a Buddhist Temple at Beiting," *Dunhuang Research*, no. 01, pp. 56–59, 2013.

[3] C. Zhang et al., "Investigation of soluble salts in Yuhuangmiao Shanrong tomb site," Chemical Research and Application, vol. 28, no. 11, pp. 1546–1555, 2016.

[4] J. Ji, Y. Wang, T. Ma, Z. Wang, S. Dong, and W. Zhou, "Analytical study of contaminants and soluble salts on the surface of stone sculptures at Mao Mausoleum,Shaanxi," *Sciences of Conservation and Archaeology*, vol. 32, no. 02, pp. 22–28, 2020.

[5] Y. Wang, Q. Yu, M. Yan, L. Ma, and G. Chen, "Research on the mobility of soluble salts for north temple murals," Sciences of Conservation and Archaeology, vol. 22, no. 03, pp. 15–20, 2010.

[6] S. Yang, Y. Wang, B. Su, Q. Guo, and Q. Pei, "The moisture and salt distribution properties of the cliff in the Yulin Grottoes at Guazhou," Dunhuang Research, no. 01, pp. 136–140, 2018.

[7] Y. Zhang, Z. Yu, L. Wang, Q. Cui, B. Shui, and S. Sun, "A study on the soluble salts used in the murals of Mogao Cave 196," Dunhuang Research, no. 01, pp. 148–155, 2021.

[8] S. Huang, G. Zhao, Y. Li, and Y. Zhao, "Simulation of migration of soluble salts in archeological sites," Acta Pedologica Sinica, vol. 48, no. 02, pp. 295–301, 2011.

[9] H. Du, L. Zhou, B. Su, and Z. Hu, "Rapid detection and analysis the salt damage of Dunhuang murals by capillary electrophoresis," Dunhuang Research, no. 06, pp. 44–49, 2009.

[10] Z. Su, B. Yang, and H. Zhang, "Soluble salt distribution and environmental monitoring of Cave 276 in the Mogao Grottoes," Journal of Lanzhou University(Natural Sciences), vol. 57, no. 02, pp. 226–232, 2021.

[11] S. Huang, Y. Li, G. Zhao, P. Jin, R. Wang, and S. Wang, "Study and analysis on salt damages of earthen archaeological sites in Tang Hanguangmen entrance Remains Museum," Chinese Journal of Soil Science, vol. 43, no. 02, pp. 407–411, 2012.

[12] H. Hu et al., "Study on the Salt Species and Types in the Emperor Qin's Mausoleum and Hanyangling Mausoleum Earthen Sites," Materials China, vol. 31, no. 11, pp. 37–47, 2012.

[13] X. Dang, B. Rong, P. Duan, H. Li, and L. Zhou, "Research on the mechanism of deterioration of polychrome pottery excavated from a Han Dynasty tomb in Xiangshan, Qingzhou," Sciences of Conservation and Archaeology, vol. 24, no. 02, pp. 50–55, 2012.

[14] X. Han, W. Zhao, C. Chen, S. Jiang, and X. Wang, "Study on the unusual weathering of the bones and eggs accumulation with embryos fossils of Hamipterus tianshanensis," Geological Review, vol. 68, no. 01, pp. 81–92, 2022.

[15] W. Zhao, X. Han, C. Chen, and X. Wang, "Spectral Analysis of the Weathering of Yardang Buried Pterosaur Fossils——A Case Study of Yardang Near the No.2 Water Source of Dahaidao," Spectroscopy and Spectral Analysis, vol. 42, no. 02, pp. 561–567, 2022.

[16] X. Han et al., "Study on weathering mechanism of dinosaur tracks from Early Cretaceous in tracksite No.8,Otog,Inner Mongolia," Acta Palaeontologica Sinica, vol. 61, no. 01, pp. 151–164, 2022.

[17] S. Weng, and Y. Xu, Fourier transform infrared spectrometric analysis, third edition, pp. 419–446, Chemical Industry Press (in Beijing, China), 2016.

[18] J. Han, L. Guo, and W. Chen, Mineral Raman Spectrum Atlas, pp. 72–74, Geology Press(in Beijing, China), 2016.

[19] M. Li, Z. Li, Z. Zhang, D. He, Y. Tang, and F. Chen, "Preparation of calcium sulfate whiskers assisted by mixed sodium fatty acid," Inorganic Chemicals Industry, vol. 54, no. 06, pp. 66–72, 2022.

[20] S. Weng, and Y. Xu, Fourier transform infrared spectrometric analysis, third edition, pp. 446, Chemical Industry Press (in Beijing, China), 2016.

[21] X. Wan, and Y. Lai, "Experimental study on the influence of cooling rate on salt crystallizing in sodium sulfate solution," Journal of Glaciology and Geocryology, vol. 38, no. 02, pp. 431–437, 2016.

[22] Z. Zheng, and X. Guo, "Experimental investigation on state transform of sodium sulfate and its damaging effect on ancient mural," Journal of Institute of Disaster Prevention, vol. 22, no. 04, pp. 43–48, 2020.

[23] "RRUFF database." https://rruff.info/

[24] L. Wang, D. Xiong, Y. Li, Y. Zong, X. Cao, and S. Ouyang, "Progress in the preparation and application of calcium sulfate whiskers," Nonferrous Metals Science and Engineering, vol. 9, no. 03, pp. 34–41, 2018.

[25] Z. Duan, J. Li, S. Zheng, W. Han, Q. Geng, and H. Guo, "Effect of water reducing agent on properties of α-hemihydrate phosphorus gypsum," Bulletin of the Chinese Ceramic Society, vol. 35, no. 01, pp. 198–203, 2016.

[26] W. Fei, Z. Li, and H. Wang, "Review of preparation and application of calcium sulfate whisker," Industrial Minerals & Processing, no. 09, pp. 31–32, 2002.

COMPARISON OF DAMAGE BY VARIOUS HYDRATION PROCESSES OF THENARDITE: WATER ABSORPTION AND MOISTURE ADSORPTION

Nobumitsu Takatori[1*], Takamasa Isomura[1], Daisuke Ogura[1], and Soichiro Wakiya[1,2]

KEYWORDS

Porous material, Phase change, Dry–Wet cycle, Wet process, Strain

ABSTRACT

Sodium sulfate, well-known as a destructive salt for porous materials, assumes multiple phases according to the surrounding environment, such as thenardite and mirabilite. Stress occurs when the phase of salt changes. Since this generated stress is not due to crystal growth, which is, crystallization pressure but rather the pressure of the saline water in which the sodium sulfate salt is dissolved, the presence of the solution is important for generating such stress. There may be a difference in damage between the process where thenardite deliquesces to mirabilite as relative humidity increases and the one where mirabilite precipitates after thenardite has absorbed water and dissolved. This study aims to explain the difference in the strain of tuff stone impregnated with sodium sulfate between moisture adsorption and water absorption. The experimental procedure began with the preparation of three specimens that contain sodium sulfate and one specimen that contains no salt for each condition. The specimens were about 3 cm^3 in size and were placed in desiccators in an incubator set at 23°C. To monitor deformation behavior, strain gages were attached to the top of the specimens. In the moisture adsorption tests, the specimens with sodium sulfate were placed in desiccators humidified by saturated Na_2SO_4 aqueous solution. As a result, strain of about 250–600 με was observed in the moisture adsorption test. Meanwhile, in the water absorption test, the specimens were impregnated with pure water whose volume is about 40%–85% of the material porosity. As a result, strain of about 200–700 με, equivalent to the results of the moisture adsorption test, was observed. These results highlighted no significant differences in the stress generated by varying wetting procedures, which is, deliquescence and dissolution.

[1] Kyoto University, Kyoto, Japan, takatori.nobumitsu@archi.kyoto-u.ac.jp
[2] Nara National Research Institute for Cultural Properties, Nara, Japan

1 INTRODUCTION

Sodium sulfate is well-known as a salt that destroys porous materials. It assumes multiple phases according to the surrounding environment, such as thenardite, which is an anhydrate salt, and mirabilite, which is a decahydrate salt. Sodium sulfate phase is determined by temperature and humidity. Sodium sulfate generates high crystal pressure during hydration, and this pressure is caused by the dissolution of thenardite precipitated in the porous media, resulting in a supersaturated salt solution compared to mirabilite, which increases the pressure of the solution [1][2].

To assess the risk of salt weathering due to sodium sulfate, it is necessary to predict the heat, moisture and ions transfer in porous media and the phase change of salts accurately. Although such numerical analyses have sometimes been performed in recent years [3], it is not available technique for everyone because it needs various material properties. Hence, as a simple evaluation method, there are often attempts to assess the risk of salt weathering based on the surrounding environment, rather than within the media [4]. However, there may be some issues in assessing salt weathering from the surrounding environment. As an example, we consider salt weathering on the exterior walls of buildings or surfaces of grounds. The phase of salt precipitated near the surface is greatly affected by the surrounding environment. On the other hand, since these are located outdoors, they are also affected by rainfall and groundwater capillary suction. When considering the wetting process, the increase in ambient humidity causes deliquescence of salt, while rainfall and capillary suction of groundwater cause dissolution of salt.

Thermodynamically, it is said that the difference in the method of salt hydration, i.e., dissolution or deliquescence via a gas-gas reaction, has no effect on the crystallization pressure. Meanwhile, some experiments have shown that different hydration processes cause slight differences in the degradation of materials [5]. Especially, it is also known that the reaction rates greatly differ between deliquescence and dissolution.

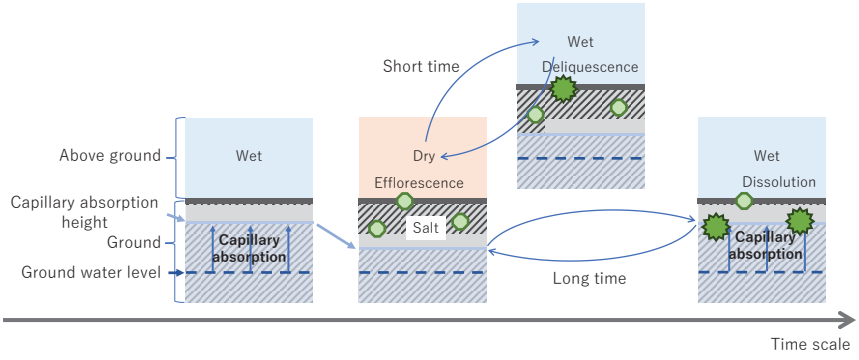

Figure 1. Difference in dry and wet cycles near and below the ground surface

What we are interested in is to know if the salt weathering of the salt is actually due to deliquescence of the sodium sulfate or if it is due to dissolution. We studied the salt weathering of the stone Buddha carved into a cliff [6]. The room inside the shelter covering the stone Buddha is subject to dry and wet cycles throughout the year. On the other hand, the rock walls on which the stone Buddhas are carved also dry and wet throughout the year, but the temperature and humidity fluctuations are different from those in the room. For example, changes in temperature and moisture content in the ground are slower than those in the room, and the cycles of changes are more long-term. Moreover, as shown in Figure 1, salt precipitated near the ground surface deliquescence and precipitates repeatedly, whereas salt inside the ground dissolves and precipitates repeatedly. In this study, we prepared several tuff specimens containing sodium sulfate, hydrated these specimens by deliquescence or dissolution, and measured the strain by each hydration processes.

2 MATERIALS AND METHODS

2.1 APPARATUS

Figure 2 shows a schematic diagram of the experimental apparatus of the moisture adsorption process and Figure 3 shows a one of the water absorption processes. Specimens were placed on Petri plates, which were then placed in desiccators in an incubator where the temperature is kept constant. The temperature and humidity inside the desiccators were measured by a datalogger (Onset Corp. UX100-011A), and specimen strain was measured by strain gages (KYOWA Corp. KFGS-5-120-C1-11). These strain gages were centered at the top of the specimens and attached to a plane parallel to the tuff lamination plane.

Temperature in the incubator was controlled at about 23℃ and humidity was controlled inside the desiccator using a saturated salt solution, magnesium nitrate ($Mg(NO_3)_2$), and sodium sulfate (Na_2SO_4) aqueous solution was used in the moisture adsorption process. Meanwhile, $Mg(NO_3)_2$ aqueous solution was used in the water absorption process. The relative humidity at equilibrium with saturated $Mg(NO_3)_2$ salt solution was about 54%, and that with $Na_2SO_4\,10H_2O$ (mirabilite) was about 94%[1]. A paper cloth was laid on the bottom of the specimens to facilitate water absorption.

2.2 SPECIMEN

Specimens were porous tuff stone (Aso pyroclastic-flow deposits in Japan[7]) with about 0.3 [m^3/m^3] porosity and approximately 3 cm^3 in size. Each experiment examined four specimens: three containing sodium sulfate and one containing no salt. The following shows how the salt-containing specimens were prepared.

1. The dried specimens were impregnated with deionized water and left for some time. Afterward, the specimens were dried in an oven at 105℃ until constant mass was reached.

2. The specimens were impregnated with Na_2SO_4 aqueous solution at 23℃ over 3 days. Also, the concentration of the saline water was 12g/100g(H_2O), which is approximately half its solubility at 23℃.

3. The specimens were dried in an oven at 105℃.

These procedures were performed to minimize as much as possible the migration of salt ions due to water evaporation and to precipitate the salt as homogeneously as possible inside the specimens. After these preparations, the specimens were left in desiccators humidified with $Mg(NO_3)_2$ for at least three days. For the specimens with no salt, the same procedures were conducted except step 2.

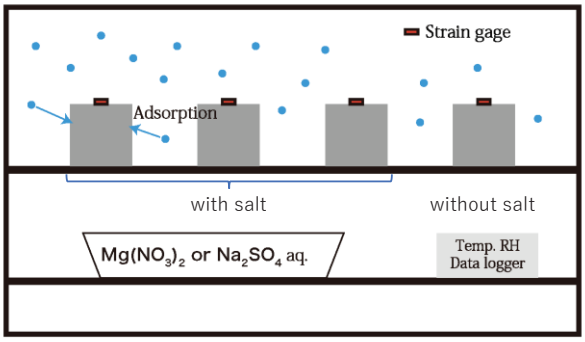

Figure 2. Schematic diagram of the moisture adsorption process

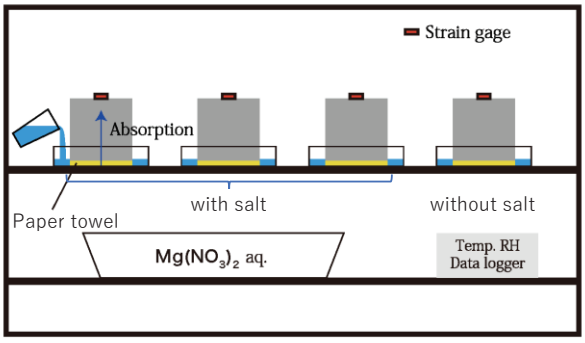

Figure 3. Schematic diagram of the water absorption process

2.3 EXPERIMENTAL PROCEDURES

The moisture adsorption tests were conducted in two ways. One is the dry–wet cycle test, in which the saturated salt solution in the desiccators was alternately replaced to dry and wet the material. For humidity control, $Mg(NO_3)_2$ aqueous solution was used during drying, and Na_2SO_4 aqueous solution during wetting. The drying period was at least four days and the wetting period at least three days,

with four cycles. The other test was a simple wetting test, in which the prepared specimens were placed in desiccators humified by Na_2SO_4 aqueous solution for more than one month.

In the experimental procedure for water absorption, 1.0, 3.5, and 7.0 g of deionized water was absorbed from the bottom of the specimens. The tests were conducted in desiccators humidified with $Mg(NO_3)_2$ saturated salt solution.

3 RESULTS

3.1 MOISTURE ADSORPTION PROCESS

Figure 4 shows the strain change in each specimen in the dry–wet cycle tests. Because the temperature fluctuates slightly in the incubator, the temperature was corrected. Strain increased during the adsorption process and decreased during the desorption process, and the average strain change in salt-containing specimens was about 35 με. Meanwhile, the specimens without salt showed a small change in strain within 10 με. The specimens' weight change due to moisture absorption was about 0.018 [kg/kg] with salt and about 0.0030 [kg/kg] without salt. Although it is not clear what caused the difference in strain with and without salt, it is thought that the change in pore structure due to precipitated salt is one of the factors, since there is a difference in the amount of moisture absorption.

Next, Figure 5 shows the strain and relative humidity of the specimens subjected to moisture adsorption in the desiccators for a long period. Strain increased rapidly after day 6, and a maximum strain of 250–600 με was measured.

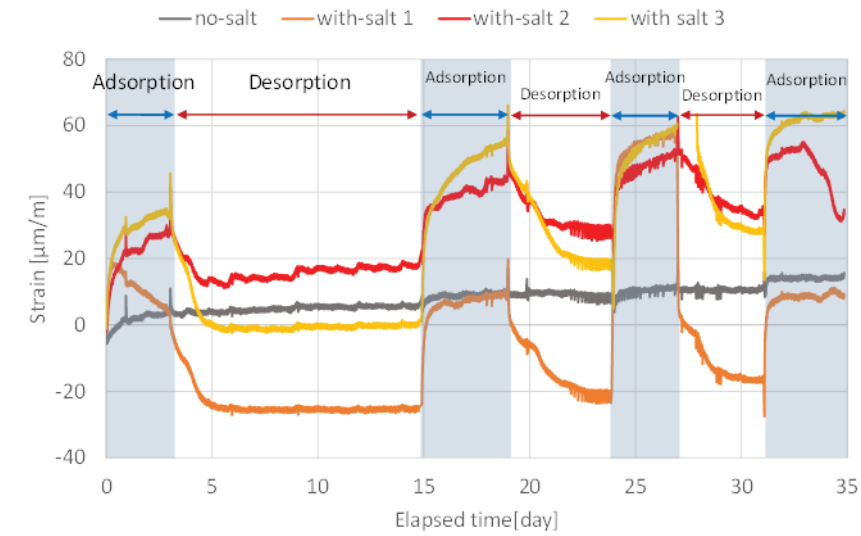

Figure 4. Strain change in specimens during dry–wet cycles

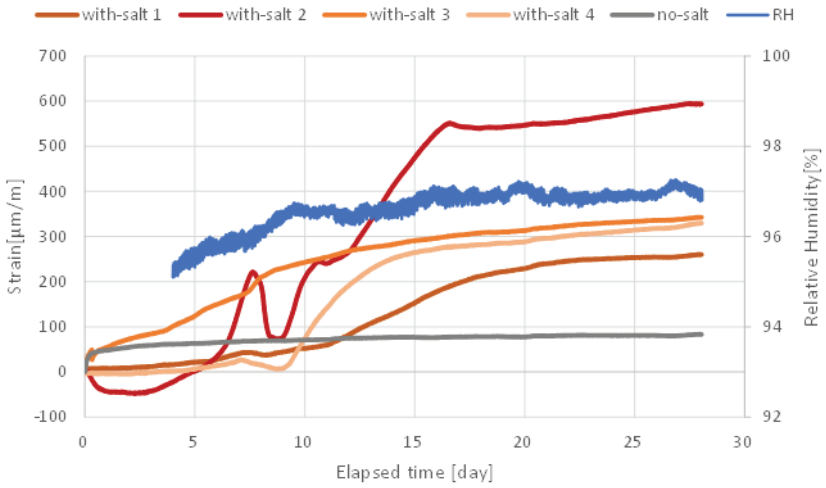

Figure 5. Strain change in specimens during long-term wetting.

Note that the proper measurement range of the equipment used in this experiment is less than 95%RH and the measurement error is 2.5%RH. Trend in RH change is reliable, but the absolute value is not.

3.2 WATER ABSORPTION PROCESS

Figure 6 shows the strain change in each specimen during water absorption, and Figure 7 shows the maximum strain change for each amount.

For the specimens with no salt, strain quickly increased after water absorption and reached a constant value. Meanwhile, for the specimens with salt, strain changed differently. Strain changes are roughly classified into two: those that increase quickly after water absorption and show a slow change after reaching a maximum value, and those that increase gradually for one to several days. Generally, strain increases earlier in specimens without salt than in those with salt.

Next, the relation between strain and the presence or absence of salt is explained. When 3.5 or 7.0 g of water was absorbed, the specimens without salt showed a strain of about 120 με, while those with salt showed a maximum strain of about 200–700 με. Meanwhile, in the specimen that absorbed 1 g of water, the strain was about 13 με even in the specimen with salt. Figure 8 shows the salt precipitation. In this test piece, salt precipitated from the bottom of the specimen. As a result, the liquid water absorbed from the bottom did not sufficiently reach the top surface where the strain gages were affixed, and therefore, sufficient strain was not observed.

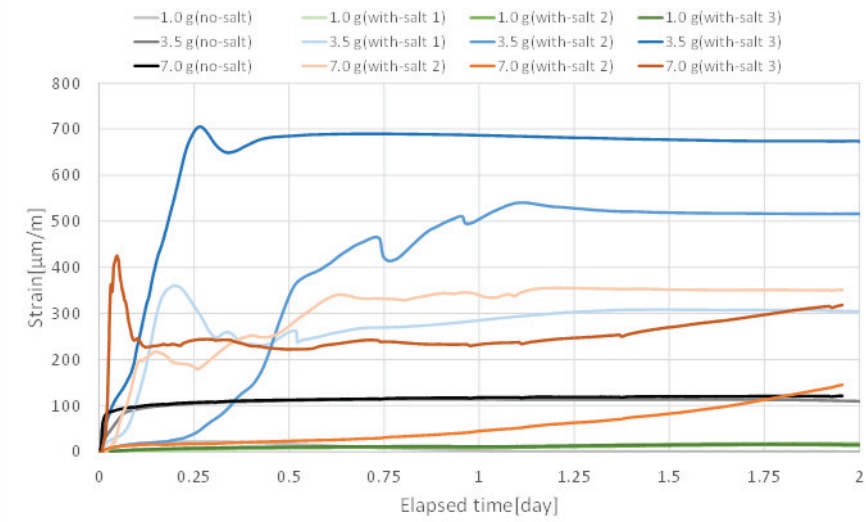

Figure 6. Strain change in specimens during water absorption.

The results for 1.0 g of water absorption are shown in green, 3.5 g in blue, and 7.0 g in orange. Even when the amount of water absorption is the same, the strain change behavior is different.

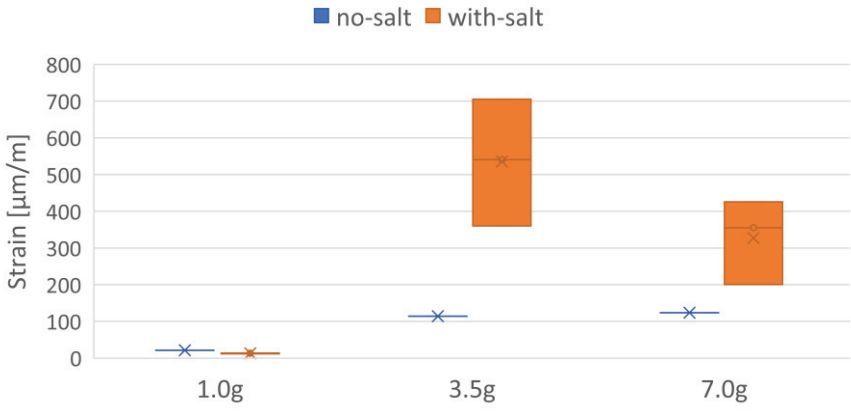

Figure 7. Maximum value of strain obtained through absorption

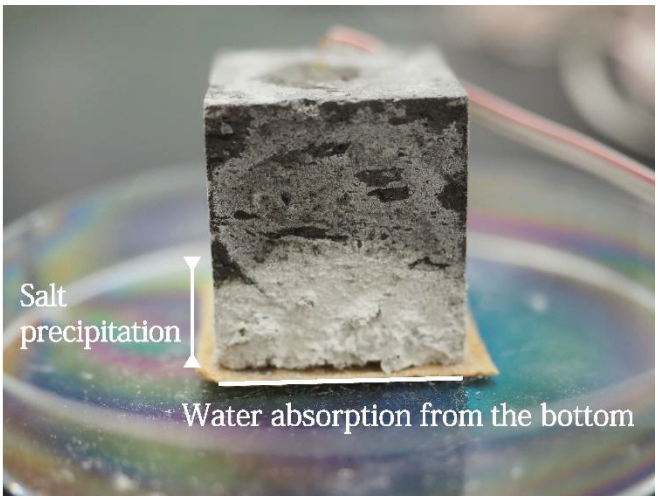

Figure 8. Appearance of precipitated salt when 1.0 g water was absorbed

4 DISCUSSION

During moisture adsorption, the strain of specimens was greater during a long wetting period than during a dry–wet cycle. This may be because the fact that the controlled humidity in the desiccators was close to the deliquescence point of mirabilite, which slowed the rate of deliquescence.

From another perspective, strain monotonically increased in the adsorption process and decreased in the desorption process during the dry–wet cycle. However, strain during the long-term wetting process and water absorption process did not monotonically increase but temporarily decreased. The latter mechanism is unclear, but we suppose that this behavior is due to a change in the phase of Na_2SO_4. A comparison of strain between the long-term wetting process and water absorption process showed maximum values of about 200–700 με for both. Considering measurement error, the difference in the stresses generated by deliquescence and dissolution are considered small.

This study compared the degree of deterioration by the strain of the specimens, but a more detailed evaluation would require a measurement of ultrasonic pulse velocity or a quantification of the crack and detachment of the specimens [8].

Figure 7, which compares the results for 3.5 and 7.0 g water absorption, shows greater strain in the former. Although a statistically more accurate verification is needed in the future due to the considerable variation in strain of each specimen, the results are extremely interesting. It is possible that one of the reasons is that excessive absorption of water during the water absorption process lowered the saturation of the solution, which in turn reduced the crystallization pressure. However, this assumption cannot be adequately explained from the results of this

measurement, and further study will be conducted with solution flow in the material.

5 CONCLUSIONS

In this study, tuff containing sodium sulfate was wetted through different methods, and differences in material strain due to different wetting methods were compared. In the moisture adsorption tests, the specimens containing sodium sulfate were placed in desiccators humidified by saturated Na_2SO_4 aqueous solution. This resulted in a strain of 250–600 με. In the water absorption test, meanwhile, the specimens were impregnated with pure water whose volume was about 40%–85% of the material porosity. As a result, strain of 200–700 με, which is consistent with the results of the moisture adsorption test, was observed. These findings clarified that no significant differences can be observed in the stress generated by different wetting procedures, that is, deliquescence and dissolution. However, understanding the nonstationary nature of deformation and differences in deformation due to varying moisture absorption and water absorption rates requires further investigation.

ACKNOWLEDGEMENTS

This study was funded by Grants-in-Aid for JSPS Fellows (grant number 21K14301; supervising researcher: Nobumitsu Takatori), and the reviewers' comments have greatly improved this paper. We extend our most sincere appreciation.

REFERENCES

[1] M. Steiger and S. Asmussen, “Crystallization of sodium sulfate phases in porous materials: The phase diagram Na2SO4-H2O and the generation of stress,” Geochimica Et Cosmochimica Acta, vol. 72, no. 17, pp. 4291-4306, 2008.

[2] R. J. Flatt, “Salt damage in porous materials: how high supersaturations are generated: Journal of Crystal Growth,” vol. 242, pp. 435-454, 2002

[3] H. Derluyn, "Salt transport and crystallization in porous limestone: Neutron X Ray imaging and poromechanical modeling," 2012.

[4] K. Kiriyama, S. Wakiya, N. Takatori, D. Ogura, M. Abuku and Y. Kohdzuma, "Environmental control for mitigating salt deterioration by sodium sulfate on Motomachi Stone Buddha in Oita prefecture, Japan," in Proceedings of SWBSS 2017 (Fourth International Conference on Salt Weathering of Buildings and Stone Sculptures), pp. 118-124, 2017.

[5] A. Stahlbuhk, J. Nissen, K. Linnow and M. Steiger, "Influence of the salt concentration on the damage potential of mirabilite and thenardite," in Proceedings of SWBSS 2014 (Third International Conference on Salt Weathering of Buildings and Stone Sculptures), pp. 35-48, 2014.

[6] N. Takatori, D. Ogura, S. Wakiya, M. Abuku, K. Kiriyama and Y. Kohdzuma, “Numerical analysis on salt damage suppression of the Buddha statue carved

into the cliff by controlling the room temperature and humidity in the shelter," in Proceedings of SWBSS 2017 (Fourth International Conference on Salt Weathering of Buildings and Stone Sculptures), pp. 125-134, 2017.

[7] N. Takatori, K. Sakai, D. Ogura, S. Wakiya, and M. Abuku, "Measurement of sodium chloride solution permeability and sorptivity in tuff stone," in Proceedings of SWBSS 2021 (Fifth International Conference on Salt Weathering of Buildings and Stone Sculptures), pp. 163-171, 2021.

[8] J. Richards, Q. L. Guo, H. Viles, Y. W. Wang, B. Zhang, and H. Zhang, "Moisture content and material density affects severity of frost damage in earthen heritage," Science of the Total Environment, vol. 819, May 2022, Art no. 153047, doi: 10.1016/j.scitotenv.2022.153047.

EXPECT THE UNEXPECTED: WHEN INCREASING RELATIVE HUMIDITY CAUSES NON-HYDRATING SALTS TO CRYSTALLIZE FROM A MIXTURE

S. Godts[1,2,3,*], A. Stahlbuhk[4], J. Desarnaud[1], S. A. Orr[5], V. Crevals[1], H. De Clercq[1], T. De Kock[3], V. Cnudde[2,6], and M. Steiger[4]

KEYWORDS

ECOS/Runsalt, Crystallization Behavior, Salt Mixture, Built Heritage

ABSTRACT

Understanding the crystallization behavior of salt mixtures is key to improving conservation strategies for porous heritage materials. The crystallization behavior of a common mixture is investigated: Cl^-, NO_3^-, Na^+, K^+, and Ca^{2+} in two concentrations - one equimolar and the other with proportionally more nitrate and calcium ions. Both examined between 15-95% relative humidity (RH) at 20 and 25 °C. The crystallization pathway was determined using the ECOS/Runsalt model, and experiments were carried out with dynamic vapor sorption, a RH generator and time-lapse imaging via microscopy. The experimental results are partly in agreement with the modelled RH points of interest, however important deviations are seen in the crystallization pathway of the non-equimolar mixture. Niter is seen to crystallize when the RH increases from 30% to 45%, a crystallization pathway only seen in the model output of the equimolar mixture. Furthermore, in both mixtures calcium nitrate is partly hindered from crystallizing and when it does the tetrahydrate is identified. Despite these deviations, the sorption measurements are in close agreement with the initial mutual crystallization RH. The results are important for evaluating risks and understanding damage phenomena in heritage materials under realistic climatic conditions.

[1] Monuments Lab, Royal Institute for Cultural Heritage (KIK-IRPA), Belgium
[2] Department of Geology, PProGRess, Ghent University, Belgium
[3] Faculty of Design Sciences, ARCHES, University of Antwerp, Belgium
[4] Department of Chemistry, University of Hamburg, Germany
[5] Institute for Sustainable Heritage, University College London, UK
[6] Department of Earth Sciences, Utrecht University, The Netherlands
* Corresponding author, e-mail: sebastiaan.godts@kikirpa.be

Expect the unexpected: when increasing relative humidity causes non-hydrating salts to crystallize from a mixture.

1 INTRODUCTION

Salt mixtures are the cause of stone decay all over the world, however few studies investigate the behavior of mixtures subjected to different environmental conditions [1]–[4]. This contribution focusses on the result of thermodynamic calculations that model the behavior of salt mixtures under changing relative humidity (RH) conditions, and the verification of the model outputs through experimental investigation. The latter permits the assessment of salt crystallization kinetics that are not considered in models. Thus, allowing the interpretation of results to identify realistic risk events when advising preventive measures to mitigate crystallization cycles. Here we focus on common mixture compositions derived from a statistical analysis of 11412 samples taken in 338 historic buildings (monuments and sites) primarily in Belgium [5], [6]. The mixtures of interest include a combination of seven ions: Cl^-, NO_3^-, SO_4^{2-}, Ca^{2+}, Na^+, K^+, and Mg^{2+}. As the least soluble salt, here gypsum, will crystallize rapidly from the mixed ions, the remaining solution will then either include calcium or sulfate ions, dependent on the mixture composition. Under these circumstances six ions remain Cl^-, NO_3^-, SO_4^{2-}, Na^+, K^+, and Mg^{2+} or Cl^-, NO_3^-, Ca^{2+}, Na^+, K^+, and Mg^{2+}. Magnesium occurs less frequently in common mixtures found in heritage sites, leaving five ions of interest,: SO_4^{2-}, Na^+, K^+, NO_3^-, Cl^- (type 1, sulfate-rich) or NO_3^-, Ca^{2+}, Cl^-, Na^+, K^+ (type 2, calcium-rich) [5] (shown in decreasing order of magnitude as found in common mixtures). Type 1 mixtures tend to be less hygroscopic, mainly crystallizing above 60% RH and contain more hydrated, and double salts. Type 2 mixtures tend to crystallize below 60% RH and contain more hygroscopic salts that are often kinetically hindered from crystallizing. Including magnesium, 14 solids are commonly found in building materials. Their minimum and maximum mutual RH crystallization and dissolution ranges have been mapped out in view of their single salt behavior [7]. Here we present experimental data on the common mixture Cl^-, NO_3^-, Ca^{2+}, Na^+, K^+ (type 2, calcium-rich) and place the results into context of conservation practice and how the combination of techniques can help us better understand crystallization processes in past and future climatic conditions.

2 METHOD

2.1 Calculated crystallization behavior

The model ECOS/Runsalt [8], [9] is used to calculate the crystallization behavior of two mixtures (type 2): one an equimolar composition of $2Cl^-$, $2NO_3^-$, $1Na^+$, $1K^+$, $1Ca^{2+}$, and the other a non-equimolar mixture with proportionally more nitrate and calcium ions, specifically $1.9Cl^-$, $4.7NO_3^-$, $1.9Na^+$, $1.9K^+$, $1.4Ca^{2+}$. The study of the latter mixture is particularly significant, as nitrate and calcium ions are typically found in greater proportions within mixtures measured in the built environment [5]. Both are modeled between a relative humidity (RH) of 15% and 95% with a resolution of 0.1% RH, at 20 and 25 °C. Details on the model input parameters and limitations are described in [10]. The output shows solids that can crystallize from the solution, for example, at a given RH the amount of crystalline solid is indicated. Because there is a limited number of independent variations of which a system of coexistent phases is possible, generally known as the phase rule [11], only four solids can coexist at a given temperature (T) and RH within the five-ion mixture.

Thus, the salts under investigation are halite (NaCl), niter (KNO_3), sylvite (KCl), and hydrated calcium nitrate $Ca(NO_3)_2{\cdot}xH_2O$. Excluding the double salts $Ca(NO_3)_2{\cdot}KNO_3{\cdot}3H_2O$ [12] and $Ca_2Cl_2{\cdot}Ca(NO_3)_2{\cdot}4H_2O$ [13] as these solids are currently not considered in the model dataset.

2.2 Experimental verification of the mixture behavior

The experiments are carried out with an equimolar solution of $2Cl^-$, $2NO_3^-$, $1Na^+$, $1K^+$, $1Ca^{2+}$, and a solution of $1.9Cl^-$, $4.7NO_3^-$, $1.9Na^+$, $1.9K^+$, $1.4Ca^{2+}$ (scaled to 0.1), further defined as mixture (A) and (B), respectively. The mixtures are prepared with a concentration of 25% below the saturation degree of the equimolar mixture (1.920 mol·kg^{-1}), the latter non-equimolar mixture was made with 11.225 g of NaCl, 19.417 g of KNO_3 and 33.431 g of $Ca(NO_3)_2{\cdot}4H_2O$ (Merck, analytical grade quality) in 86.173 g ultra-pure H_2O, accounting for the hydrated salt. The calculated crystallization behavior of the mixtures is verified experimentally following two methods.

i.) Duplicate time-lapse imaging under changing RH experiments, mixture (B)

Dissolution and crystallization times of the non-equimolar mixture (B) were recorded via time-lapse imaging (3D-digital microscopy, HIROX—imaged at a magnification of 140 or 160 (lens: MXG-2500REZ, KH-8700), a field of view of 2079.49 µm and special resolution of 1.30 µm). Intervals between images were either 2, 5, 30 or 60 seconds (s), subject to visually observed phase transitions during the first run. The solution/crystals were imaged under changing RH in a windowed climate chamber (GenRH/Mcell) with a constant gas flow (H_2O and N_2) at 200 sccm (standard cubic centimeters per minute). All measurements were recorded under laboratory temperature 20 °C (±1) and between 15% and 95% RH. Solid phases were analyzed at specific RH intervals when crystals became visible with a portable Raman spectrometer for environmental analysis (Renishaw, Virsa™), focusing on specific solids through the windowed climate chamber. Further verification was carried out after long-term conditioning of the samples (3 months) at 15% RH and 20 °C with micro-Raman spectroscopy (Renishaw InVia). In both cases the measurements were carried out with a 785 nm (100 to 400 mW) near infrared diode laser through a long-distance objective with a magnification of x5, x20 or x50. An exposure time of 10 s and a measurement range between 100 and 2000 cm^{-1} was sufficient to obtain identifiable spectra. Additionally, after the same long-term conditioning, X-ray diffraction analysis (Bruker D8 theta/2theta configuration) was carried out on the 'dried' solution.

The experiments under this method were carried out with 6 droplets of solution (the initial volume of each drop was 0.5 µL) placed on an 18 mm x 18 mm glass slide into the windowed climate chamber. The droplets were conditioned at 95% RH followed by drying at 15% RH (1 hour for each RH plateau step). The main experiment involves cycles of decreasing and increasing RH, each cycle maintained for 1 hour. The increasing cycle starts at 15%, increasing by 5% each cycle until 95%. The decreasing cycle starts at 95%, reducing by 5% each cycle until 15%:

- 95%-*X*%-95%; with *X* = 90%, 85%, 80%, 75%, 70%, and so forth until 15%;
- and 15%-*X*%-15%; with *X* = 20%, 25%, 30%, 35%, 40%, and so forth until 95%.

This experimental series reaches a total of 64 steps (total duration 64 h). RH and T were logged every 2 seconds in the climate chamber near the droplets (Rotronic, RH and T measurement probe). The experimental method involves time steps for achieving the target RH in the climate chamber and attaining the calculated RH points of interest when crystallization or dissolution is expected (the mutual crystallization or dissolution relative humidity for each solid), and the effective crystallization and dissolution times at first and completed microscopic observation of a crystallization or dissolution. Specifically, we consider:

- t_1 = the start time of the experiment until the first mutual crystallization or dissolution RH is reached, as calculated by ECOS/Runsalt, with respect to the given RH target. The mean and median values were summarized here as derived from the calculated slopes from the obtained datapoints, for increasing RH and decreasing RH separately. For increasing RH, the mean slope is approximately 0.77% s^{-1} (median 0.69% with a standard deviation (sd.) of 0.30%), for decreasing RH: the mean slope is approximately -0.47% s^{-1} (median: -0.49% with sd. 0.22%).
- t_2 = from t_1 until the first visible crystal or dissolution, which is considered as the induction time.
- t_3 = the time from t_2 until complete visible crystallization or dissolution, thus the effective crystallization/dissolution time.
- t_4 = the induction time plus completed crystallization/dissolution, thus $t_2 + t_3$.
- t_{exp} = the total experimental time of the step (here always 1h), however $t_4 + t_1$ can be less or exceed t_{exp}.

ii.) Quadruplicate dynamic vapor sorption experiments, mixtures (A and B)

Similar to experiments described by Rörig-Dalgaard [14], sorption and desorption isotherms of both mixtures (A and B) were determined via dynamic vapor sorption (SPSx-1µ high load, proUmid, SPS: sorption testing system, 1 µg resolution). All isotherms were recorded at 25 °C within a range of relative humidities between 15% and 95%. Simultaneous imaging and Raman spectra were obtained throughout the experiment. Images were obtained at each RH step with a 50 mm lens, CMOS sensor (11.3 mm x 11.3 mm, 2046 pixel x 2046 pixel resolution 5.5 x 5.5 µm pixel size). A Wasatch Photonics WP 785 (nm laser) was used to obtain Raman spectra at the end of each RH step, with the following parameters: laser power 450 mW, resolution 7 cm^{-1}, 10 s integration time, 270-2000 cm^{-1} spectral range, working distance 50 mm.

The experiments with the non-equimolar mixture (B) following this method were carried out with either 20 to 30 droplets of 0.5 µL or one droplet of 20 µL solution, placed in one of the 23 aluminum sample pans of the SPS autosampler. The larger volume droplets were used to obtain Raman spectra and time-lapse images. The equipment was set to weighing intervals of 10 or 15 min, with an initial temperature of 40 °C and 15% RH for 12 h to ensure stable weight (reasonable under realistic conditions), followed by the main experiment carried out at 25 °C and RH steps of 1 or 2%, from 15 to 95% for sorption and from 95 to 15% for desorption, each RH step was maintained for 2 or 6 hours. For the equimolar mixture (A), sample masses varied between 6.1 mg and 13 mg for salt solutions (weight before drying at 60 °C).

The isotherms for this mixture were recorded at 25 °C, the range of relative humidities starting at 0% or 15%, the upper limit varying between 80 and 95%. The experiments were carried out with fixed rates of 2% steps every five and ten hours. We consider non-equilibrium conditions (d_m/d_t, derivative of mass (m) with respect to time (t)) as the equilibrium limit is set to 0.01% per 40 min.

3 RESULTS

The crystallization behavior of the two mixtures (A) and (B) are calculated by ECOS/Runsalt and shown in Figure 1. In both mixtures, the first solid that the model indicates at 25 °C is halite, respectively at an RH of 60% and 55% (rounded). For mixture (B), at 20 °C niter shifts and becomes the first to crystallize, from initially 53% at 25 °C to 66% at 20 °C before halite. This is an unusually large RH shift and suggests a possible issue with the model parameters. For the equimolar mixture (A) at 20 °C, an unexpected phenomenon is observed with niter crystallizing at 56% reaching a maximum of crystalline solid around 41% followed by redissolution under drying condition until completely dissolved again at 34%. The process of niter dissolution corresponds with the crystallization of potassium chloride (sylvite) starting at 40%. While potassium ions from niter are going into solution, they are incorporated into sylvite crystals, and nitrate ions become available in the solution, under drying conditions until 32% when the remaining halite and sylvite crystallize.

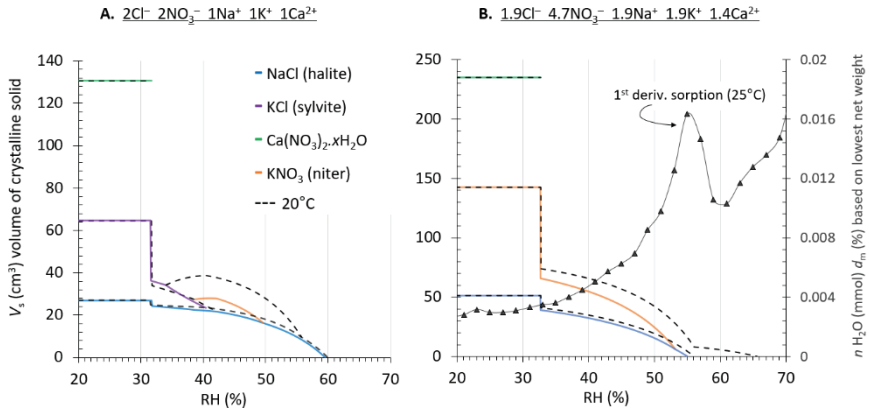

Figure 1. ECOS/Runsalt crystallization results for two ion mixtures at 25 and 20 °C, across 15%-95% RH (x-axis: 20-70% RH with 0.1% resolution). Left: mixture (**A**) and right: mixture (**B**). The y-axis depicts crystalline solid volumes in a stacked format. The legend distinguishes 25 °C (colored lines) and 20°C (dashed lines) solid phases. The secondary y-axis shows the 1st derivative of the sorption measurement for mixture (**B**), reflecting dynamic vapor sorption data at 25 °C and 2% RH intervals every 6 hours. This aligns with the initial mutual halite crystallization at 55% RH and 25 °C.

The same pathway is seen at 25 °C between 50 and 39% RH. However, for the non-equimolar mixture (B), the calculated behavior does not indicate any redissolution of niter or crystallization of sylvite. The model also predicts the crystallization of anhydrous calcium nitrate in both mixtures; however, it is known error in

ECOS [10], [15]. If it were to be physically possible the calcium nitrate phase would be tetrahydrate (nitrocalcite). We can assume that calcium and nitrate ions remain available in solution throughout the experiments as described further. Vice versa under wetting conditions the first mutual dissolution RH is noted around 32% (for both mixtures and temperatures), followed by a slow dissolution of sylvite and halite at higher RH values. The behavior of mixture (A) continues with niter crystallizing under increasing RH, a logical process under these conditions where the solution becomes oversaturated with respect to potassium and nitrate ions to provoke crystallization until dissolution starts again from 40% RH upwards. As the model dataset does not include the double salts $Ca(NO_3)_2{\cdot}KNO_3{\cdot}3H_2O$ and $Ca_2Cl_2{\cdot}Ca(NO_3)_2{\cdot}4H_2O$ there remain open questions whether these salts form and how the pathway might change. The calculated crystallization and dissolution behavior is further verified experimentally.

i.) Duplicate time-lapse imaging under changing RH experiments, mixture (B)

During the time-lapse imaging, through the windowed climate chamber, the first and last crystal formations were expected to contain chloride, therefore no discernible Raman spectra could be obtained. To identify these salts the morphology was examined. The first set of crystals revealed a dendritic and cubic pattern, thereby suggesting their classification as halite. The crystallographic behavior of sylvite mirrors that of halite as an isometric system. However, the final crystals exhibited habits inclusive of octahedral and dodecahedral forms [16], [17]. Given these observations, a specific identification between either halite or sylvite was not possible. Between the two solid phases typical orthorhombic crystals, that is, long prismatic shapes with needle-like or plate-like forms were visible, these crystals were identified with Raman as niter (principal Raman shift at 1050.3 cm^{-1}). Crystallization of calcium nitrate was not observed; however, Raman spectra were obtained with a clear identification of nitrocalcite (principal Raman shift at 1051.1 cm^{-1}). The latter was also identified in the equimolar mixture (A). Despite the long-term conditioning of the samples (over 3 months) at 15% RH and 20 °C, the XRD analysis was unable to identify any minerals. This was attributed to persistent calcium nitrate solution surrounding all solids, which had become extremely viscous and exhibited amorphous properties, thus obscuring the definitive crystalline characteristics required for identification of all crystalline solids in the mixture. The same results were obtained in the vapor sorption experiments.

The experimental results of the time-lapse imaging under changing RH (20 °C) are presented in Table 1 (limited to mixture B). When reducing the relative humidity (RH) from 95% to the designated target values (95%-*X*%), halite formation was first observed at 40% RH. This observation is not in agreement with the calculated behavior where niter was expected to crystallize first, keeping in mind that the specific RH noted is subject to the rate of RH change (see method section). The time before the first crystallization is observed is approximately 15 minutes for 95%-40% and 7 minutes for 95%-15% (t_2). This general trend can be derived from the RH steps with faster crystallization occurring at lower RH targets. A similar trend is derived for complete crystallization (t_3) for *X*%-15%, with an increased time when *X* is set to a higher RH, for *X* = 65% to 95%, these times are respectively 10 and 35 minutes. Accordingly, the delay is caused by the evaporation rate of the

diluted solution at higher RH before critical saturation was reached, a kinetic property of the solution. Complete crystallization times (t_3) are recorded with roughly 42 minutes for 95%-40%, and 20 minutes for 95%-15%. The opposite trend is seen for the dissolution experiments (15%-*X*%), with faster complete dissolution (t_3) when the RH target is higher, with 54 minutes for 15%-75%, and 12 minutes for 15%-95%. However, the dissolution times remain reasonably constant for the dissolution experiment *X*%-95%, with 11 minutes on average for every step between 15%-95% and 40%-95%.

Table 1: The median logged time in minutes (rounded to 1 min.) and spread (or standard deviation (sd.)) considering the target RH (*X*) of all crystallization and dissolution experiments with mixture (**B**) carried out in steps of 5% with a total time for each RH step of 1 h (t_{exp}) at 20 °C (±1). Specified time intervals are considered with t_1 = the time for the equipment to reach the first mutual crystallization/dissolution RH (see method section), t_2 = the time when t_1 is reached until the first visible crystallization or dissolution occurs and t_3 = the time from first crystallization/dissolution (t_2) until completed (excluding incomplete processes, thus the RH cut-off as indicated by *X*, however not considering kinetically hindered crystallization of calcium nitrate).

median logged time (min.) and spread considering *X*	crystallization 95%-*X*% (*X* = 40 to 15)	dissolution *X*%-95% (*X* = 40 to 15)	crystallization *X*%-15% (*X* = 65 to 95)	dissolution 15%-*X*% (*X* = 75 to 95)
t_2	10 (15 to 7)	1 (2 to 0.5)	4 (2 to 7)	0.3 (sd. 0.1)
t_3	26 (42 to 20)	11 (sd. 0.5)	26 (10 to 35)	17 (54 to 12)

These values are important in view of high-resolution climatic data (minutes). More specifically, when considering crystallization and dissolution cycles and linking phase transitions to decay phenomena, further described in [18]. The experiments show that, within a time frame of 1 h, complete crystallization takes longer compared to dissolution, unless the target RH for dissolution is close to the critical crystallization RH. These results are in contrast with general literature that states that under the same conditions dissolution is often faster than crystallization. This is because dissolution only requires the breaking of the ionic lattice of the salt, while crystallization requires the ordered arrangement of ions into the crystal lattice, the latter often a slower process. However, our observations show that the process is dependent on the initial and target RH.

When verifying crystallization and dissolution of niter, the time-lapse images show that niter crystallizes out of the existing solids (unidentified) in the solution with increasing RH. This process is illustrated in Figure 2. Again, this behavior was not calculated for mixture (B), yet it can be derived from the equimolar mixture (A). The opposite process is seen under drying conditions with niter dissolution and possibly sylvite, nitrocalcite, halite or the calcium potassium nitrate double salt crystallizing. Crystallization of niter from solution is observed after a median time (t_2) of 2 minutes (sd. = 0.3), considering 20 dissolution experiments 15%-*X*% (*X* = 65 to 95) and *X*%-95% (*X* = 40 to 15). When the RH is set at 35% and 40%, niter crystallizes and remains stable, while the crystals are observed to dissolve again

above 40%. The results are critical as they illustrate the crystallization behavior in comparison with the modeled behavior indicated by ECOS.

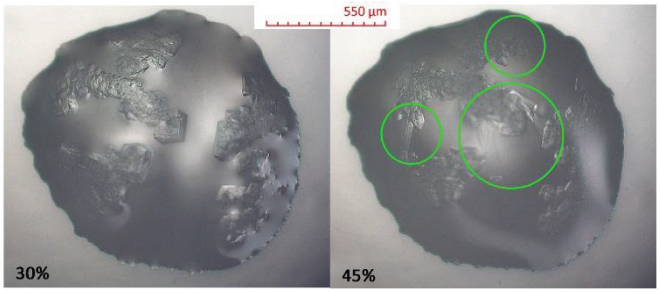

Figure 2. Illustration of niter crystal growth (inside the green circles) from a mixed salt solution, non-equimolar mixture (B), under increasing relative humidity from 30 to 45% (5% increments every 60 min) at 20 °C, respectively left and right image.

ii.) Quadruplicate dynamic vapor sorption experiments, mixtures (A and B)

The results of the sorption and desorption experiments with the SPS equipment are compared to the crystallization and dissolution behavior of both mixtures (A and B) as calculated with ECOS at 25 °C (Figure 1). The individual sorption and desorption curves exhibit consistent trends with few distinguishable weight changes where transitions could be identified (not shown). However, a hysteresis between sorption and desorption occurs, as supersaturation precedes crystallization. As a result, crystallization happens at a lower relative humidity than the deliquescence of the final crystalline phase during sorption. The hysteresis is thus an indication for the first transition. For the non-equimolar mixture (B) this is seen between 59 and 43% RH. The more complex the mixture the more the hysteresis is less pronounced, thus calculating the first derivative can provide useful insights. When looking at the first derivative of the sorption curve we can identify a first maximum at 55% and a smaller less pronounced maximum at 23% RH. The first value is in perfect agreement with the calculated mutual crystallization RH of 55% for halite in mixture (B) at 25 °C. While for the equimolar mixture (A) the maxima detected were at 21%, 46% and 58%. It is assumed that the steps around 22% (in both mixtures) are the result of calcium nitrate hydration, a delayed reaction due to kinetics. The step at 58% is in close agreement with the calculated value of halite crystallization at 60% and the step at 46% is likely associated with niter crystallization at 50% in mixture (A) at 25 °C. Some deviation is likely due to the lower degree of supersaturation for the small amount of niter that crystalizes.

The identification of crystallization and dissolution times is limited to the experimental parameters. However, the results of both time-lapse imaging and dynamic vapor sorption experiments, with the non-equimolar mixture (B), allow us to define patterns between the widely different RH step-width and time intervals applied. In the sorption experiments we identify the onset of dissolution at approximately 33% RH and completed dissolution at 68% RH (Figure 3). This agrees with the former Gen-RH experiments where the onset of dissolution is first observed at 35% RH and near complete dissolution at 70% (part of the dissolution experiment 15%-

X%). Considering that the experimental procedure for the latter (experiment i.) is significantly shorter in time with increasing RH at 0.77% s^{-1} and decreasing RH at -0.49% s^{-1} (maintaining the target for 1h) compared to the slower run maintaining each % change for 2 h (experiment ii.). In line with the different time steps, during desorption at slower rate, we can observe halite crystallization at 51% RH and niter crystallization at 48% RH. While at faster rate, halite and niter crystallization were observed at 40% and 35% RH, respectively. These results are notable for practical considerations when looking at realistic climate data, where the effect of boundary conditions such as the averaging time frame and the minimum RH on the determined number of salt phase transitions is important (see [18], [19]).

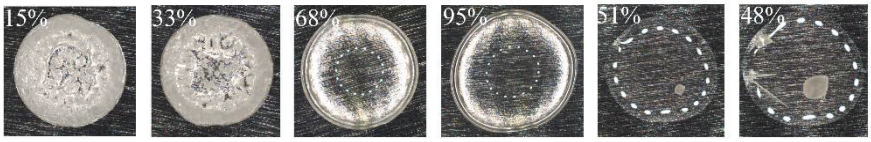

Figure 3. Illustration of image capture during sorption and desorption measurements with the non-equimolar mixture (B) at 25 °C (15-95-15%, step width 1% for 2 h) of a 20 µL droplet in an aluminum pan in the SPS experiment, observations from left to right (complete) crystallization 15%, first dissolution 33%, completed dissolution 68%, undersaturated solution 95%, onset of first crystallization 51%, and onset of second crystallization 48%.

4 CONCLUSION

The crystallization behavior under varying relative humidity conditions of a common hygroscopic salt mixture with two different compositions was investigated (an equimolar mixture $2Cl^-$, $2NO_3^-$, $1Na^+$, $1K^+$ $1Ca^{2+}$ and a non-equimolar mixture with proportionally more nitrate and calcium ions $1.9Cl^-$, $4.7NO_3^-$, $1.9Na^+$, $1.9K^+$, $1.4Ca^{2+}$. ECOS/Runsalt was used for modeling the behavior and the output was experimentally investigated with different methods. The experimental results were also used to determine crystallization and dissolution times of the non-equimolar mixture under different rates of environmental changes. It was observed that initial crystallization is delayed compared to initial dissolution that starts rapidly, however complete crystallization is in most instances slower than the complete dissolution process. During the dissolution phase, the mixture starts to dissolve quickly when the RH hits around 35%. However, to fully dissolve, it requires higher humidity levels, specifically between 68% and 75%. This full dissolution happens over different timescales depending on how quickly the humidity rises. In slower conditions (RH rising 2% every 6 hours), it takes roughly 72 hours. But in faster conditions (RH rising at a rate of 0.69% s^{-1}), the timescale is shortened to under 1 hour. Remarkably, if the humidity increases rapidly to 95%, the mixture can dissolve completely in as little as 11 minutes. In contrast, during the drying phase, salts begin to crystallize at 51% RH for slower drying conditions and at 40% RH for faster ones, taking approximately 16 hours and 16 minutes, respectively. Excluding calcium nitrate, full crystallization takes around 24 hours in slower conditions, and 40 minutes in faster ones. When the RH plummets rapidly to 15%, full crystallization can occur in just 26 minutes. This data helps us understand how salt mixtures react to different humidity conditions, giving us insights into its behavior under realistic, fluctuating climatic scenarios. In view of practical considerations

when the dissolution and crystallization times are correlated with high resolution climate data, cycles of phase changes can be determined more precisely.

The kinetics of niter and calcium nitrate behavior were also of particular interest. In the non-equimolar mixture niter crystallized from solution under increasing RH, a behavior that seems to follow the crystallization pathway of the equimolar one. Crystallization of calcium nitrate tetrahydrate was also observed in both mixtures. Additionally, it was observed that over longer periods of time most of the calcium nitrate remained in solution and amorphous phases might also occur. More research is needed to understand the crystallization behavior of this salt in terms of risk assessment to building materials. These kinetic properties are substantial enough to warrant consideration when using the model, in-site evaluation, and preventive conservation recommendations. Further research is also needed to understand the pore-scale processes and verification of effective decay potential in terms of crystallization cycles, pressure, and pore filling. In summary, this study helped to identify possible issues with the model parameters and underscores the significance of understanding the interplay of RH and time in the crystallization and dissolution cycles of salt mixtures.

ACKNOWLEDGEMENTS

The research presented is funded by the Belgium Science Policy (Belspo) within the framework of BRAIN-be 2.0, Belgian Research Action through Interdisciplinary Networks: project B2/191/P1/PREDICT (Research action B2); joint PhD project PREDICT, Phase Transitions of Salts under Changing Climatic Conditions. The authors further acknowledge the funding for the GenRH humidity generator through “BOF, project UG_2832369580”, “JPI-JHEP project KISADAMA” and “FWO Research Grant 1521815N”.

REFERENCES

[1] B. Menéndez, “Estimation of salt mixture damage on built cultural heritage from environmental conditions using ECOS-RUNSALT model,” *Journal of Cultural Heritage*, vol. 24, pp. 22–30, Mar. 2017, doi: 10.1016/j.culher.2016.11.006.

[2] S. Godts, R. Hayen, and H. De Clercq, “Investigating salt decay of stone materials related to the environment, a case study in the St. James church in Liège, Belgium,” *Studies in Conservation*, vol. 62, no. 6, pp. 329–342, Aug. 2017, doi: 10.1080/00393630.2016.1236997.

[3] S. Laue, D. Poerschke, and B. Hübner, “Investigation and conservation of salt damaged epitaphs in the church of Werben (Saxony-Anhalt, Germany). SWBSS 2017 fourth Int Conf salt Weather Build stone Sculpt.,” in *Fourth Int Conf salt Weather Build stone Sculpt., Potsdam, Germany, 20-22 September 2017*, S. Laue, Ed., Potsdam: Verlag der Fachhochschule, 2017.

[4] S. L. Clegg, K. S. Pitzer, and P. Brimblecombe, “Thermodynamics of Multicomponent, Miscible, Ionic Solutions. 2. Mixtures Including Unsymmetrical Electrolytes,” *J. Phys. Chem.*, vol. 96, pp. 9470–9479, 1992, doi: 10.1021/j100202a074.

[5] S. Godts *et al.*, "Charge balance calculations for mixed salt systems applied to a large dataset from the built environment," *Sci Data*, vol. 9:324, Dec. 2022, doi: 10.1038/s41597-022-01445-9.

[6] S. Godts, S. A. Orr, M. Steiger, and T. De Kock, "Mixed salt systems in the built environment - charge balance calculations [Data set]. Available at https://zenodo.org/record/6280617#.Y3yzyUnMJjF," *Zenodo*, 2022. https://doi.org/10.5281/zenodo.6280617 (accessed Sep. 22, 2022).

[7] S. Godts *et al.*, "Salt Mixtures in Stone Weathering," *Scientific Reports*, In Review.

[8] C. Price, *An expert chemical model for determining the environmental conditions needed to prevent salt damage in porous materials: protection and conservation of the European cultural heritage; project ENV4-CT95-0135 (1996-2000) final report*. in Protection and conservation of the European Cultural Heritage, no. 11. London: Archetype, 2000.

[9] D. Bionda, *RUNSALT - A graphical user interface to the ECOS thermodynamic model for the prediction of the behaviour of salt mixtures under changing climate conditions. http://science.sdf-eu.org/runsalt/*. 2005. Accessed: Oct. 24, 2022. [Online]. Available: http://science.sdf-eu.org/runsalt/

[10] S. Godts *et al.*, "Modeling Salt Behavior with ECOS/RUNSALT: Terminology, Methodology, Limitations, and Solutions," *Heritage*, vol. 5, no. 4, pp. 3648–3663, Nov. 2022, doi: 10.3390/heritage5040190.

[11] J. W. Gibbs, "On the Equilibrium of Heterogeneous Substances," *Transactions of the Connecticut Academy of Arts and Sciences*, vol. III, p. 306, 1878 1874.

[12] R. Flatt and P. Bocherens, "Sur le système ternaire Ca^{++}_K^{+}_NO_3^{-}_H_2O," *Helv. Chim. Acta 45*, vol. 45, no. 1, pp. 187–195, 1962, doi: https://doi.org/10.1002/hlca.19620450124.

[13] W. F. Ehret, "Ternary Systems: CaCl2-Ca(NO3)2-H2O (25°), CaCl2-Ca(ClO3)2-H2O (25°) SrCl2-Sr(NO3)2-H2O (25°), KNO2-Pb(NO3)2-H2O (0°)," *Journal of the American Chemical Society*, vol. 54, pp. 3126–3134, 1932.

[14] I. Rörig-Dalgaard, "Direct Measurements of the Deliquescence Relative Humidity in Salt Mixtures Including the Contribution from Metastable Phases," *ACS Omega*, vol. 6, no. 25, pp. 16297–16306, Jun. 2021, doi: 10.1021/acsomega.1c00538.

[15] M. Steiger, "Salts in Porous Materials: Thermodynamics of Phase Transitions, Modeling and Preventive Conservation," *Restoration of Buildings and Monuments*, vol. 11, no. 6, pp. 419–432, 2005, doi: 10.1515/rbm-2005-6002.

[16] O. Braitsch, *Salt Deposits Their Origin and Composition*. Berlin, Heidelberg: Springer Berlin Heidelberg, 1971. doi: 10.1007/978-3-642-65083-3.

[17] E. S. Dana and W. E. Ford, *A Textbook of Mineralogy, with an extended treatise on crystallography and physical mineralogy*, Third. New York: Jhon Wiley & Sons, Inc., 1922.

[18] T. De Kock *et al.*, "Implications of using meteorological records to assess the environmental risk of salt crystallization cycles in stone," in *Fifth International Conference on Salt Weathering of Buildings and Stone Sculptures: proceedings of SWBSS 2021 / 22-24 September*, B. Lubelli, A. Kamat, and W. J. Quist, Eds., Delft, the Netherlands: TU Delft Open, 2021, pp. 31–39.

Expect the unexpected: when increasing relative humidity causes non-hydrating salts to crystallize from a mixture.

[19] S. Godts *et al.*, "NaCl-related weathering of stone: the importance of kinetics and salt mixtures in environmental risk assessment," *Heritage Sci*, vol. 9, no. 44, p. 1:13, Dec. 2021, doi: 10.1186/s40494-021-00514-3.

EXPERIMENTAL STUDY ON MOISTURE DIFFUSIVITY OF SINTERED BRICKS WITH DIFFERENT SODIUM CHLORIDE CONTENT

Zixin Yang[1], Huarong Xie[1], Changchang Xia[1], Yonghui Li[1*], and Shuichi Hokoi[2]

KEYWORDS

Moisture diffusivity, ruler method, salt content, capillary absorption experiment, sintered brick

ABSTRACT

Sintered brick is one of the common porous building materials of architectural heritage. Salt migration with capillary water inside sintered bricks results in the various deterioration. Moisture diffusivity is an important hygroscopic physical parameter for accurate analysis of moisture transfer in sintered bricks. To clarify the effect of salt content on the moisture diffusivity of Chinese sintered blue bricks, the capillary absorption coefficient and capillary absorption content of the bricks contaminated by 0%, 1%, 5% and 10% sodium chloride (NaCl) solution were determined by capillary absorption experiment and the 'ruler method' proposed by Evangelides et al. was used to determine the moisture diffusivity (D_l). Results showed that 1) the capillary absorption coefficient (A_{cap}) decreased with the increase of NaCl content, and the maximum decrease was 18%; 2) the presence of salt in bricks decreased the capillary moisture content (w_{cap}) with the maximum decrease of 8.6%; 3) the moisture diffusivity at the same water content increases with the salt content. This research contributes to understanding the effect of salt on moisture migration in sintered bricks and provides data support for the moisture simulation, energy consumption calculation, and heritage conservation of sintered brick architectural heritage.

[1] School of Architecture, Southeast University, Nanjing, China, liyonghui@seu.edu.cn

[2] Architecture Internalization Demonstration School, Southeast University, Nanjing, China

1 INTRODUCTION

Sintered brick is one of the common porous building materials of architectural heritage. Generally, the salt solution migrates with capillary water inside bricks, resulting in the deterioration of bricks caused by the crystallization of soluble salts, especially when a variety of salt mixtures exist in porous materials [1] – [3].

Numerical simulation is a common tool for calculating the moisture migration in the porous material [4]. The moisture diffusivity of materials is required in the HAM model, and is obtained, for example, based on the water absorption experiment. However, it requires the transient moisture distribution in the material. There are both destructive and non-destructive methods to obtain the transient moisture distribution. The destructive methods (such as the slice-dry-weight method [6]) are not suitable for continuous measurement. Consequently, the non-destructive methods have been developed, such as X-ray attenuation [7], nuclear magnetic resonance [8], time domain reflectometry [9], etc. However, these methods have not been standardized for continuous measurement and not applied widely due to expensive facilities and the complexity of data processing. To overcome these difficulties, many simplifying mathematical models have been proposed to determine moisture diffusivity which solve one-dimensional moisture diffusion equation, including multi-step method [10], ruler method [11], Kießl-Künzel method [12], etc.

Many researches on the determination of moisture diffusivity are commonly carried out in laboratory conditions where there is no salt in the pores of the material [13] – [15]. Although building material frequently contains salt under the natural environment due to the interaction with the chemicals from the surrounding air or water, the effect of salt on moisture diffusivity of porous materials was studied rarely. Therefore, it is necessary to explore the effect of salt content on the moisture diffusivity of porous building materials.

In this study, the capillary absorption experiment of Chinese sintered blue bricks was carried out to determine the moisture diffusivity of sintered blue bricks by the ruler method. To further examine the effect of salt on moisture diffusivity of sintered bricks, the moisture diffusivity of sintered blue bricks contaminated by 1 %, 5 % and 10 % sodium chloride (NaCl) solution was also obtained. It provides basic data for the moisture simulation, energy consumption calculation, and heritage conservation of sintered brick architectural heritage.

2 MATERIALS AND METHODS

2.1 Materials

In this study, the sintered blue bricks produced in southeast of China were used with the size of 50×50×50 mm, as shown in Fig. 1(a). The bulk density, porosity and critical pore size of three brick samples were tested by mercury intrusion porosimetry (MIP) method. The bulk density of three samples were 2.63, 2.68 and 2.66 g/cm^3, and the corresponding porosity were 31.25%, 32.21% and 32.19%, respectively. The pore size distributions obtained from MIP method are illustrated in Fig. 1(b). The major pore size of the samples ranged from 500–5000 nm, and the average pore diameter were 396.26, 409.44 and 428.49 nm, respectively. Although

there is slight difference among the properties of different samples, it may be inevitable considering uncontrollable factors in manufacture process.

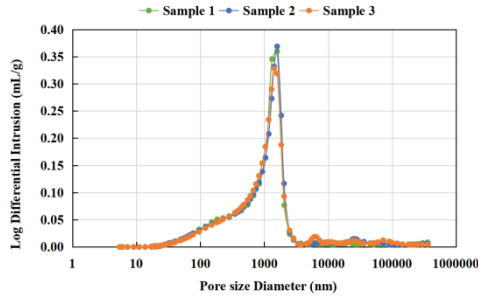

(a) (b)

Figure 1: Sintered blue brick sample and pore diameter distribution of samples

2.2 Methods

2.2.1 Capillary Absorption Experiment

The capillary absorption experiment is one of the most common material physical properties tests. The absorption process is represented by plotting the amount of water absorbed per unit area against the square root of time. Typically, the capillary absorption process can be divided into a first fast absorption stage and a second slow stage. The slope in the first stage is defined as the capillary absorption coefficient (A_{cap}, kg/(m^2·s$^{-1/2}$)):

$$A_{cap} = \frac{\Delta M}{A \cdot \sqrt{t}} \tag{1}$$

where ΔM is the moisture mass absorbed by the sample, kg; A is the water absorption area equal to the bottom area of the sample, m^2; t is the time, s.

The moisture content at the cross point of the fitting lines for the first and the second stages is defined as the capillary moisture content (w_{cap}, kg/m^3):

$$w_{cap} = \frac{\Delta M}{A \cdot H} \tag{2}$$

where ΔM is the moisture mass absorbed by the sample, kg; H is the height of the sample, m.

The capillary absorption test was done based on ISO 15148-2002 standard. The experiment was carried out at the temperature of 15 (±2) ºC and relative humidity of 50 (±2) %, which was determined according to the annual average climatic conditions in Nanjing, China. Five samples were tested to eliminate errors caused by individual differences. Before the experiment, five brick samples were soaked in

distilled water, and the soaking solution was changed every 24 hours until its conductivity decreased to 100–200 μs/cm, which usually last 3–5 days. Next, the samples were dried at 105 °C drying oven until constant weight. After that, the five surfaces of the samples except the water absorbing bottom surface were sealed by plastic films to prevent the influence of water evaporation. In order to inhibit the liquid from rising along the gap between the samples and the plastic films, the plastic films wrapped on four sides surfaces were set aside a 10 mm gap from the bottom. A certain number of exhaust holes were made on the top surface plastic film of the samples to keep air pressure.

During the standard measurement, the dry samples were placed in a shallow tank for one-dimensional (1-D) isothermal free water uptake. The water level in the tank was kept constant at 5 mm above the bottom surface of samples. When the samples touched water, the timer was started. The samples were removed from water every 3–5 min, and the free water attached to the bottom was wiped with a dry cloth. The wet mass of samples was measured regularly with their corresponding times. When the sample weight change during two consecutive measurements was less than 5%, the first stage was considered to be over. In the second stage, the wet mass of samples was recorded at intervals of 30–60 min and the experiment was stopped when recorded at least 5 sets of data. In our study, four groups of different salt concentration experiments were carried out with the same brick samples. After the capillary water absorption experiment of salt free bricks, the samples were dried and then immersed into 1% NaCl solution for two days. After the samples were dried, the above capillary water absorption process was repeated. The samples were soaked in distilled water for desalting until the conductivity of soaking solution decreased to 100–200 μs/cm after the capillary water absorption experiment with salt in each group was completed, and then the next group of salt content experiments was started following the above procedure.

2.2.2 Ruler Method to Determine Moisture Diffusivity

The ruler method is a simplified version of the standard capillary absorption test without complicated facilities to determine moisture distribution in a porous material [16]. During the first stage of the capillary absorption process, the height of the water front was also measured visually by a ruler. The 1-D moisture diffusion under isothermal conditions in porous materials can be described as:

$$\frac{\partial w}{\partial t} = \frac{\partial}{\partial x}\left(D_l \frac{\partial w}{\partial x} \right) \tag{3}$$

where w is the moisture content, kg·m^{-3}; x is the position, m.

By defining the Boltzmann variable λ (m·s$^{-0.5}$) as:

$$\lambda = \frac{x}{\sqrt{t}} \tag{4}$$

The moisture diffusivity with different moisture content can be express as:

$$D_l = -\frac{1}{2} \cdot \frac{\int_{w_0}^{w} \lambda dw}{\left(\frac{dw}{d\lambda}\right)_w} \tag{5}$$

where w_0 is the initial moisture content, kg·m^{-3}.

According to Evangelides et al. (2010) [11], the w-λ profile is approximated by an empirical function as follows:

$$\lambda(w) = \frac{1}{b}\left[\tan\left(-\frac{w + w_{cap}}{a}\right) - c\right] \tag{6}$$

where a, b and c are all fitting parameters, which are obtained by combining the following three boundary conditions, Eq. (7) and Eq. (8).

$$w = w_{cap} : \lambda = 0 \; ; \quad w = 0 : \lambda = \lambda_f \tag{7}$$

$$A_{cap} = \int_0^{w_{cap}} \lambda \, dw \tag{8}$$

where λ_f is the average value of the Boltzmann variable λ at different t, m·s$^{-0.5}$.

Finally, the moisture diffusivity is calculated by substituting the determined w-λ profile into Eq. (5).

3 RESULTS AND ANALYSIS

3.1 Capillary Absorption Coefficient

In Fig. 2(a), the capillary absorption processes of salt free samples are shown. For all five samples, the capillary absorption processes were very similar. The value of ΔM/A is different between 5 samples, but the slope shows an almost the same value, meaning only slight difference of capillary absorption coefficients.

Fig. 2(b) presents the capillary absorption process of Brick 5 sample with different salt content. The slope for the first stage and the corresponding moisture content at the cross point of the fitting lines for the first and the second stages both decreased gradually as salt content increased. With respect to other samples, the influence of salt content was basically consistent with Brick 5.

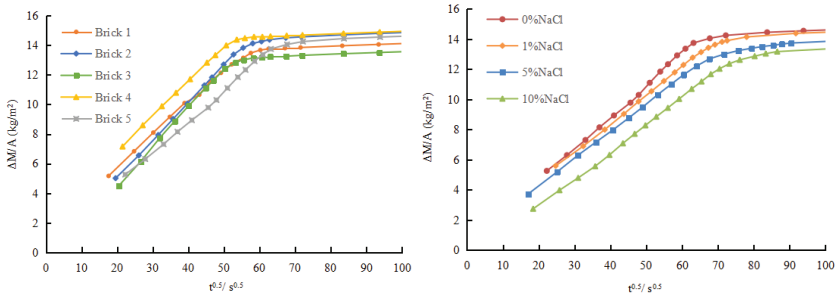

(a) (b)

Figure 2: The capillary absorption process of 5 samples; (a) five salt free bricks, (b) Brick 5 sample with different salt content

Fig. 3 shows the capillary absorption coefficient (A_{cap}) of five sintered blue bricks with different salt content. For all five samples, the A_{cap} of salt bricks was smaller than that of salt free bricks and showed a decreasing trend with the increase of salt content. The slightly obvious difference for Brick 2 with 10% NaCl is a bit abnormal but it is still very limited. By dividing the standard deviation by the average of experimental results [17], the material relative errors of sintered blue bricks with the same salt content were calculated and all less than 15%, which further verifies the validity of the experimental results. The average A_{cap} of five samples with four salt content were 0.230, 0.202, 0.201 and 0.189 kg/(m^2·s$^{-1/2}$), respectively, and the maximum decrease was 18%.

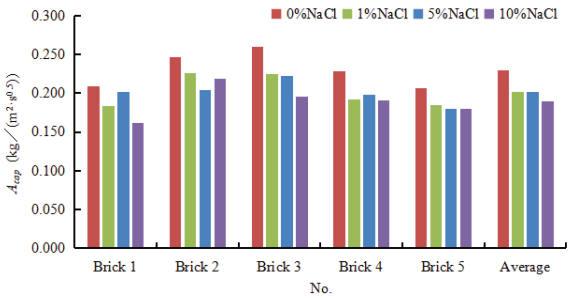

Figure 3: The A_{cap} of five brick samples with different salt content

3.2 Capillary Absorption Content

The experimental results of capillary absorption content (w_{cap}) of five samples with different salt content are presented in Fig. 4. For five samples, the w_{cap} all decreased with the increase of salt content of bricks. The average w_{cap} of five brick samples with four salt content were 275.37, 272.10, 260.27, 251.94 kg/m^3, respectively, and the maximum decrease was 8.6%. The material errors of sintered blue bricks with different salt content were about 5%.

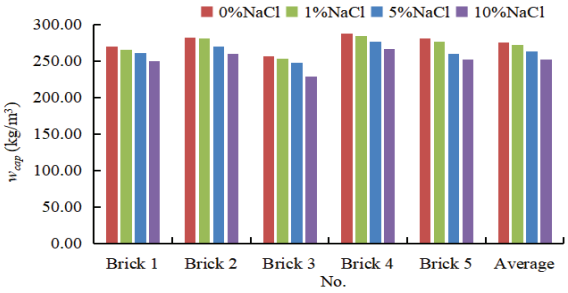

Figure 4: The w_{cap} of five brick samples with different salt content

3.3 Moisture Diffusivity

Fig. 5 presents the w-λ profiles and the moisture diffusivity (D_l) of sintered blue bricks with different salt content, which were obtained from the ruler method described in Section 2.1. In Fig. 5(a), the moisture content of bricks slowly decreased first and then decreased suddenly with the λ increase for all brick samples with four salt content, indicating the sharp water front. The detalied results of fitting parameters in Eq. (5) are shown in Table 1. According to Eq. (6), the D_l with different water content was calculated, as shown in Fig. 5(b). The D_l of salted bricks was obviously higher than that of salt free bricks. The D_l of samples with 1%, 5% and 10% NaCl were similar in low moisture content range. But in the high moisture content range, the D_l of samples with the same water content increased significantly with the increase of salt content of sintered blue bricks.

Table 1: The fitting parameters obtained from ruler method.

	A_{cap} cm^3/(cm^2·min$^{0.5}$)	w_{cap} cm^3/cm^3	λ_f cm/min$^{0.5}$	a	b	c
0%NaCl	0.178	0.276	0.683	0.3544	108.1924	-74.8821
1%NaCl	0.156	0.272	0.663	0.3577	28.6481	-19.9448
5%NaCl	0.155	0.260	0.674	0.3395	36.5535	-25.5987
10%NaCl	0.156	0.252	0.665	0.3306	30.9282	-21.5219

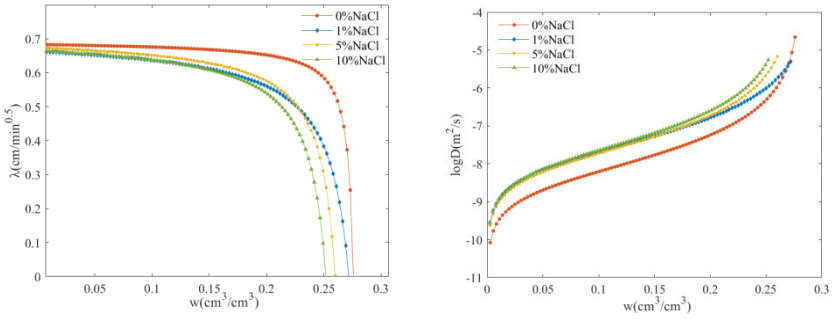

(a) (b)

Figure 5: The w-λ profiles and moisture diffusivity obtained from ruler method

4 DISCUSSION

The capillary absorption process of sintered blue bricks is similar to the laminar flow in a circular tube and the capillary absorption coefficient (A_{cap}) may be approximately quantified by Poiseuille equation, as shown in Eq. (9) [18].

$$A_{cap} = \varphi\rho\sqrt{\frac{r\gamma\cos\theta}{2\eta}} \tag{9}$$

where φ is the porosity of materials; ρ is the fluid density, kg/m^3; r is the capillary radius, m; γ is the surface tension of the water phase, N/m; θ is the contact angle, ^{o}; η is the viscosity coefficient of liquid, (N·s)/m^2.

According to the experimental results, the A_{cap} of salt bricks was smaller than that of salt free bricks, illustrating the salt in the sintered blue bricks has a certain hindrance to the capillary migration of water. In our experiments, some pores in brick samples were filled with salt after soaking in salt solution and drying. As a result, the porosity of materials decreased. On the other hand, with increases of the salt content, the viscosity of the solution increases. According to the Eq. (9), the A_{cap} has a positive correlation with the porosity and has a negative correlation with the viscosity coefficient. Consequently, the A_{cap} of sintered blue bricks decreased as the salt content increased.

The capillary moisture content is the total mass of water absorbed in the first stage of capillary absorption process. In salt-immersed sintered bricks, during the capillary adsorption, some salt dissolved into water and migrated with water, while others remained in the pores because the first stage of capillary absorption process was very fast . In addition, the salt in bricks may reduce the number of open pores, resulting in the inability of water to enter the pores. Therefore, the total water absorption in the first stage decreased with the increase of salt content in bricks.

The moisture diffusivity is not just a transport property but it includes the effect of moisture capacity. Based on the results in Section 3.3, although the A_{cap} of sintered blue bricks decreased with the increasing salt content of bricks, the moisture diffusivity still increases in almost the whole moisture range, especially in high moisture content range. These results are mainly attributed to the effect of salt on microscopic porous structure of bricks, which still need further discussion.

5 CONCLUSION

In this study, the capillary absorption coefficient (A_{cap}) and capillary moisture content (w_{cap}) of sintered blue bricks were measured by the capillary absorption experiment, and moisture diffusivity (D_l) was determined using ruler method. The results were compared with 0%, 1%, 5% and 10% sodium chloride (NaCl) solution to analyze the effect of salt on mechanism of moisture transport of sintered blue bricks. The conclusions are as follows:

(1) With the increase of NaCl content of bricks, the capillary absorption coefficient (A_{cap}) decreased probably due to the decrease of the porosity and the increase of

the viscosity. The average A_{cap} of sintered blue bricks with 10% NaCl was 18% lower than that of salt free bricks.

(2) The presence of salt in bricks decreased the capillary moisture content (w_{cap}) and the w_{cap} decreased with the increase of salt content of bricks. This is because undissolved salt occupied part of the pores, resulting in the decrease of water absorption. The average w_{cap} of brick samples with 10% NaCl was 8.6% smaller than that of salt free bricks.

(3) The moisture diffusivity of bricks with the same water content increases as the salt content of sintered blue bricks increases, especially in high moisture content range. The further research will be carried out from the perspective of the influence of salt on microscopic pore structure.

ACKNOWLEDGEMENTS

This work was supported by the National Natural Science Foundation of China under grant number 5210081745.

REFERENCES

[1] D. D Ayala and Y. D. Aktas, "Corrigendum to "Moisture dynamics in the masonry fabric of historic buildings subjected to wind-driven rain and flooding" [BAE 104C (2016) 208–220]," *Building and Environment*, vol. 108, p. 295, 2016.

[2] Y. Li, Y. Ma, H. Xie, J. Li, and X. Li, "Cross validation of hygrothermal properties of historical Chinese blue bricks with isothermal sorption experiments," *Frontiers of Architectural Research*, vol. 10, pp. 164-175, 2021.

[3] N. Takatori, K. Sakai, D. Ogura, S. Wakiya, and M. Abuku, “Measurement of sodium chloride solution permeability and sorptivity in tuff stone,” in *Proceedings of SWBSS 2021* (*Fifth International Conference on Salt Weathering of Buildings and Stone Sculptures*), pp. 163–171, 2021.

[4] M. Seredyński, M. Wasik, P. Łapka, P. Furmański, Ł. Cieślikiewicz, K. Pietrak, M. Kubiś, T. S. Wiśniewski, and M. Jaworski, "Analysis of Non-Equilibrium and Equilibrium Models of Heat and Moisture Transfer in a Wet Porous Building Material," *Energies*, vol. 13, p. 214, 2020-01-02 2020.

[5] C. Evangelides, G. Arampatzis, A. Tsambali, E. Tzanetaki, and C. Tzimopoulos, "Moisture estimation in building materials with a simple procedure," *Construction and Building Materials*, vol. 164, pp. 830-836, 2018.

[6] M. Záleská, M. Pavlíková, Z. Pavlík, T. Simos, and C. Tsitouras, "Liquid moisture diffusivity of environmentally exposed plasters accessed by inverse analysis," *AIP Conference Proceedings*, vol. 1863, 2017-01-01 2017.

[7] L. Yang, D. Gao, Y. Zhang, J. Tang, and Y. Li, "Relationship between sorptivity and capillary coefficient for water absorption of cement-based materials: theory analysis and experiment," *R Soc Open Sci*, vol. 6, p. 190112, 2019-06-01 2019.

[8] H. Zhao, X. Wu, Y. Huang, P. Zhang, Q. Tian, and J. Liu, "Investigation of moisture transport in cement-based materials using low-field nuclear magnetic resonance imaging," *Magazine of Concrete Research*, vol. 73, pp. 252-270, 2021.

[9] Z. Pavlík, M. Jiřičková, R. Černý, H. Sobczuk, and Z. Suchorab, "Determination of Moisture Diffusivity using the Time Domain Reflectometry (TDR) Method," *Journal of Building Physics*, vol. 30, pp. 59-70, 2006.

[10] M. Bianchi Janetti, "Moisture Absorption in Capillary Active Materials: Analytical Solution for a Multiple Step Diffusivity Function," *Transport in Porous Media*, vol. 125, pp. 633-645, 2018.

[11] C. Evangelides, G. Arampatzis and C. Tzimopoulos, "Estimation of Soil Moisture Profile and Diffusivity Using Simple Laboratory Procedures," *Soil Science*, vol. 175, pp. 118-127, 2010.

[12] H. M. Kunzel, "Simultaneous Heat and Moisture Transport in Building Components," *IRB Verlag, Stuttgart*, 1995.

[13] O. Koronthalyova, M. Holubek, A. Trnik, J. Avsec, and I. Medved, "Effect of particular material parameters on wetting process of capillary-porous material," *AIP Conference Proceedings*, vol. 1866, 2017-01-01 2017.

[14] J. Kočí, J. Maděra, M. Jerman, and R. Černý, "Experimental Determination of Heat and Moisture Transport Properties of AAC in the Range of Subzero to Room Temperatures," *International Journal of Thermophysics*, vol. 40, 2019.

[15] Y. Zhao, Y. Wu, C. Dong, S. Han, D. Elsworth, and L. He, "Hydraulic characterization and modeling of water diffusivity through direct neutron radiography measurement on unsaturated cracked sandstone," *International Journal of Heat and Mass Transfer*, vol. 196, p. 123256, 2022.

[16] P. Ren, C. Feng and H. Janssen, "Hygric properties of porous building materials (V): Comparison of different methods to determine moisture diffusivity," *Building and Environment*, vol. 164, p. 106344, 2019.

[17] C. Feng, H. Janssen, Y. Feng, and Q. Meng, "Hygric properties of porous building materials: Analysis of measurement repeatability and reproducibility," *Building and Environment*, vol. 85, pp. 160-172, 2015.

[18] Q. Jia, W. Chen, Y. Tong, and Q. Guo, "Experimental Study on Capillary Migration of Water and Salt in Wall Painting Plaster A Case Study at Mogao Grottoes, China," *International journal of architectural heritage*, vol. 16, pp. 705-716, 2022-01-01 2022.

[19] M. Bianchi Janetti, T. A. Carrubba, F. Ochs, and W. Feist, "Heat flux measurements for determination of the liquid water diffusivity in capillary active materials," *International Journal of Heat and Mass Transfer*, vol. 97, pp. 954-963, 2016.

EXPERIMENTAL STUDY ON THE CAPILLARY ABSORPTION OF CHINESE BLUE BRICKS TO DIFFERENT CONCENTRATIONS OF NACL SOLUTIONS

Fan Wu[1], Huarong Xie[1], Nobumitsu Takatori[2], Daisuke Ogura[2], Shuichi Hokoi[3], and Yonghui Li[1*]

KEYWORDS

Sintered brick, Water absorption coefficient by capillary, concentration of salt solution

ABSTRACT

Sintered blue brick is one of the commonly used materials in traditional Chinese buildings. The ubiquitous salt in environment enters the brick in the form of salt solution through water absorption by capillary, the crystallization and dissolution of salt inside of brick will lead to the salt damage. In order to study the relationship between the rate of liquid transfer in brick and the concentration of salt solution, two kinds of sintered bricks were used for capillary water absorption experiments under 0% to 10% NaCl solution respectively, and the influence of salt solution concentration on water absorption coefficient by capillary (A_{cap}, $kg/(m^2 \cdot s^{0.5})$) were compared. The experiment result shows that, With the increase of NaCl solution concentration from 1% to 10%, the A_{cap} of the two kinds of bricks increased first and then decreased. Compared with pure water, the bricks have a higher A_{cap} for low concentration (1%) solution, while for the relatively high concentration (10%), the A_{cap} will reduce to the same or slight lower level than that of pure water. However, the effect of salt solution concentration on capillary moisture content of brick is not obvious.

[1] School of Architecture, Southeast University, Nanjing, China, liyonghui@seu.edu.cn

[2] Department of Architecture and Architectural Engineering, Graduate School of Engineering, Kyoto University, Kyoto, Japan

[3] Architecture Internalization Demonstration School, Southeast University, Nanjing, China

1 INTRODUCTION

The migration and phase change process of soluble salts in porous building materials is one of the main factors contributing to the deterioration of masonry building materials. Generally, the ubiquitous salt in the environment enters the brick or stone in the forms of capillary moisture absorption after being dissolved in water, while the salt generates crystallization and deliquescence of salt inside and on the surface of the brick or stone. This process will generate the pressure change which exceeds the strength of most bricks, and the pore structure inside and on the surface of the material will be destroyed, thus leading to the deterioration of brick or stone [1]. Chinese blue bricks are porous building materials made from sintered clay, as the complete reduction of iron is inhibited by the addition of water during the sintering process, thus giving them a blue color that distinguishes them from other countries bricks. Degradation caused by soluble salts in blue bricks is very common.

Water absorption coefficient by capillary (A_{cap}, kg/(m^2·s$^{0.5}$)) is an important index to evaluate the hydrophilicity of porous materials and the ability of water-carrying ions to enter the brick [2]. This coefficient is usually measured by capillary water absorption experiments, where the absorption rate in the first stage of the capillary moisture absorption process is the capillary moisture absorption coefficient, and the intersection of the first and second stages is the capillary moisture content(W_{cap}, kg/m^3)[3]. These parameters cannot be ignored when analyzing the transfer properties of water in porous materials [4].

Distilled water was often used in previous capillary water absorption experiment, which did not consider the fact that the water entered the brick in the form of salt solution. To our knowledge, few studies have paid attention on the difference in salt solution absorption rate in Chinese blue brick up to now. An experiment showed that mass fraction of 5% NaCl salt concentration had little effect on water absorption rate of sandstone (Kandla Grey Stone) [5], but other study on the stone indicated that the water absorption rate would linearly decrease with the increase of salt (Na_2SO_4) solution concentration [6].

Therefore, the capillary water absorption experiments under the different concentrations of salt solution for Chinese blue brick were carried out to clarify the relationship between the rate of salt solution entering brick and the concentration of salt solution.

2 MATERIAL AND METHOD

2.1 Material

The objects are two kinds of blue bricks commonly used in southeast of China, whose code names are LB and CB respectively. Both of these bricks were made into samples of 50*50*50mm. The porosity, density and major pore diameter of the two kinds of bricks are shown in the Table 1. It can be seen from the table that CB sample has higher porosity than LB sample while a smaller density and main pore diameter. It can be seen from the table that there are obvious differences in the properties of the two bricks, so it is convenient to compare the experimental results.

Table 1: General information.

	Porosity	Density (g/cm^3)	Main pore diameter (μm)
LB	25.95%	2.02	5-10
CB	31.25%	1.80	0.5-2

Pure water and 1%, 2%, 4%, 5% and 10% (mass fraction) NaCl solutions were used for capillary water absorption experiments. By comparing the experimental results, the relationship between the rate of salt solution entering brick and the concentration of salt solution was studied.

2.2 Methods

2.2.1 Basic theory

Capillary water absorption experiment can be used to standardize the absorption capacity of porous materials to liquid water and as an indicator of liquid transport performance. The experiments were completed according to ISO 15148:2002 standard [3].

In this experiment, the properties of water absorption of porous materials is usually expressed by water absorption coefficient by capillary (A_{cap}, $kg/(m^2 \cdot s^{0.5})$), which is defined as:

$$A_{cap} = \frac{\Delta M}{A\sqrt{t}} \tag{1}$$

Where, A is the bottom area of the specimen in contact with water, m^2; t is time, s; ΔM refers to the moisture mass absorbed by the specimen at time t, kg. In the capillary water absorption experiment, the slope of the linear fitting line in the first stage is the water absorption coefficient by capillary (A_{cap}).

The moisture storage capacity of porous building materials is often expressed as capillary moisture content (W_{cap}， kg/m^3). Through linear fitting of the first and second stages of the experiment, the longitudinal coordinate of the intersection of the first and second stages of the fitting line ($\Delta M/A$, kg/m^2) is obtained, and the value is divided by the height of the specimen (h, m), can be expressed as:

$$w_{cap} = \frac{1}{h} \cdot \frac{\Delta M}{A} \tag{2}$$

As shown in Table 2, the density of different solutions was different, so the actual volume of solution absorbed by the specimen was different, which named as the capillary moisture volume (V_{cap}, m^3/m^3), was calculated by dividing the capillary moisture content (W_{cap}) by the corresponding solution density (ρ, kg/m^3), can be expressed as:

$$v_{cap} = \frac{w_{cap}}{\rho} \tag{3}$$

Table 2: Density of different solutions (the data were obtained at 15℃).

	Pure water	1% NaCl	2% NaCl	4% NaCl	5% NaCl	10% NaCl
Density (kg/m^3)	998.23	1005	1012	1027	1034	1071

2.2.2 Capillary moisture absorption experiment

In order to eliminate the influence of the salt of the brick itself, the brick was desalted before the experiment. The desalination method is as follows: the specimen was soaked in distilled water in 15 (±2) ℃ and 50 (±2) % relative humidity, the soaking solution was changed every 24 hours, and the electrical conductivity of the soaking solution was tested. When the conductivity of the three consecutive soaking solution decreased to 100-200μs/cm, the salt removal in the brick was considered to be complete.

Figure.1 shows the schematic of experimental equipment. The experiment was conducted at a temperature of 15 (±2) ℃ and relative humidity of 50 (±2) %. The five sides of the specimen except the test surface (which is the bottom) were wrapped to prevent the influence of water evaporation on the accuracy of the experiment, meanwhile, the four sides were set aside a gap 10mm near the bottom to prevent the liquid from rising along the gap. A certain number of exhaust holes were set aside on the upper surface of the specimen to balance the air pressure. The water in the tank will be about 5mm above the underside of the brick to ensure continuous water absorption.

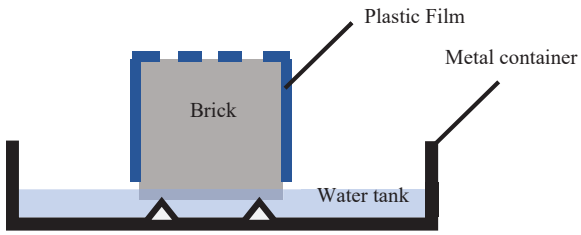

Figure 1: The bottom of specimen is located below the water and is wrapped with plastic film.

Five specimens were used in each group of experiments at the same time, and the average value of the five specimen was used to eliminate errors caused by individual differences. Before the formal experiment, two repeat experiments were carried out, and the repeated error was less than 5%.

3 RESULT AND DISCUSSION

The experimental results of two kinds of bricks under the action of pure water (0%NaCl solution) are shown in Figure 2. It can be seen that for the pure water, the experimental data of both kinds of bricks showed obvious changes in the first stage and the second stage, which was is consistent with the experimental results in ISO

15148:2002. The experimental results of salt solution with other concentrations are also consistent with the expected experimental results.

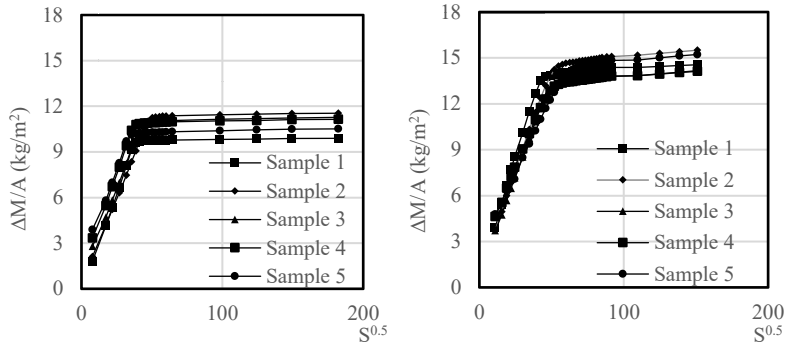

Figure 2: The experiment result of two kinds of bricks on pure water (left is LB and right is CB).

3.1 Experiment result of LB

Figure 3 shows the results of capillary water absorption experiment of LB under the action of salt solutions with 6 concentrations. From left to right are water absorption coefficient by capillary (A_{cap}), capillary moisture content (W_{cap}) and capillary moisture volume (V_{cap}) respectively.

Figure 3 shows that the A_{cap} for NaCl solutions in range of 1% to 10% is great than that in pure water. With the increase of concentration of salt solution, the A_{cap} decline after rising first. When the concentration of solution is 1%, the A_{cap} increased to 0.306 kg/(m^2·s$^{0.5}$), increased by 20.31% compared with pure water. With the further increase of solution concentration, the A_{cap} decreased obviously. When the concentration of solution is 10%, the A_{cap} decreased to 0.256 kg/(m^2·s$^{0.5}$), almost recovered to the level of pure water.

The change of the W_{cap} of LB showed no explicit correlation with the change of solution concentration, but the actual absorbed volume of the solution V_{cap} decreased with the increase of the solution concentration. When the solution concentration is 10%, the V_{cap} decreases by 7.11% compared with that of the pure water.

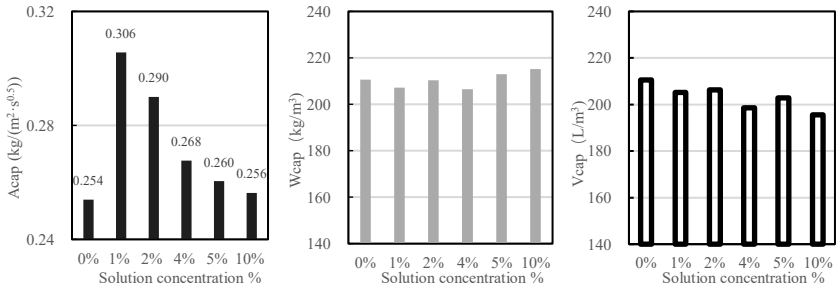

Figure 3: The results of capillary water absorption experiment of LB, from left to right: water absorption coefficient by capillary (A_{cap}), capillary moisture content (W_{cap}) and capillary moisture volume (V_{cap}).

3.2 Experiment result of CB

Figure 4 shows the results of capillary water absorption experiment of CB under the action of 6 concentrations of salt solutions.

The A_{cap} of CB also showed a trend of decline after rising first with the increase of solution concentration, which was similar to that of LB, and the maximum was also observed at a solution concentration of 1%. However, different to LB, the A_{cap} for NaCl solutions in range of 1% to 10% is not all greater than that for pure water. It is smaller than that for pure water when the concentration of NaCl solution greater than 5%. The A_{cap} at 1% NaCl solution is 0.250 kg/(m^2·s$^{0.5}$), only increases by 4.18% compared with pure water, and when the solution concentration increases to 10%, the A_{cap} is 0.223 kg/(m^2·s$^{0.5}$) and decreases by 7.16% compared pure water.

The W_{cap} of CB showed a trend of slight increase with the increase of solution concentration. When the solution concentration was 10%, the value of W_{cap} increased by 4.66% compared with pure water. The trend of V_{cap}, of CB is similar to LB, showing a decreasing trend with the increase of solution concentration. When the solution concentration increases to 10%, the V_{cap} decreases by 4.86% compared with pure water.

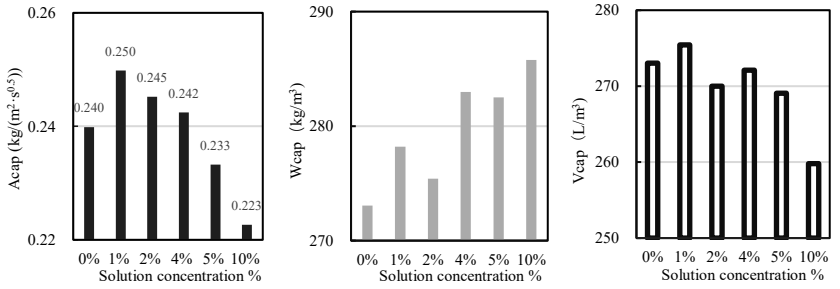

Figure 4: The results of capillary water absorption experiment of CB, from left to right: water absorption coefficient by capillary (A_{cap}), capillary moisture content (W_{cap}) and capillary moisture volume (V_{cap}).

3.3 Discussion

CB and LB bricks showed similar results in the experiment that with the increase of solution concentration, the A_{cap} firstly increased and then decreased, and the A_{cap} reached the maximum at a solution concentration of 1%. When the solution concentration further rises to 5%-10%, the A_{cap} of the two kinds of bricks decrease to the same or lower than that of pure water.

Pan et al. (2017) conducted capillary water absorption experiments with pure water, 3.5% and 26.3% (mass fraction) NaCl solutions respectively on sintered ceramic pieces, and the results were similar to those in this study, which is the low concentration of NaCl solution (3.5%) will increase the A_{cap} of materials, while high concentration of NaCl solution (26.3%) will reduce the A_{cap} of materials. They believed the results are related to the change of the properties of the solution [7]. Takatori et al. (2021) conduct capillary water absorption experiments on pure water and

0.61mol/L NaCl solution (mass fraction 3.5%) for tuff stone. It showed that compared with pure water, 3.5% NaCl solution will increase the A_{cap} of materials by about 20% [8].

The movement of water in pores is characterized by small flow channels and slow movement, which is similar to laminar flow in fluid mechanics and can approximately satisfy the Hagen - Poiseuille law [9] [10]. Therefore, the pores of brick are simplified into circular tubes with various distribution. A_{cap} can be expressed as:

$$A_{cap} = \varphi\rho\sqrt{\frac{\gamma \cdot r \cdot \cos\theta}{2\mu}} \tag{4}$$

Where, φ is the porosity, ρ is the liquid density (kg/m^2), γ is the surface tension of the solution (N/m), r is the pore radius (m), θ is the contact angle, μ is the liquid viscosity (Pa·s).

The values of liquid density (ρ), surface tension of solution (γ) and liquid viscosity (μ) of the solution are obtained by referring to Chemical Physical Property Data Manual [11]. The pore radius(r) of the bricks were derived from the results of mercury injection experiment (test equipment: Micromeritics-Autopore 9505). The values of contact angles (θ) between bricks and NaCl solutions of different concentrations were derived from experimental results (test equipment: Dataphysics-OCA20).

Table 3 shows the relevant data of LB obtained through reference and experimental results and the results of A_{cap} obtained by calculation. The calculation results of the A_{cap} of LB show that A_{cap} decreases with the increase of solution concentration. It does not reproduce the experiment results of A_{cap} that shows a trend with decreasing after rising first. Table 4 shows the relevant data of CB. The calculation results show that the A_{cap} of CB also show a trend of increase with the increase of solution concentration, it declines only when the NaCl solution exceeds 5%. The trend does not correspond to our experimental results.

Table 3: Relevant data used for calculation of the A_{cap} of LB.

	ρ kg/m^3	γ mN/m	μ mPa • s	φ %	θ	r m	Calculation of A_{cap} kg/(m^2·s$^{0.5}$)
Pure water	998.23	72.8	1.005	25.95	28	6.55*10^{-7}	1.186
1%NaCl	1005	72.2	0.9954	25.95	36	6.55*10^{-7}	1.144
2%NaCl	1012	73.9	1.002	25.95	43	6.55*10^{-7}	1.104
4%NaCl	1027	74.4	1.019	25.95	58	6.55*10^{-7}	0.949
5%NaCl	1034	74.4	1.027	25.95	65	6.55*10^{-7}	0.850
10%NaCl	1071	75.7	1.103	25.95	61	6.55*10^{-7}	0.918

Table 4: Relevant data used for calculation of the A_{cap} of CB.

	ρ kg/m^3	γ mN/m	μ mPa • s	φ %	θ	r m	Calculation of A_{cap} kg/(m^2·s$^{0.5}$)
Pure water	998.23	72.8	1.005	31.25	19	1.98*10^{-7}	0.812
1%NaCl	1005	72.2	0.9954	31.25	20	1.98*10^{-7}	0.816
2%NaCl	1012	73.9	1.002	31.25	20	1.98*10^{-7}	0.828
4%NaCl	1027	74.4	1.019	31.25	21	1.98*10^{-7}	0.833
5%NaCl	1034	74.4	1.027	31.25	21	1.98*10^{-7}	0.835
10%NaCl	1071	75.7	1.103	31.25	26	1.98*10^{-7}	0.827

Takatori et al. (2021) proposed that equation 5 can also be used to estimate A_{cap} of the different concentration salt solution [8]:

$$A_{cap}(\mathrm{x}) = A_{cap}(0)\frac{\rho_{sl}}{\rho_0}\cdot\frac{\mu_0}{\mu_{sl}} \tag{5}$$

Where, $A_{cap}(\mathrm{x})$ and $A_{cap}(0)$ are the A_{cap} of different concentration of solutions and pure water on the bricks, ρ_{sl} and ρ_0 are the density of different concentration of solutions and pure water. μ_{sl} and μ_0 are the liquid viscosity of different concentration of solutions and pure water. If we normalize the pure water absorption coefficient $A_{cap}(0)$=1 kg/(m^2·s$^{0.5}$), then the A_{cap} of different concentration of solutions can be calculated according to the value of ρ and μ of different concentration of solutions [11]. The calculated result is shown in Figure 5. It shows a certain agreement with the experimental results, when the concentration of the solution is lower than 5%, the A_{cap} will increase, while when the concentration of the solution is greater than 5%, the A_{cap} will be lower than that of pure water.

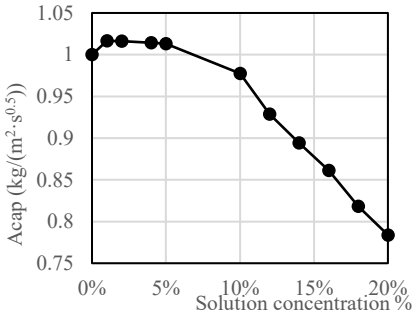

Figure 5: According to the equation 5, the value of A_{cap} changes with the increase of solution concentration.

The calculated results of equation 5 shows a relatively consistent trend with the experimental results. However, in this equation, the value of A_{cap} is only related to the density (ρ) and liquid viscosity (μ) of the solution, and the difference in the material properties, such as contact angles, is not taken into account. We think that is why there are still differences with the actual situation.

Takatori et al. (2021) also pointed out that the change of salt solution concentration may change surface electric charge of brick. The blue brick used in the experiment

contains clay, so the surfaces of the brick may carry electric charges. When it comes into contact with the salt solution, a double electric layer will be formed on the surface of the blue brick (including the pore surface). The electric potential of the double electric layer is higher than the potential energy of water molecules, so the solution cannot pass through the double electric layer. The thickness of the double electric layer is called the Debye length, and the Debye length under low concentration salt solution is much smaller than that under the action of pure water [12]. Therefore, under the low concentration salt solution, the water molecules could easily pass the double electric layer. This is thereby expressed macroscopically as an increase in the capillary moisture absorption rates [8].

By comparing the A_{cap} of LB and CB (Figure 6), it can be found that under the action of salt solution with the same concentration, the A_{cap} of LB is significantly higher than that of CB, with a maximum difference of 46.77% and an average difference of 19.07%.

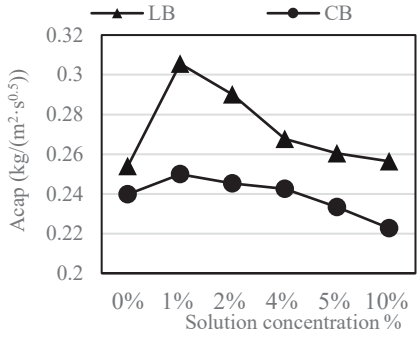

Figure 6: Comparison of A_{cap} of CB and LB, The A_{cap} of LB was significantly higher than CB.

The reason could be explained by that the pores of LB are smaller than that of CB, which was shown in Figure 7, and the smaller pores will generate greater capillary pressure which leads to the higher water absorption coefficient by capillary of sample.

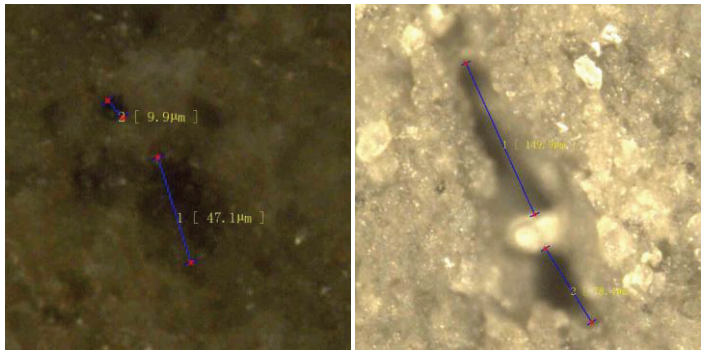

Figure 7: Micrographs of LB and CB surfaces, in which LB and CB have pore diameter of 9.9-47.1µm and 78.4-149.9µm, respectively.

When discussing capillary moisture content (W_{cap}), the W_{cap} of LB did not change significantly with the increase of solution concentration (Figure 3), while the W_{cap} of CB showed a slow increase trend with the increase of solution concentration (Figure 4). However, the capillary moisture volume (V_{cap}) of both bricks showed a decreasing trend with the increase of solution concentration. It shows that the change of solution concentration does not affect the absorbed mass (W_{cap}) of solution of the brick, but it does affect the absorbed volume (V_{cap}) of solution of the brick. Therefore, the moisture storage capacity of the brick, as one of its basic moisture properties, should be expressed in terms of absorbed mass of solution rather than absorbed volume.

4 CONCLUSION

In this paper, we compared the water absorption coefficient by capillary (A_{cap}), capillary moisture content (W_{cap}) and capillary moisture volume (V_{cap}) of two kinds of blue bricks under the action of salt solution with six kinds of concentrations. Through the discussion of the results, we can conclude that:

1. When the concentration of NaCl solution is below a certain concentration (around 5%), the water absorption coefficient by capillary of blue brick to NaCl solution is greater than to pure water. With the increase of solution concentration, the water absorption coefficient by capillary shows a trend of increasing and then decreasing, when the solution concentration is about 1%, it reaches the maximum. But after the NaCl solution exceeds a certain concentration (around 5%), the water absorption coefficient by capillary will be lower than that of pure water. Under the action of the same concentration of salt solution, the higher the proportion of small pore size, the higher the capillary water absorption rate of the brick.
2. The change of solution concentration has a limited effect on the capillary moisture content of blue brick, but has a significant effect on the capillary moisture volume of brick, indicating that the factor determining the moisture absorption of brick is the quality of solution rather than the volume.
3. Most of the existing relevant analysis do not consider the effect of the existing of salt, but the results of this experiment show that the existing of salt cannot be ignored.

REFERENCES

[1] Flatt, Robert J. “Salt damage in porous materials: how high supersaturations are generated.” *Journal of crystal growth,* vol.242.3-4, pp. 435-454, 2002.

[2] Sabir, B. B., S. Wild, and M. O'farrell. “A water sorptivity test for mortar and concrete.” *Materials and structures,* vol. 31, pp. 568-574, 1998.

[3] EN, “ISO 15148:2002, “Hygrothermal performance of building materials and products Determination of water absorption coefficient by partial immersion,” 2002.

[4] Carmeliet J, Hens H, Roels S, et al. "Determination of the liquid water diffusivity from transient moisture transfer experiments ". Journal of Thermal Envelope and Building Science, 27(4), pp. 277-305, 2004.

[5] Cnudde, Veerle, et al. "Multi-disciplinary characterization and monitoring of sandstone (Kandla Grey) under different external conditions." *Quarterly Journal of Engineering Geology and Hydrogeology,* vol. 46.1, pp. 95-106, 2013.

[6] Gonçalves, T. Diaz, et al. "Drying of porous building materials possibly contaminated with soluble salts: summary and findings of the DRYMASS research project." in *3rd International Conference on Salt Weathering of Buildings and Stone Sculptures Brussels*, 2014.

[7] Pan Zhenhao, Meng Qinglin, and Li Qiong, "Water Absorbing Characteristics of Porous Firing Clay Tiles in Saline Solutions," *Journal of Chongqing Jianzhu University* vol. 39, no. 6, pp. 117–122, 2017.

[8] N. Takatori, K. Sakai, D. Ogura, S. Wakiya, and M. Abuku, "Measurement of sodium chloride solution permeability and sorptivity in tuff stone," in *Proceedings of SWBSS 2021* (*Fifth International Conference on Salt Weathering of Buildings and Stone Sculptures*), pp. 163–171, 2021.

[9] Cao Feng, Wu Yu-qing, and Wang Ju-lin. "Capillary Water Absorption of Grey Bricks of Ming Dynasty Great Wall in Beijing and Its Influencing Factors." *Science Technology and Engineering*, vol.19(22), pp. 286–292. 2019.

[10] Leventis, A., et al. "Capillary imbibition and pore characterisation in cement pastes." *Transport in Porous Media*, vol.39, pp. 143-157, 2000.

[11] LIU, Guang-qi, Lian-xiang MA, and Jie LIU. "Handbook of substances properties data in chemical and engineering (inorganic Vol)," 2002.

[12] Israelachvili and Jacob N. *Intermolecular and Surface Forces,* Burlington, 2011

INVESTIGATIONS ON THE DAMAGE POTENTIAL OF SALTS PRECIPITATING FROM MIXED ELECTROLYTES

Amelie Stahlbuhk[1] and Michael Steiger[1]

KEYWORDS

Salt damage, mixed electrolytes, supersaturation

ABSTRACT

Crystallization of salts in porous building materials is one of the major threats to our cultural heritage, as the crystallization pressure can act on the pore walls during crystal growth from a supersaturated solution. For both single and mixed electrolytes, the climatic conditions for precipitation and deliquescence can be calculated using appropriate thermodynamic models, allowing, e.g., the formulation of a recommended climate to prevent critical cyclic crystallization events. However, thermodynamic calculations do not allow the determination or prediction of the damage potential of salts, which requires experimental investigations. In studies of some binary salt solutions, the critical supersaturation achieved by cooling or evaporation proved to be an adequate approach to assess the damage potential of salts. Taking into account that real objects are not contaminated with single salts but rather with complex salt mixtures, this study focuses on ternary and quaternary hygroscopic salt mixtures in the system Na^+–K^+–Cl^-–NO_3^-–H_2O, which is highly relevant for cultural heritage. Supersaturation by cooling was determined by calorimetric measurements, while microscopic investigations with filled glass capillaries were used for evaporation experiments. By comparing supersaturations detected for specific salts in binary and mixed electrolytes, the influence of accompanying ions and of the mixture composition on the damage potential was investigated.

[1] University of Hamburg, Department of Chemistry, Institute of Applied and Inorganic Chemistry, amelie.stahlbuhk@uni-hamburg,de

1 INTRODUCTION

Salt damage as a result of an effective crystallization pressure is one of the most relevant factors threatening our cultural heritage. Pressure is generated when salts precipitate from a supersaturated solution and grow against a constraint [1]. Different salt sources, such as groundwater, sea salt spray or conservative actions, cause the problem of salt-contaminated structures to be widespread [2,3]. Once enriched, climatic conditions determine whether crystallization from the saline pore solution or dissolution of crystalline salts by absorption of water vapor from the environment occurs – conditions leading to cyclic dissolution and crystallization are extremely critical, as they allow the crystallization pressure to act repeatedly.

In terms of the climatic conditions, each salt has a specific and temperature-dependent value of the relative humidity above which water vapor from the environment is taken up and a saturated solution is formed, called the deliquescence humidity DRH. Below the DRH, the crystalline salt is present, above the DHR an increasingly dilute solution. For salt mixtures, there is no such distinct value, as the ions in the mixture influence each other. In that case, the crystallization (or dissolution) of phases occurs in a relative humidity range limited by the mutual deliquescence humidity (MDRH, RH at which all salt is present in its crystalline form) and the critical crystallization humidity (RH at which the last crystalline phase dissolves completely) [4,5]. Crystallization pathways and critical values of relative humidity can be calculated for equilibrium conditions using appropriate thermodynamic models (e.g. [6]) that help to determine object-specific climatic conditions that prevent critical crystallization events. However, these calculations do not allow an assessment of the damage potential of the individual salts. In very practical terms, the damage potential of a salt is reflected in the extent of damage inflicted on the material during crystallization. Damage tests with salt-contaminated samples represent a method to investigate the damage extent and have been used, for example, to thoroughly investigate the high damage potential of sodium sulfate [7,8]. They provide essential information, e.g. on damage patterns, but the extent of damage in these experiments depends on various aspects (e.g., salt content, drying and impregnation conditions, material properties) [7], impeding a direct comparison of the salts.

Looking at the equation for the crystallization pressure Δp [1]

$$\Delta p = \frac{RT}{V_m} \cdot \ln S$$

(where R is the ideal gas constant, T is the absolute temperature in Kelvin, V_m is the molar volume of the salt and S is the supersaturation), it is obvious that the pressure is largely controlled by the supersaturation S:

$$S = \frac{a}{a_0}$$

which is the ratio of the actual solution activity a and the saturation activity a_0, describing the deviation from thermodynamic equilibrium. The numerical value of S directly influences the magnitude of Δp and is a prerequisite for pressure generation. Thus, the determination of S allows the assessment of the damage potential

of a salt as an alternative method to damage tests. Using the same detection methods and experimental conditions, a quantitative comparison of different salts or of the same salt in different mixed electrolytes is possible.

Crystallization is always preceded by some degree of supersaturation to overcome the kinetic barrier for nucleation and can therefore be observed in cooling and evaporation experiments [9]. In the latter, evaporation of a solution of initial molality m_{start} causes a concentration increase and crystallization starts at the crystallization molality m_{cry}, which is higher than the actual saturation molality m_{sat} at this temperature. Cooling of a solution with m_{start} and a corresponding saturation temperature T_{sat} leads to crystallization at a lower temperature T_{cry}. The solution molality does not change until the onset of crystallization. It should be noted that these methods yield the supersaturation present at the onset of crystallization (the critical S) and, therefore, only allow the calculation of a maximum crystallization pressure. For material damage, the relevant value is the pressure acting when the crystal has reached a size large enough to effectively grow against the pore wall. At this point, the supersaturation will be lower because it decreases during crystal growth [1,10,11]. Nevertheless, the higher the initial supersaturation the more likely is a high crystallization pressure.

The present study follows previous ones on the investigation of supersaturations in some binary solutions [12,13] and focuses on hygroscopic mixed solutions in the quaternary system Na^+–K^+–Cl^-–NO_3^-–H_2O, which is highly relevant for cultural heritage. The consideration of mixed electrolytes in these experiments is particularly important because in real objects an accumulation of ions may proceed over long periods of time, leading to more or less complex ion mixtures in the pores. The supersaturation is investigated by means of evaporation experiments with glass capillaries and calorimetric measurements.

2 MATERIALS AND METHODS

The salts NaCl, $NaNO_3$, KCl and KNO_3 (Carl Roth and Merck) of analytical grade quality (p.a.) were used without further purification. The solutions were prepared with doubly distilled water. Prior to the experiments, all solutions were filtered (0.45 µm pore size, Celtron 30, CAGF93, Whatman, GE Healthcare Life Sciences, UK) to exclude the effect of nuclei on the achievable supersaturation.

Calorimetric investigations were performed at a cooling rate of 0.05 $K \cdot min^{-1}$ using a Calvet-type differential scanning calorimeter (BT2.15, Setaram, France) with a resolution of 0.10 µW. The heat flow curves (peak onsets, maxima and offsets, T_{on}, T_{off}, T_{max} and signal integrals) were evaluated using the Calisto software (Setaram). As the crystallization from supercooled solutions was the focus of these experiments, heating scans were not included in the evaluation. For the calculation of S, T_{on} was used as the crystallization temperature, since this is the temperature at which the supersaturation starts to break down.

Evaporation experiments were performed with cylindrical glass capillaries with diameters of 0.40 and 0.75 mm, filled with the salt solutions. Images of the capillaries were taken every 30 minutes using an optical microscope with an adjustable stage (VHX 600D and VH-S30K, Keyence, Japan). The relative humidity and temperature were measured in vicinity of the stage. Mean values were 25.5±4.5 % and

21.3±0.6 °C for Na^+–K^+–NO_3^- and 22.4±16 % and 22.6±0.7 °C for Na^+–K^+–Cl^-–NO_3^- mixtures, respectively. The solution concentrations at the crystallization onset were determined from the initial length of the solution column with known starting molality and from its length in the last image without visible crystals. Solution densities required for the conversion between molality and volumetric concentrations were calculated with an existing volumetric Pitzer model [14].

The studies include mixtures of Na^+–K^+–NO_3^- and of Na^+–K^+–Cl^-–NO_3^-. They contained different ratios of Na^+:K^+ (for Na^+–K^+–NO_3^-) and NaCl:KNO_3 as well as Na^+:K^+ at equimolality of Cl^-:NO_3^- for Na^+–K^+–Cl^-–NO_3^- at a total molality m_{total}=4 mol·kg^{-1} (m_{total} being the sum of mixed salts). For the calorimetric investigations, equimolar mixtures with varying total molalities were also included, as the latter influences T_{cr}. For evaporation experiments, the initial total molality does not affect the achievable supersaturation. For comparison, cooling experiments with pure KNO_3 solutions were also performed.

The calculation of $S=a \cdot a_0^{-1}$ requires the calculation of activity coefficients and saturation concentrations. For this purpose, we used that same Pitzer model as in previous work [15].

3 RESULTS AND DISCUSSION

The critical supersaturation of pure KNO_3 solutions by cooling at a rate of 0.1 K·min^{-1} has been thoroughly investigated in a previous work [12]. However, solutions of different molalities were measured again at a rate of 0.05 K·min^{-1} to allow a better comparison with the results for the mixtures that were measured at the same low cooling rate in this study. Despite kinetic influences and a stochastic character of the process, a good reproducibility was observed in multiple determinations of pure KNO_3 solutions at a rate of 0.1 K·min^{-1} [12]. Although it cannot be excluded that such a good reproducibility would be obtained in mixed electrolytes, calorimetric measurements were only carried out in a single determination.

Investigations on the supersaturation of pure KNO_3, $NaNO_3$ and NaCl solutions during evaporation under similar conditions gave $S(KNO_3)$=1.56–1.77 [12], $S(NaNO_3)$=1.43–4.00 [13] and S(NaCl)=1.13–9.35 [13] and are used for comparison. Although, in previous studies, the capillary diameter had no effect on S in the considered size range [12,16], two different diameters were investigated also in this work. The performed evaporation experiments give an average S for the whole solution column. It was shown for the pure solutions that with the used set-up ion diffusion is fast enough to level out concentration gradients, leading to a homogeneous ion distribution and yielding a representative supersaturation at the onset of crystallization [12,13], which is also assumed for the mixed electrolytes in this work.

3.1 KNO_3 solutions

As shown in Figure 1a (black crosses), the supersaturation in pure KNO_3 solutions varied between 1.59 and 2.04 in the investigated concentration range. Even though the values show some scatter, there might be a tendency of increasing supersaturation with decreasing concentration, as was already found for KNO_3 solutions at a cooling rate of 0.1 K·min^{-1} [12].

3.2 Mixtures of Na^+–K^+–NO_3^-

In calorimetric measurements of mixtures prepared from $NaNO_3$ and KNO_3 all solutions were supersaturated with respect to KNO_3 (Figure 1a). For equimolar mixtures with different m_{total} it was found that $S(KNO_3)$ increases with decreasing molality as also observed for pure KNO_3 solutions. Compared to the latter, S is higher, especially at the lower molalities. For samples with different ratios of $NaNO_3$:KNO_3 and m_{total}=4 mol·kg^{-1}, the data do not show of a clear trend, though S could increase with a decreasing amount of KNO_3. This could imply that the presence of Na^+ inhibits KNO_3 precipitation during cooling. Since an increase in Na^+ ions correlates with a decrease in $m(KNO_3)$, it could also be an effect of the dilution with respect to KNO_3. For these measurements, $S(KNO_3)$ is lower than in pure KNO_3 solutions for $m(KNO_3)$=3 mol·kg^{-1} but it can also be higher or in the same range with decreasing KNO_3 contents.

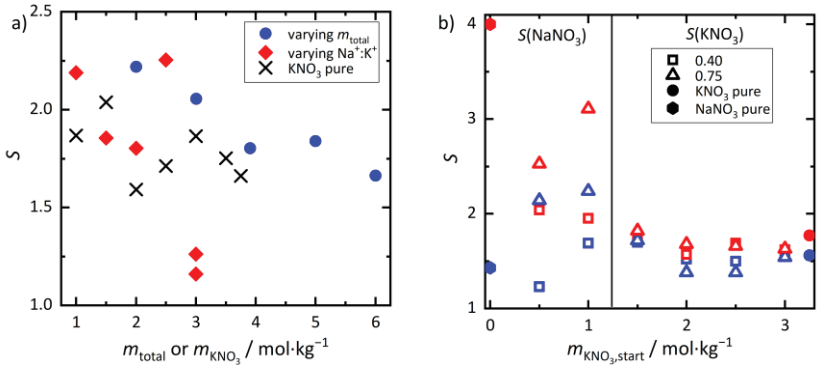

Figure 1: Supersaturations determined in a) calorimetric measurements with pure KNO_3 solutions and Na^+–K^+–NO_3^- mixtures (black crosses: pure KNO_3 solutions with different m_{KNO3}; blue circles: different m_{total} for equimolar mixtures of $NaNO_3$ and KNO_3; red diamonds: m_{total}=4 mol·kg^{-1} with variable m_{KNO3}) and b) evaporation experiments with Na^+–K^+–NO_3^- mixtures for different start m_{KNO3} in solutions with m_{total}=4 mol·kg^{-1} (numbers in the legend: diameter of the capillaries; blue and red symbols: minima and maxima detected in the experiments; comparative values determined for pure KNO_3 and $NaNO_3$ solutions are included [13]).

In evaporation experiments with solutions containing different $NaNO_3$:KNO_3 ratios, the highest supersaturation was observed for $NaNO_3$ or KNO_3 depending on the solution composition. For $m(KNO_3)\leq1$ mol·kg^{-1} the highest supersaturation was obtained with respect to $NaNO_3$ (Figure 1b, only the supersaturation of the phase that achieves the highest supersaturation in the solution is given, but the solution may be supersaturated with respect to more than one phase). Compared to the supersaturations detected in pure KNO_3 solutions [12], comparable values were obtained for the mixtures with $m(KNO_3)\geq2$ mol·kg^{-1}. A slight increase of S at $m(KNO_3)$=1.5 mol·kg^{-1} may imply that Na^+ ions only affect $S(KNO_3)$ when present in excess. In addition, it can be noted that the values obtained from multiple determinations are well reproducible, as already observed for pure KNO_3 solutions [12]. For mixtures containing $m(KNO_3)\leq1$ mol·kg^{-1}, a significant scatter of $S(NaNO_3)$ is

evident, as was also observed for pure $NaNO_3$ solutions [13]. It could be argued that the salt is more sensitive to the presence of nuclei or impurities favoring crystallization, while in fact it has a higher tendency to supersaturate than KNO_3. In the mixtures, $S(NaNO_3)$ may increase with an increasing amount of KNO_3, but all values were lower than the detected maximum in pure $NaNO_3$ solutions [13], suggesting that even small amounts of K^+ ions facilitate its crystallization upon evaporation. Overall, $S(KNO_3)$ and $S(NaNO_3)$ seem to increase with an increasing amount of the other salt in the mixture, or rather when a threshold of Na^+ ions is reached in case of KNO_3 precipitation.

3.3 Mixtures of Na^+–K^+–Cl^-–NO_3^-

Also for this salt system, all solutions were supersaturated with respect to KNO_3 in the calorimetric measurements (Figure 2a). For equimolar mixtures (blue dots) $S(KNO_3)$ seems to increase with increasing m_{total}, which is the opposite of what was found for Na^+–K^+–NO_3^- mixtures or pure KNO_3 solutions (Figure 1a), suggesting an effect of Cl^- ions in this mixture. In most cases, higher supersaturations were detected than in the system without Cl^- ions. For mixtures with m_{total}=4 mol·kg^{-1} and different NaCl:KNO_3 ratios (red diamonds in Figure 2a), S increases with decreasing amount of KNO_3, as observed in the ternary system. Thus, the same interpretation as above applies, with Cl^- ions amplifying the effect. In case of equimolality of Cl^- and NO_3^- ions, but changing Na^+:K^+ ratios (grey squares in Figure 2a), S increases significantly for $m(K^+)\leq$2 mol·kg^{-1}. Thus, the same interpretation as for different NaCl:KNO_3 ratios applies here. Mostly higher supersaturations than in pure KNO_3 solutions could be obtained in all measuring sequences. However, for the mixtures with varying m_{total} or NaCl:KNO_3 ratios, significant differences can only be observed for the highest m_{total} or the lowest KNO_3 contents, respectively.

In principle, the results obtained from capillary experiments with this salt system are similar to the results for the system without Cl^- ions. Again, only the supersaturation of the phase achieving the highest supersaturation is given, but it should be noted that the solution may be supersaturated with respect to more than one phase. For solutions prepared from different NaCl:KNO_3 ratios (Figure 2b, left), the highest S was calculated for KNO_3 for $m(KNO_3)\geq$1.5 mol·kg^{-1}. The values were barely different from $S(KNO_3)$ determined in binary solutions of this salt [12], but scatter increases with decreasing KNO_3 content. For S(NaCl), as for pure NaCl solutions [13,17], a drastic scatter can be observed, indicating again that this characteristic is maintained in the mixture (as already mentioned for $NaNO_3$ in the ternary system). Contrary to what was stated for $S(NaNO_3)$ in the ternary system, S(NaCl) seems to decrease with increasing KNO_3 content in the solution.

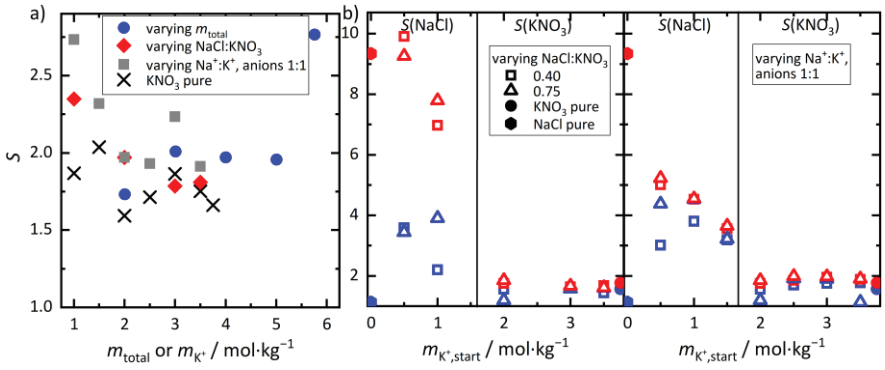

Fig. 2: Supersaturations determined in a) calorimetric measurements with pure KNO_3 solutions and Na^+–K^+–Cl^-–NO_3^- mixtures (crosses: pure KNO_3 solutions with different m_{KNO3}; circles: different m_{total} for equimolar mixtures of NaCl and KNO_3; diamonds: different m_{K+} at varying NaCl:KNO_3 ratio; squares: varying Na^+:K^+ ratio at equimolality of Cl^-:NO_3^- with m_{total}=4 mol·kg^{-1}) and b) evaporation experiments with different start m_{K+} at varying NaCl:KNO_3 ratio (left) and at varying Na^+:K^+ ratio at equimolality of Cl^-:NO_3^- with initially m_{total}=4 mol·kg^{-1} (right) (numbers in the legend: diameter of the capillaries; blue and red symbols:minima and maxima detected in the experiments; comparative values determined for pure KNO_3 and $NaNO_3$ solutions are included [13]).

In case of equimolality of the anions (Figure 2b, right), the highest supersaturations were obtained for KNO_3 up to $m(K^+)\geq 1.5$ mol·kg^{-1}. Again, $S(KNO_3)$ is comparable to values found in the binary solutions of KNO_3 [12], but scattering increases at 2 mol·kg^{-1}. S(NaCl) and its scatter range increase at lower K^+ ion contents, with the maximum values being smaller than in binary NaCl solutions, suggesting that S is generally smaller in case of an excess of Na^+ over Cl^- ions, and an increasing amount of K^+ ions facilitates NaCl precipitation. Compared to compositions with varying NaCl:KNO_3 ratios, S(NaCl) is smaller when Cl^- and NO_3^- ions are equimolar at the same K^+ ion content, indicating that NO_3^- ions are also an important factor in the reduction of S(NaCl).

3.4 Interpretation with regard to the damage potential

Table 1 summarizes the achievable supersaturations with respect to KNO_3 in the Na^+–K^+–NO_3^- and Na^+–K^+–Cl^-–NO_3^- mixtures as well as in binary solutions, showing an overlapping range for S by cooling and evaporation, while higher maximum values were determined in the mixtures by cooling and broader ranges of S resulted for the mixtures. For the latter, Cl^- ions seem to increase the achievable S. Thus, using S as a measure for the damage potential, for KNO_3 it may be higher upon cooling, but is comparable to that of the salt precipitating from its binary solution [12] in case of evaporation. However, a high damage potential, not negligible in terms of salt damage, has already been identified for the binary solutions [12].

Table 1: Supersaturations determined in cooling and evaporation experiments.

	pure KNO_3	Na^+–K^+–NO_3^-	Na^+–K^+–Cl^-–NO_3^-
$S(KNO_3)$ cooling	1.59–1.75	1.16–2.25	1.55–2.77
$S(KNO_3)$ evaporation	1.56–1.77 [12]	1.27–1.82	1.13 to 1.99

For $NaNO_3$ as the first precipitating salt in evaporation experiments with $m(KNO_3) \leq 1$ mol·kg^{-1} in Na^+–K^+–NO_3^- mixtures, the results imply a lower damage potential for mixtures compared to crystallization from its binary solution [13], reflected by lower critical supersaturations detected in the presence of K^+ ions. Almost the same applies to NaCl as the first precipitating phase from the quaternary system at low K^+ ion contents. Depending on the solution composition, the maximum critical supersaturation can be drastically reduced compared to pure NaCl solutions [13]. However, the critical supersaturations detected for the mixture compositions would be high enough to provoke a crystallization pressure exceeding the tensile strength of common building stones if pore fillings are sufficiently high.

Considering the pronounced scatter observed for NaCl and $NaNO_3$, and the suggestion that they are more sensitive to crystallization triggers, it should be noted that the supersaturation at the lower end of the range is much more relevant when discussing the damage potential, as nucleation sites in porous materials always provoke a reduction in the achievable S compared to bulk solutions. The latter also means that the supersaturations in real materials are generally not expected to be as high as those detected here in bulk solutions. However, the measurements allow an investigation of the dependencies and influences in mixed electrolyte solutions with respect to the maximum achievable S and, thus, represent an important step in the development of a better understanding of such solutions, which are more realistic considering salt-contaminated objects. Comparing experimental and realistic conditions, it has already been discussed that the crystallization temperatures in the cooling experiments are often unrealistic for structures [12] (in this work the lowest T_{cr} was –29.9 °C). Thus, the evaporation experiments seem to be more suitable for a realistic comparison, since the pore solution in an object is also concentrated by evaporation (also under non-constant temperature conditions, but less drastically than in the cooling experiment). Nevertheless, calorimetric investigations have some advantages (easy performance, perfectly controlled conditions) and are still a promising method to investigate the behavior of salts (and ice) in mixed electrolytes, provided that their heat of crystallization allows their detection. The main advantage, however, is the possibility of investigating salt solutions in porous host materials, which will be carried out in the near future for some of the mixtures.

4 CONCLUSIONS

The presented results provide very interesting insights into the behavior of salts precipitating from mixed solutions and their damage potential compared to the respective pure salts. Since the supersaturation allows the comparison of the damage potential of salts in different mixtures, it was shown that the damage potential of KNO_3 precipitating from Na^+–K^+–NO_3^- and Na^+–K^+–Cl^-–NO_3^- mixtures is at least as high as in its pure solutions. Crystallization of KNO_3 during evaporation of these mixtures does not result in an increased damage potential compared to precipitation

from its binary solutions. However, as in binary solutions, the supersaturation obtained would lead to crystallization pressures exceeding the tensile strength of common building materials. In contrast, the supersaturation with respect to NaCl and $NaNO_3$ can be reduced compared to their pure solutions, lowering their damage potential in the respective mixtures. Other interesting results were, e.g., that the supersaturations of the sodium salts also scatter in the mixtures (as observed for their binary solutions) and that for NaCl this range can be strongly reduced in mixtures, depending on the solution composition.

Building on important results for the individual salts, the study can provide essential information on the behavior of the salts in mixtures relevant to realistic salination situations. This work represents a further step towards a more realistic representation of the processes taking place in pores of real objects. As has already been shown for the individual salts, the methods represent an adequate approach to assess the damage potential. In a next step, corresponding mixtures will be investigated in porous materials by means of cooling calorimetry. In addition, further mixtures will be considered, and the investigation of supersaturation will be complemented by classical damage tests in order to determine whether they also reflect the tendency to a higher or lower damage potential of respective salts in mixtures.

5 ACKNOWLEDGEMENTS

The funding of this research by the German Research Foundation (DFG) is gratefully acknowledged.

6 REFERENCES

[1] M. Steiger, “Crystal growth in porous materials—I” J. Cryst. Growth, vol. 282, pp. 455–469, 2005.

[2] P. Mora, L. Mora, P. Philippot, Eds., Butterworths series in conservation and museology, Butterworths, 1984.

[3] A. Arnold, K. Zehnder, “Monitoring Wall Paintings Affected by Soluble Salts” in The Conservation of Wall Paintings. Proceedings of a Symposium Organized by the Courtauld Institute of Art and the Getty Conservation Institute, London, July 13-16, 1987, pp. 103–135, 1996.

[4] M. Steiger, A. E. Charola, K. Streflinger, “Weathering and Deterioration” in Stone in Architecture, pp. 225–316, 2014.

[5] C. A. Price, P. Brimblecombe, “Preventing salt damage in porous materials” in Preventive Conservation: Practice, Theory and Research, pp. 90–93, 1994.

[6] K. S. Pitzer, “Ion interaction approach: theory and data correlation” in Activity Coefficients in Electrolyte Solutions, pp. 75–153, 1991.

[7] B. Lubelli et al., “Towards a more effective and reliable salt crystallization test for porous building materials: state of the art,” Mater. Struct., vol. 51, 2018.

[8] R. Flatt et al., “Predicting salt damage in practice – A theoretical insight into laboratory tests“, RILEM Tech. Lett., vol. 2, pp. 108-118, 2017.

[9] J. W. Mullin, Crystallization, 4th ed. Butterworth-Heinemann, 2001.

[10] A. Naillon et al., "Evaporation with Sodium Chloride Crystallization in a Capillary Tube" J. Cryst. Growth, vol. 422, pp. 52–61, 2015.

[11] A. Naillon, P. Joseph, M. Prat, "Ion Transport and Precipitation Kinetics as Key Aspects of Stress Generation on Pore Walls Induced by Salt Crystallization" Phys. Rev. Lett., vol. 120, 2018.

[12] A. Stahlbuhk, M. Steiger, „Damage potential and supersaturation of KNO3 and its relevance in the field of salt damage to porous building material" Constr. Build. Mater., vol. 325, 2021.

[13] A. Stahlbuhk, Dissertation, University of Hamburg, 2021.

[14] M. Steiger, "Total volumes of crystalline solids and salt solutions" in Studies / European Commission / Community Research, Vol. 11, pp. 53–63, 2000.

[15] M. Steiger, J. Kiekbusch, A. Nicolai, „An improved model incorporating Pitzer's equations for calculation of thermodynamic properties of pore solutions implemented into an efficient program code" Const. Build. Mater., vol. 22, pp. 1841–1850, 2008.

[16] J. Desarnaud et al., "Metastability Limit for the Nucleation of NaCl Crystals in Confinement" J. Phys. Chem. Lett., vol. 5, pp. 890–895, 2014.

[17] Y. Shen, K. Linnow, M. Steiger, "Crystallization behavior and damage potential of Na_2SO_4–NaCl mixtures in porous building materials" Cryst. Growth Des., vol. 20, pp. 5974–5985, 2020.

MEASURING THE AMOUNT OF ACCUMULATED SALT ON THE SURFACE OF POROUS MATERIALS USING X-RAY FLUORESCENCE

Kotaro Sakai[1], Nobumitsu Takatori[1], Soichiro Wakiya[2], and Daisuke Ogura[1]

KEYWORDS

Saline water absorption, Salt concentration, Calibration curve, Tuff, Sodium chloride solution

ABSTRACT

Techniques for measuring salt concentration in porous materials are an important concern in cultural property conservation, where there is a risk of salt weathering, because they help predict salt crystallization. However, conventional measurement methods, such as electrical conductivity (EC) sensors and nuclear magnetic resonance (NMR), may not suitable for cultural properties because the former involves the destruction of materials and the latter is difficult to implement in on-site measurements. Thus, this study focused on a method using X-ray fluorescence (XRF), which is expected to be nondestructive and applicable in the field. In this study, we conducted experiments using an XRF analyzer to measure the concentration of accumulated salt on the surface of porous materials over time and examine the method's applicability. At first, we performed XRF analysis on tuff surfaces impregnated with several NaCl concentrations to confirm a proportional relation between the XRF intensity of Cl and salt concentration. Next, we compared the XRF intensities of Cl on different thicknesses of tuff surfaces impregnated with NaCl solution to determine the depth which can reached by XRF for the tuff. Finally, salt was accumulated on the tuff surface (by absorbing NaCl solution from the bottom of the tuff and evaporating the water from the top), and the change in salt concentration near the evaporation surface during this process was measured using XRF analysis. Analysis results showed that the salt concentration near the tuff surface could not be measured well using XRF if salt precipitated at the surface, and that salt precipitation was uneven, suggesting that tuff may vary in salinity by part or that even if the salinity is uniform, ease of salt precipitation is different.

[1] Department of Architecture and Architectural Engineering, Graduate School of Engineering, Kyoto University, Kyoto Daigaku-katsura, Nishikyo-ku Kyoto, Japan, sakai.kotaro.67n@st.kyoto-u.ac.jp

[2] National Institutes for Cultural Heritage Nara National Research Institute for Cultural Properties, 2-9-1 Nijo-cho, Nara-shi, Japan.

1 INTRODUCTION

Measuring the amount of accumulated salt in a material is crucial in the field of cultural property conservation, where there is a risk of salt weathering, because it can confirm and predict salt precipitation. Such methods in the field include sampling using drilling [1, 2], inserting electrical conductivity (EC) sensors into the wall surface to measure electrical conductivity [3], and collecting salt from the material with a poultice [4]. However, these methods involve being in contact with or destroying the material and are unsuitable for cultural properties or for understanding changes in salt concentration over time. While nuclear magnetic resonance (NMR) [5, 6] is a noncontact and nondestructive method of measuring salt concentration in materials, it is inappropriate for on-site measurement because NMR equipment is large size and can only measure relatively small, portable objects.

Meanwhile, energy-dispersive X-ray fluorescence (XRF) analyzers are capable of noncontact and nondestructive elemental analysis of liquid samples and solid samples. Soil studies have suggested the possibility of using a portable XRF to measure salt concentration in soil [7] and also expected its applicability as a method for measuring salt concentration in materials in the field. Moreover, an XRF analyzer has been used to measure the content of elements that constitute salt in porous materials such as concrete and limestone [8, 9, 10]. However, these measurements target salt crystals in materials; only a few examples exist of measurements of solutions in materials. Therefore, it is unclear whether a method that uses XRF can measure the concentration of salt solutions held as capillary condensates in porous materials.

This study aims to develop a nondestructive technique for measuring the concentration of salt in solution accumulating in materials in cultural property conservation. As a first step, the amount of accumulated salt in solution on porous material surfaces was measured using an XRF analyzer and the applicability of this method was examined. This study followed three steps. First, XRF analysis was performed on tuff surfaces impregnated with several concentrations of NaCl solutions to generate calibration curves of the XRF intensity of the Cl element and salinity. Next, the XRF intensities of the Cl elements on different thicknesses of tuff surfaces impregnated with NaCl solution were compared to determine the depth of XRF measurement. Finally, an XRF analyzer was used to measure how salt accumulating near the surface changed over time by absorbing the NaCl solution from the lower surface and evaporating water from the upper surface.

2 MATERIALS AND METHODS

This study conducted three experiments to measure the amount of accumulated salt on the surface of porous materials using an XRF analyzer.

2.1 Materials and Preparation

All experiments used porous tuff stone (Aso pyroclastic-flow deposits in Japan [11]). This tuff was collected near the site where salt weathering was observed. The reason for using this tuff is that the goal of this study is to measure the salt concentration of the solution in the material using XRF in the field. The specimens were immersed in pure water for about a week, and dried at 105°C for about a day.

2.2 Apparatus

An energy-dispersive XRF analyzer (M6 JETSTREAM (BRUKER)) was used in the experiments (Figure 1). This device can measure XRF on the object surface in two dimensions and quantitatively analyze XRF spectra to examine the types of elements and their concentration distribution on the surface. Rhodium (Rh) target has been used to generate XRF, the tube voltage was 15 kV, the tube current was 300 μA, the X-ray spot size was 580 μm, and the measurement atmosphere was atmospheric. The detection intensity of the quantitative elements was obtained by averaging the count values of elements within a manually defined region in the two-dimensional analysis results.

Figure 1: M6 JETSTREAM energy-dispersive XRF analyzer.

2.3 Methods and Measurement Conditions

In all the experiments, the room temperature was set to 23°C, controlled by an air conditioner.

Experiment 1

Using the XRF analyzer, we measured the XRF intensity of the Cl element of tuff surfaces impregnated with several concentrations of NaCl solutions to determine the relation between the concentration of the impregnated NaCl solution and the XRF intensity of Cl. We created a calibration curve for this relation based on the results. The test specimen was a 2 cm cubic tuff. The experimental procedure was as follows: first, the XRF analyzer was used to measure the surface of the dry specimen, and then the same specimen was impregnated with NaCl solution for about half a minute; and after about 30 minutes, the surface of the specimen was measured using the XRF analyzer. Figure 2 shows an actual image of the measurement.

Fifteen different concentrations (from pure water to a saturated solution (6.15 mol/kg)) of NaCl solutions were used.

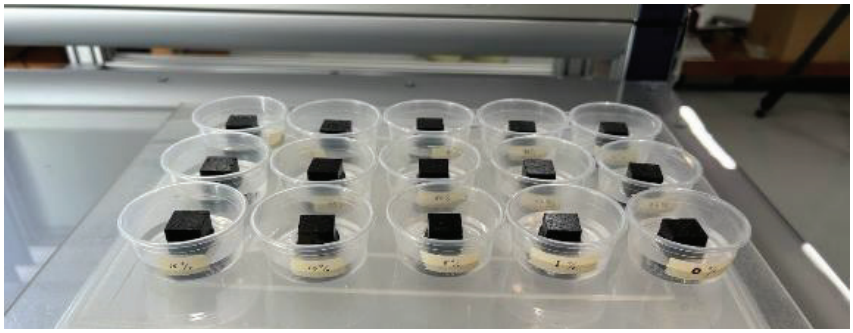

Figure 2: Measurement of XRF intensity at different salt concentrations.

Experiment 2

Since there is a limit to the depth at which the XRF generated from the sample can be detected and because the depth varies with the type of material and target element, the depth which can reached by XRF must be determined for the specific material/element combination. Therefore, we impregnated tuff specimens of different thicknesses with NaCl solutions and compared the detection intensity of Cl. About 5-10 minutes after impregnation in the solution, measurement of the specimens was started using the XRF analyzer, and the time required to measure each specimen was about 5 minutes. The test specimens were tuffs with 2 x 2 cm base and eight different heights (1.7 mm, 2.85 mm, 3.2 mm, 5.0 mm, 6.1 mm, 8.2 mm, 10.0 mm, 14.4 mm). The NaCl concentration was 0.615 mol/kg.

Experiment 3

Salt was accumulated on the tuff surface by absorbing the NaCl solution from the bottom surface and leaving the top surface open to the atmosphere. During this process, the XRF intensity of the Cl element on the tuff evaporation surface was measured using the XRF analyzer, and the change in accumulated salt content near the surface of the material over time was determined using the calibration curve.

Figure 3 shows the experimental setup. The specimen was a cylindrical tuff 5.1 cm in diameter and 10 cm high. Four specimens were used in the experiment and the sides of all specimens were moisture-proof with paraffin. One of these specimens used as a reference for surface and solution temperature measurements. The NaCl concentration was 0.0615 mol/kg.

First, a water tank was filled with NaCl solution, and the bottom surface of the specimen was immersed in the solution up to about 10 mm. The test specimen was allowed to absorb the solution and was left for two weeks with only the top, evaporation surface open to the atmosphere. During this process, XRF measurements of the top surface of the tuff were performed at approximately 24 h intervals. We also calculated the evaporation rate by measuring weight change of the specimen using a digital scale.

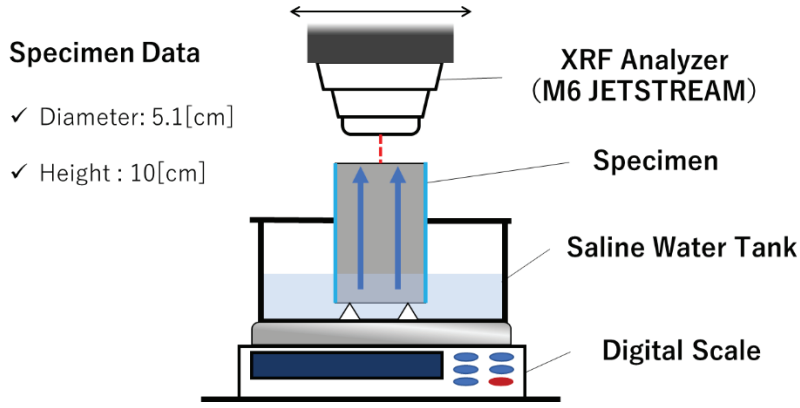

Figure 3: Schematic of experiment 3.

3 RESULTS

Figure 4 shows the results of the two-dimensional analysis of Cl using the XRF analyzer on the surface of the specimens impregnated with NaCl solution in experiment 1. These show that the detection intensity of Cl on tuff surfaces becomes stronger with increasing NaCl concentration.

Figure 5, which shows the detection intensity of Cl for each salt concentration on the tuff surface, confirms a proportional relation between the Cl detection intensity of tuff surfaces impregnated with NaCl solution and the salt concentration in the NaCl solution. Based on these results, we created a calibration curve for the concentration of the impregnated NaCl solution and the detection intensity of Cl (Figure 5). Note that in experiment 3, the detection intensity of Cl was mainly in a range of up to about 0.8 counts/pixel, so the calibration curves were prepared only for salt concentrations from 0.0 to 1.23 mol/kg.

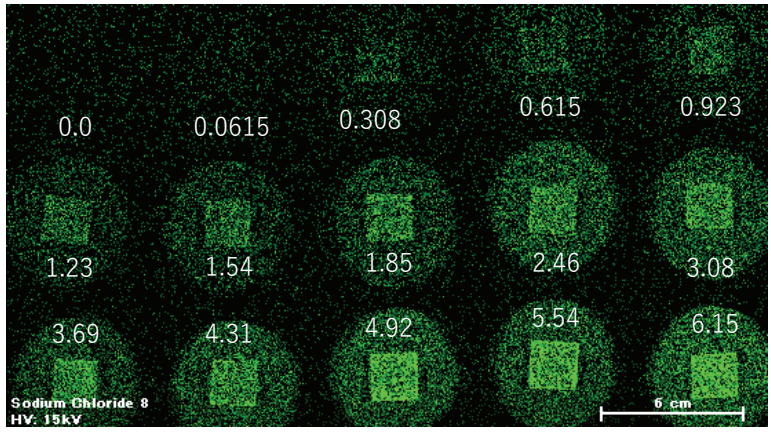

Figure 4: 2D analysis results of Cl of tuff surfaces impregnated with NaCl solution using the XRF analyzer in experiment 1. The detection intensity of Cl is proportional to the color intensity in the image.

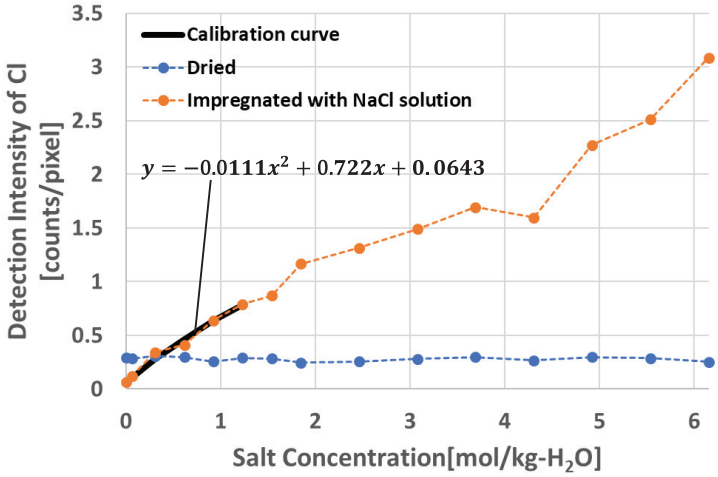

Figure 5: The detection intensity of Cl on tuff surfaces for each NaCl solution concentration and a calibration curve.

Figure 6 shows the average detection intensity values of Cl for each specimen thickness in experiment 2. These detection intensities were not much different within the range of specimen thickness and were very similar to those obtained for the same salt concentration in experiment 1. Note that the detection intensities of Cl were slightly lower at some thicknesses, and this difference is considered to be within the range of error, due to differences in material composition and measurement errors. Therefore, the measured depth of the XRF of the tuff was estimated to be within 1.7 mm or less from the surface.

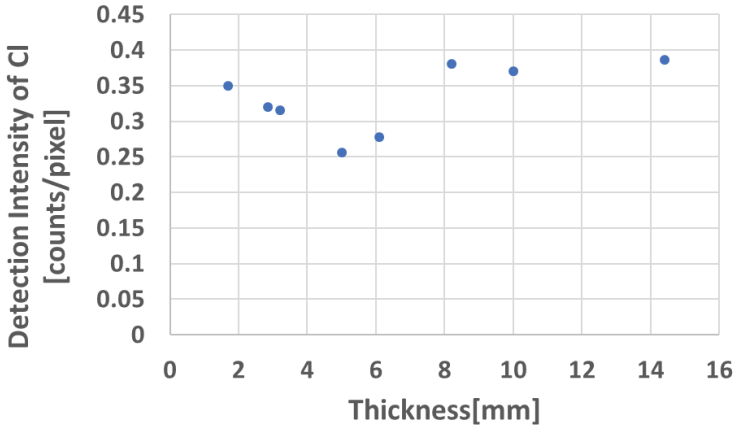

Figure 6: Detection intensities of Cl on tuff surfaces for each specimen thickness.

Figure 7 shows the change in salt concentration on the surface of each specimen in experiment 3, calculated based on the calibration curve in Figure 5. The salt concentration on the surface of all specimens increased with time; it increased almost constantly in S-1 but rapidly at some point in S-2 and S-3. As shown in Figure 8, salt precipitation at the surface was observed by photo 7 days (about 160 hours) after the start of the experiment for S-2 and 9 days (about 210 hours) for S-3 during the experimental period. Since the precipitated salt is not ionized (dissolved) salt in solution, after salt precipitation was observed, the results deviated from the objective of measuring the salt concentration of the solution in the material. Note that Figure 7 excludes the results of S-2 after 260 h because salt precipitation was observed and the results of S-2 were significantly different from those of S-1 and S-3.

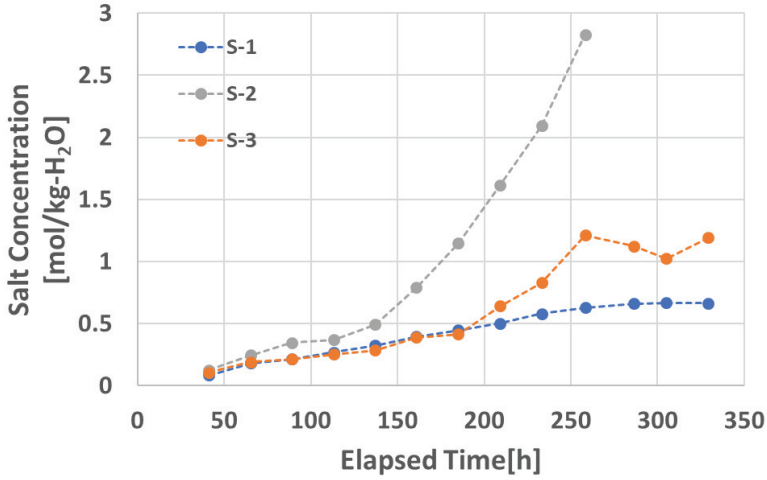

Figure 7: Variation in Cl ions concentrations of solution present nearby tuff surfaces over time in experiment 3.

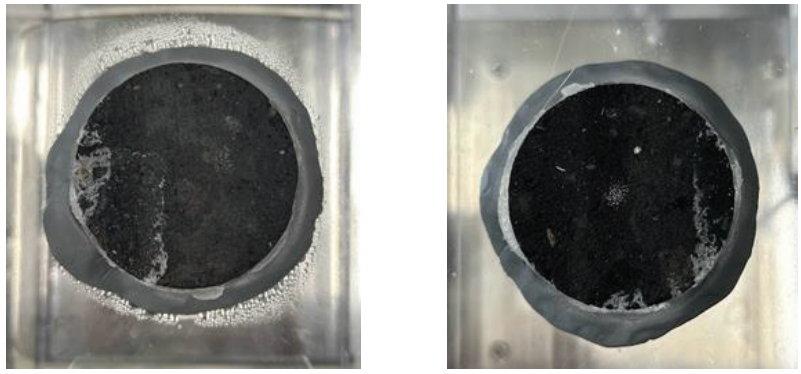

Figure 8: Surfaces of specimen 2 (left) and specimen 3 (right) with NaCl crystals 13 days after the start of experiment 3.

4 DISCUSSION

Na cannot be detected using an XRF analyzer under atmospheric conditions because it has a relatively small atomic weight. Thus, this study estimated sodium chloride concentration based only on Cl detection intensity. If ion exchange occurs between Na or Cl (or both) and the remaining ions in the material, Na and Cl may not be in equal amounts. Thus, whether the amount of Na increases at the same rate as Cl with increasing salt concentration is unclear. However, measurements using $CaCl_2$ solution have shown that the detection intensities of Ca and Cl increase similarly with increasing salt concentration [12]. Therefore, it was assumed that Na and Cl would increase at the same rate with higher salt concentration in the measurement using NaCl solution as $CaCl_2$ solution.

Figure 9 shows the cumulative evaporation in experiment 3. All specimens had an almost constant evaporation rate and minimal differences. Thus, the average salt concentration on the surfaces is expected to increase at almost the same rate for all specimens, but the salt concentration for each specimen increased at different rates from some point in this experiment. The possible cause of this is as follows. Salt crystals were observed on the surface of some specimens from some point. Before salt precipitation, all specimens showed similar trends in salt concentration changes. Therefore, assuming that the XRF detection intensity of Cl in salt crystals is greater than in solution, salt precipitation may have affected analysis results of the average salinity. In addition, the reason for the difference in salt precipitation tendency may be that the tuff used for the test specimens is not a homogeneous material, so the pore structure differs locally, and the salt concentration and ease of salt precipitation may have differed by part. Thus, we plan to verify local salinity differences of the tuff surface by comparing the XRF detection intensities of Cl in areas where salt is not precipitated at the surface.

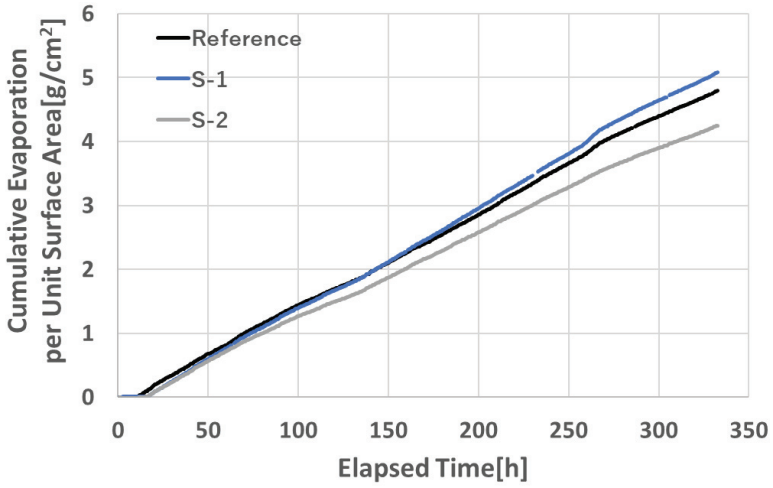

Figure 9: Variation in cumulative evaporation over time in experiment 3.

5 CONCLUSIONS

This study focused on using XRF to measure salt concentration in porous materials nondestructively and in the field. To measure accumulated salt concentration on stone surfaces over time using an XRF analyzer and examine the applicability of this method, we conducted three experiments. In these experiments, XRF analysis of tuff surfaces impregnated with several NaCl concentrations was performed, and results showed that the XRF intensity of Cl is proportional to salt concentration. By comparing Cl detection intensities on different thicknesses of tuff surfaces impregnated with NaCl solutions, this study found that the measured depth of XRF of the tuff is less than 1.7 mm. Finally, the change in the detection intensity of Cl on the surfaces was measured using an XRF analyzer by absorbing NaCl solution from the bottom and evaporating water from the top surface, and the change in the amount of salt that accumulated near the surface of the material was estimated. These analysis results demonstrated that the salt concentration near the surface of the tuffs measured using XRF analyzer increased with evaporation, and some specimens showed a sharp increase in the salinity, presumably due to salt precipitation. It is possible that salt precipitation affects the results of the average salinity analysis, and tuff may vary in salt concentration and ease of salt precipitation by part. Therefore, we plan to verify local salinity differences of the tuff surface.

ACKNOWLEDGMENTS

This work was supported by JSPS KAKENHI grant numbers JP20K22445 and JP18H01596. The authors would like to express their gratitude.

REFERENCES

[1] I. Rörig-Dalgaard, “Potential salt damage assessment and prevention based on micro samples,” in *Proceedings of SWBSS 2021 (Fifth International Conference on Salt Weathering of Buildings and Stone Sculptures)*, pp. 21–30, 2021.

[2] M. Balawi et al., “Matter loss quantification and chemical analysis for the diagnosis of powdering: the case study of the chapel of maurepas, chambord, france,” in *Proceedings of SWBSS 2021 (Fifth International Conference on Salt Weathering of Buildings and Stone Sculptures)*, pp. 337–344, 2021.

[3] R. Plagge, and T. Ishizaki, “Moisture and salt mapping by TDR in a historical stone building,” *Hozon Kagaku*, vol. 46, pp. 137-144, 2007.

[4] I. Egartner, and O. Sass, “Using paper pulp poultices in the field and laboratory to analyse salt distribution in building limestones,” *Heritage Science*, vol. 4, no. 1, pp. 1-13, 2016.

[5] L. A. Rijniers, “Salt crystallization in porous materials: an NMR study,” Ph.D. thesis, Eindhoven university of technology, 2004.

[6] T.A. Saidov et al., “Sodium sulfate salt weathering of porous building materials studied by NMR,” *Materials and Structures*, vol. 50, no. 2, pp. 1-11, 2017.

[7] A. A. A. Aldabaa et al., “Combination of proximal and remote sensing methods for rapid soil salinity quantification,” *Geoderma*, vol. 239, pp. 34-46, 2015.

[8] T. Amino and T. Habuchi, "Measurement of chloride content in recycled fine aggregate produced from waste marine concrete using fluorescent X-Ray analyzer," *Concrete Research and Technology*, vol. 24, no. 2, pp. 19-28, 2013.

[9] M. K. Moradllo et al., "Using micro X-ray fluorescence to image chloride profiles in concrete," *Cement and Concrete Research,* vol. 92, pp. 128-141, 2017.

[10] C. Nunes et al., "Experimental research on salt contamination procedures and methods for assessment of the salt distribution." *Construction and Building Materials,* vol. 298, 123862, 2021.

[11] Oita City Board of Education, "Kunishiteishiseki Oita Motomachi Sekibutsu Hozonsyurijigyo Hokokusho (in Japanese)," Education Board of Oita-shi, 1996.

[12] N. Takatori et al., "Investigation of a method for analyzing salt concentration near the surface of porous materials using X-ray fluorescence," *Summaries of technical papers of Annual Meeting of Architectural Institute of Japan (Hokkaido)*, pp. 1259-1260, 2022.

ON THE DEVELOPMENT OF A MICROMECHANICS-BASED RELATIONSHIP BETWEEN SALT CRYSTALLIZATION PRESSURE, PORE FILLING, AND DAMAGE IN POROUS BUILDING MATERIALS

Nicolò Lo Presti[1], Antonio Maria D'Altri[1,2,*], Luca Patruno[1], Giovanni Castellazzi[1], Tinhinane Chekai[3], Hannelore Derluyn[3], Noushine Shahidzadeh[4], and Stefano de Miranda[1]

KEYWORDS

Pore pressure; Salt crystallization-induced damage; Pore Structure; Finite element analysis; Damage modelling

ABSTRACT

This contribution investigates the relationship between salt crystallization pressure, pore filling, and damage in porous building materials through a micromechanics-based approach. A 3D finite element (FE) model of a microscale representative volume element (RVE) of the porous material is developed, and several load scenarios are applied to the RVE to correlate salt crystallization pressure, pore filling, and damage in the RVE. The resulting relationships are then condensed into a computationally efficient off-line phenomenological model, calibrated on a large FE-based database, capable of predicting the macroscopic damage in the RVE due to any pseudo-time history of salt crystallization pressure and pore filling. The effectiveness of the phenomenological model is verified by comparing its results with the ones computed through the FE model, for load scenarios not included into the calibration dataset, achieving good agreement of results. Finally, the possibility of using this phenomenological model together with available multiphase models to

[1] DICAM Department, University of Bologna, Italy, am.daltri@unibo.it
[2] CEE Department, Princeton University, USA
[3] Universite de Pau et des Pays de l'Adour, E2S UPPA, CNRS, TotalEnergies, LFCR, Pau, France
[4] Institute of Physics, Van der Waals-Zeeman Institute, University of Amsterdam, The Netherlands

predict moisture transport, salt crystallization pressure, and damage into porous building materials is discussed.

1 INTRODUCTION

Environmental actions, such as moisture transport and salt crystallization, are known to play a major role in the deterioration process of porous building materials [1]. Although significant efforts have been devoted to the development of experimental procedures for the assessment of resistance of porous building materials against salt crystallization [2], the development of reliable numerical tools to predict salt weathering is still challenging.

In this contribution, the possibility to derive a micromechanics-based relationship between salt crystallization pressure, pore filling, and damage in porous building materials is investigated and discussed.

Firstly, a 3D finite element (FE) model of a microscale representative volume element (RVE) of the porous material [3] is developed. The RVE geometry is based on a simplified pore structure with statistically representative properties in agreement with experimental data [4]. Secondly, several load scenarios in terms of salt crystallization pressure and pore filling are applied to the RVE, through various pseudo-time histories, and the macroscopic damage is directly measured on the RVE. Accordingly, relationships between salt crystallization pressure, pore filling, and overall damage in the RVE are obtained (Section 2).

Such micromechanics-based relationships are then condensed into a computationally efficient offline phenomenological model, calibrated on a large FE-based database, able to predict the damage in the RVE due to any pseudo-time history of salt crystallization pressure and pore filling. The effectiveness of the phenomenological model is then checked by comparing its results with the ones computed through the FE model, for load scenarios not included into the calibration dataset (Section 3).

The possibility to use this phenomenological model together with available multiphase models [5,6] to predict moisture transport, salt crystallization, pressure and damage into porous building materials is finally discussed (Section 4).

2 FINITE ELEMENT MODEL

A solid FE model of the RVE is generated by considering the actual porosity and the mean pore radius of the material. A nonlinear plastic-damage constitutive law is adopted for the material matrix, by assuming homogenized mechanical properties. Several load scenarios are applied to the RVE with varying salt crystallization pressure and pore filling pseudo-time histories. After de-loading the pore pressure, the macroscopic damage D is directly measured on the actual condition of the RVE by assessing the overall stiffness loss. According to this, relationships between salt crystallization pressure, pore filling, and macroscopic damage are obtained (Figure 1). In particular, Figure 1 shows an example of macroscopic damage D – pressure relationship for constant pore filling (in particular, the saturation degree of crystallized salt, S_s^s, is set equal to 1), as well as an example of damaged RVE.

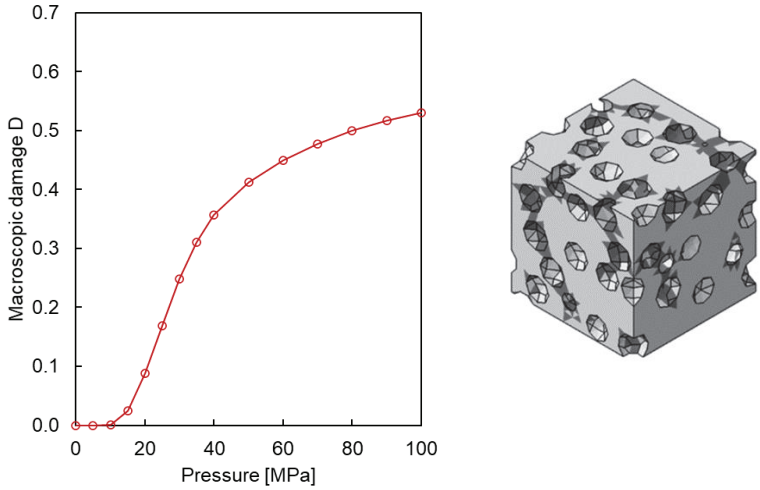

Figure 1: Example of macroscopic damage D – pressure curve for constant pore filling (S_S^S=1), left, and example of damaged RVE (damaged FEs are highlighted in dark grey), right.

3 PHENOMENOLOGICAL MODEL

The aforementioned relationships are subsequently condensed into an offline phenomenological model that is computationally efficient. Such model is calibrated using a large database of FE simulations. To verify the efficacy of the phenomenological model, its outcomes in terms of predicted macroscopic damage D* are compared against those obtained by the FE model (in terms of macroscopic damage D) for load scenarios that were not part of the calibration dataset, as shown in Figure 2 (for an ideal load scenario).

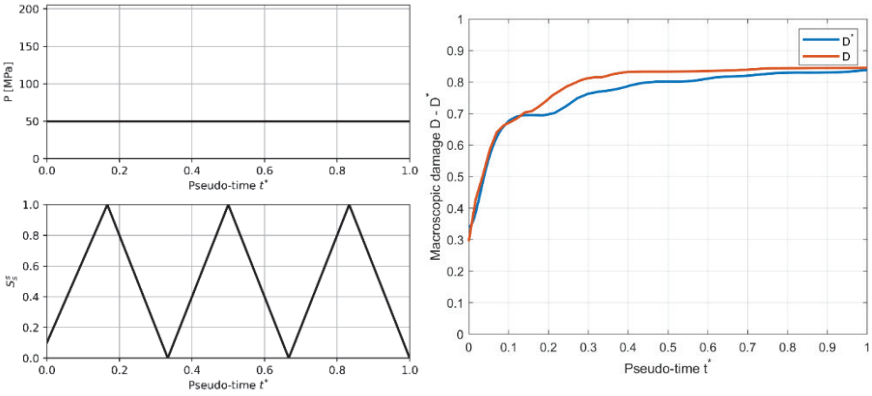

Figure 2: A posteriori comparison between FE and phenomenological models. Top left: adopted pseudo-time history of the pore pressure. Bottom left: adopted pseudo-time history of the pore filling. Right: comparison of the evolution of macroscopic damage between FE (D) and phenomenological (D*) models.

4 MULTIPHYSICS SIMULATIONS

Such phenomenological model is finally coupled with existing multiphase models [4,5] to predict moisture transport, salt crystallization, pressure and damage into porous building materials through multiphysics simulations. An example of application is shown in Figure 3, where the drying of a porous building material initially saturated with saline solution and an evaporating top surface is shown in terms of pore filling (left) and macroscopic damage D* (right) contour plots.

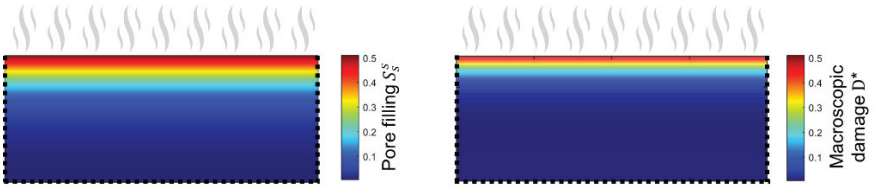

Figure 3: Example of multiphysics simulation of a drying phase: pore filling (left) and macroscopic damage D* (right) contour plots at the end of the drying phase.

5 CONCLUSIONS

In conclusion, this study explored the possibility to develop relationships between salt crystallization pressure, pore filling, and damage in porous building materials using a micromechanics-based approach. In this context, a phenomenological model based on micro-FE outcomes has been employed together with existing multiphase models to conduct multiphysics simulations to account for salt crystallization-induced damage into porous building materials.

ACKNOWLEDGEMENTS

The support from the European project CRYSTINART through the Joint Programming Initiative on Cultural Heritage (JPI-CH) is gratefully acknowledged. This project has received funding from the European Union's Horizon 2020 research and innovation programme under the Marie Sklodowska-Curie grant agreement No 101029792. H. Derluyn acknowledges the support from the European Research Council (ERC) under the European Union's Horizon 2020 research and innovation programme (grant agreement No 850853)".

REFERENCES

[1] Lubelli, B., et al., "Towards a more effective and reliable salt crystallization test for porous building materials: state of the art." *Materials and Structures* 51 (2018): 1-21.

[2] Lubelli, B., et al., "Recommendation of RILEM TC 271-ASC: New accelerated test procedure for the assessment of resistance of natural stone and fired-clay brick units against salt crystallization," *Materials and Structures* 56.5 (2023): 101.

[3] Grementieri, L., et al., "A multi-scale approach for the analysis of the mechanical effects of salt crystallisation in porous media". *International Journal of Solids and Structures* 126 (2017): 225-239.

[4] Castellazzi, G., et al. "A coupled multiphase model for hygrothermal analysis of masonry structures and prediction of stress induced by salt crystallization." *Construction and Building Materials* 41 (2013): 717-731.

[5] D'Altri, A. M., et al. "Towards a more effective and reliable salt crystallisation test for porous building materials: Predictive modelling of sodium chloride salt distribution." *Construction and Building Materials* 304 (2021): 124436.

[6] Castellazzi, G., et al. "A staggered multiphysics framework for salt crystallization-induced damage in porous building materials." *Construction and Building Materials* 304 (2021): 124486.

On the development of a micromechanics-based relationship between salt crystallization pressure, pore filling, and damage in porous building materials

QUANTIFICATION OF MOISTURE IN MASONRY VIA AI EVALUATED BROADBAND RADAR REFLECTOMETRY

Daniel Frenzel[1*], Oliver Blaschke[2], Christoph Franzen[3], Felix Brand[2], Franziska Haas[1], Alexandra Troi[1], and Klaus Stefan Drese[2]

KEYWORDS

Moisture detection, non-destructive testing, ground penetrating radar, neural network, machine learning

ABSTRACT

Humidity, salt content, and migration in building materials lead to weathering and are a common challenge. To understand damage phenomena and select the right conservation treatments, knowledge on both the amount and distribution of moisture and salt load in the masonry is crucial. It was shown that commercial portable devices addressing moisture are often limited by the mutual interference of these values. This can be improved by exploiting broadband radar reflectometry for the quantification of humidity in historic masonry. Due to the above-mentioned limitations, today's gold standard for evaluating the moisture content in historic buildings is still conducted by taking drilling samples with a subsequent evaluation in a specially designed laboratory, the so-called Darr method. In this paper, a new broadband frequency approach in the range between 0.4 and 6 GHz with improved artificial-intelligence data analysis makes sure to optimize the reflected signal, simplify the evaluation of the generated data, and minimise the effects of variables such as salt contamination that influence the permittivity. In this way, the amount of water could be determined independently from the salt content in the material and an estimate of the salt load. With new machine learning algorithms, the analysis of the permittivity is improved and can be made accessible for everyday use on building sites with minimal intervention by the user. These algorithms were trained

[1] Faculty of Design, Coburg University of Applied Sciences and Arts, Am Hofbräuhaus 1b, 96450 Coburg, Germany
[2] Institute of Sensor and Actuator Technology, Coburg University of Applied Sciences and Arts, Am Hofbräuhaus 1b, 96450 Coburg, Germany
[3] Institut für Diagnostik und Konservierung an Denkmalen in Sachsen und Sachsen-Anhalt e. V., Schloßplatz 1, 01067 Dresden, Germany
[*] Correspondence: daniel.frenzel@hs-coburg.de

with generated data from different drying studies on single building bricks from the masonries. The findings from the laboratory studies were then validated and evaluated on real historic buildings at real construction sites.

1 INTRODUCTION

Humidity and water are environmentally abundant, and ingress into and migration within the building material leading to weathering is a common challenge [1–5]. In order to prevent permanent damage to the building shell due to weathering, it is necessary to determine the exact moisture and salt content of the building and its masonry [6]. Wetting–drying cycles, acidic rain, and the effect of salt crystallization can weaken the internal structure of mineral building materials and change important material properties such as compressive strength [7–9]. According to the current state-of-the-art methods acknowledged by independent institutions, only invasive methods work reliably [10,11], such as the Darr method (gravimetric moisture measuring method). In order to completely understand the cause of damage, it is necessary to know how moisture and salt are distributed in masonry and how they change over time (winter/summer or on a day-to-day basis). The interplay of the crystallization and dissolution of salts leads to immense damage and is often the cause of structural weaknesses in building materials [12,13]. Such monitoring with invasive methods over longer time periods and on larger areas is not possible in the historical stock, or only possible with a considerable loss of substance. The demand for non-destructive methods and instant results which can measure large areas fast and easy to determine the moisture and salt content in building structures is therefore immense.

2 METHOLOGY

A promising method is the coupling of radar waves into a masonry wall and detecting the reflected signal with a subsequent analysis of the complex permittivity. This method utilizes the strong differences in the complex-valued dielectric constant (permittivity) between the water and building materials.

The following formula displays the complex permittivity:

$$\varepsilon=\varepsilon'-\mathrm{i}\cdot\varepsilon'' \tag{1}$$

The real part ε' describes the classic dielectric constant, while the imaginary part ε'' describes the dielectric losses.

The characterization of materials using the permittivity was already shown by Hasted and Shah in 1964 [14] and Pisa et al. in 2017 [15].

Different studies with ground-penetrating radar (GPR), which is already established in construction practices, show that measurements with different frequencies are very promising [16,17]. Other studies [18–22] also demonstrate the suitability of GPR modules for determining the water content. Other studies [23–27] stated that radar measurements are also possible on wet brick walls with varying materials.

In this study, various masonry test specimens were built and placed under different moisture and salt loads (Figure 1). These were then measured by radar at different

times, and the complex-valued permittivity of the generated data was analyzed using trained neural networks. Measurements were carried out on individual building blocks as a database for the machine learning algorithms of the neural network. The predictions of the AI-based data evaluation were then compared with the current standard procedure, the Darr method. Finally, the measurement system was tested under real-life conditions at construction sites on historical buildings.

Figure 1 Stored test specimens in steel profile troughs.

The extensive laboratory test measurements were performed on masonry models and single bricks typical for historic buildings in Upper Franconia. For the eight laboratory masonry models (four out of sandstone, 4 out of solid brick material), in total, three different materials with historic relevance came into use to construct the masonry models.

Sander sandstone (SST), a regionally occurring building stone, which has already been quarried for a thousand years;

Solid brick material (SBM) of company Wienerberger, corresponding in its material properties widely to a historic brick;

Trass-lime mortar (TLM) Mur958 of company Maxit, a cement-free mortar that is also well-suited for masonry with natural stone.

For the radar measurements, the commercial radar system GP 8800 from screening eagle was used. It is a stepped-frequency continuous wave ground penetrating radar with a frequency between 400 and 6000 MHz [28]. For a frequency-resolved determination of the (complex) permittivity, an evaluation in the frequency domain is necessary. In this study, we used the phase spectrum analysis (see e.g., [29,30]). The analysis uses the calculation of the cross power spectral density to retrieve the information about the phase and attenuation of the reflected signal in the frequency domain. While the first one can be transformed into a phase velocity and thus into the real part of frequency dependent, complex permittivity, the latter one was used

to calculate an extinction coefficient which was necessary for calculating the imaginary part of the complex permittivity. This approach is described in detail in another study, which derived from this research project [31].

A further step in optimization is the usage of machine learning algorithms. Due to the complex data structures of the frequency domain, a neural network is used to retain information. For the moisture model, a regressor is used, which gives a definitive value as output. On the other hand, the model for salt prediction is a classifier, which gives a probability of how far a measurement fits into the previously trained categories.

3 RESULTS

Single Stones

The individual bricks were placed in small tubs and immersed either in deionized water or in a NaCl solution, respectively, $MgSO_4$ and KNO_3, until completely saturated. The concentration of the salt load should correspond to a medium level of contamination according to the tables for the restoration of historic buildings when completely saturated (the saturation moisture of the brick was used as the reference) [32]. The drying process was accompanied by measurement of the reflected radar signal at the back of the stone. In addition, the mass of the stones was determined during drying to calculate the amount of water remaining in the stones in mass percent (m%).

By comparing the model parameters of the wet bricks with the moisture data obtained by weighing, a link can be established between the measured curves and the moisture, as can be seen in Figure 2 (for solid brick materials) and Figure 3 (for sander sandstone). An in depth explanation is presented in the other paper from this project mentioned earlier [31].

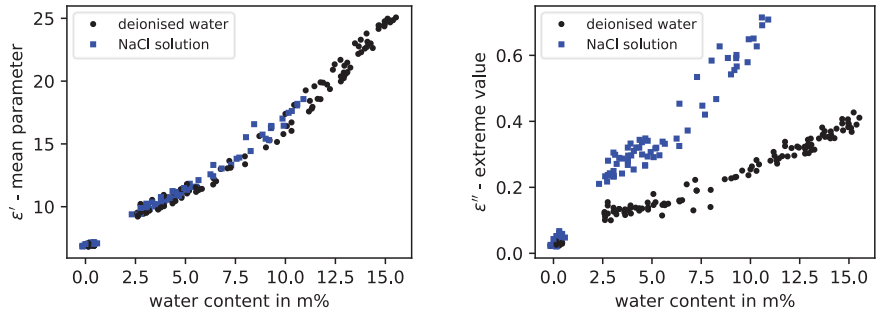

Figure 2 Studies on SBM for different moisture contents. One group was exposed to a salt solution with NaCl (blue squares), while the other group was only exposed to deionizsed water (black dots). The displayed real part (left side) was not affected by the contained salt. The imaginary part, on the other hand, was affected, and the offset increased with increasing moisture content. That is due to the higher number of dissolved salt ions, which results in a higher damping of the reflected signal. It is possible to measure the moisture content independently from the salt content.

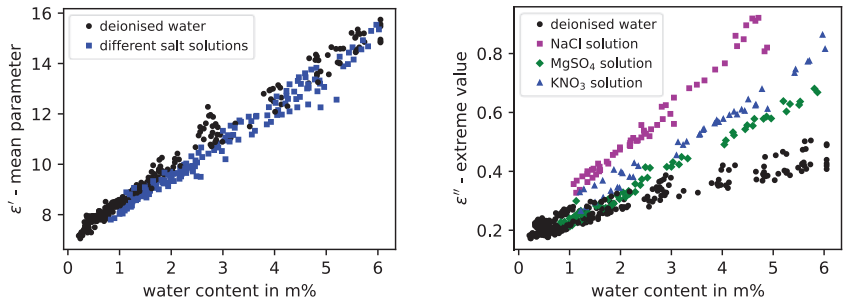

Figure 3 (Left) Model values of the real-part permittivity for sandstone specimens with different salt solutions and deionized water against the water content. No offset between the salt solutions and the deionized water is seen here. (Right) Model values of the imaginary-part permittivity for sandstone specimens, again with different salt solutions and deionized water against water content. Here, a clear offset can be seen between the salt-contaminated samples and the specimens with deionized water.

For other studies with constant molalities of the salt solutions, the sandstones (same type as in the walls) were divided into two groups. By choosing two molalities of 0.012 mol/kg or 0.02 mol/kg, a solution for each of the three types of salt was prepared accordingly. Monovalent anions such as chloride and nitrate showed similar values in the imaginary-part parameter (attenuation of the signal), whereas values of solutions with bivalent anions, such as the $MgSO_4$ solution, had a lower attenuation of the signal. This can be seen for both groups in Figure 12.

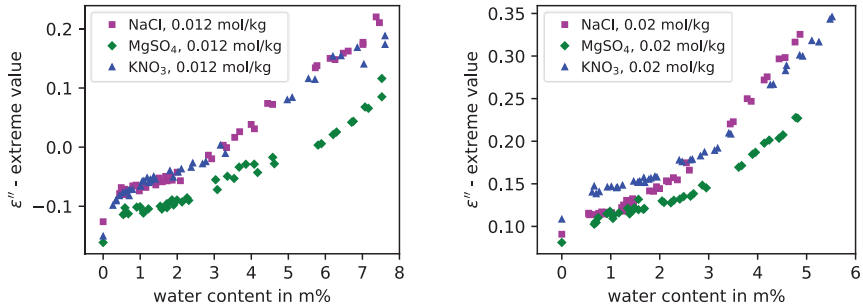

Figure 4 Influence of different types of salt on radar measurement at two constant molalities (left side 0.012 mol/kg, right side 0.02 mol/kg). Displayed here are the model parameters of the imaginary part measured from the sandstone. Monovalent ions such as chloride and nitrate show similar results for the imaginary part. Negative values are possible if the measured wave has a higher amplitude compared to the measured reference signal.

This study shows that the differences between the various salts (especially for the ones with monovalent ions) are low to not present at all. Thus, according to the

current status, the qualitative differentiation of salts is not possible. On a real building with an unknown quantity and types of salts contained, it is not possible to distinguish between the different types of salt, especially when there is a mixture of salts with different valences. Furthermore, only a classification into high, medium, and low/no salt load seems feasible.

Measurements on Masonries

In the next steps, the neural network trained with the data from the previous section was applied to the radar measurements of the masonry, which were accompanied by measurements using the Darr method.

The following Figure 5 summarizes the results of the gravimetric evaluation of the first concerted drilling operation in comparison to the radar measurement evaluated with the help of the trained AI model from the single brick study.

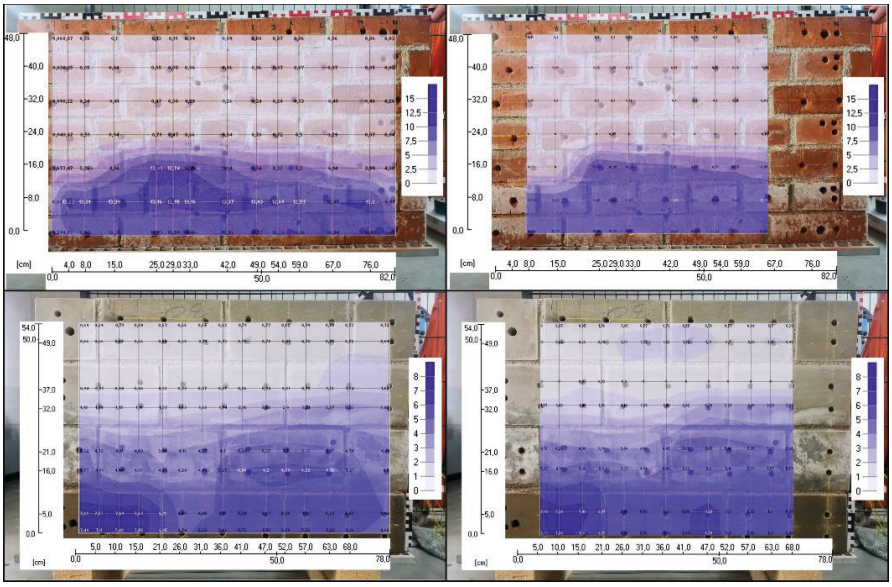

Figure 5 Results of the gravimetrically determined moisture content on the left and the predictions of the radar measurements on the right. Top picture brick wall, bottom picture sandstone wall. The graphical representation shows the moisture distribution across the whole surface. The scale on the right shows the moistures in (m%). The bricks have a higher porosity than the sandstone, but the pore size distribution of the sandstone allows a higher maximum of capillary rise.

While taking the drill dust samples with subsequent weighing and evaluation took about three days, the measurements with the radar probe on both masonries were completed in a few hours. The subsequent evaluation took about another few hours because the workflow had not yet been optimized. With an automated evaluation with little user interaction, this time would be significantly reduced.

On-site measurements of Historic Buildings

The challenge regarding on-site measurements are the unknown materials and the thickness of the masonries. Often the GPR used here was too weak to penetrate the whole thickness of the masonries with about 0.8–0.9 m.

The aim was to find a good and clear reflected signal from the material boundaries inside the masonry. Via drill core samples, the construction of the wall can be determined, and possible material boundaries such as between brick stone and mortar can be seen.

Figure 6 summarizes the results of both measurement methods in a diagram. The predictions of the radar measurements are predominantly higher than the absolute moisture content.

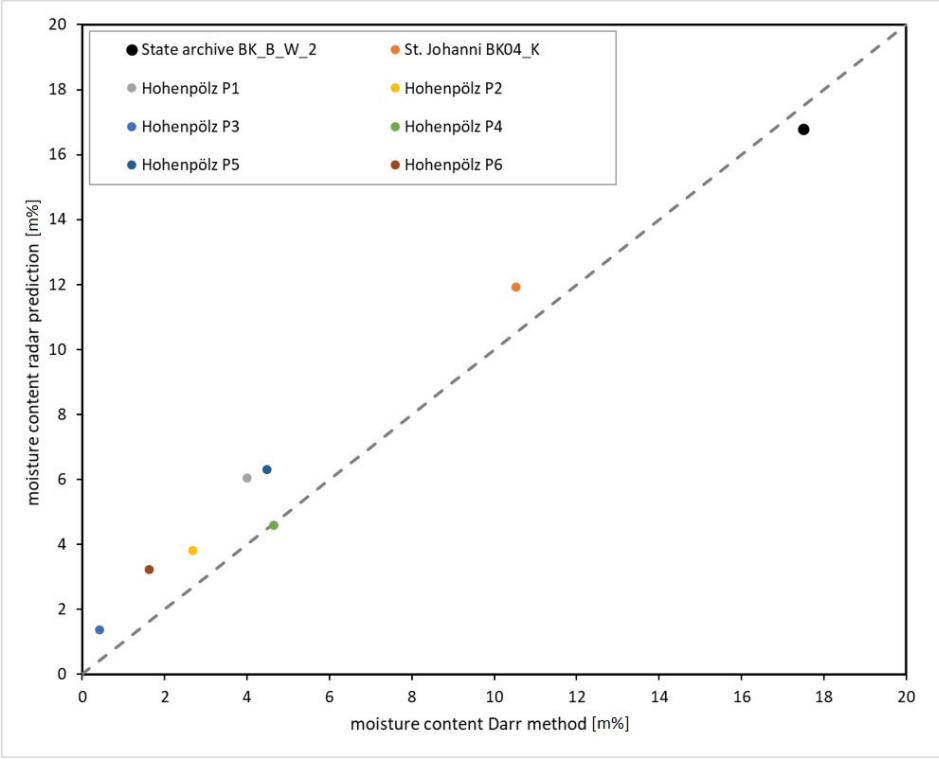

Figure 6 Graphical representation between the gravimetrically determined moisture data and the predictions from the radar measurements.

4 DISCUSSION AND CONCLUSION

The measuring system described here can detect moisture independently of the salt content in masonries. Therefore, an evaluation of the complex permittivity over a wide frequency range was conducted. To determine the moisture, model parame-

ters related to the real part are used, as these values show no impact on salt-contaminated specimens. The imaginary part, on the other hand, is highly influenced by the salt content and is therefore suited for a possible salt detection.

Two limits of the procedure must be accepted: Crystallized salts cannot be detected; It is not possible to determine the type of the dissolved salts. Due to the dielectric losses caused by the dissolved salts, a division into low, medium, high salt loads seems possible but should be further investigated.

With machine learning algorithms, the analysis of the complex permittivity becomes more accessible, and only a few user interactions are necessary. With an algorithm that searches the raw data for the relevant reflection signals and automatically applies a window function, the user interaction is reduced to the input of the wall thickness and the selection of the appropriate material model (here in our case bricks or sandstone).

The neuronal networks can process multiple sets of data (regressor model for moisture prediction and classifier model for the salt prediction) simultaneously and can sort out insufficient signals automatically. It should be noted that the required data are generated in a single radar measurement.

The concerted drill operations show that the device presented here can measure a large area in a short amount of time in comparison to the Darr method. While the collection of drill dust samples with subsequent analysis in the laboratory took about three days, the radar measurements and the evaluation of the generated data were completed in a few hours. Another big advantage is the non-invasive nature of this method where the device only needs good contact with the surface.

The device has proven to be very practicable under real conditions at construction sites and historic buildings. Like in the concerted drill operations, measurements on large areas can be performed easily and fast. Nevertheless, the best results can be obtained on relatively smooth surfaces and on thin masonries.

The mortar joints on the masonry specimen were so thin (~1 cm) compared to the stones that they had no influence on the measurements because the distance between the antennas of the GPR was bigger than thickness of the mortar joints. In this sense, the stone was always measured as well. Measurements near the joints behave similar to areas without mortar nearby.

Many of these limitations are hardware-related, as the available radar equipment is not designed for such measurements. For further studies, a more focused radiation characteristic of the transmitter should be chosen. This would allow for a higher measuring depth with the same power and therefore a significantly improved quality of the back-reflected signal. This would also minimize possible scattering effects that could superimpose the signal. Furthermore, the transmitter should have a higher power to be able to measure a sufficiently good signal even at higher salt loads with corresponding dielectric losses.

The method developed in this project opens up new possibilities for moisture determination in monument conservation. It is possible to carry out large-scale, temporally repeatable monitoring with the same physical unit as the current destructive standard method. For an exact determination of the composition and quantity of

salts in the masonry, the radar method can be used to identify the relevant locations for meaningful drilling samples in advance and thus reduce the frequency of destructive intervention in the building fabric.

REFERENCES

[1] Franzen, C.; Mirwald, P.W. Moisture content of natural stone: Static and dynamic equilibrium with atmospheric humidity. *Environ. Geol.* **2004**, *46*, 391–401. https://doi.org/10.1007/s00254-004-1040-1.

[2] Hall, C.; Hoff, W.D. *Water Transport in Brick, Stone and Concrete*; CRC Press: Boka Raton, FL, USA, 2021.

[3] Steiger, M.; Charola, A.E.; Sterflinger, K. Weathering and deterioration. In *Stone in Architecture: Properties, Durability*; The Metropolitan Museum of Art: New York, NY, USA, 2011; pp. 227–316.

[4] Franzen, C.; Zötzl, M.; Trommler, U.; Hoyer, C.; Holzer, F.; Höhlig, B.; Roland, U. Microwave and radio wave supported drying as new options in flood mitigation of imbued decorated historic masonry. *J. Cult. Herit.* **2016**, *21*, 751–758. https://doi.org/10.1016/j.culher.2016.04.007.

[5] Adamowski, J.; Hoła, J.; Matkowski, Z. Probleme und Lösungen beim Feuchtigkeitsschutz des Mauerwerks von Baudenkmälern am Beispiel zweier großer Barockbauten in Wrocław. *Bautechnik* **2005**, *82*, 426–433. https://doi.org/10.1002/bate.200590148.

[6] Zhou, X.; Derome, D.; Carmeliet, J. Analysis of moisture risk in internally insulated masonry walls. *Build. Environ.* **2022**, *212*, 108734. https://doi.org/10.1016/j.buildenv.2021.108734.

[7] Noor-E-Khuda, S.; Albermani, F. Flexural strength of weathered granites under wetting-drying cycles: Implications to steel structures. *Adv. Steel Constr*. 2019, 15, 225–231.

[8] Franzoni, E.; Sassoni, E. Correlation between microstructural characteristics and weight loss of natural stones exposed to simulated acid rain. *Sci. Total Environ.* **2011**, *412–413*, 278–285. https://doi.org/10.1016/j.scitotenv.2011.09.080.

[9] Delgado, J.M.P.Q.; Guimarães, A.S.; de Freitas, V.P.; Antepara, I.; Kočí, V.; Černý, R. Salt Damage and Rising Damp Treatment in Building Structures. *Adv. Mater. Sci. Eng.* **2016**, *2016*, 1280894. https://doi.org/10.1155/2016/1280894.

[10] *DIN EN 16682:2017-05*; Conservation of Cultural Heritage—Methods of Measurement of Moisture Content, or Water Content, in Materials Constituting Immovable Cultural Heritage; Deutsches Institut für Normung: Berlin, Germany, 2017.

[11] WTA (2002): Messung der Feuchte von mineralischen Baustoffen. WTA Merkblatt 4-11. Referat 4 Bauwerksabdichtung. Unter Mitarbeit von Uwe Schürger und Heinrich Wigger. Ausgabe: 12.2002/D, Endgültige Fassung:

Oktober 2003. Stuttgart, [Pfaffenhofen]: Fraunhofer IRB-Verlag; WTA Publications (WTA-Merkblatt, 4–11).

[12] Flatt, R.J.; Caruso, F.; Sanchez, A.M.A.; Scherer, G.W. Chemo-mechanics of salt damage in stone. *Nat. Commun.* **2014**, *5*, 4823. https://doi.org/10.1038/ncomms5823.

[13] Scherer, G.W. Crystallization in pores. *Cem. Concr. Res.* **1999**, *29*, 1347–1358. https://doi.org/10.1016/s0008-8846(99)00002-2.

[14] Hasted, J.B.; Shah, M.A. Microwave absorption by water in building materials. *Br. J. Appl. Phys.* **1964**, *15*, 825–836. https://doi.org/10.1088/0508-3443/15/7/307.

[15] Pisa, S.; Pittella, E.; Piuzzi, E.D.; Atanasio, P.; Zambotti, A. Permittivity measurement on construction materials through free space method. In Proceedings of the I²MTC 2017 IEEE International Instrumentation and Measurement Technology Conference, Torino, Italy, 22–25 May 2017; IEEE: Piscataway, NJ, USA, 2017; pp. 1–4.

[16] Dérobert, X.; Villain, G. Effect of water and chloride contents and carbonation on the electromagnetic characterization of concretes on the GPR frequency band through designs of experiment. *NDT E Int.* **2017**, *92*, 187–198. https://doi.org/10.1016/j.ndteint.2017.09.001.

[17] Du Plooy, R.L.; Villain, G.; Lopes, S.P.; Ihamouten, A.; Dérobert, X.; Thauvin, B. Electromagnetic non-destructive evaluation techniques for the monitoring of water and chloride ingress into concrete: A comparative study. *Mater. Struct.* **2015**, *48*, 369–386. https://doi.org/10.1617/s11527-013-0189-z.

[18] Hugenschmidt, J.; Loser, R. Detection of chlorides and moisture in concrete structures with ground penetrating radar. *Mater. Struct.* **2008**, *41*, 785–792. https://doi.org/10.1617/s11527-007-9282-5.

[19] Kalogeropoulos, A.; Van Der Kruk, J.; Hugenschmidt, J.; Busch, S.; Merz, K. Chlorides and moisture assessment in concrete by GPR full waveform inversion. *Near Surf. Geophys.* **2011**, *9*, 277–286. https://doi.org/10.3997/1873-0604.2010064.

[20] Ihamouten, A.; Villain, G.; Dérobert, X. Complex Permittivity Frequency Variations From Multioffset GPR Data: Hydraulic Concrete Characterization. *IEEE Trans. Instrum. Meas.* **2012**, *61*, 1636–1648. https://doi.org/10.1109/tim.2012.2190330.

[21] Senin, S.; Hamid, R. Ground penetrating radar wave attenuation models for estimation of moisture and chloride content in concrete slab. *Constr. Build. Mater.* **2016**, *106*, 659–669. https://doi.org/10.1016/j.conbuildmat.2015.12.156.

[22] Wutke, M.K. Use of Ground Penetrating Radar measurement combined to resistivity measurement for characterization of the concrete moisture. In Proceedings of the 17th International Conference on Ground Penetrating Radar (GPR). 2018 17th International Conference on Ground Penetrating

Radar (GPR), Rapperswil, 18–21 June 2018; IEEE: Piscataway, NJ, USA, 2018; pp. 1–7.

[23] Lai, W.W.-L.; Kind, T.; Kruschwitz, S.; Wöstmann, J.; Wiggenhauser, H. Spectral absorption of spatial and temporal ground penetrating radar signals by water in construction materials. *NDT E Int.* **2014**, *67*, 55–63. https://doi.org/10.1016/j.ndteint.2014.06.009.

[24] Binda, L.; Colla, C.; Forde, M. Identification of moisture capillarity in masonry using digital impulse radar. *Constr. Build. Mater.* **1994**, *8*, 101–107. https://doi.org/10.1016/s0950-0618(09)90019-8.

[25] Binda, L.; Cardani, G.; Zanzi, L. Nondestructive Testing Evaluation of Drying Process in Flooded Full-Scale Masonry Walls. *J. Perform. Constr. Facil.* **2010**, *24*, 473–483. https://doi.org/10.1061/(asce)cf.1943-5509.0000097.

[26] Agliata, R.; Bogaard, T.A.; Greco, R.; Mollo, L.; Slob, E.C.; Steele-Dunne, S.C. Non-invasive estimation of moisture content in tuff bricks by GPR. *Constr. Build. Mater.* **2018**, *160*, 698–706. https://doi.org/10.1016/j.conbuildmat.2017.11.103.

[27] Orr, S.A.; Fusade, L.; Young, M.; Stelfox, D.; Leslie, A.; Curran, J.; Viles, H. Moisture monitoring of stone masonry: A comparison of microwave and radar on a granite wall and a sandstone tower. *J. Cult. Herit.* **2020**, *41*, 61–73. https://doi.org/10.1016/j.culher.2019.07.011.

[28] Proceq GP8800|Ground Penetrating Radar. 2023. Available online: https://www.screeningeagle.com/en/products/proceq-gp8800-ultraportable-concrete-gpr-radar (accessed on 2 March 2023).

[29] Sachse, W.; Pao, Y.-H. On the determination of phase and group velocities of dispersive waves in solids. *J. Appl. Phys.* **1978**, *49*, 4320–4327. https://doi.org/10.1063/1.325484.

[30] Singer, F. Mess- und Analysemethoden in der Laserakustik bei breitbandiger Laseranregung. *Tech. Mess.* **2015**, *82*, 45–51. https://doi.org/10.1515/teme-2014-0030.

[31] Blaschke, O.; Brand, F.; Drese, K.S. Quantification of Humidity and Salt Detection in Historical Building Materials via Broadband Radar Measurement. *Sensors* **2023**, *23*, 4616. https://doi.org/10.3390/s23104616.

[32] Wissenschaftlich-Technische Arbeitsgemeinschaft für Bauwerkserhaltung und Denkmalpflege (2019): Salzreduzierung an Porösen Mineralischen Baustoffen Mittels Kompressen. Deutsche Fassung vom Dezember 2019, Ausgabe 12/2019/D. Stuttgart, [Pfaffenhofen]: Fraunhofer IRB-Verlag. (WTA-Merkblatt, 3-13).

SALT WEATHERING MECHANISM OF ANCIENT EARTHEN MATERIAL IN ARID AREA OF NORTHWEST CHINA: A CASE STUDY OF NA2SO4-NACL SALT MIXTURES

Yunxia Shen[1,2], Michael Steiger[2], Chuxin Liang[1], and Manli Sun[1*]

KEYWORDS

Earthen sites, Na_2SO_4-NaCl salt mixtures, Deterioration Model

ABSTRACT

Research on salt weathering mechanism of earthen sites is an important theoretical basis for weathering prevention and treatment. Considering different soil structures and environmental conditions, the deterioration characteristics of earthen sites with Na_2SO_4-NaCl salt mixtures are studied by simulation experiments. The results show that a large number of $Na_2SO_4 \cdot 10H_2O$ crystals are precipitated on the surface of the pure Na_2SO_4 sample during the evaporation process at room temperature, which is a typical surface crystal growth (efflorescence). With the addition of NaCl, the deterioration mode changes to the combination of efflorescence and subflorescence. When the mole fraction of NaCl is above 0.8, only the crust is formed on the surface of the sample. The mass loss ratio of soil increases linearly with the increase of NaCl content, and the increase rate decreases with the increase of dry density and initial water content.

[1] School of Cultural Heritage,Northwest University,No.229 Taibai North Street, Xi'an, Shaanxi, 710069,P.R. China

[2] Chemistry Department, Inorganic and Applied Chemistry, University of Hamburg, Martin-Luther-King-Platz 6, 20146 Hamburg, Germany

* Corresponding author, e-mail: sunml68@sohu.com

1 MATERIALS AND METHODS

The capillary test was carried out with a self-made capillary transfer device (Patent No: 201620696245.7) at room temperature (22-24℃, RH=43±4%). During the test, due to the large concentration of the solution and the high dry density of the sample, the soil is easy to absorb water and expand or even crack when the surface of the sample is open. Therefore, it is necessary to wrap the surface of the sample with cling film and tape before the start of the test to ensure that it will not be damaged by water expansion during the capillary rise process. During the test, the height of water and salt migration was read and recorded at certain interval to obtain the relationship curve between the height of capillary rise and time. When the solution reaches and diffuses to the entire top surface of the sample, the capillary migration test was completed. After the capillary migration test, the samples were dried under laboratory conditions to measure the pore size distribution and mass loss.

2 RESULTS AND DISCUSSION

2.1 capillarity

The results of capillary migration test show that the presence of salt has a certain effect on the capillary migration of the solution in the soil sample. The capillary rise rate of distilled water in soil is the fastest, and the the mixed solution (1mol/kg Na_2SO_4+4mol/kg NaCl) with the highest concentration is the slowest. The capillary rise rate of other solutions is between the above two. However, the duration curve of the height change of various solutions did not show obvious changes with the increase of the concentration of the solution, the main reason may be that the mixed solutions with different concentration ratios were used.

2.2 Mass loss

Mass loss ratio among samples with the same initial water content (ω=15%) and different dry densities are shown in Figure 1. Generally speaking, no matter what kind of sample it is, Na_2SO_4, NaCl or soil, the mass loss ratio decreases with the increase of dry density. The mass loss ratio of Na_2SO_4 not only depends on the dry density of the sample, but also greatly influenced by the concentration of NaCl in the solution. When dry density is 1.4g/cm^3, the mass loss ratio of Na_2SO_4 increased with the increase of NaCl concentration. When the dry density increases to 1.6g/cm^3, the mass loss ratio of Na_2SO_4 first decreased and then showed a trend of increasing. For samples with dry density of 1.8g/cm^3, the mass loss ratio of Na_2SO_4 decreased with the increase of NaCl concentration. In terms of mass loss of NaCl and soil, for the soil sample with dry density of 1.4g/cm^3, the mass loss ratio of NaCl to soil is the largest, reaching 50% and 35%. Compared with the other two samples with different dry density, the mass loss ratio was much greater. The mass loss ratio of soil also presents a linear increase trend with the increase of NaCl solubility, and the growth rate increases with the decrease of dry density.

As can be seen in Figure 2, when the initial water content of the soil sample was 10% and 15%, the mass loss ratio of Na_2SO_4 was not much different, and the trend was similar with the change of solution concentration, showing a change law of first decreasing and then increasing. When the initial water content increased to

20%, the mass loss ratio of Na_2SO_4 for the sample decreased with the increase of NaCl content. The mass loss ratio of NaCl obviously decreased with the increase of initial water content, and increased with the increase of NaCl concentration, which is similar to the change law of the mass loss ratio of soil. The higher the initial water content of the sample, the smaller the mass loss ratio of the soil, and the increase of NaCl solubility will also cause the increase of the corresponding soil mass loss ratio. However, the higher the initial water content of the sample, the slower the growth rate of the mass loss ratio of the soil.

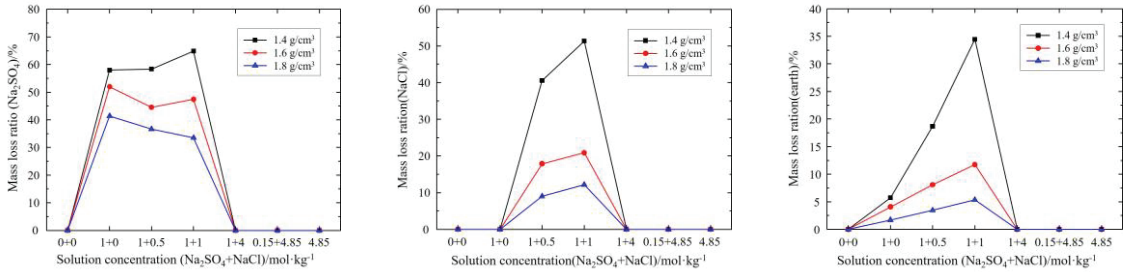

(a)Mass loss ratio of Na_2SO_4 (b)Mass loss ratio of NaCl (c)Mass loss ratio of earth

Figure 1. Mass loss ratio of samples with different dry density and the same initial water content

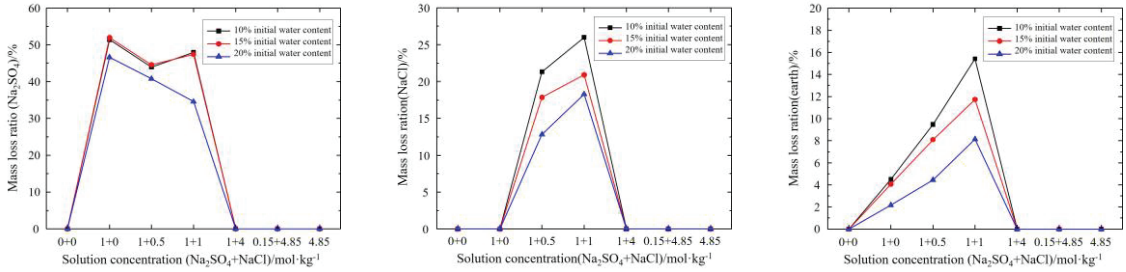

(a)Mass loss ratio of Na_2SO_4 (b)Mass loss ratio of NaCl (c)Mass loss ratio of earth

Figure 2. Mass loss ratio of samples with different initial water content and the same dry density

3 CONCLUSION

In general, in the process of capillary rise, the capillary rise height increased logarithmically with time, and the migration rate of the solution in the soil was not uniform, and gradually decreased with the increase of the capillary rise height. According to the prediction formula of capillary rise rate of unsaturated soil, the capillary rise rate depended largely on the permeability coefficient of soil, and the increase of dry density or initial water content reduced the permeability of soil. The diffusion effect of solution in soil could have a certain positive effect on the capillary rise rate, but its viscosity coefficient and bulk density have a more significant effect on the capillary rise rate, especially for high concentration solutions. In addition, the capillary migration test of the same type of sample was carried out with different solutions. After the test, the final volume containing solution of the soil was not very different. The difference in dry density and initial water content leads

to the significant difference in the final volume containing solution of the soil, but the saturation of the soil was mostly above 90%, which is relatively close.

During the drying process, the mixed salts did not precipitate out in equal proportion. In general, the mass loss ratio of samples with different dry density, initial water content and solution concentration was roughly sorted as follows: Na_2SO_4 > NaCl > Earth. Regardless of Na_2SO_4, NaCl or soil, the mass loss ratio decreased with the increase of dry density and initial water content, and the mass loss ratio of soil to NaCl also presented a linear increase trend with the increase of NaCl solubility, and the growth rate decreased with the increase of dry density and initial water content. The mass loss ratio of Na_2SO_4 gradually decreased with the increase of NaCl concentration when the density is small, and gradually increased with the increase of NaCl concentration when the density becomes large. For soil samples with initial water content of 10% and 15%, the mass loss ratio of Na_2SO_4 also showed a similar trend with the change of solution concentration, showing a change law of first decreasing and then increasing. When the initial water content increased to 20%, the mass loss ratio of Na_2SO_4 for samples decreased with the increase of NaCl content.

THE EFFECT OF SALT CONTENT ON THE ISOTHERMAL HYGROSCOPIC PROPERTIES OF CHINESE BLUE BRICKS

Lei Huo[1], Huarong Xie[1], Fan Wu[1], Yan Ma[1], Yonghui Li[1,*], and Shuichi Hokoi[1,2]

KEYWORDS

Isothermal sorption curves, Chinese blue bricks, Salt weathering

ABSTRACT

Moisture fluctuations within the brick are an important internal factor in the deterioration of the material. The presence of salt alters the hygroscopic behavior of the brick material, for example by increasing the frequency and degree of swelling, and freeze-thaw damage in winter due to moisture absorption. To investigate the differences in isothermal hygroscopic properties of blue bricks at different NaCl contents, isothermal hygroscopic curves were determined for bricks containing 0.07%, 0.4%, and 0.6% NaCl content. The results showed that the equilibrium moisture content of the bricks increased with increasing salt content at relative humidity levels ranging from 15% to 93%, particularly at high relative humidity levels. When the relative humidity is higher than 75%, the moisture absorption of the blue bricks with salt is much greater than that of salt-free blue bricks. This study explores the effect of the internal NaCl content on the hygroscopic properties of the bricks, giving fitted equations for the variation of equilibrium moisture content with relative humidity, and provides basic data to support the analysis of thermal and hygroscopic coupling of bricks considering salt.

[1] School of Architecture, Southeast University, Nanjing, China, liyonghui@seu.edu.cn

[2] School of Architecture Internationalization Demonstration, Southeast University, Nanjing, China

1 INTRODUCTION

As one of the major traditional building materials in China, blue bricks have been widely used in constructions ranging from city walls, palaces, tombs to humble dwellings. Blue brick belongs to the sintered brick, which is made mainly of clay. After blending with water, the clay is extruded into a brick billet, dried in the shade and then calcined in the brick kiln (about 1000℃), cooled with water, and then open and cooled out of the kiln [1]. Historical buildings constructed mainly with blue bricks have been subjected to physical, chemical, and biological erosion caused by natural and human factors in the environment over a long period of time, resulting in deterioration and diseases of the building structure. One of the factors that contribute to this is the variation in moisture content within the blue bricks, which can damage the internal pores of the bricks and ultimately lead to various forms of deterioration, such as salt crystallization, powdering, blistering, and spalling [2]. Therefore, it is necessary to predict the moisture variation inside the material.

The isotherm moisture sorption curve is one of the indicators that reflects the moisture variation within the material, and it is an important fundamental parameter for studying the degradation mechanism of material properties [3]. It is a smooth curve that connects the equilibrium moisture content of the material measured in air with different relative humidity under isothermal conditions, and can be used to measure the basic characteristics of material moisture absorption in natural environments [4].

In numerous studies on isothermal moisture adsorption, the focus has primarily been on the effects of factors such as materials [5-8], regions [3], ages [2], and experimental processes [4] [9-10] on the isothermal moisture adsorption characteristics, with insufficient consideration given to the influence of salt content within the materials. The presence of salt content within porous materials can alter their moisture adsorption behavior, accelerating their deterioration by increasing the frequency and degree of material expansion due to moisture absorption [11]. Currently, research on the influence of salt content has mainly focused on stone, mortar [12], and concrete materials [13-14], with relatively little attention given to traditional Chinese blue brick materials.

Therefore, it is necessary to conduct isothermal moisture adsorption experiments on blue bricks with different salt contents to study the relationship between salt content and isothermal moisture adsorption performance. In this study, the differences in isothermal moisture adsorption performance of bricks containing 0.07%, 0.4%, and 0.6% NaCl content were measured and analyzed. This provides fundamental data support for the hygrothermal coupling analysis of blue bricks considering salt content.

2 MATERIALS AND METHODS

2.1 Methods

The equilibrium moisture content (μ, EMC) represents the stable moisture content that a material reaches under a certain air state (temperature, relative humidity), and is calculated by the following formula:

$$\mu = \frac{m-m_0}{m_0} \quad (1)$$

where, the unit of μ is kg/kg. For convenience of calculation and comparison in this article, the unit in the later figures is g/kg. m and m_0 represent the mass of the blue brick sample at equilibrium state and dry state (the samples are dried in an oven at 105±5℃ until the difference in mass between the first and second measurements was less than 0.1%), respectively, kg.

To reflect the effect of material salt content on the equilibrium water content, the salt influence factor η proposed by Bai et al. [15] is used and defined as follows:

$$\eta = \frac{\mu_e}{\mu_c} \quad (2)$$

where μ_e is the EMC of each salt-contaminated group, g/kg; μ_c is the EMC of the control group without salt, g/kg.

2.2 Experimental Setup and Materials

The basic equipment used in the experiment includes a constant temperature box, desiccators, a weighing balance with an accuracy of 0.01g, a temperature and humidity recorder with a display resolution of 0.1℃/1%, and a conductivity meter with an accuracy of 2%FS.

The experimental blue brick samples have a porosity of about 18.2% and a density of 1.99 g/cm^3. The main pore diameter ranges from 100 nm to 10000nm, as shown in Fig. 1. In this study, brick samples with 4*2*2cm^3 size were divided into 4 groups, with group 1 as the control group without salt, and the other groups as the NaCl-contaminated groups. All groups were immersed in deionized water until the conductivity of the soaking liquid was below 200 us/cm, which was considered as complete desalination. The specimens were then dried in a drying oven until the difference in mass between the first and second measurements did not exceed 0.1%. After cooling at room temperature, the samples in salt-contaminated groups were then completely immersed in NaCl solutions with mass concentrations of 1%, 5%, and 10% for 12 hours, and then dried in the oven at 105±5℃ until completely dry. The samples were cooled to room temperature in a desiccator, and the experimental samples were prepared.

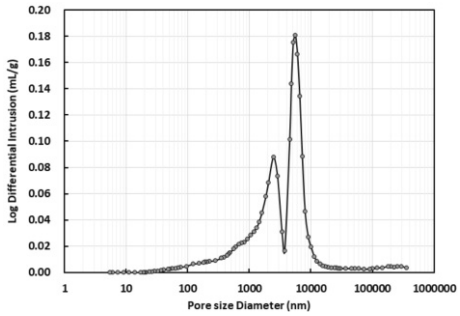

Figure 1: Pore structure of blue brick sample.

The salt content inside the samples was expressed in terms of chloride ion invasion amount, referring to the industry standards "Test Methods of Concrete for Water Transportation Engineering" (JTJ270-1998) [16] and "Standard for Quality and Inspection of Sand and Stone for Ordinary Concrete" (JGJ 52-2006) [17]. The salt content inside the blue bricks was determined by titration method, as shown in Table 1.

Table 1: Salt content and filtrate conductivity of blue bricks after salt invasion.

Salt solution concentration	0%	1%	5%	10%	Untreated samples
Conductivity of the filtrate (us/cm)	111	308	1250	out of range	129
The concentration of soluble ions (ppm)	2.485	74.55	407.3625	601.725	4.4375
Salt content (%)	0.000	0.072	0.405	0.600	0.002

2.3 Experiment

According to the national standard "Determination of Moisture Absorption/Desorption Performance of Wet and Thermal Properties of Building Materials and Products" (GB/T 35166-2017) [18] and "ISO 12571:2021" [19], the equilibrium moisture content of the blue brick samples was measured. Firstly, the samples were dried in an oven at (105±5℃) until completely dry, and the mass m_0 of each dried sample was measured at room temperature and 6% relative humidity (with a difference of less than 0.1% between two measurements). Secondly, the samples were placed in desiccators with relative humidity of 15%, 32%, 59%, 72%, 78%, 88%, and 93%, respectively, with five samples of every salt content in desiccators, for a total of 20 samples. The desiccators were placed in a constant temperature box at 20℃. The samples underwent moisture exchange in the desiccators until reaching moisture equilibrium (with a difference of less than 0.1% between two measurements). Finally, the equilibrium mass was measured using a weighing balance, and the mass of the saturated sample m was recorded. Different relative humidity environments were created using different saturated salt solutions. The measured values of relative humidity environment produced by different saturated solutions are shown in Table 2. Due to the measurement error of the thermohydrometer (accu-

racy of T&D RTR53A is 5% during 10%-95%), reagents and environmental factors, it will lead to differences in the measurement results. However, according to the results of the thermohydrometer, the relative humidity in the desiccator is always in a stable state, therefore it will not affect the hygroscopic equilibrium of the samples.

Table 2: The measured values of relative humidity environment produced by different saturated solutions.

Saturated salt solution	LiCl	$MgCl_2$	NaBr	KI	NaCl	KCl	Na_2SO_4
Relative humidity (%)	15±1	32±1	59±1	72±1	78±1	88±1	93±1

3 RESULTS

Fig. 2 shows the isothermal moisture absorption curve of the desalted blue bricks in the control group. The horizontal axis represents the relative humidity of the surrounding air, and the vertical axis represents the equilibrium moisture content of the sample after reaching thermal and moisture equilibrium. The figure shows the average, maximum and minimum values. The upper dotted line is maximum, and the bottom dotted line is minimum, and the solid black line is the mean value. The mean values in different relative humidity are connected. From the figure, the moisture absorption range of the blue bricks varies from 0.43 to 0.66 g/kg, 0.17 to 0.86 g/kg, 0.50 to 0.74 g/kg, 0.19 to 0.75 g/kg, 0.41 to 1.54 g/kg, 0.52 to 1.30 g/kg, and 0.88 to 1.94 g/kg at relative humidity of 15% to 93%, respectively. The blue bricks of the same batch showed significant differences in their isothermal moisture absorption capacity. The largest difference in equilibrium moisture content of blue brick samples was observed at a relative humidity of 78%, while the smallest difference was observed at a relative humidity of 15%. Some individual blue brick samples had moisture absorption capacity more than three times that of other blue brick samples at a relative humidity of 78%.

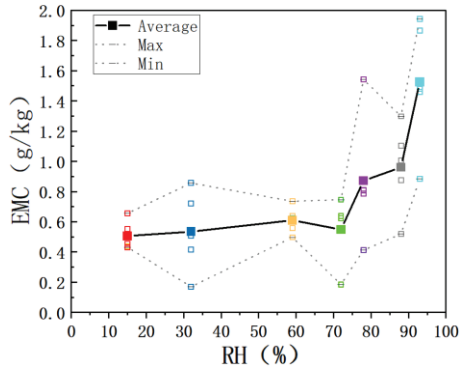

Figure 2: Isothermal moisture absorption curve of the desalted blue brick in the control group.

Fig. 3 shows the comparison of mean isothermal moisture absorption curves for blue bricks with different salt contents. From the perspective of relative humidity changes, for the desalted blue bricks in the control group, as the relative humidity

increases, the equilibrium moisture content shows an increasing trend, but the increase is relatively slow. For the blue bricks with salt content, as the relative humidity increases, the equilibrium moisture content shows an exponential increasing trend. When the humidity is below 75%, the equilibrium moisture content slowly increases with the increase of relative humidity. When the humidity is above 75%, the equilibrium moisture content increases rapidly at first, then slowly, and finally increases rapidly again, with the largest increase in the range of 88% to 93% relative humidity. From the perspective of salt content, when the relative humidity is below 75%, there is no significant correlation between the salt content and the equilibrium moisture content, and the equilibrium moisture content fluctuates within a range of 0.5 g/kg with the increase of salt content. When the relative humidity is above 75%, at the same humidity level, the equilibrium moisture content increases significantly with the increase of salt content, and the maximum equilibrium moisture content can reach 84.13 g/kg. At an environmental relative humidity of 93%, the equilibrium moisture content of blue brick samples with a NaCl concentration of 0.6% is about 54 times that of desalted blue brick samples.

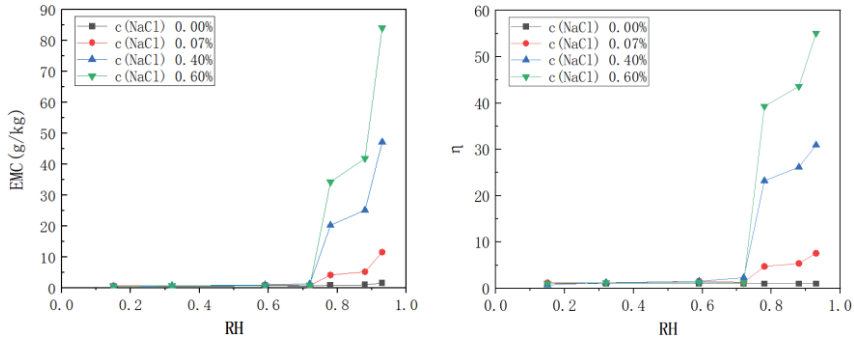

Figure 3: Comparison of mean isothermal moisture absorption curves for bricks with different salt contents. (a) The x-axis is the relative humidity, and the y-axis is the EMC. (b) The x-axis is the relative humidity and the y-axis is the salt influence factor η.

4 DISCUSSION

4.1 The applicability of the existing fitting formula

In blue brick samples, the presence of NaCl caused a sudden increase in equilibrium moisture content due to the absorption of a large amount of water through deliquescence when the relative humidity was above 75%. As shown in Fig. 3(a), the isotherm curve of the desalted control group can be approximated as a smooth curve and can be fitted using commonly used moisture equilibrium models [20-21]. Different models were used to fit the experimental data of the control group, as shown in Fig. 4, the Oswin equation has the best fit. As shown in Fig. 3, however, the isotherm curve of the samples with salt-contaminated groups is not consistent before and after 75% relative humidity. When the relative humidity was below 75%, the moisture absorption of blue bricks was mainly due to the physical adsorption

of its own porosity and pore structure and the chemical adsorption of other salts. The relative humidity was below the critical humidity for NaCl deliquescence, and although capillary condensation in the pores may have allowed a small amount of NaCl to dissolve, it was extremely weak. Furthermore, the weight of the blue brick samples increased slowly because the experimental samples were desalted samples with no other salts in the material. When the relative humidity is higher than 75%, NaCl will absorb a large amount of water and dissolve, resulting in a rapid increase in sample weight and making the equilibrium moisture content curve unable to be approximated as a smooth curve. Therefore, commonly used fitting models are not applicable in this case.

The hygroscopic process of salt-containing porous materials is roughly divided into two parts: firstly, the physical adsorption caused by the porosity and pore structure, and then the chemical adsorption in which the water molecules combine with the salts inside the materials to produce hydrates [22]. Therefore, the moisture content of salt-containing porous materials can be expressed as the sum of physical absorption moisture and chemical adsorption moisture affected by salt. In this paper, the fitting formula of adding salt content factors on the basis of Oswin model proposed by He et al. [13] is shown as Equation 3:

$$EMC = k_1\left(\frac{\varphi}{1-\varphi}\right)^{k_2} + \frac{k_3 S}{-ln\varphi} \tag{3}$$

where k_1, k_2, and k_3 are constants, φ is relative humidity, %, and S is salt content, kg/kg.

Fig. 5 shows the fitting results of the 0.6% NaCl content specimen with the Oswin and He model. As can be seen from the graphs, the He model has a better fit. However, when the relative humidity is below 40%, the fitting results show negative values, which is not consistent with the actual results. Therefore, this new model still needs to be optimized, for example, by adopting segmented fitting.

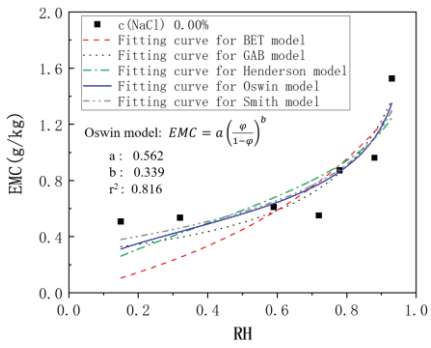

Figure 4: The fitting results of desalted samples with different models.

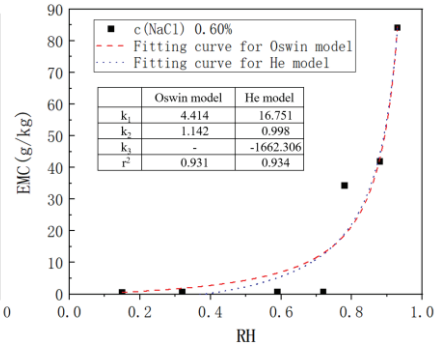

Figure 5: The fitting results of the 0.6% NaCl content samples.

4.2 Discussion on the actual salt content of cultural heritage

This article compared the differences in equilibrium moisture content of blue bricks under three different salt content conditions ranging from 74 to 601 ppm, all of which are consistent with the range of chloride ion concentration in brick and stone

cultural relics under actual conditions. Chen et al. [23] measured the salt content of various walls in the Mogao Grottoes, with the chloride ion concentration ranging from about 100 to 4217 ppm. Baptista et al. [24] measured the salt content of masonry at different locations on the exterior walls of historic buildings in downtown Rio de Janeiro, with the chloride ion concentration being less than 850 ppm. Therefore, the salt content conditions used in this article are within the range of actual engineering backgrounds of brick and stone cultural relics.

In actual historical buildings, the blue bricks, due to long-term invasion by groundwater and rainwater, contain different kinds and degrees of salt, and under the influence of these salts, the equilibrium moisture absorption of the bricks will be considerably higher than that of the bricks with lower salt content after being baked. Abuku et al. [14] conducted isothermal hygroscopic experiments of autoclaved aerated concrete immersed magnesium chloride solution, and showed that autoclaved aerated concrete in the environment above 32% of the equilibrium water content increases. This is due to the conditions of 20℃, magnesium chloride in the equilibrium relative humidity higher than 32% will be deliquescent hygroscopic.

5 CONCLUSION

In this study, the differences in isothermal moisture adsorption performance of bricks containing 0.07%, 0.4%, and 0.6% NaCl content were measured and analyzed. The main results are as follows:

(1) When the relative humidity exceeds 75%, the NaCl crystals within the blue bricks absorbs moisture from the air and deliquesces, resulting in a rapid increase in the moisture content of the sample, which is greater than that of the blue brick samples that do not contain NaCl.

(2) At a relative humidity of less than 75%, the effect of salt concentration on the moisture absorption of blue bricks is not obvious. However, at a relative humidity greater than 75%, the higher the salt content, the greater the equilibrium moisture content of the blue bricks. At 20°C and 93% RH ambient condition, the moisture absorption of bricks with 0.4% NaCl concentration was 30 times that of bricks without NaCl, and that of bricks with 0.6% NaCl concentration was 54 times that of bricks without NaCl.

(3) The fitted relational equation with good performance on NaCl-containing concrete materials does not apply to the salt-containing blue bricks that were the subject of this experiment, and it may be necessary to consider relative humidity segmentation.

ACKNOWLEDGEMENTS

This work was supported by the National Natural Science Foundation of China under grant number 5210081745.

REFERENCES

[1] W. Yang, and X. Wen, " Antique blue brick and fired common brick on the quality of the research," *China Building Materials Science & Technology*, vol. 26, no. 03, pp. 20-22, 2017.

[2] Y. Li, Y. Cai, H. Xie, and J. Zhang, "Comparison of isothermal sorption properties of gray bricks in different ages in Wenzhou Qiaolou site," *Journal of Southeast University. Natural Science Edition,* Article vol. 50, no. 2, pp. 327-333, 2020.

[3] Y. Li, H. Xie, J. Wang, and X. Shi, "Comparative Study of Isothermal Sorption Properties of Traditional Blue Bricks in Historic Building," *Journal of Building Materials,* Article vol. 17, no. 6, pp. 1092-1095, 2014.

[4] C. Feng, "Study on the Test Methods for the Hygric Properties of Porous Building Materials," D.E.thesis, South China University of Technology, 2014

[5] A. A. Chiniforush, A. Ataei, H. R. Valipour, T. D. Ngo, and S. Malek, "Dimensional stability and moisture-induced strains in spruce cross-laminated timber (CLT) under sorption/desorption isotherms," *Construction and Building Materials,* vol. 356, 2022.

[6] L. Li, X. Zhang, X. Han, and D. Zhu, "Experimental Research of Isothermal Sorption Curve of Building Materials," *Journal of Building Materials,* Short Paper vol. 12, no. 1, pp. 81-84, 2009 2009.

[7] H. Zhao, Z. Yan, W. Bi, L. Sun, X. Wang, and Z. Zhang, "Study on the moisture absorption isotherms of the simulation test block in Mogao Grottoes' plaster in Dunhuang," *Journal of Xi'an University of Architecture & Technology. Natural Science Edition,* Article vol. 50, no. 5, pp. 704-707, 2018 2018.

[8] Y. Li, H. Xie, J. Wang, X. Li, and J. Wu, "Experimental research on isothermal sorption properties of early modern and modern gray bricks in Wujiang, Suzhou, China," *Journal of Southeast University. Natural Science Edition,* Article vol. 44, no. 2, pp. 441-444, 2014 2014.

[9] J. Wang, M. H. N. Yio, T. Zhou, H. S. Wong, C. T. Davie, and E. Masoero, "Water sorption isotherms and hysteresis of cement paste at moderately high temperature, up to 80 °C," *Cement and Concrete Research,* vol. 165, 2023.

[10] T. Colinart, P. Glouannec, M. Bendouma, and P. Chauvelon, "Temperature dependence of sorption isotherm of hygroscopic building materials. Part 2: Influence on hygrothermal behavior of hemp concrete," *Energy and Buildings,* vol. 152, pp. 42-51, 2017.

[11] B. Taye, H. Viles, and H. Zhang, "Influence of salt (NaCl) on hydric and hygric dilatation of clay-rich rocks," *Journal of Cultural Heritage,* vol. 58, pp. 137-145, 2022/11/01/ 2022.

[12] M. PavlÍKovÁ, Z. PavlÍK, and P. MatiaŠOvskÝ, "Water Vapour Storage Capacity of Masonry Renovation Plasters Contaminated with Chlorides," *Materials Science,* vol. 24, no. 4, 2018.

[13] J. He, Q. Li, Q. Meng, P. Ren, S. Li, and H. Wu, "Experimental investigation of the effect of salt on the hygroscopic properties of autoclaved aerated concrete," *Construction and Building Materials,* vol. 370, 2023.

[14] M. Abuku, D. Ogura, and S. Hokoi, "Measurement and Modeling of Water Sorption Isotherm of Autoclaved Aerated Concrete with Salt," *Journal of Environmental Engineering (Transactions of AIJ),* vol. 79, no. 700, pp. 499-506, 2014.

[15] L. Bai, J. Xie, J. Liu, and Y. Xie, "Effect of salt on hygroscopic properties of cement mortar," *Construction and Building Materials,* vol. 305, 2021.

[16] "Test Methods of Concrete for Water Transportation Engineering (JTJ270-1998)," Chinese version JTJ270-1998, 1999

[17] "Standard for Quality and Inspection of Sand and Stone for Ordinary Concrete (JGJ 52-2006)," Chinese version JGJ 52-2006, 2006

[18] "Hygrothermal performance of building materials and products - Determination of hygroscopic sorption properties (GB/T 35166-2017)," Chinese version GB/T 35166-2017, 2017.

[19] "Hygrothermal performance of building materials and products - Determination of hygroscopic sorption properties (ISO 12571:2021)," German version EN ISO 12571:2021.

[20] Y. Gu, D. Zhang, and F, Ming, "Experimental Research on the Isothermal Hygroscopic Performance of Thermal Insulation Materials," *China Rural Water and Hydropower*, Article vol. 175, no. 4, pp. 162-165, 2022.

[21] M. Mozaffari Majd, V. Kordzadeh-Kermani, V. Ghalandari, A. Askari, and M. Sillanpaa, "Adsorption isotherm models: A comprehensive and systematic review (2010-2020)," *Sci Total Environ,* vol. 812, p. 151334, Mar 15 2022.

[22] Y. Wen, M. Ran, R. Zheng, and R. Liu, "Inquiring into the law of wetting and unwetting properties of salt and porous materials," Journal of Sichuan Normal University(Natural Science), vol. 19, no. 2, pp.105-110,1996.

[23] G. Chen, B. Min, L. Zhao, Z. Yu, J. Li, and A. Neville, "Simulation test of efflorescencefor murals in Cave 85 of Mogao Grottoes," *Dunhuang Research*, vol. 92, no. 4, pp. 62-66, 2005

[24] J. A. Baptista Neto, C. Gaylarde, I. Beech, B. J. Smith, and J. J. McAlister, "Degradação de gnaisse e granito em fachadas de edifícios históricos no centro do Rio de Janeiro," *Sistemas & Gestão,* vol. 15, no. 1, pp. 80-90, 2020.

THE NEW RILEM TC 271-ASC RECOMMENDATION FOR THE DURABILITY ASSESSMENT OF POROUS BUILDING MATERIALS AGAINST SALT CRYSTALLIZATION

D. Gulotta[1] and RILEM TC 271-ASC members[2]

KEYWORDS

Salt accelerated aging, sodium sulfate, sodium chloride, stone, brick.

EXTENDED ABSTRACT

Salt crystallization is among the most harmful deterioration mechanisms impacting the preservation of porous building materials worldwide. Therefore, predicting the materials' response to salt damage is crucial in the conservation practice and building sector to guarantee adequate performance and durability. These, in turn, are instrumental to achieving sustainable interventions. Numerical models have been developed to describe the salt decay susceptibility quantitatively, but the most diffused approach still relies on performing accelerated weathering tests in laboratory conditions.

So far, the main limitations associated with most of the available experimental and standard accelerated weathering tests arise from the generally long time they require, the lack of consensus on the methods for assessing the damage progression and extent, and the use of testing scenarios hardly representative of real-world conditions. These include simulating unrealistic accumulation and salt transport processes, which in turn significantly affect the resulting deterioration patterns and the final damage extent, and the use of remarkably high salt solution concentrations.

The RILEM Technical Committee (TC) 271-ASC, active between 2016 and 2022, pursued an innovative direction to simulate more realistic salt crystallization pathways to test single porous materials (stone and fired-clay brick units). The TC aimed to develop a reliable accelerated aging procedure for laboratories in the architectural heritage conservation and construction sectors. The requirements for the

[1] Getty Conservation Institute, Science Department, Los Angeles, US, dgulotta@getty.edu

[2] www.rilem.net/groupe/271-asc-accelerated-laboratory-test-for-the-assessment-of-the-durability-of-materials-with-respect-to-salt-crystallization-355

new procedure focused on achieving realistic results in a relatively limited time, without significantly altering the deterioration process and allowing for a simple damage assessment based on readily available and non-sophisticated techniques. The test simulates the deterioration effects induced by capillary transport of sodium sulfate and sodium chloride aqueous solutions, considered as single salts, toward the evaporative surface of cylindrical specimens.

Building on the experience of reinforced concrete durability research, the TC has explored the feasibility of a two-stage approach (Fig. 1) to trigger damage development and progression, only after a certain degree of pore filling – as a result of salt accumulation – is reached.

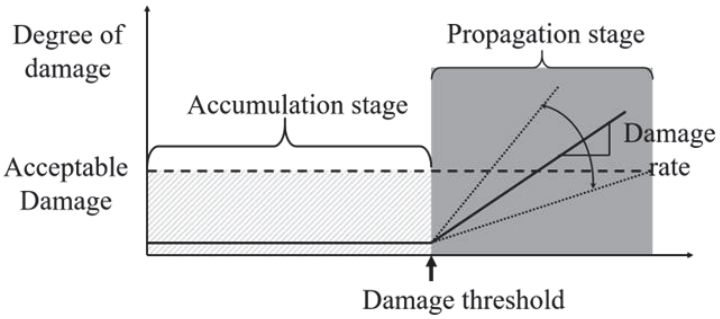

Figure 1: Two-step damage development of stone/brick substrates due to salt crystallization (from [1])

The new procedure translates this theoretical assumption into two distinct testing phases: a preliminary salt accumulation phase, during which the porous substrate is contaminated with a salt solution with fixed concentration and capillary transport promotes its accumulation close to the evaporation surface without causing visible damage, followed by a propagation phase (Fig. 2).

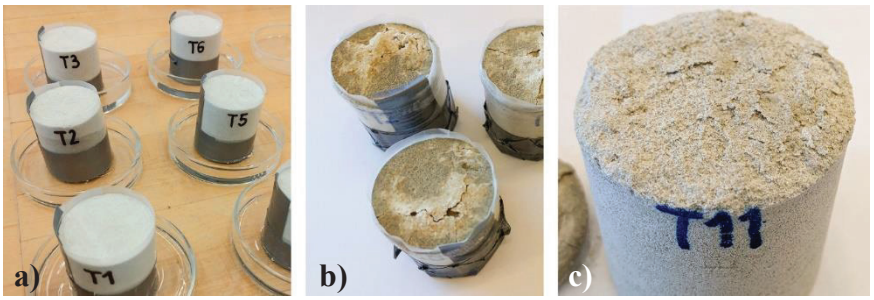

Figure 2: Photographic documentation of stone specimens (Tuffeau limestone) during the accumulation phase (a), after two propagation cycles (b), and at the end of the accelerated aging procedure (c).

The propagation phase activates the damage development due to repeated crystallization and dissolution cycles. The testing conditions for the accumulation phase are the same for both salts. Specimens are subjected to capillary absorption of 5% and 10% concentrations (mass %) of sodium sulfate and sodium chloride solutions and then dried until the evaporation of at least 80% of the absorbed water.

The propagation phase follows, based on four 3-week cycles. Differently from the accumulation phase, the set conditions of such cycles differ (i.e., T and RH values, duration, and use of rewetting stages) depending on the type of salt employed. In brief, each single 3-week cycle of the propagation phase of NaCl employs a series of high relative humidity adsorption sub-cycles alternated with drying stages, followed by a rewetting step and a final drying (Fig. 3a). Each Na_2SO_4 propagation phase starts with a cooling and rewetting sub-cycle at room conditions, followed by drying (Fig. 3b). The rewetting steps for both salts are carried out with deionized water only.

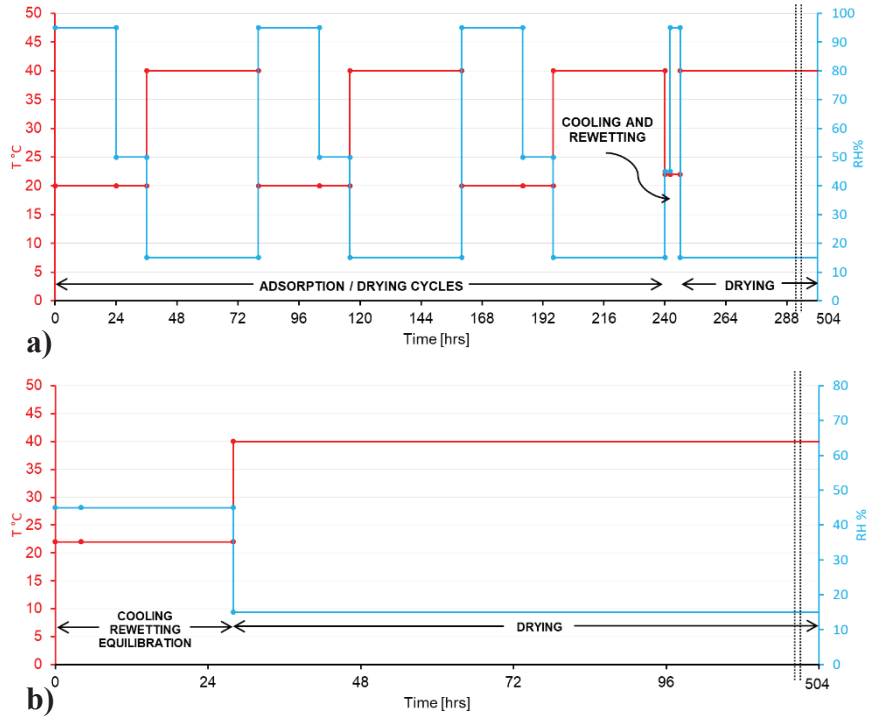

Figure 3: Testing conditions (propagation phase) characterizing each 3-week cycle of the NaCl (a) and Na_2SO_4 (b) testing procedure.

Two round-robin testing programs have been conducted to validate the accelerated weathering procedure, involving ten research laboratories across Europe and the US [2]. The substrates tested during the validation phase include five stones (Lecce, Massangis and Migné limestone, Tuffeau, and Mšené "Prague" sandstone) and two

fired-clay bricks. The physical characteristics of such substrates cover an open porosity range between 13% and 50% (vol %) and a capillary water absorption interval between 50 and 1070 $g/m^2s^{0.5}$.

The new accelerated aging procedure has been recently published as a RILEM recommendation [3]. The document details the two procedures for testing single porous materials and includes a simplified methodology based on visual observations, photographic documentation, and mass loss recording to guide the evaluation of the salt crystallization results. A damage glossary for identifying the deterioration patterns is also provided, derived from selected terms of the ICOMOS-ISCS Stone Deterioration Glossary [4] and the MDCS Damage Atlas [5].

REFERENCES

[1] J. Flatt et al., "Predicting salt damage in practice: a theoretical insight into laboratory tests," RILEM Tech. Lett., vol. 2, pp. 108–118, 2017.

[2] B. Lubelli et al., "A new accelerated salt weathering test by RILEM TC 271-ASC: preliminary round robin validation," *Materials and Structures*, 55: 238, 2022.

[3] B. Lubelli et al., "Recommendation of RILEM TC 271-ASC: New accelerated test procedure for the assessment of resistance of natural stone and fired-clay brick units against salt crystallization," *Materials and Structures*, in press.

[4] ICOMOS-ISCS, Illustrated glossary on stone deterioration patterns. 2008. www.icomos.org/public/publications/monuments_and_sites/15/pdf/Monuments_and_Sites_15_ISCS_Glossary_Stone.pdf (accessed May 4, 2023)

[5] "MDCS Damage Atlas." https://mdcs.monumentenkennis.nl/damageatlas (accessed May 4, 2023).

WATER AND SALT MIGRATION MODELS AND SALT CRYSTALLIZATION EROSION MECHANISMS FOR STONY ARTEFACTS IN MICROCLIMATES

FUZHI WANG[1,2], JIZHONG HUANG[1,2,*], and QITING ZHOU[1,2]

KEYWORDS

Salt damage, Crystallization pressure, Water and salt migration, Microclimates, Capillary absorption

ABSTRACT

Environmental factors control salt destruction characteristics in porous materials and determine the salt weathering mode and salt-action mechanism. The article focuses on the influence of cultural heritage microclimate on salt weathering, and the study aims to understand the weathering mechanism by combining the theory of crystalline weathering with temperature and humidity variation. Studies include sandstone salt solution immersion and simulation of salt deterioration under on-site cyclic variable temperature and humidity conditions. The article designs the accumulation of salt crystallization at the sandstone surface under the effect of salt evaporation and visualizes the water-salt migration and crystallization process by ion chromatography (IC), microelectrode, and hyperspectral techniques. The corresponding types of sulfate deterioration under different weathering simulation conditions are investigated to probe the mechanism behind different weathering patterns. In the first part, we construct a water-salt migration test, combining hyperspectral techniques and microelectrodes to visualize the weathering patterns, compositional characteristics, and spatial and temporal changes of water-salt transport based on Fick's law to establish a mathematical model and simulate it in COMSOL multi-physics field simulation software. Then, variable temperature and humidity tests of sulfate solution were conducted on sandstone to simulate the salt weathering process. It was demonstrated that different salt solutions, such as Na_2SO_4 and $MgSO_4$, exhibit different weathering patterns after multiple weathering cycles, and

[1] Institute for the Conservation of Cultural Heritage, Shanghai University, 99 Shangda Road, Shanghai, China, 20044，1264171204@shu.edu.cn

[2] Department of Civil Engineering, Shanghai University, 99 Shangda Road, Shanghai, China, 200444

the salt crystallization patterns under variable temperature and after the cycle of variable humidity differ significantly.

1 INTRODUCTION

Salt crystallization is one of the most critical factors affecting the preservation of stone cultural heritage, and the repeated dissolution and crystallization of soluble salts and the migration and crystallization of salt solutions in rock pores with water precipitation are the leading root causes of salt weathering of stone cultural heritage [1].

The critical factor affecting salt weathering is water-salt migration, where soluble salts from the natural environment rise by capillary action, and the movement of water salts through porous materials also disperses and deposits the salts into the pores and cracks of the sandstone, resulting in sandstone destruction [2]. Salt weathering is usually reproduced in the laboratory by accelerated aging tests, and the combination of in situ deterioration samples, microscopic characterization of associated damage patterns, and chemical and mineralogical analysis is a hot research topic. Regarding the laboratory simulation of salt weathering, there is no universally accepted aging test; in addition, the analysis and evaluation of samples after salt aging tests usually vary with demand, and multiple visualization tools such as CT, NMR, and SEM have been used to study the deterioration of sandstone caused by salt crystallization.

The dynamic changes of water-salt distribution and sandstone properties during salt weathering involve complex mass transfer mechanisms. Existing studies on water-salt capillary transport mechanisms indicate that the lower the relative humidity of air with microenvironmental changes, the more water migrates to air during capillary ascent, while crystalline stratification of soluble salts occurs during capillary water ascent [3]. The simulation study of water-salt migration kinetics is a means to predict the change and spatial distribution of soluble salt content. In mathematical modeling, advanced visualization tools and physicochemical methods are used to obtain model parameters to explore ion migration phenomena during salt transport in sandstone. The standard approach to studying the effect of environmental conditions and salt weathering on sandstones is to simulate the salt weathering process under laboratory conditions, usually based on "cyclic immersion" conditions, which is very different from the in situ salt weathering model of stone artifacts [4]. The partial immersion is based on the phenomenon of capillary rise of the salt solution, which is more reasonable. The samples were subjected to various environmental conditions by controlling the temperature and humidity, and various techniques were used to test the samples while obtaining the relationship between salt crystallization and sandstone deterioration.

In this study, the microenvironmental reconstruction of the endowment environment of stone artifacts was carried out in the laboratory, and the salt concentration of sulfate solution in Yungang sandstone under natural immersion conditions was experimentally analyzed [5]. Microelectrode equipment, hyperspectral and ion chromatography were used to detect the sandstone samples to obtain the distribution of continuous elemental content and the diffusion coefficient of aqueous salt

at the sampling points; Fick's law was introduced to establish the diffusion coefficient of sulfate ions in the sandstone, and finite element analysis was carried out to intuitively understand the content and distribution state of salt in the sandstone. The effect of aqueous salt migration to the sandstone surface on the damage pattern of sandstone was investigated, and the salt damage triggered by capillary migration of sulfate solution to the evaporated surface of sandstone was reproduced by setting up a temperature and humidity cycling group in the laboratory [6]. The deterioration mechanism of the grotto sandstone under the action of sulfate was revealed by analyzing the evolution law of ultrasonic velocity, porosity, and other physicomechanical indexes with cycling [7].

2 MATERIALS AND METHODS

2.1 Sandstone materials and characterisation

The samples used in this experiment were taken from sandstone from the Yungang Grottoes and were dry-cut. Only Yungang sandstone was used for the salt immersion test and cut into rectangular sizes of 50 × 10 × 200 mm; sandstone was selected for the salt temperature and humidity cycling test and processed into sizes of 50 × 50 × 50 mm. Lithologically the Yungang sandstone is a medium to coarse-grained feldspathic quartz sandstone with predominantly calcareous cementation. The physical properties and chemical composition of the sandstones used in the tests are shown in Table 1 and Table 2. According to Figure 1b X-ray diffraction, the sandstone detects a characteristic peak of $KAlSi_3O_8$, which from the results of Figure 1a and b, is because the sandstones all contain some amount of orthoclase ($KAlSi_3O_8$) and the sandstones all have a high specific gravity of clay minerals, dominated by limonite, illite, and kaolinite.

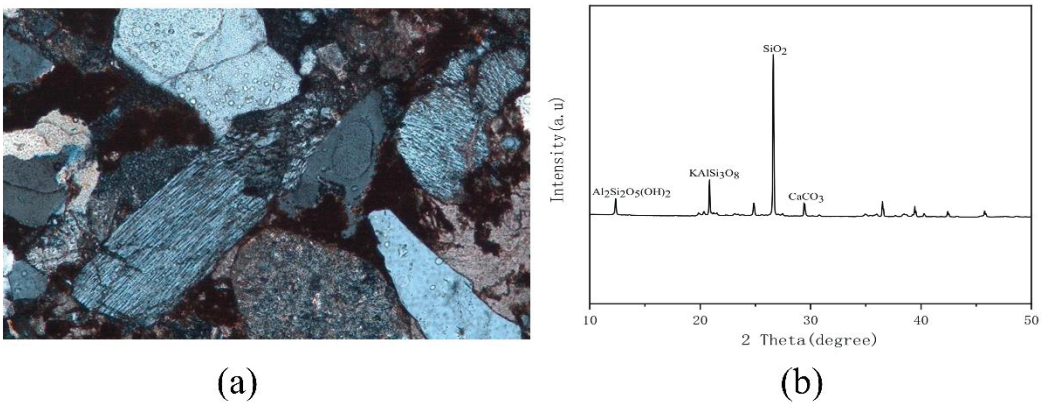

Figure 1: Characterization of fresh Yungang sandstone: a) Polarimetric petrographic images; b) XRD.

Table 1: Physical properties of the sandstones.

Sample locations	Properties					
	Dry density (g/cm^{-3})	Compressive strength (MPa)	Free absorption of water (%)	Saturated water absorption Rate (%)	Ultrasonic speed (km/s)	Porosity （%）
Yungang Grottoes	2.41	56.74	3.16	3.24	2.46	3.75

Table 2: Chemical properties of the sandstones.

Sample locations	Major element (%)				
	SiO_2	Al_2O_3	CaO	Fe_2O_3	K_2O
Yungang Grottoes	47.90	5.54	2.58	2.01	1.38

2.2 WATER-SALT MIGRATION TESTS AND FINITE ELEMENT ANALYSIS

2.2.1 Salt immersion test

In order to study the mechanism of water salt migration in sandstone specimens set up for evaporation conditions while visualizing the migration model set up for capillary absorption experiments, the natural immersion method was used to characterize the movement of sulfate ions and indirectly obtain the diffusion coefficients of sulfate in Yungang sandstone, the test method is shown in Figure 2. The test temperature was 22 °C, 66% RH, and the immersion time (2 d, 4 d, 6 d, 8 d, and 10 d) to simulate the water-salt migration time in the field. The sandstone size was 50 × 100 × 200 mm, and the bottom was immersed in 1 mol/L saturated sodium sulfate solution for 20 mm, and the solution was replenished with the same concentration every five days. Microelectrode, hyperspectral, and ion chromatography tests were performed on the test samples at every 2 d. Microelectrode and hyper spectroscopy were non-destructive, and ion chromatography was used to collect samples in the form of boreholes, and the sandstone was analyzed by taking a total of 4 points at a depth of 25 mm internal sandstone at 50 mm height intervals at the midline position of the sandstone.

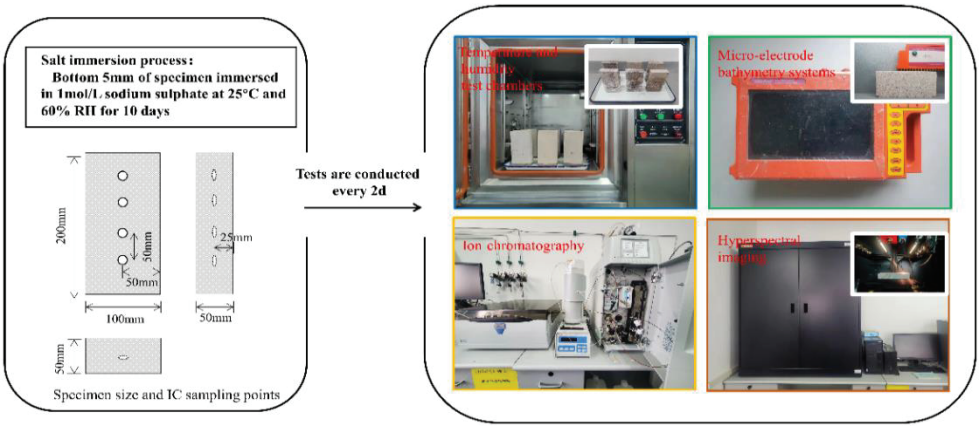

Figure 2: Salt immersion test processing procedures.

2.2.2 Basic theory of ion diffusion

Fick's law is the fundamental law followed by the diffusion of substances. Fick's second law applies to steady-state and transient solutions and considers the relationship between concentration and distance. In this study, the effective diffusion coefficient of Na2SO4 in the Yungang sandstone was calculated by substituting the content of different sites at different moments in time into the mathematical model of Fick's second law. The model assumes that the sandstone is rectangular, the salt solution migrates in one direction, the diffusion coefficient is constant, resistance and temperature variations are neglected, and the mathematical expression is shown in equation (1).

$$\frac{\rho_T^{Na_2SO_4} - \rho_S^{Na_2SO_4}}{\rho_0^{Na_2SO_4} - \rho_S^{Na_2SO_4}} = 2\sum_{n=0}^{\infty} \frac{1}{\lambda_n^2 - L^2} e^{-D\lambda_n^2 T} \tag{1}$$

here $\rho_0^{Na_2SO_4}$, $\rho_T^{Na_2SO_4}$, and $\rho_S^{Na_2SO_4}$ is Ionic content of Na_2SO_4 in sandstone at initial state, equilibrium and time T; T is Maintenance time; L is half of the thickness of the sample (cm); and λ_n^2 is Eigenvalue $\lambda_n L = (2n+1)\frac{\pi}{2}$.

The diffusion coefficient D describes the ratio between the flux and the concentration gradient and is related to Fick's law. The concentration of ions passing through a unit area of sandstone sample per unit of time is expressed as the diffusion flux, as in equation (2):

$$J = \frac{1}{A}\frac{d\Delta M}{dt} \tag{2}$$

Where A is the area of diffusion and is the cross-sectional area of the specimen (m^2); $\frac{d\Delta M}{dt}$ is the rate of salt solution loss during the experiment. Based on Fick's first law, the following equation (3) for the variation of ion concentration with distance at each location during diffusion:

$$J = -D\frac{d_\rho}{d_y} \tag{3}$$

where D is the effective diffusion coefficient of the sandstone, d_ρ /d_y is the ionic concentration gradient of the soluble salt, with the negative sign indicating the diffusion of sulfate ions from higher to lower concentrations.

As the thickness of the sandstone specimen used in the steady-state test was taught to be thin, the differential rewriting of equation (2) gives equation (4):

$$J = -D\frac{\rho_T - \rho_0}{L} \tag{4}$$

The effective diffusion coefficient D can be obtained from equations (2) and (4), see equation (5):

$$D = -\frac{1}{A}\frac{d\Delta M}{dt}\frac{L}{\rho_T - \rho_0} \tag{5}$$

The diffusion coefficients were calculated according to Eq. (5) and brought into COMSOL Multiphysics, finite element analysis-based multiphysics field simulation software with multiphysics field modeling of complex points, to model ion diffusion.

2.3 Assessment of sandstone salt ageing under evaporative conditions

2.3.1 Variable temperature and humidity salt ageing test

In order to simulate the deterioration mechanism of sandstone sulfate caused by water-salt migration under different ambient temperatures and humidity, the aging test of soluble salt crystallization under variable temperature and humidity conditions was carried out in the laboratory. The test procedure is shown in Figure 3. Based on the reproduction of the climate microenvironment at the Yungang Grottoes site in China, two test conditions, temperature and humidity cycling, were set to investigate the specific effects of individual environmental factors on the crystallization behavior of sulfate in porous media. Different soluble salt solutions used for capillary absorption, corresponding to the specimen names in Table 3, were infiltrated by different sulfates with a solution concentration of 1 mol/L, setting up humidity and temperature groups. In the relative temperature group, only the relative humidity conditions were varied from 30% to 80%, with a total of nine 96-h cycles (80% high RH for 72 h and 30% low RH for 24 h), and the temperature was set at a constant 25 °C. In the relative temperature group, the humidity was controlled to be 60%, and the relative temperature was varied between high and low, with a relatively low temperature of 15 °C for 72 h and a relatively high temperature of 50 °C for 24 h. The same setup was performed for nine cycles. The bottom of the specimen was immersed into the salt solution for 5 mm, and the temperature and humidity were changed every 2 h. Surface photographs were taken to measure the ultrasonic velocity and mass change; the same specimen was taken to do a nuclear magnetic resonance (NMR) test every three cycles.

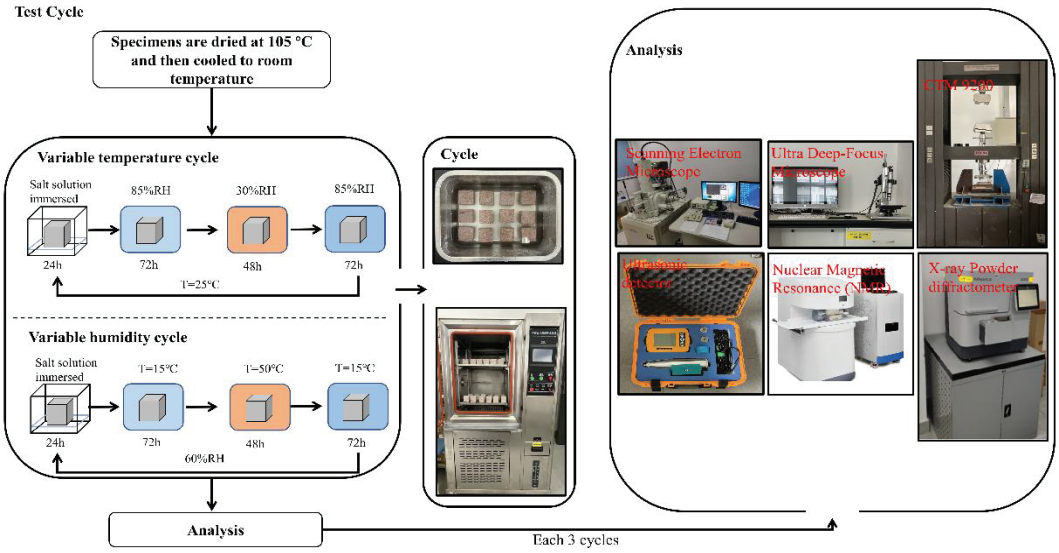

Figure 3: Variable temperature and humidity cycling tests on Yungang sandstone under sulphate （Na_2SO_4、$MgSO_4$）solution.

Table 3: Experimental scheme.

	Sample	solutions	Relative humidity (%)		Temperature (°C)	
			a) Low RH	b) High RH	c) Low Temp	d) High Temp
Relative humidity cycles	N-H	Na_2SO_4	30	80	25	25
	M-H	$MgSO_4$	30	80	25	25
Relative temperature cycles	N-T	Na_2SO_4	60	60	15	50
	M-T	$MgSO_4$	60	60	15	50

3 RESULTS AND DISCUSSION

3.1 Water-salt migration and salt assessment

3.1.1 Water-salt migration and diffusion coefficients

Figure 4 shows the dry and wet interface depths for different days of the salt immersion test. The spatial and temporal evolution characteristics of capillary rise and salt accumulation were determined by resistivity.

The distribution of sulfate ions in different cross-sections of sandstone with time was obtained by hyperspectral image analysis combined with resistivity and ion chromatography. Among the 2 d test days, the diffusion of Na_2SO_4 in the sandstone is shown in Figure 4. According to the high resistivity with hyperspectral imaging to define the location of water salt, with the increase of test days, the surface salt cover of sandstone thickened, resulting in the absorption of a large amount of salt solution in the middle of sandstone at 6 d, and the salt migration rate slowed down,

and the change of salt with days is shown in Figure 5. Figure 4(d) results show that the content of sulfate ions at different locations, with the time increase, the 40 mm, 80 mm, and 120 mm locations of sulfate ion concentrations had the same trend, increasing with increasing immersion time. By 6 d, the increase in concentration at the top increased, and the ion concentration at the middle shifted due to the replenishment of sulfate ions from the top by the middle during immersion.

The rate of salt migration has a similar transmission time at different depths, and the sandstone surface is firstly aggregated, and then the rate of aqueous salt rise is gradually stabilized, and the effective diffusion coefficient D of Na_2SO_4 in sandstone is calculated as 3.937×10^{-7} m^2/s according to The Fick's law.

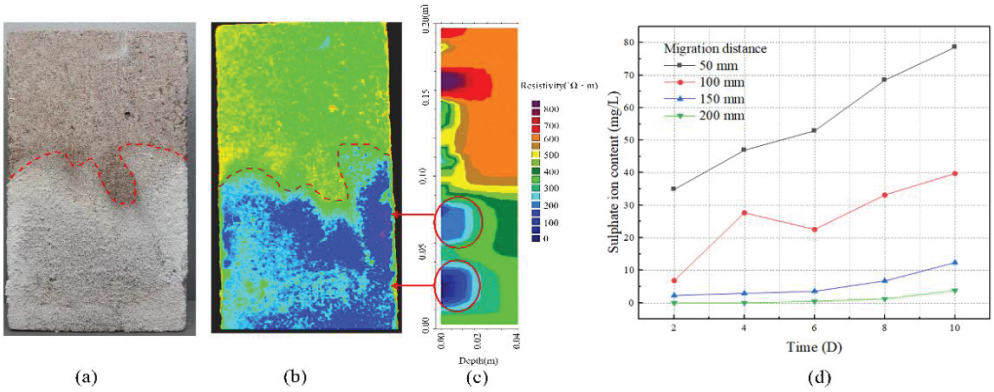

Figure 4: Measurement of capillary rise of water salts over time: 2 d immersion test：a) Visible light images; b) Hyperspectral images; c) Resistivity images; d) Sulphate ion content at different locations.

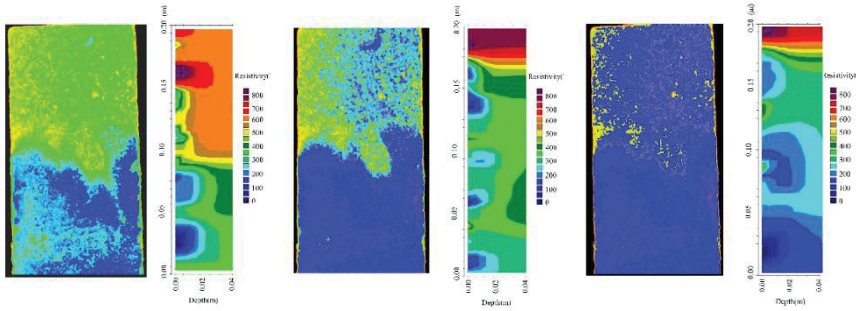

Figure 5: 10 d sodium sulphate solution immersion test.

3.1.2 Analysis of COMSOL simulation results

As shown in Figure 6, Na_2SO_4 gradually decreases with increasing diffusion distance, and the trend of sodium sulfate content changes with increasing maintenance time in the region of flat and uniform distribution. The sandstone model was used to verify further the effective diffusion coefficient in the sandstone obtained from

the test. The initial Na_2SO_4 content was 0 mol/m^3, and the contact surface Na_2SO_4 content was 1 mol/L. The diffusion coefficient of Na_2SO_4 in the sandstone was set to 3.937×10^{-7} m^2/s. The initial Na_2SO_4 content was 0 mol/m^3, and the contact surface Na_2SO_4 content was 1 mol/L. The changes in water salt distribution with time were analyzed using COMSOL for porous sandstone immersed in Na_2SO_4 concentration of 1 mol/L for 10 d. Figure 6b plots the variation of ion concentration with time for sandstone at different distances from the bottom position. The diffusion process of Na_2SO_4 in sandstone with an increasing number of days had a similar trend. The Na_2SO_4 content in the sandstone for the same number of days gradually decreases with increasing distance of Na_2SO_4 diffusion, and the salt concentration grows faster in the first 4 d, and the increasing trend becomes slower with time. Tests were conducted to collect soluble salt crystallization data to be used for further validation of the model, and a comparison of the model results for salt migration over time and the test results is shown in Figure 6b, where it can be seen that there is a good agreement at the specimen 150 mm and 200 mm, where some deviation is due to the asynchronous migration between the surface and the interior of the specimen at 100 mm, but the final trend is consistent.

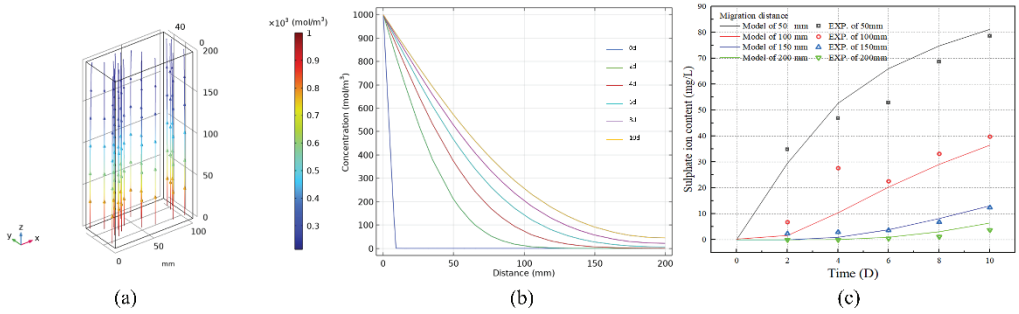

Figure 6: Schematic diagram of the COMSOL simulation: a) Sandstone flow diagram after 10 d of simulation; b) 1D line diagram of Na_2SO_4 concentration; c) Comparison of experimental data and modeling results on the migration of sodium sulfate solutions

3.2 Sandstone properties under variable temperature and humidity tests

3.2.1 Ultrasonic velocity and Mass loss rate

The changes in the ultrasonic velocity of the specimens during the temperature and humidity cycling test are shown in Figure 7. In Figure 7a, for the humidity cycling group, the ultrasonic velocity of the specimens in the N-H group was reduced to 60% of the wave velocity of fresh sandstone after nine humidity cycles, and that of the specimens in the M-H group was reduced to 72%; the ultrasonic velocity changes of the temperature cycling specimens are shown in Figure 8b, and the N-T and M-T groups were 78% and 88% of the initial sandstone wave velocity after temperature cycling, respectively.

The initial mass measured varies between fresh specimens, and the rate of mass loss, C, is used to express the flaking of the specimens, see equation (6):

$$C = \frac{\Delta m}{m_0} \tag{6}$$

where Δm is the mass lost, and $m_0$is the mass of fresh sandstone. The variation of specimen mass loss rate with the number of humidity cycles during humidity cycling is shown in Figure 7c. It can be seen that the sandstone exfoliated mass in the sulfate solution saturated over specimens under the action of humidity cycling keeps rising, and the rate of rise gradually increases, and the temperature cycling group, as shown in Figure 7d, shows the same trend as the humidity cycling group. It can be seen that the mass loss rate of sandstone in sodium sulfate solution saturated over is higher than the value of magnesium sulfate solution saturated over, which indicates that the destructive effect of sodium sulfate crystallization on sandstone under humidity cycle is greater than that of magnesium sulfate. Figure 7e shows the surface morphology of the sandstone for different numbers of cycles, with a more severe loss of specimen surface details under the relative temperature group, which corresponds to the wave speed and mass results.

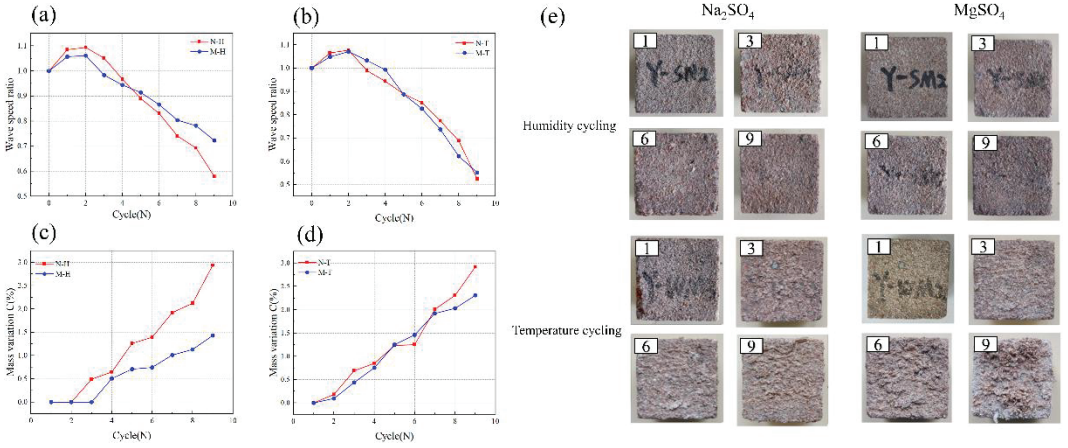

Figure 7: Variation of ultrasonic velocity and mass of specimens under different temperature and humidity cycles: a) Humidity group wave speed variation; b) Temperature group wave speed change; c) Moisture cycle group mass loss; d) Temperature cycling group mass loss; e) Surface morphology of sandstone during temperature and humidity cycling.

3.2.2 Nuclear Magnetic Resonance

The T2 distribution curves of the sandstones at different numbers of wet humidity cycles are shown in Figure 8. The T2 distribution curves of the fresh sandstone specimens from the caves all have only one prominent peak, and the T2 time points at which the peaks are located vary with the model signal intensities, which indicates the differences in the overall porosity and pore structure of the fresh sandstone from the caves. The NMR signal intensities of all sandstone specimens showed an

increasing trend with the increase in humidity cycles. The T2 distribution curves of the Yungang sandstone specimens gradually showed double peaks, which indicated that large pores began to appear and increase in the specimens, while the peak increase of the T2 distribution curves of the specimens from the sodium sulfate group was more evident than that of the magnesium sulfate group.

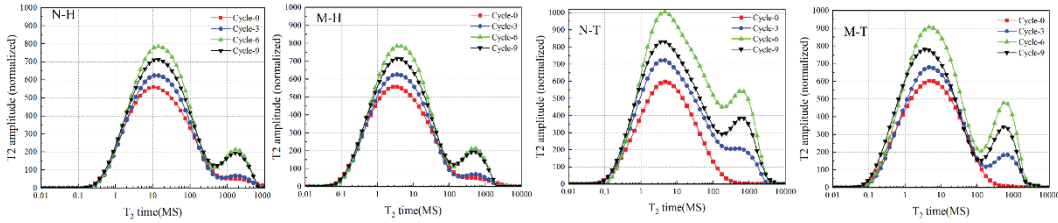

Figure 8: NMR T2 distribution of sandstone specimens: a) Humidity cycling under Na_2SO_4 solution; b) Humidity cycling under $MgSO_4$ solution; c) Temperature cycling under Na_2SO_4 solution; d) Temperature cycling under $MgSO_4$ solution.

4 CONCLUSION

In this study, a water-salt migration test and variable temperature and humidity salt ageing test were used to show the water-salt migration mechanism and damage mechanism, and salt weathering characteristics evaluated the effect of microenvironment on sandstone deterioration under multiple environmental conditions, and the results are as follows:

(1) The sulfate ion migration rate decreases with increasing immersion time. The salt in the sandstone with aqueous salt migration will gradually precipitate until the sulfate ion diffusion behavior is exhausted in the long term time. The simulation results of diffusion can be extended to the kinetic diffusion behavior of the remaining soluble salts in the sandstone.

(2) The humidity varied cyclically between 30% and 85%. The results show that changes in ambient humidity lead to changes in the amount of crystalline water contained in the salts in the sandstone specimens. The cyclic variation in humidity accelerates the weathering of the grotto sandstone by sulphate.

(3) Relative temperature changes exacerbated sulfate damage to sandstones, and sulfate crystallization cycles conducted in the humidity cycling group produced less damage than the relative temperature cycles; Sandstone porosity increased under cycling in the temperature group, along with higher wave velocity decline and mass loss rates than in the humidity group. This finding emphasizes the critical role of temperature factors in studying sandstone susceptibility to salt crystallization decay.

REFERENCES

[1] Li Q, Jin H, Zhang X, et al. Effect of salt penetration and water migration on cooked salted egg yolk gel during storage: Physicochemical properties,

structural characteristics and flavor changes[J]. Food Chemistry, 2023, 404: 134510.

[2] Xu O, Yang X, Xiang S, et al. Migration characteristic and model of chloride ions for NaCl-based salt storage asphalt mixtures[J]. Construction and Building Materials, 2021, 280: 122482.

[3] Pietruszczak S, Przecherski P, Stryszewska T. Impact of salt crystallization on the mechanical properties of structural masonry: An experimental and numerical study[J]. Construction and Building Materials, 2022, 344: 128062.

[4] Navarro R, Pereira D, Fernández de Arévalo E, et al. Weathering of serpentinite stone due to in situ generation of calcium and magnesium sulfates[J]. Construction and Building Materials, 2021, 280: 122402.

[5] Franzoni E, Gentilini C, Graziani G, et al. Towards the assessment of the shear behaviour of masonry in on-site conditions: A study on dry and salt/water conditioned brick masonry triplets[J]. Construction and Building Materials, 2014, 65: 405-416.

[6] Rao B, Su J, Xu S, et al. Thermal and non-thermal mechanism of microwave irradiation on moisture content reduction of municipal sludge[J]. Water Research, 2022, 226: 119231.

[7] Diaz Gonçalves T. Salt Decay and Salt Mixtures in the Architectural Heritage: A Review of the Work of Arnold and Zehnder[J]. International Journal of Architectural Heritage, 2022.

DESALINATION OF BRICK MASONRY BY MEANS OF A TRADITIONAL LIME PLASTER

V. Crevals[1], S. Godts[1], and J. Desarnaud[1]

KEYWORDS

Conservation, salt transport, ion chromatography, salt distribution, porous materials

ABSTRACT

Several techniques used for the desalination of salt laden brick masonry can require laborious preparations and bring with them practical difficulties, while only slightly lowering the salt content. When faced with brick masonry that is suffering both from high salt contents and a moisture source, the drying process can be utilized in the desalination of the brickwork. The application of a traditional lime plaster shortly after cutting off the water supply, such as rising damp, allows for the migration of salts to the plaster during the drying period, and consequently a slow and effective desalination of the brickwork. This technique can be carried out during the overall restoration period. Once the drying process is completed the salt laden plaster can be removed. Large sections of the brick masonry of the 17th century farmstead Hof te Bree-Eik in Lennik, Belgium, were subject to high salt contents and rising damp. Ion analysis of the brickwork in the 18th century stable before the treatment and after the complete drying of the plaster reveals a considerable decrease of the salt content in the original masonry, also in depth. This trend was also seen for equimolar contents of calcium and sulfate ions (considered as the gypsum content), which has a much lower solubility compared to other common salts. Besides bringing little risk to harm the original masonry, this desalination technique is economically favourable and does not require an elaborate set-up.

[1] Royal Institute for Cultural Heritage (KIK-IRPA), Monuments lab, Jubelpark 1, 1000 Brussels, Belgium, vincent.crevals@kikirpa.be

1 INTRODUCTION

Building materials such as brick masonry inevitably contain a certain amount of salts, but in historic masonry these contents are often higher as a result of the build-up over time. While the mere presence of salts does not necessarily cause an issue for the building materials or even a visual hinderance, their presence does hold a risk for the future. Salts that come into contact with moisture, in liquid or vapour form, can dissolve depending on their solubility and equilibrium relative humidity. Subsequent changes in climate conditions, such as a rise in temperature or a reduction of the relative humidity can cause the salts to undergo phase changes, such as crystallisations [1]. When crystallisation occurs on the surface of a porous material, that is efflorescence, which mainly causes visual hinderance [2]. When crystallisation takes place inside the pore structure, that is subflorescence. In the latter, when pore filling is sufficient and salt crystal pressure exceeds the strength of the pore walls, damage can occur [2], [3]. While damage caused by a one-off crystallisation is limited, repeated cycles of dissolution and crystallisation are more relevant. Even though all processes involved are not fully understood, it is known that multiple factors play a role, such as, the nature and amount of ions, degree of supersaturation, kinetics, and material characteristics [2]-[4]. Another issue that arises with the dissolution of salts is their transport. Once dissolved the ions can migrate through the building materials. While salts can be inherent to the building materials themselves, the influx of water might bring along more ions, as is often the case with rising damp and leaking pipes and gutters [3]. The new salt solution, with dissolved salts from the building materials and the additional salt ions from the moisture source will migrate to the drying front leading to the accumulation of salts in certain locations [1], [3]. Certain materials lend themselves to better absorb water and are thus more susceptible to salt accumulation. In historic brick masonry this is often the case for mortar and plaster, since these materials usually have finer and more pores and a higher capillary absorption coefficient compared to brick or stone [5].

In many historic buildings rising damp is one of the main moisture sources. Decades or even centuries of recurring rising damp will have often led to water damage and the accumulation of salts in the building materials. To avoid further damage the occurrence of cycles of dissolution and crystallisation needs to be halted. This can partly be obtained by preventing the influx of water in the construction by cutting off all water sources. Moisture from the ambient air, however, can still be absorbed by certain salts present at the surface and subsurface of the wall, which can lead to moisture stains. Therefore, climate control might be necessary to avoid further damage [6]. However, climate control brings with it certain difficulties and feasibility issues. Another strategy is to attempt desalination. Nonetheless, several desalination techniques can require laborious preparations or an impractical set-up, without the guarantee that the salt contents will decrease sufficiently [7]. By addressing both problems simultaneously, the drying process can be used advantageously for the desalination. Here the results are presented of a case study carried out on the stable of the 17th century farmstead Hof te Bree-Eik in Lennik in Belgium. The 18th century stable (figure 1) showed both signs of rising damp and several types of damage related to salt crystallisation, such as, powdering of the brick and mortar joints, severe loss of material, staining, and efflorescence

[8]. The stable wall was treated against rising damp and simultaneously the process of desalination was initiated by the application of a traditional lime plaster to the masonry. The goal was to allow dissolved salts to migrate to the plaster during the entire restoration campaign, thus allowing a long drying process. For the plaster to be effective in the extraction of salts it must comply with two requirements. The first is the presence of pores with a bigger diameter than the mean pore diameter of the original building materials, so water can migrate into the brick and mortar in areas where the masonry is not wet enough. The second being an adequate amount of fine pores smaller than those of the original building materials to allow for the migration of water and dissolved salts to the plaster (by advection [9]) and the subsequent storage of the crystallised salts there.

Figure 1: The 18th century stable wall before the treatment. Samples were taken in the three indicated zones at 20, 115 and 200 cm above floor level.

2 METHODOLOGY

A small sample of brick and two samples of the mortar were taken from the stable wall to evaluate the accessible porosity, density, median pore diameter and pore size distribution by mercury intrusion porosimetry (MIP) (Micrometitics Autopore IV). For the extraction plaster, a non-direct measurement has been done. Its data properties were obtained by taking three samples of two different plasters with a composition that is quite similar to the plaster used for this case. The mean values obtained for these six samples are considered to be a good approximation of the values for the used extraction plaster. Powder drill samples were taken of the brick and mortar at three different heights (20, 115 and 200 cm) on two depths (0-2 cm and 2-5 cm) before the desalination procedure (figure 1). Of these samples the actual moisture content (AMC) was determined gravimetrically after drying at 60 °C. Ultrapure water was added to the dried samples to extract the salts. This extract was analysed by ion chromatography (Metrohm) to quantify the amount of Na^+,

K^+, Mg^{2+}, Ca^{2+}, Cl^-, NO_3^- and SO_4^{2-}. After a correction for the detected excess of cations the amount of carbonates was calculated. ECOS/RUNSALT [10]-[12] was used to model the crystallisation behaviour of the salts at 15 °C (the average temperature in the stable) between 15 and 95 % relative humidity (%RH), based on the ion contents. After the removal of the paint layer, the wall was treated against rising damp by injecting a damp-proofing agent based on silanes and siloxanes under light pressure into horizontally drilled holes in the mortar joints, right above ground level. After injection, the holes were plugged with hydrophobic cement (figure 2). Shortly after the salt laden mortars were removed as deep as possible, and a layer of 1 to 1.5 cm of a traditional lime plaster was applied on the wall. The plaster consisted of 1 part hydrated lime (Tradical – Lhoist), 1 part natural hydraulic lime (NHL) 2.0 (Saint-Astier) and 5 parts river sand. After seven months the plaster was removed and powder drill samples were taken of the brick at the same heights and on the same depths as before the treatment as well as of the plaster on the same heights. The AMC and ion content were determined in the same manner as before the treatment.

Figure 2: The stable wall showing the drill holes used for the injection with the damp-proofing agent after they were plugged with hydrophobic cement.

3 RESULTS AND DISCUSSION

The results of the MIP measurements for brick, mortar and the extraction plaster are shown in table 1 and figure 3. The bricks have a high accessible porosity of 30.7 vol.% and a small median pore diameter of 5.27 µm. The pore size distribution of the brick shows a bimodal distribution with most of the pores in the range of 1 to 10 µm, especially between 1 and 4 µm and between 5 and 7 µm. A small amount of the pores has a size between 0.1 and 1 µm. The contributions to the porosity of pores smaller than 0.1 µm and larger than 10 µm are neglectable. The values for the brick are consistent with those found for bricks in other parts of the farmstead, of which the results are not discussed here. The mortar has a higher accessible porosity and smaller median pore diameter than the brick, as expected. The distribution of the pore diameter is unimodal with a small amount of pores smaller than 0.1 µm, the majority of the pores in the size range from 0.1 to 10 µm and a neglectable amount of the pores having a size larger than 10 µm. The extraction plaster shows

a bimodal distribution with the majority of the pores having a size below 1 µm or above 4 µm. As is shown in figure 4 the pore size distribution of the extraction plaster shows an overlap with that of the mortar below 0.3 µm. In the range of 0.3 to 0.7 µm there are more pores in the extraction plaster than in the mortar. The comparison between pore size distribution of the plaster and the brick shows that below a pore size of 0.8 µm there is a larger amount of pores in the plaster. These pores will allow transport by advection of the salts dissolved in water from both the brick and the mortar toward the plaster. The plaster also contains a small amount of pores in the range of 1 to 4 µm and a larger amount of pores with a diameter above 4 µm. These pores will allow the storage of salts in solid state.

Table 1: Results of the mercury intrusion porosimetry (MIP) measurements on one brick and two mortar samples taken from the stable and estimated values for the extraction plaster based on two plasters with a composition similar to the used plaster. Density (ρ), accessible porosity (Φ_0) and the median diameter of the pores (d_{median}).

	ρ kg/dm^3	Φ_0 vol.%	d_{median} µm
Brick	1.564	30.7	5.27
$Mortar_{mean}$	1.566 ± 0.014	37.8 ± 0.5	1.78 ± 0.10
$Extraction\ plaster_{mean}$	1.843 ± 0.035	29.4 ± 1.2	3.64 ± 3.71

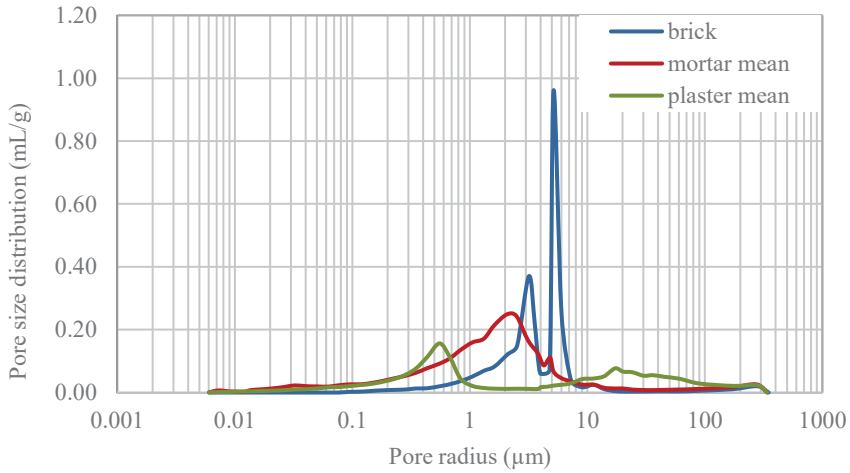

Figure 3: Pore size distribution of the brick, mean pore size distribution of the mortar and mean pore size distribution of the extraction plaster estimated based on two plasters with a composition similar to the used plaster.

Before the treatment, the high AMC of the bricks and the mortar that decreases with height (figure 4) indicates the presence of rising damp. The AMC is considerably higher for the mortar compared to the brick, as expected. A treatment against rising damp was deemed necessary in this case to prevent further damage.

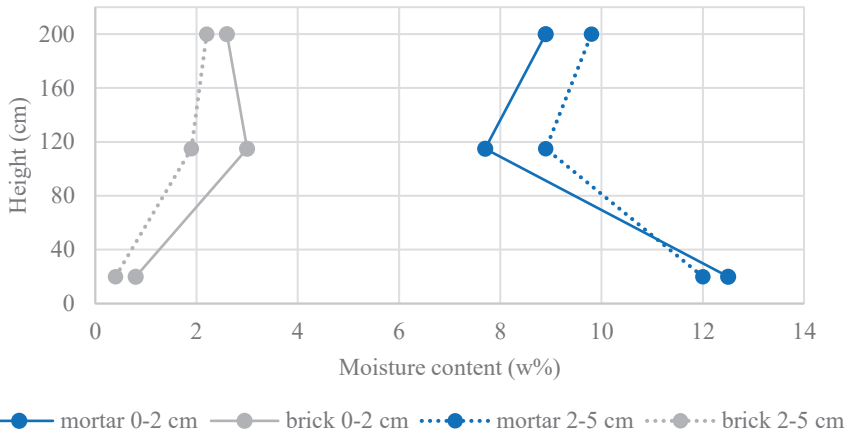

Figure 4: Actual moisture contents (AMC) in the bricks and mortar at several heights (20, 115 and 200 cm above floor level) and depths (0-2 and 2-5 cm) before the treatment. The values on the *x*-axis are expressed as wt.% of the dried sample.

Before the treatment against rising damp the salt contents including equimolar contents of calcium and sulfate ions (regarded as the gypsum content) are high in both brick and mortar. These values, excluding gypsum, as well as the values for gypsum are illustrated for the bricks in figure 5. The highest values for the ions are found in the samples taken at a height of 115 cm. The increase of salt contents with height is symptomatic for the occurrence of rising damp and salt deposit. The build-up of gypsum at 115 cm above the floor level, despite its low solubility compared to other common salts, indicates moisture contents must have been very high until this height. Rising damp will have also reached above 115 cm as is indicated by the high salt contents at 200 cm.

Modelling the crystallisation behaviour of the salt mixtures before desalination shows small differences between samples but nearly all samples show crystallisation behaviour as shown in figure 6. The crystallisation of KNO_3 starts above 85 %RH and continues until 35 %RH, with most of the crystal formation occurring above 50 %RH. Between 65 and 50 %RH most of the NaCl, $NaNO_3$ and $MgSO_4$ hydrates are formed. The range of relative humidity in which most of the crystal formation takes place is quite wide and overlaps with the range in which fluctuations in relative humidity occur in buildings, leading to a high number of dissolution/crystallisation cycles and consequently the heavily deteriorated state.

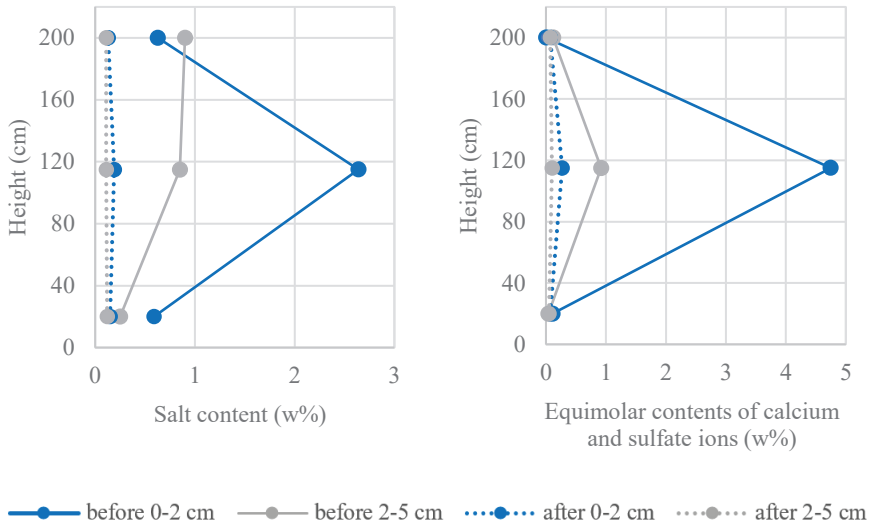

Figure 5: Total ion contents, excluding gypsum (equimolar contents of calcium and sulfate ions), and the equimolar contents of calcium and sulfate ions in the bricks at several heights (20, 115 and 200 cm above floor level) and depths (0-2 and 2-5 cm) before and seven months after the application of the lime plaster. The values on the *x*-axis are expressed as wt.% of the dried sample.

Table 2: Percentual decrease of gypsum contents and salt contents excluding gypsum in the bricks at several heights (20, 115 and 200 cm above floor level) and depths (0-2 and 2-5 cm).

Height (cm)	Salts, excluding gypsum 0-2 cm	Salts, excluding gypsum 2-5 cm	Gypsum 0-2 cm	Gypsum 2-5 cm
20	74.6	52.0	36.4	0.0
115	92.8	87.1	94.3	89.1
200	79.4	87.8	/	41.7

Seven months after the treatment against rising damp and the application of the plaster, the lime plaster and the brickwork had completely dried, and the plaster was removed to expose the original brick masonry again without any damage to the wall. The ion data showed that salt contents, excluding gypsum as well as the gypsum contents had drastically decreased for the bricks on both depths on all three heights (table 2). For the salt contents excluding gypsum the decline exceeds 52 % for all samples, with the highest percentual decrease generally occurring in the first two centimeters of the brick. The greatest decrease is measured in the first two centimeters of the brick at 115 cm and equals a reduction of 92.8 % of the original salt content. This sample also displayed the largest decrease in gypsum content, with a reduction of 94.3 % of the original gypsum content. The salt contents in the bricks do not require further reduction. This observation also applies to the gypsum contents. The amounts of salts that were measured in the lime plaster (0.26 wt.% at a height of 20 cm, 0.54 wt.% for a height of 115 cm and 0.43 wt.% at a height of

200 cm) appear to be lower than would be expected to account for the decline of salt contents in the brick. This is the result of the large quantity of plaster that was applied on the wall up until great height. The salts from the masonry will have spread over the entirety of the plaster, thereby resulting in a lower weight percentage of salts in the samples taken from the plaster.

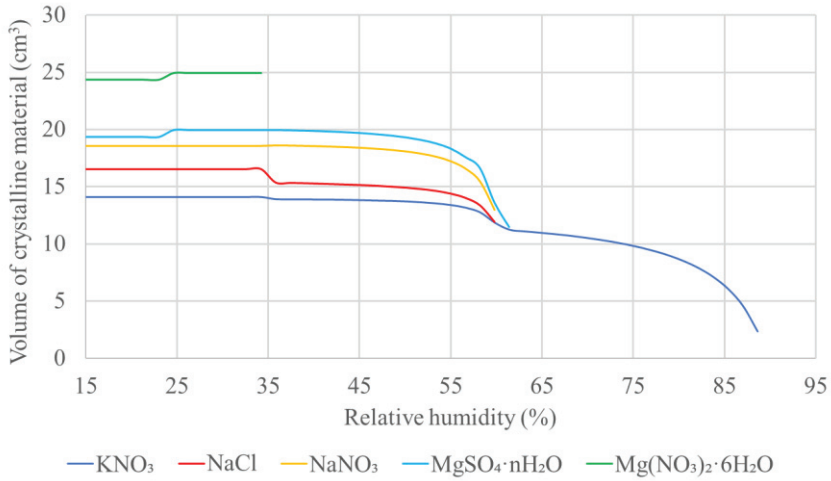

Figure 6: ECOS/RUNSALT output for the crystallisation behaviour at 15 °C of the ion mixture in the first two centimetres of the brick at 115 cm above floor level, excluding equimolar contents of calcium and sulfate ions.

4 CONCLUSIONS

Despite the high contents of gypsum and salts excluding gypsum the application of a simple traditional lime plaster during the drying of the wall sufficed to accumulate the majority of the ions from the bricks and reduce the salt and gypsum contents to acceptable levels. In cases where masonry suffers from high moisture contents, such as rising damp, which need treatment and also require desalination, the method of eliminating the water source and applying a lime plaster to the masonry might prove useful as an intervention. To fulfil the task of an extraction plaster, the lime plaster needs to have an adequate amount of pores that are finer than those of the original building materials as well as pores that are large enough to store the crystallised salts that are extracted. The knowledge of the pore size distribution of the original building materials is therefore imperative in choosing the correct plaster. When these simple conditions are met this offers a low-cost technique that does not require an elaborate set-up, brings little risk to the masonry, and can be executed during the restoration process.

ACKNOWLEDGEMENTS

We would like to thank Sander Peeters and Maarten Van Hout of Verstraete-Vanhecke to involve us in the restoration of Hof te Bree-Eik and their collaboration during our research.

REFERENCES

[1] V. Crevals, S. Godts, J. Desarnaud, 'Salts in the 16th century mural painting of The Last Judgment in the leper hospice in Rumst, Belgium, in Proceedings of 2nd International Conference on Moisture in Buildings (ICMB23), (to be published).

[2] H. Derluyn, P. Moonen, and J. Carmeliet, "Deformation and damage due to drying-induced salt crystallization in porous limestone," *J. Mech. Phys. Solids.*, vol. 63, pp. 242-255, 2014.

[3] G.W. Scherer, "Stress form crystallization of salt," *Cement and Concrete Research*, vol 34, pp 1612-1624, 2003.

[4] F. Caruso, T. Wangler, R.J. Flatt, "Easy illustration of salt damage in stone," *J. Chem. Educ.*, vol 95, pp. 1615-1620, 2018.

[5] R. Hayen, "Vorst. Algemeen gedrag van poreuze bouwmaterialen wat betref vocht en bevriezen," in *Handboek Onderhoud, Renovatie en Restauratie*, Wolters Kluwer Belgium NV, 2002, pp. 111-168.

[6] V. Crevals, S. Godts, J. Desarnaud, "Salt problems and climate control in the case of the church of Sint-Aldegondis in Mespelare, Belgium, an ECOS/RUNSALT approach," in *Proceedings of SWBSS" 2021* (*Fifth International Conference on Salt Weathering of Buildings and Stone Sculptures*), pp. 13-20, 2021.

[7] S. Godts, H. De Clercq, R. Hayen, Poulticing vs electrophoresis desalination of historic masonry, the case of the mill at Hoksem," in *Proceedings of the International RILEM Conference, pp.*145-153, 2016.

[8] ICOMOS-ISCS, *Illustrated glossary on stone deterioration patterns*, 2008.

[9] A. Sawdy, A. Heritage, L., Pel, "A review of salt transport in porous media assessment methods and salt reduction treatments," in *Salt Weathering on Buildings and Stone Sculptures. Proceedings from the International Conference*, pp. 1-27, 2008.

[10] D. Bionda, *RUNSALT - A graphical user interface to the ECOS thermodynamic model for the prediction of the behaviour of salt mixtures under changing climate condition*s, 2005. [Online], Available: http://science.sdf-eu.org/runsalt/. [Accessed May 12, 2022].

[11] C. Price, *An expert chemical model for determining the environmental conditions needed to prevent salt damage in porous materials: protection and conservation of the European cultural heritage; project ENV4-CT95-0135 (1996-2000) final report.* In Protection and conservation of the European Cultural Heritage, no. 11. London: Archetype Publications, 2000.

[12] S. Godts, M. Steiger, S. A. Orr, A. Stahlbuhk, J. Desarnaud, H. De Clercq, V. Cnudde, T. De Kock, "Modeling Salt Behavior with ECOS/RUNSALT: Terminology, Methodology, Limitations, and Solutions," *Heritage*, vol 5*,* pp. 3648-3663, 2022.

DESALINATION OF POROUS MATERIALS WITH HYDROGELS

Julie Bartholdy[1, 2]*, Inge Rörig-Dalgaard[2], and Poul Klenz Larsen[1]

KEYWORDS

Desalination, hydrogels, near-surface salts, poultices, wall paintings

ABSTRACT

Hydrogels are increasingly used by conservators for cleaning of water-sensitive and delicate objects due to their high water retention and non-abrasive properties. Previously it has been shown that some hydrogels are additionally capable of extracting near-surface salts from porous materials. This combination makes hydrogels an interesting poultice material for desalination of fragile porous materials with a high concentration of salts in the surface area. It is believed that with the use of hydrogels as desalination poultices, a shallow water intrusion will be obtained due to their high water retention. By only bringing near-surface salts into solution, a local and controlled treatment can be achieved, without salt ions relocating deeper into the masonry.

The transportation of salt ions during application of hydrogels to salt contaminated porous substrates, was investigated in laboratory experiments performed on specimens of clay brick contaminated with sodium chloride. The ion content stratigraphy of the specimens was analyzed before and after gel application. One or two applications of two commercially available gels commonly used in conservation, Nanorestore Gel® Peggy 6 and Agar Art were tested.

The experiments showed that the agar gel with two applications performed a very satisfactory extraction of near-surface salts without substantial redistribution of ions to deeper parts of the specimens. The Peggy 6 gel was found to perform more undesirably as a desalination poultice, as a substantial relocation of salt ions to subsurface areas of the specimens was achieved by the treatment.

[1] The National Museum of Denmark, Kgs. Lyngby, Denmark, julie.bartholdy@natmus.dk
[2] DTU, Technical University of Denmark, Kgs. Lyngby, Denmark

1 INTRODUCTION

Salts embedded in the paint layer constitute one of the primary threats to the preservation of wall paintings of high cultural value in Danish medieval churches [1]. Two different strategies are used in parallel or separately when preventing salt deterioration: keeping a constant relative humidity (RH), thereby avoiding repeated crystallization of salts, or carrying out salt-reducing treatments. In recent years, the first-mentioned strategy has been the dominant approach in relation to Danish medieval wall paintings [2]. However, most churches are still actively used for services, and in many cases, it has proven to be a great challenge to maintain a stable RH. Unfortunately, the inappropriate climate has in several cases caused a dramatic and rapid fading of the paintings due to salt efflorescence, as illustrated in fig. 1.

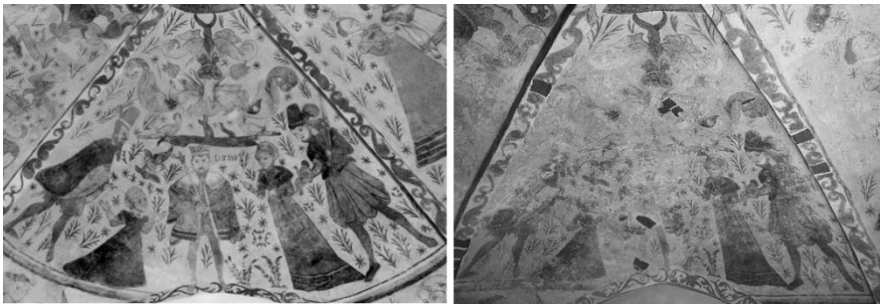

Figure 1: Wall painting in the vault of Sejerø Church photographed in 1998 (left) and before restauration in 2022 (right). A high content of salts in the masonry and an inappropriate climate have caused a serious fading and loss of the pictorial contents and detachment of plaster. Photo: Roberto Fortuna

As a supplement to RH stabilization, a suitable desalination method is therefore sought to decelerate the deterioration. The most common desalination method for immobile cultural heritage is to extract salt ions into a moist poultice of clay minerals or cellulose pulp applied to the wall paintings, plaster or masonry [3]. For effective salt reduction to occur, the poultice material must contain pores of a smaller size than the salt-containing substrate, thereby inducing advection-based salt transport towards the drying surface [4]. Due to the high content of fine pores in medieval lime plaster, only clay-containing poultices are in theory suitable. However, since surface contamination by clay particles is unavoidable, and subsequent cleaning would cause serious harm to the paint layer, clay is avoided as poultice material for wall paintings. Cellulose pulp has, therefore, been used for desalination of Danish medieval wall paintings [5], even though it is well known that the porosity of the material is not suitable. The drawback of cellulose poulticing is the large influx of moisture into the plaster and masonry, causing mold growth, redistribution of salt to areas not previously salt contaminated and a poor long-term effectiveness of the treatment [6].

In the search for more suitable poultice materials for wall paintings, interest has recently fallen on hydrogels, which are increasingly used in conservation treatments of water-sensitive and delicate objects due to their high water retention and

non-abrasive properties [7]. Recent studies have shown that hydrogels have very good properties regarding cleaning of Danish medieval wall paintings [8]. This especially pertains to gels with high flexibility that ensure good adhesion to lime plaster, and where application and removal are performed without abrasive action, greatly reducing or eliminating mechanical damage on frail surfaces. Previous studies have shown that hydrogels can also absorb salts to a degree that make them suitable as poultice materials for desalination [9].

In this present study an in-depth examination the ion content stratigraphy of brick specimens before and after gel application was accomplished, thereby investigating the salt extraction abilities of different gels. In the experiment, brick was substituted for wall painting plaster replicas to avoid the time-consuming and challenging task of replicating medieval plaster [10]. The hypothesis was that the limited moisture release from the gels, combined with good ion absorption abilities would result in an effective desalination of surface and near-surface salts without redistribution of ions deeper into the matrix. Two different gels, representing different water retention and polyelectrolytic properties were examined.

1.1 Salt extraction by hydrogels – theory in short

Hydrogels consist of networks of interconnected polymers, which can hold a very large amount of water. The swelling capacity of gels is controlled by the balance between the elasticity of the polymer network, determined by the density of cross-links, and the interaction energy between the polymer and the solvent [11]. The polymers are either polyelectrolytes possessing dissociable functional groups (ionic gels) or non-polyelectrolytes with no dissociable functional groups (non-ionic gels). When the functional groups of a polyelectrolyte polymer dissociate, they form non-mobile charged ions along the chain, as well as oppositely charged mobile counter ions that act as solutes in the gel water [12]. Ionic gels thereby absorb water, not only as a matter of the hydrophilicity of the polymer, but also as a matter of the osmotic pressure difference obtained between ion-containing water inside the gel, and deionized water outside.

An important property of gels in desalination is obviously the ability to absorb ionic solutions. A recently published modified theory of thermodynamics of hydrogels [13] shows how the pressure gained by the retractive forces of the polymer network allows the gel water in non-ionic gels to achieve a corresponding or even higher ion content than in the external solution. Non-ionic gels, on the other hand, will, due to disturbances of the osmotic pressure in the gel, repel ions and thereby achieve a lower ion content than in the external solution. For weak polyelectrolytes, the salt repelling effect will decline with increasing salt concentration in the external solution and for very weak polyelectrolytes, the salt content in the gel will be approximately the same as in the external solution.

Another variable property affecting the gels' performance as poultices in desalination is their ability to retain water. It is the hypothesis that high water retention causing a limited moisture release from the gels will be an advantage, as this will result in a controlled local dissolution and extraction of salts, without advection of ions with the water flow to deeper parts of the masonry. Also, a retained large reservoir of water in the gel throughout application will allow for the diffusion of more ions into the gel before the gel water is saturated.

2 MATERIALS

2.1 Gels

Desalination was tested with two gels, each representing different gel types, commercially available and commonly used in conservation.

Nanorestore Gel® Peggy 6 (PG6) is a poly(vinyl alcohol) gel produced by CSGI. In the manufacturing process, gelation is initiated by freezing the polymers (cryogelation), whereby physical crosslinks are formed. The gel was specially developed for application on rough and/or irregular surfaces and has high flexibility and rigidity [14]. PG6 gels have a thickness of approx. 1 mm when obtained from the supplier.

Agar gels (AA3%) were prepared from the commercially available product Agar Art supplied by CTS. Agar (or agar-agar) comprises two polysaccharides, agarose and agaropectin, extracted from red algae. Gelation is obtained from a network of double helix structures formed by agarose when heated to above 85°C and subsequently cooled [15]. Agar is weakly ionic, as agaropectin contains groups of sulfated galactouronide and a smaller number of ester sulfate groups, D-glucuronic acid and pyruvic acid. Counter ions to the acid groups are either Ca or Mg ions or a combination of both. The ratio of the compounds can vary, as it is a natural product, but usually agarose makes up approximately 70 %. Agar gels were prepared for experiments by mixing agar powder (Agar Art) in UPW water at a concentration of 3% (w/v). The suspension was heated to boiling point while stirring, and after a short cooling, it was reheated to boiling point. The warm homogeneous and translucent liquid was poured into a plastic container and left to cool, whereby gelation took place. The AA3% gels were prepared with a thickness of approx. 3 mm.

2.2 Brick specimens

Specimens for laboratory tests were made from Falkenløwe brick, which is a type of brick made for restauration purposes using traditional fabrication methods. The selection of this brick was based on previous studies that have shown similar hygrophysical properties to those of Danish medieval bricks [16] (table 1). Consequently, this brick has been used several times in desalination experiments regarding Danish medieval wall paintings [1, 17], which provides a basis for comparing the effectiveness of the method.

Table 1: Physical properties of Falkenløwe brick. Porosity (open), WAC (Water Absorption Coefficient) and CMC (Capillary Moisture Content) of the bricks as described in [18]. Porosity calculated from the maximum water absorption, WAC being the slope of the first, linear part of the absorption curve, and CMC being the water content in percentage of total weight of specimens at the end of the first stage of water absorption.

Porosity (vol%)	**Density (kg/m^3)**	**WAC (kg/m^2 s$^{0.5}$)**	**CMC (wt%)**
25.5%	1676	0.29	12.5

The specimens were cylindrically shaped with height and diameter of 50 mm. Cores were drilled from bricks with sufficient supply of water and cut with a saw

to the specified height. The specimens were then dried to constant mass in a ventilated oven at 105° and brick dust was removed with compressed air. The upper surface of the specimen, constituting the test surface, was the water stroked bed face of the brick and the bottom was the cut face.

3 METHOD

3.1 Salt contamination of specimens

Salt contamination of brick specimens was implemented by capillary absorption of 5% (w/w) NaCl solution in accordance with the salt introduction phase described by Nunes et al. [19]. During absorption sides of the specimens were sealed with para-film and duct tape. After full saturation, the underside was also sealed, and the specimens were dried at 40°C / 15 % RH (+/- 5 %). After evaporation of at least 90% of the absorbed water (approx. 30 days), the specimens were transferred to a climate chamber and stored at 20°C / 65% RH (+/- 5 %) until the desalination test was performed.

With the use of the referred salt contamination protocol, a high surface salt content was achieved, concentration then declining with distance from the surface, regularly following a decreasing power function (fig. 1). With an average salt content of 1,9% (w/w) in the upper 1 cm layer of the brick the salt distribution in the specimens was considered to reflect a realistic level.

3.2 Desalination tests

Prior to the experiments, the gels were stored in UPW water, which was changed three times at intervals of at least 24 h to wash out any unbound polymers. Before application to the horizontally positioned face of the brick specimens, gels were dabbed with paper towels until they appeared dry on the surface. The application procedure involved holding the gels in place while rubbing the gel surface with a finger for some seconds to improve adhesion. The gels were detached after 30 minutes. The effective contact time of 30 minutes was chosen, based on preliminary studies that have shown, that a contact time between 5 and 60 minutes gave the most efficient salt extraction [9]. Moisture release from gels during contact time to specimens was determined by weighing gels and specimens before and after gel application. One series of specimens was only desalinated once, whereas another series was desalinated twice. The second treatment was accomplished repeating the same procedure after an interval of one week, where an average of 80% of moisture had evaporated after application of AA3% and 97% after application of PG6. Specimens were stored at 20°C / 65% RH (+/- 5%) throughout the experiment.

Samples were extracted one week after finishing the treatment by grinding layers every 1 mm for the first 10 mm and then for every 5 mm to a depth of 30 mm. The grinding powder was then analyzed for ion content. As a destructive measurement method was used, the reference measurement was done on a non-desalinated specimen and results therefore do not represent the salt content in the same specimen before and after desalination. The experiments were performed in triplicates, however, the series desalinated twice only in duplicate. The reported results represent the average of the outcomes.

3.3 Salt analyses

The Ion content in the sampled brick was determined by ion chromatography (IC) on a Thermo Fischer Scientific Dionex ICS1100. Drilling powder was suspended in UPW water for 24 hours after which the slurries were filtered, and the ion content of the water was analyzed. Only anions were analyzed, and the total content of NaCl was thereby an assumption calculated from the Cl^- content.

Salt content was also analyzed in gels using the same instruments. Salts absorbed in the gels were leached out by immersing the gels in 100 ml UPW water for 7 days, after which IC-analyses of ion content in the water were carried out.

4 RESULTS AND DISCUSSION

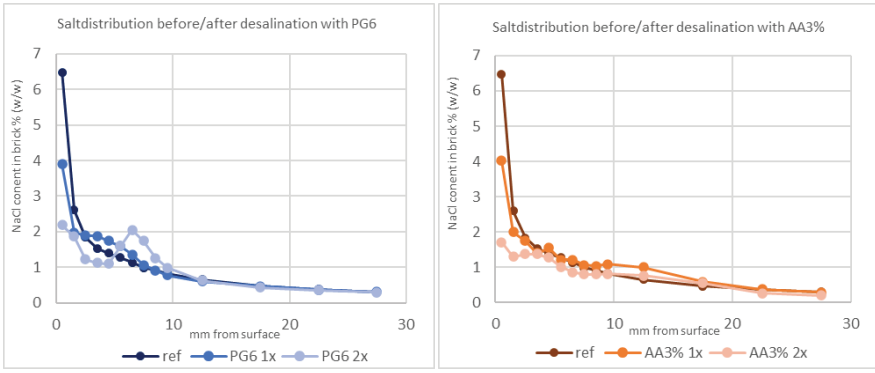

Figure 3: The total salt content in brick before and after laboratory desalination with PG6 gel (left) and agar gel (right). Ref indicates non-desalinated specimens, 1x indicates desalinated once, 2x indicates desalinated twice.

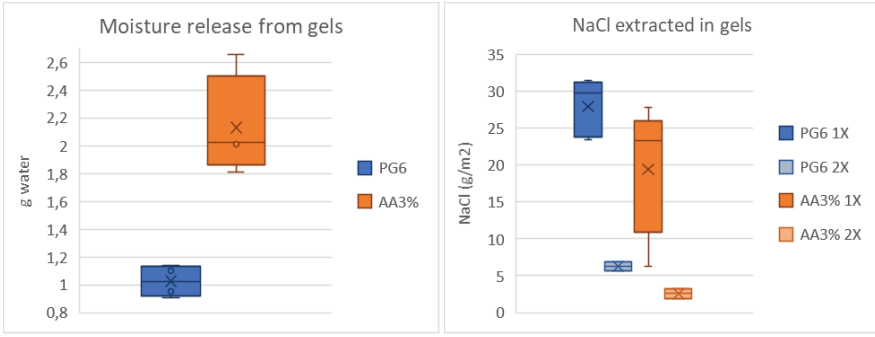

Figure 4 (left): Mean and standard deviation of moisture transferred from gels to brick samples during 30 min contact time (each boxplot represents results from 4 gel applications, all at the first desalination).
Figure 5 (right): Mean and standard deviation of NaCl content in gels after application to brick specimens. Dark- colored bars show salt content in gels after first desalination (each boxplot represents results from 5 gels), whereas light-colored bars show salt content in gels after second desalination (each boxplot represents results from 2 gels).

4.1 Desalination with PG6

For specimens desalinated one time with PG6, the salt content in the outermost layer was considerably reduced from 6,5% to 4% (fig. 3), which constitutes a 40% reduction. However, the salt concentration slightly increased in the layers 2-6 mm from the surface, indicating that salts were redistributed deeper into the specimen by the treatment. The second desalination further reduced the salt content at the surface layer down to 2,2%, constituting a 66% reduction, but at the same time, the salt content in the deeper layers increases to an even more significant extent than after the first application. Salt content in the deeper layers of the specimens was not affected by the gel application, which indicates that the moisture did not penetrate deeper than appr. 6 mm into the brick matrix at the first gel application and 15 mm at the second.

Measurements of moisture release (fig 4) revealed that PG6 secretes a very small amount of water (average 1 ml.) into the brick. It was assumed this would prevent redistribution of ions in the deeper layers. Furthermore, because of PG6 gel's non-ionic nature, it was expected to have good salt extracting properties. This expectation was validated by the analyzes of salt content in gels measured after application (fig. 5), revealing a quite reasonable extraction of salts by the gels after first application corresponding to a desalination of 23-31 g/m^2. The second application showed a more limited result corresponding to 5-7 g/m^2 desalination

To sum up, good extraction of surface salts was shown for PG6. However, the satisfying result was offset by an unsatisfactory increase in salt content in the layers just below the surface. An explanation for this unexpected redistribution of ions can be found in a contraction and thereby change in texture of the gels observed immediately upon contact with the surface salts on the specimens. The contraction happens as a result of water release caused by the osmotic pressure difference in the deionized gel water and the saturated salt solution formed on the surface of the specimen. The water release would theoretically be replaced by a withdrawal of water as ions diffuse into the gel, thereby equalizing the salt content in the gel and external solution. However, for poly(vinyl alcohol), the contraction leads to the formation of permanent crosslinks and thereby decreased water absorption abilities. Crosslinking of PVA by immersion in saturated solutions of NaCl is a known phenomenon e.g. described by Choi et al [20]. The contraction instigates two phenomena which may be important for the subsequent transport of salts. Firstly, it reduces the contact with the brick surface and thereby the diffusion of ions into the gel. Secondly, the influx of water released in a sudden pulse might push ions into the specimen.

4.2 Desalination with AA3%

Salt distribution in specimens desalinated one time with AA3% showed a decreased salt concentration in the outermost layer falling from 6,5% to 4% (fig. 3), corresponding to a 38% reduction, which is similar to PG6. Again, a slight increase in salt content was seen in the deeper layers, but compared to the specimens desalinated with PG6, the rise was less pronounced and appeared to be distributed over an extended area (appr. 4-17 mm from the surface). The second application of AA3% further reduced the salt content in the surface layer to 1,7%, corresponding to a 74%

reduction. In the subsurface layers, the salt content was also reduced by the second application and lied slightly below the content in the specimens desalinated once. For specimens both desalinated once and twice, the salt content from 17 mm depth and deeper seemed unaffected, indicating that this was the maximum penetration depth of moisture in the present experiment.

Moisture release measurements (fig. 4) showed that AA3% emitted an average of more than twice the amount of water (about 2,1 ml) compared to PG6 during a contact time of 30 min., and that the amount highly variated. The latter could be explained by a greater variation in gel thickness, as the AA3% gels were prepared in the lab, contrary to the readymade PG6. A limited water release was expected to be an advantage, as a greater penetration depth in theory results in redistribution of salts rather than extraction. It was therefore surprising that the higher water release from AA3% apparently caused less redistribution of salts. An explanation for this result could be sought in the better adherence of the AA3% maintained throughout the contact period. As previously explained, PG6 loses adhesion upon application due to permanent contraction of the gel. For AA3%, the osmotic pressure difference between gel water and the saturated salt solution formed on the surface of the specimen apparently do not induce a sudden release of water. Instead, water is apparently released more steadily, allowing a simultaneous diffusion of salt ions into the gel to occur. AA3% is a weakly ionic gel and theoretically this should not be an advantage in ion absorbance. However, the dissociation of functional groups in the polymers is probably so negligeable that the AA3% gels actually act as non-ionic gels. This was seen in the analyzes of salt content in gels (fig. 5), where AA3% gels were shown to extract salts corresponding to a 6-28 g/m^2 desalination, which is at levels similar to PG6. However, the measured salt content in the agar gels was much more inconsistent. This, in combination with the fact that the salt distribution in desalinated bricks showed a more effective salt extraction by AA3% when compared to PG6, could indicate that the method used to leach salts from the gels might be problematic, and thus, the values of salts extracted in agar gels may not present the correct value. Salt ions may be bound more strongly in agar gels than in PG6 and therefore they may be more difficult to leach out. This assumption is emphasized by the fact that an extraction of salts corresponding to a almost negligible 2-3 g/m^2 desalination is detected in the AA3% gels after the second application, although the analyzes of the salt distribution in brick samples show a satisfactory desalination.

5 CONCLUSION

This study shows that hydrogels are indeed an interesting material for desalination of wall paintings. However, it also shows that application of different gels to salt-contaminated bricks specimens for the purpose of desalination produces various levels of near-surface ion distribution. For the agar gel AA3%, the result after two applications was very satisfactory, as an effective (74%) reduction of the surface salts had been accomplished with only a negligible redistribution of ions to the subsurface layers. The gel desalination thereby changed the salt content in the brick from dangerously high in the surface layers to a stable approx. 1% salt content throughout the whole sample, which is not considered to be harmful. For the poly(vinyl alcohol) gel PG6, the result was less satisfactory, despite the reasonable

(66%) reduction of the surface salts after two gel applications, as this was accompanied by a more significant redistribution of ions to the sub-surface layers. Thereby, the gel desalination had the exact same side effect that the method sought avoided.

The hypothesis that non-ionic gels with high water retention would be advantageous in desalination was not entirely confirmed. However, this study shows that other properties of gels can have an even higher impact on their salt extraction ability than high water retention. First of all, the permanent contraction reaction of the poly(vinyl alcohol) gel seems to be crucial for the efficiency of desalination, as this reduced the contact with the brick surface and thereby the diffusion of ions into the gel. Secondly, it seems, that a very low moisture release from the gel is not unambiguously an advantage, as the significantly higher water release from AA3% compared to PG6 didn't have a negative influence on the redistribution of ions.

It is important to emphasize that the promising results achieved here for agar gels apply only to bricks. A very important next step will be to investigate whether gels are also suitable for desalination of lime plaster which, as described in the introduction, might pose challenges due to the demands of matching porosity requirements between the substrate and poultice material. At the same time, whether the gels will be able to fulfil these requirements or not, a comparison of their effectiveness in relation to traditional poultice materials will be useful.

6 ACKNOWLEDGEMENTS

This project was financially supported by the Independent Research Fund Denmark

7 REFERENCES

[1] P. K. Larsen, "Desalination of painted brick vaults", PhD thesis, Technical University of Denmark, 1999

[2] P. K. Larsen, "Climate control in Danish churches", In *Museum Microclimates,* National Museum of Denmark, pp. 167-174, 2007.

[3] V. Vergès-Belmin & H. Siedel, "Desalination of masonries and monumental sculptures by poulticing: A review", *Restoration of Buildings and Monuments*, vol 11, pp. 1-18, 2005

[4] A. Sawdy, B. Lubelli, V. Voronina, & L. Pel, "Optimizing the extraction of soluble salts from porous materials by poultices", *Studies in Conservation,* vol 55, no 1, pp. 26-40, 2010.

[5] I. Brajer, & P. K. Larsen, "The salt reduction treatment on the wall paintings in Tirsted Church", In *Proceedings of the 1st International Conference on Salt weathering on buildings and stone sculptures*, The National Museum, Copenhagen, Denmark, pp. 219-228, 2008-

[6] V. Vergès-Belmin, A. Heritage, & A. Bourgès, "Powdered cellulose poultices in stone and wall painting conservation-myths and realities", *Studies in conservation*, vol 56, no 4, pp. 281-297, 2011.

[7] L.V. Angelova, B. Ormsby, J.H. Townsend, & R. Wolbers, *Gels in the Conservation of Art*, London, UK: Archetype Publications Ltd, 2017.

[8] K. Segel, I. Brajer, M. Taube, C. M. de Fonjaudran, M., Baglioni, D. Chelazzi, R. Giorgi, & P. Baglioni,."Removing Ingrained Soiling from Medieval Limebased Wall Paintings Using Nanorestore Gel® Peggy 6 in Combination with Aqueous Cleaning Liquids", *Studies in Conservation*, vol 65, sup1, pp. 284-291, 2020.

[9] J. Bartholdy, P. K. Larsen, & I. Brajer, "Hydrogels as Poultice Material for Desalination–A Preliminary Study", In *Proceedings of the Fifth International Conference on Salt Weathering of Buildings and Stone Sculptures*, TU Delft, The Netherlands, pp. 215- 224, 2021.

[10] M. Midtgaard, T. Seir & I. Brajer, "Replicating Medieval Wall Painting Plaster using the Hot-mix Technique", *Studies in Conservation*, vol 66, no. 4, pp. 230-246, 2021.

[11] P. J. Flory, *Principles of Polymer Chemistry*, 15th ed., Cornell University Press., 1953.

[12] F. L. Buchholz & A. T. Graham, *Modern Superabsorbent Polymer Technology*, John Wiley & Sons, Inc., 1998.

[13] G. Chen, "Thermodynamics of hydrogels for applications in atmospheric water harvesting, evaporation, and desalination*", Physical Chemistry Chemical Physics*, 24(20), 12329–12345, 2022.

[14] A. Bartoletti,, R. Barker, D. Chelazzi, N. Bonelli, P. Baglioni, J. Lee, L. V. Angelova, & B. Ormsby, "Reviving WHAAM! A comparative evaluation of cleaning systems for the conservation treatment of Roy Lichtenstein's iconic painting", *Heritage Science,* vol. 8, no. 9, 2020

[15] C. L. Scott, "The use of agar as a solvent gel in objects conservation", Objects Specialty Group Postprints, vol. 19, pp 71-83, 2012

[16] P. K. Larsen, "Moisture physical properties of bricks. An investigation of Falkenløwe, Stralsund and Hartmann bricks," Technical report 343, Technical University of Denmark, 1995.

[17] I. Rörig-Dalgaard, "Preservation of murals with electrokinetic-with focus on desalination of single bricks", PhD thesis, Technical University of Denmark, 2009.

[18] "DS/EN 1925 Natural stone test methods. Determination of water absorption coefficient by capillarity", 1999

[19] C. Nunes, A. M. A Sanchez, S. Godts, D. Gulotta, I. Ioannou, B. Lubelli, B. Menendez, N. Shahidzadeh, Z. Slížková, & M. Theodoridou, "Experimental research on salt contamination procedures and methods for assessment of the salt distribution", *Construction and Building Materials*, 298, 123862, 2021.

[20] J. Choi, H. Bodugoz-Senturk, H. J. Kung, A. S, Malhi, & O. K. Muratoglu, "Effects of solvent dehydration on creep resistance of poly (vinyl alcohol) hydrogel", *Biomaterials,* 28(5), pp. 772–780, 2007.

DESALINATION OF THE BALUSTRATE OF GOSLAR TOWNHALL USING DIRECTED MOISTURE FLOW

Wanja Wedekind[1], Justyna Hrabska[1], and Johanna Lutze[1]

KEYWORDS

Desalination, capillary moisture transport, directed moisture flow, poultices, hot lime mortar

ABSTRACT

Continuous exposures to moisture and wetting-drying cycles lead to the concentration of salts and salt-induced damage in many externally exposed monuments and objects made of stone. However, the same forces of nature can also be used specifically for desalination.

In this case study a stone staircase with a balustrade was employed to perform a directed moisture. The procedure can be used with thin-walled parapets of historical buildings, which often have a decorative function as well. The treatment presented in this article was realized on the staircase of the medieval town hall of the UNESCO World Heritage city of Goslar in Germany. The staircase with ornamental decoration was heavily affected by road salt.

Here, too, a desalination process with a directed water transport was used over a large area. In this case a hot lime mortar was applied as the poultice material. The rock properties and preliminary investigations of the salt content are presented and the desalination results are specified both qualitatively as well as quantitatively.

[1] Applied Conservation Science (ACS), www.acs-online.eu, info@wanjawedekind.de

1. INTRODUCTION

The damaging effect of salts on monuments and works of art made of stone and other mineral materials has been known since ancient times. Already the ancient Greek historian, geographer and ethnologist Herodotus of Halicarnassus (480 BC – 430/420 BC) described salt weathering of buildings.

A scientific examination of the subject began as early as the 19th century. From the beginning of the 20th century, technical articles on stone weathering were published more frequently. Since then, numerous scientific articles have dealt with the phenomenon of salt weathering. Goudi and Viles presented an extensive standard work in 1997 [1]. Comprehensive overview articles were written by Charola [2] and Doene [3].

The amount of scientific research into salt weathering is matched only by a disproportionately smaller number of technical articles on salt reduction and desalination techniques.

When searching the Internet on a major search engine using the keywords "salt stone heritage," approximately 22 million results are displayed. With the keywords “desalination stone heritage” only around 3.000.000 are listed. While the topic or the problem of salt weathering has been described in detail from a scientific point of view, conservation solutions are rather scarce.
Most publications focus on salt reduction using poultices the effectiveness of which is often limited. However, two publications should be mentioned here as representative examples: Vergès-Belmin, V. [4] and Heritage, A, Heritage A. and Zezza [5].

2. DESALINATION BY DIRECTED MOISTURE FLOW

The mechanism used to desalinate porous materials in directional moisture flow is the convective transport of salts dissolved in water into another medium. Salt reduction and structural desalination via a directed moisture flow use solution and diffusion as well as convective water transport with the added effect of gravity as a pressure gradient and increased drying temperature.

We can look back on many years of experience in the desalination of tomb monuments and salt-contaminated architectural elements according to the principle of directed moisture flow [6, 7].

Numerous grave stelae have been treated for salt contamination by the application of permanent wet poultices to the back of the stelae. This created a moisture flow that drew out any concentrated salts from the drying side and into the poultice. The area on which the poultice was applied was then allowed to dry naturally. The rest of the stone object was wrapped with a plastic sheet. (Fig. 1). A compact pedestal cube of an obelisk tomb monument was also treated in a similar manner. In this case, distilled water was directed through boreholes and a drip, which was inserted deep into the contaminated areas [6]. A similar method was used to desalinate columns and deeply salt-contaminated masonry [8].

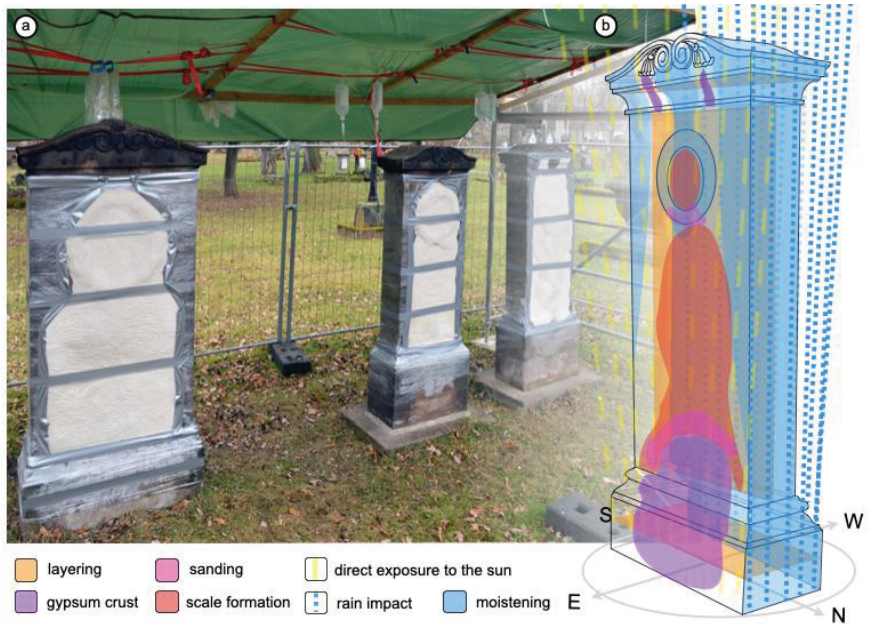

Figure 1: a) Three stelae desalinated by a directed moisture flow and b) weathering model.

3. THE MIDDLEAGE TOWN HALL

The silver wealth of the Rammelsberg in Goslar, Germany, which had been tapped since 970, created the basis for Goslar's great economic and political importance. Around the middle of the 15th century, the city experienced a second flowering. It was during this period that it acquired its splendid townscape and a new late Gothic town hall. It is a Gothic half-timbered building with a colorful facade. On a predecessor building of the 12th century, the present rectangular building on the market square was erected in the middle of the 15th century. In 1992, the historic old town of Goslar was inscribed on the UNESCO World Heritage List together with the Rammelsberg mine. Today, the town hall is the world heritage and visitor center of the historic town.

The open staircase with a decorated balustrade adorns the entrance area to the town hall on the second floor. (Fig. 2a, Fig. 3b and 5a). The balustrade of the south facade features star-shaped tracery ornamentation consisting of six eight-pointed and five four-pointed profile courses with a pear-shaped cross-section. Most importantly, the year 1537 is inscribed on the parapet, which suggests that the balcony was built at that time. On the staircase, there are additional tracery decorations and a figural relief. The relief depicts an animal resembling a monkey holding a mirror, which is a symbol of vanity (Fig. 2a, Fig. 3b and 5a).

The main facade of the medieval town hall of Goslar is not oriented to the market side (northeast) but to the southeast. The most representative architectural element is the staircase leading to the large council chamber on the second floor. The balustrade of this staircase is decorated with figural reliefs and ornaments.

The individual balustrade elements are made of "on gap" stone coffers of Hilssandstein and Lutter sandstone and have a height of about one meter and a varying width between 17 and 20 cm.

4. STONE MATERIAL

The bedrock of the Hilssandstein of the Goslar region is thick-bedded and light grey to whitish yellow in color. It is a medium to fine-grained sandstone. It contains 88 % quartz, 11 % rock fragments, about 1 % glauconite grains in some places, and accessory minerals of less than 1 % of tourmaline, and zircon [9]. It is clayey-kaolinitic and rarely calcareous-bound. The Lutter sandstone is brownish, reddish and greenish, furthermore, cross-bedded as well as obliquely bedded. It is highly porous and moderately weathering resistant. Its porosity is high at 21 % and its compressive strength is low. A larger fragment was examined in the company's own laboratory: The water absorption value ranges between 15.6 to 20.3 kg/(m2 · √h) with an anisotropy of 23 %.

5. PRESERVATION AND THE CAUSES FOR DAMAGE

Damage caused by road salt to historic buildings and staircases is a common occurrence in Goslar. This can also be observed on the monumental stairways to the Imperial Palace (Fig. 2). It can be seen here that the contamination and salt efflorescence can change greatly depending on the season and a progressive loss of substance can be traced (Fig 2 a – c).

Figure 2: a) the Staircase in summer 2009, b) in summer 2020 and c) during springtime 2021. d) Detail area in summer 2009 and e) the same area in 2021.

The outer wall of the south-facing staircase of the town hall has been showing clear signs of weathering for a long time. Cracks and damage were noticed on the balustrade and walls as early as ten years ago. The stone damage on the balcony was attributed solely to moisture and the need for proper drainage was highlighted (Goslarsche Zeitung, 10.09.2011): "Wind and weather have left their mark on the historic town hall". The town hall would have "wet feet" stated the local

newspaper (Goslarsche Zeitung, 8.05.2010). However, "salt" as a possible damage-contributing factor was not mentioned, neither in the daily press nor in a survey of a local engineering company which was tasked with investigating the situation (Fig. 2a).

The cracking is primarily a result of rust formation on iron elements. The wrought-iron brackets, with which the parapet elements were connected to each other and to the parapet cornice, showed significant corrosion. This led to a volume increase of up to 200 % (Fig. 3b and c).

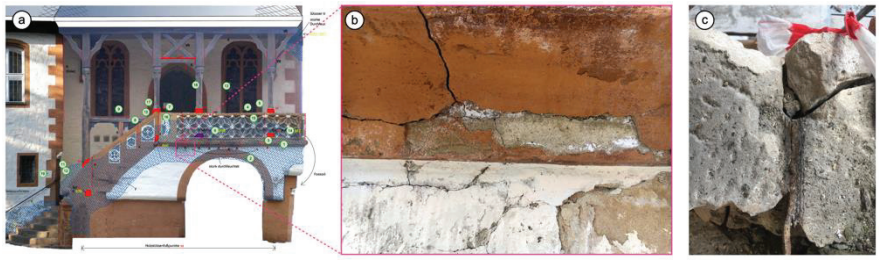

Figure 3: a) A damage mapping by the mentioned engineering firm showing cracks (red) and moisture areas (blue) and b) cracks, broken areas and salt efflorescence c) Corroded iron brace with a volume increase of about 200 %.

In addition, salt exposure accelerates iron corrosion. This was evidently the case here, but it has not been the subject of expert opinion or more detailed investigation in the past. The cracks were so big that the upper elements of the parapet had to be removed and repositioned (Fig. 3c). Only in an expert opinion by an academic restorer, the salt weathering was pointed out and a large-scale stone replacement was recommended [10].

6. PRELIMINARY INVESTIGATION

Preliminary investigation of the monuments included measurements of the electrical capacity with a portable Protimeter Surveymaster (General Electric) on the tomb stela and the outer facade of the staircase. The results ranged from around 100 REL to nearly 1000 REL (Fig. 4). The instrument manufacturer specifies values 70-169 as dry, values 170-199 as risky, and values 200 - 999 as wet.

The Lower Saxony State Office for the Preservation of Monuments (NLD), Department of Specialist Services - Unit for the Preservation of Monuments, Buildings and Art - Materials Analysis, had carried out a salt analysis [11]. For this purpose drill dust samples in the depth profile at various areas of the masonry surfaces were taken. The report states: "The sampled efflorescence (…) on the natural stones of the staircase facade (boreholes 2 and 3, see Fig. 4, marked in red) consists predominantly of sodium chloride. As can already be assumed from the damage pattern, the masonry in the area of the outdoor staircase contains a very high salt content. On the basis of the drillings it can be seen that the salt contents decrease into the masonry, but are still high at a depth of 3 - 5cm."

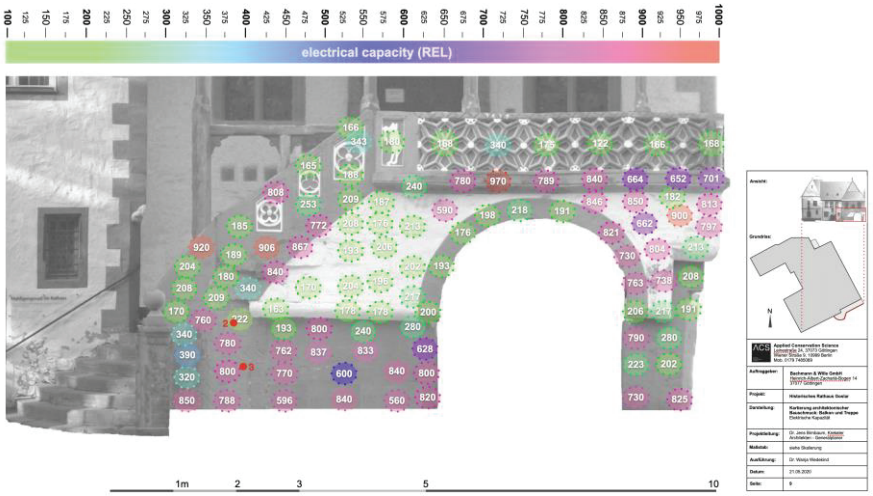

Figure 4: Electrical capacity measurements on the staircase and balustrade of the town hall in Goslar with boreholes of the drill dust samples (red).

7. DESALINATION TREATMENT

Before the restoration project began, the grout of the joints on the salt-contaminated components had already been removed, which is a common mistake. The work was obviously carried out in the hope that the masonry will dry out and this goal was indeed achieved. As a result, however, the damaging salts crystallized not in the joint mortar (typically the weakest link in the masonry bond) but on the historic surface (Fig. 5b and c).

Figure 5: a) The staircase and balustrade in 2018 and b) and c) the stone elements right before desalination treatment.

The masonry below the parapet was also found to be permeable to moisture and heavily contaminated with salts. Here, the mechanism that had led to stone damage was used for the desalination and a directed moisture flow was set up. For this purpose, a second wall of polystyrene panels was built in front of the inner parapet side (Fig. 6a and b). The sand was poured in between the wall and the parapet to a height of about 50 cm, and this was filled with 10 liters of water per segment and working day. A hot lime mortar was applied to the south-facing exterior wall, and its surface was covered after hardening to increase its surface area.

Figure 6: a) The design of the desalination procedure and b) a polystyrene panel behind the balustrade.

The moisture now continuously diffused from the inside to the outside, and the salts were systematically leached out and accumulated in the poultice-plaster which led to visible efflorescence (Fig. 7 a-d). The salt efflorescence was concentrated in the joint areas (Fig. 7 d). This efflorescence was swept off weekly, loosely during the first two weeks, and from the third week onward they were removed with a wire brush and analyzed (Fig. 7 e-g) because, at about this time, a dense salt crust had formed on the plaster surface.

The results of the preliminary investigation clearly showed that the soluble salts concentrated along the footpaths of the people (Fig. 3a and 4). The location of the salt contamination and the type of salt suggests that the source of the damage is road salt that was either spread on the staircase or introduced into the historic fabric by visitors of the town hall.

The heavily salt-contaminated areas can be specified as about 8-10 square meters of the object's surface. The attached diagram 2e illustrates the amount of plaster/salt material removed, 2g shows the percentage amount of salt in this material, and 2f expresses the amount of salt in grams. The amount of salt removed increased enormously due to the scraping of the plaster surface in the course of the third manual salt reduction (Fig. 6e). Manual salt removal over the seven cycles led to the extraction of approximately 2 kg of light soluble salts from the plaster surface. In addition, the plaster was taken from a sample area of 80 x 80 cm and examined to determine its salt content. For this, a content of 120 grams per square meter can be given.

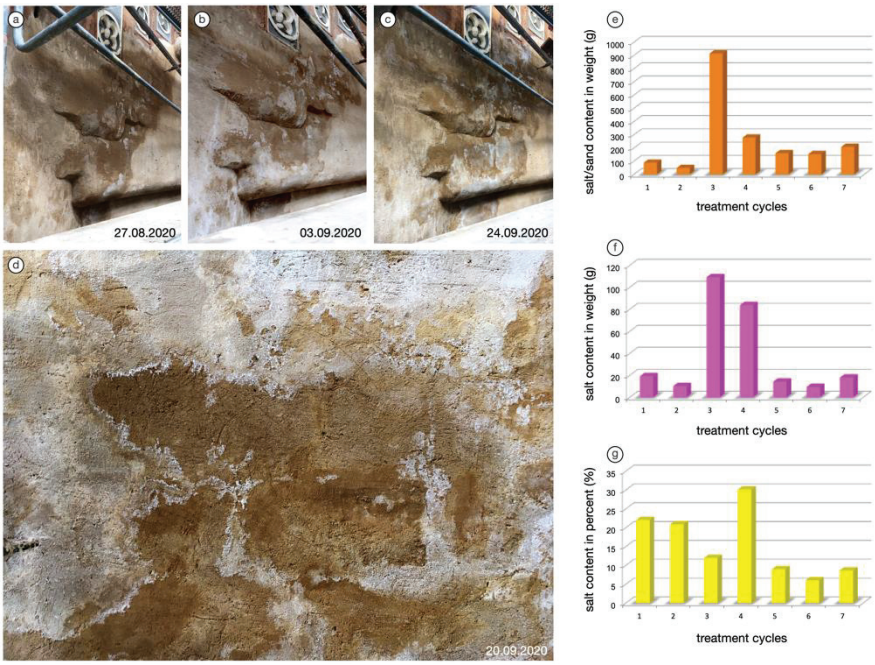

Figure 7: a-c) A section during one month of treatment. d) Salt efflorescence shows the intense concentration along the joints. e) The extracted salt and sand mixture according to the treatment cycles, f) the salt content in weight by gram and g) the salt content in percent.

In total, about 2000 grams could be extracted from the heavily contaminated areas. Repeated analyses of drill dust samples in the immediate vicinity of sampling points 2 and 3 showed a salt reduction of up to almost 75% compared to the results before desalination.

8. CONCLUSIONS

In the assessment of structural damage, the role of salts harmful to the building is still insufficiently understood, even among experts. The Goslar case study is just one example of this. Damage is usually attributed to moisture and the remedy is seen in the drying of historic building materials, which subsequently leads to salt crystallization and further deterioration of the monument. This is also the reason why in many projects the problem of salt weathering is not taken into account and possible solutions are only found during project execution, in many cases rather counterproductive measures being taken.

The measurement of electrical capacity suitable for a quick and preliminary overview of the distribution of salts and moisture in the near-surface area of mineral surfaces, although it must be taken into account that the results are also strongly dependent on the density of the materials.

Hot lime mortars are excellent as storage plasters for salts harmful to the building. This is due to their particularly intensive bond to the treated substrate as well as

to the favorable pore structure [12]. Hot lime mortars are well suited as poultice mortars for long-term application under alternating humid conditions. Conventional poultices made of cellulose and sand tend to detach and develop mould.

Utilizing the preexisting moisture transport pathways in stone that are naturally present or are a result of secondary porosity during weathering processes is an obvious strategy. It facilitates and promotes the desalination process. Almost total desalination is possible, largely independent of the size of the object even if there is a high salt contamination. A large-scale stone replacement is not necessary. This minimizes costs and preserves the historic substance. The method is particularly suitable in the case of high structural salt contamination.

9 REFERENCES

[1] A. Goudie, H. Viles, "Salt Weathering Hazards," John Wiley & Sons, 1997.

[2] A.E. Charola "Salts in the Deterioration of Porous Materials: An Overview," *Journal of the American Institute for Conservation*, no. 39, pp. 327-343, 2000.

[3] E. Doene**,** "Salt weathering: a selective review" in Siegesmund, S., Vollbrecht, A. & Weiss, T. Natural Stone, *Weathering Phenomena, Conservation Strategies and Case Studies*, *Geological Society Special Publication*, no. 205, London, pp. 51 – 64, 2002.

[4] V. Vergès-Belmin, "Desalination of porous building materials: a review," in H. Leitner, S. Laue and H. Siedel (Eds.) *Mauersalze und Architekturoberflächen – Tagungsbeiträge Hochschule für Bildende Künste Dresden. 1. bis 3. Februar 2002*, Leipzig, pp. 121 – 137, 2003.

[5] A. Heritage, A. Heritage, F. Zezza (Eds.) "Desalination of Historical Buildings, Stone and Wall Paintings," Plymouth, 2014.

[6] W. Wedekind, J. Ruedrich, T. Kracke, T. Licha, S. Siegesmund, "Objectspecific Desalination of Tomb Monuments," in J. W. Lukaszewicz & P. Niemcewicz (Eds.) *Proceedings of the 11th International Congress on Deterioration and Conservation of Stone*, 15. - 20. September 2008, Torún, vol. II, 2008, pp. 1339 – 1347, 2008.

[7] W. Wedekind, C. Schmidt "The three tomb-stelea project," in S. Siegesmund & B. Middendorf (Eds.) *Monument Future: Verfall und Konservierung von Stein. Proceedings of the 14th International Congress on the Deterioration and Conservation of Stone*, Band I and Band II. Mitteldeutscher Verlag, pp. 263 – 268, 2020.

[8] P. Friese, A. Protz "Entsalzung von Mauerwerk und Wandmalerei – Transportmechanismen und Beispiele für die praktische Anwendung," in H. Leitner, S. Laue, H. Siedel (Eds), *Mauersalze und Architekturoberfläche. Tagungsbeiträge Hochschule für Bildende Künste Dresden, 1. - 3. Februar 2002*, pp. 148 – 153, 2003.

[9] W.D. Grimm, "Bildatlas wichtiger Denkmalgesteine der Bundesrepublik Deutschland," Gestein Nr. 128, Lipp-Verlag, Munich 214, 1990.

[10] B. Skasa-Lindermeir, "Stadt Goslar, Historisches Rathaus – Steinrestauratorische Untersuchungen – Zwerchgiebel, Maßwerk, Freitreppe" Bericht Nov./Dec. 2012 (unpublished report), 2012.

[11] R. Niemeyer "Goslar, Rathaus - Freitreppe an der Südostfassade Salzanalysen," Laborbericht 20200611. 10.07.2020, Niedersächsisches Landesamt für Denkmalpflege (unpublished report), 2020.

[12] W. Wedekind, R. Lopéz-Doncel, J. Ruedrich, M. Siedel, S. Siegesmund "Evaluation of innovative treatments and materials for the conservation of the strongly salt-contaminated Michaelis church in Zeitz, Germany" in J.J. Hughes, T. Howind, (Eds.) Science and Art: A Future for Stone. *Proceedings of the 13th International Congress on the Deterioration and Conservation of Stone*, vol. II, pp. 981 – 990, 2016.

EFFECTIVENESS OF WATER REPELLENT COATING ON SALT WEATHRINGOF JAPANESE TUFFS WITH VARIOUS ROCK PROPERTIES

C. T. Oguchi[1*] and Y. Ikeda[2]

KEYWORDS

Tuff, Salt weathering experiment, Pore size distribution, P-wave velocity, Surface protectant

ABSTRACT

Tuff is used as a stone material because of its rich colours, and it is also a rock that forms a unique landscape in volcanic Japan. However, it is generally a fragile rock susceptible to weathering and deterioration. In this study, salt weathering experiments were conducted to confirm the effectiveness of water repellent coating on rocks using a sodium sulfate solution on five tuff types with various pore size distributions and different tensile strengths. The experiment was repeated at 20°C-40°C for 48 hours up to 20 cycles. The weight and P-wave velocity of each specimen were measured after each cycle. In the case of the uncoated specimen, the P-wave velocity decreased gradually as the solution reached the surface. The salt crystals precipitated, and the surface of the specimen peeled off. On the other hand, in the case of the stone coated with the repellent, no salt crystallization and no decrease in P-wave velocity were observed soon after the start of the experiment. However, as the experiment progressed, cracks propagated and the P-wave velocity began to decrease, and the surface layer peeled off.

1 INTRODUCTION

Tuff has long been used as cultural heritage and building stone in Japan because it is fire-resistant, easy to cut. It has a wide range of colours, which is also the one of the reasons to be popular usage. However, it is generally a fragile rock and therefore susceptible to weathering and deterioration. Many experiments using water repellents have been studied to protect rocks, however, most of those studies evaluate by water absorption [1)], which is not enough because rock properties have not been evaluated during experiments. The purpose of this study is to evaluate the

[1] Graduate School of Science and Engineering, Saitama University, Japan
[2] Civil and Environmental Engineering Course, Saitama University, Japan

weathering phenomena of various types of tuffs through laboratory experiments and to verify the effectiveness of using water repellents coating on the surface of those stones.

2 METHODS

In this study, five tuff types (Oya-ishi[2], Nikka-ishi[3], Ashino-ishi[4], Tatsuyama-ishi[5], and Towada-ishi[6]) with various pore size distributions and different tensile strengths were used. Physical and mechanical tests (true density, bulk density, porosity, pore size distribution, echo chip hardness, elastic wave (P-wave) velocity, compressive tensile strength, uniaxial compressive strength) were carried out.

These tuffs were cut with a size of 5 cm × 5 cm × 15 cm for the starting materials. Water-repellent specimens were prepared by alkyl-alkoxysilane coating on the five surfaces except for bottom. As a control, non-treatment specimens were also prepared. Both specimens were oven-dried at 110°C, and then partially immersed lower 2 cm from the bottom in a sodium sulphate solution with the 1/2 solubility at 20°C. This partial immersion test was performed in 48h cycles, i.e., immersion at 20°C for 24h and drying at 40°C for 24 hours. At each drying period, weight of each specimen and replenishment of saline solution, P-wave velocity, and Equotip hardness values were measured. This experiment was continued up to 20 cycles.

3 RESULTS AND DISCUSSION

3.1 P-wave velocity, Equotip hardness and salt susceptibility index

P-wave velocity (V_p) and Equotip hardness (L) is common non-destructive tests that reflects the fracture and void conditions within a rock. In this study, the decrease rates of those changes are considered as the salt weathering rate, the number of cycles is x and the rate of weathering is C_p, which is approximated as Equation (1): higher values of C_p indicate greater degradation at the end of the cycle.

$$Vp/Vp_0 = 1 - Cpx \ldots (1)$$

$$L/L_0 = 1 - C \cdot n \ldots (2)$$

Table 1: Initial surface flaking occurred for stones with/without water repellent coating.

Rock	C_p		C_L		Initial surface flaking	
	Non-Coating	Coating	Non-Coating	Coating	Non-Coating	Coating
OY	0.1100	0.1100	0.190	0.130	2	2
NK	0.0100	0.0210	0.030	0.028	7	14
TY	0.0100	0.0130	0.040	0.020	9	11
AN	0.0035	0.0035	0.018	0.014	-	15
TW	0.0060	0.0055	0.014	0.016	8	4

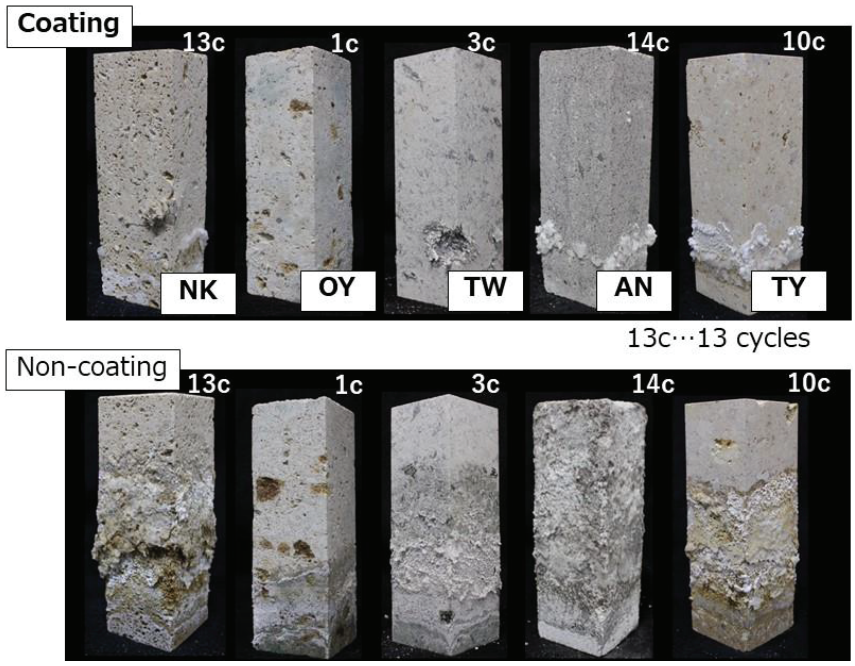

Figure 1. Observation after the salt weathering experiment. The coating specimens show before the exfoliation. OY: Oya-ishi, NK: Nikka-ishi, TY: Tatsuyama-ishi, TW: Towada-ishi, and AN: Ashino-ishi.

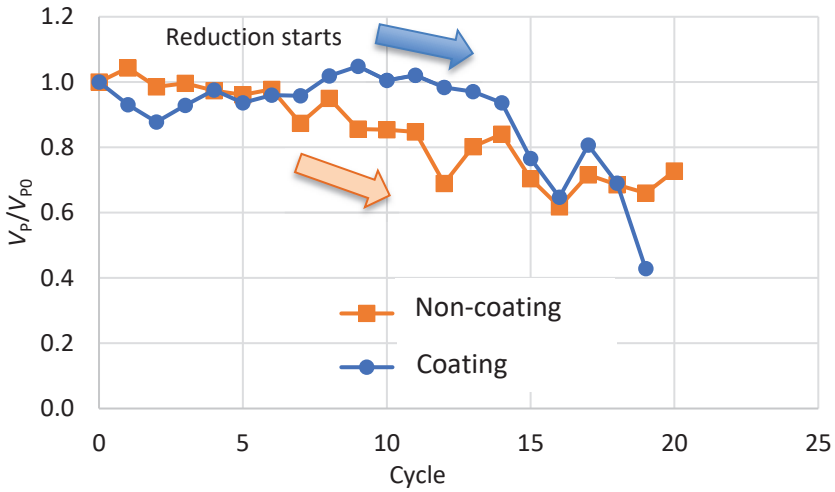

Figure 2. Example of the results of P-wave velocity during weathering experiment for Nikka tuff (NK).

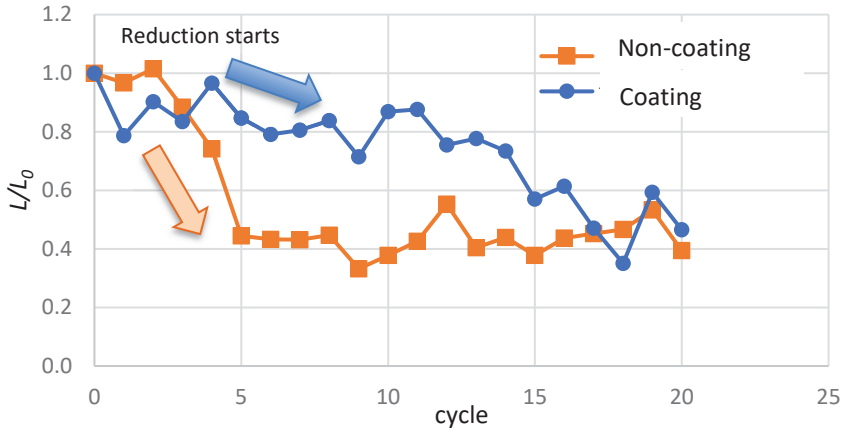

Figure 3. Example of the results of Equotip hardness (L) during weathering experiment for Nikka tuff (NK).

Figure 1 shows the observation after the salt weathering experiment. The coating specimens show before the exfoliation. The timing of the initial weathering (flaking, exfoliation, etc) was determined from the appearance of the stone and the timing at which the P-waves or Equotip hardness started to decrease, respectively in Figures 2 and 3. It was defined as when *initial surface flaking* occurred for stones with/without water repellent coating, indicating with arrows.

Rock deterioration due to salt weathering is influenced by the stress (crystalisation pressure) associated with salt precipitation in the pore space, which depends on the pore size. However, the Salt Susceptibility Index (*SSI*) [7] can estimate the degree of influence of salt weathering on rocks based on pore properties alone (Table 2).

$$SSI=(I_{PC}+I_{Pm0.1})(P_{m5}P_c) \quad \ldots (3)$$

Table 2: Salt Susceptibility Index (*SSI*)[7] for tuffs.

Parameter	Rock				
	OY	NK	TY	AN	TW
P_c (%)	37.1	41.3	14.3	20.1	23.8
I_{Pc}	9	10	4	6	6
$P_{m0.1}$ (%)	18.9	13.6	12.4	3.1	17.3
$I_{Pm0.1}$	9	7	6	3	8
P_{m5} (%)	34.0	34.6	13.1	19.0	22.8
P_{m5}/P_c	0.92	0.84	0.92	0.95	0.96
SSI	16.5	14.3	9.2	8.5	13.4

OY: Oya-ishi, NK: Nikka-ishi, TY: Tatsuyama-ishi, TW: Towada-ishi, and AN: Ashino-ishi.

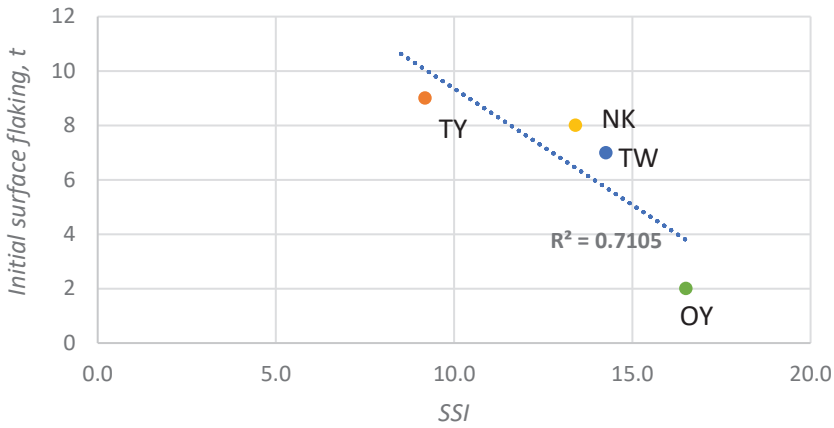

Figure 4. Relationships between *SSI* and *initial surface flaking*. OY: Oya-ishi, NK: Nikka-ishi, TY: Tatsuyama-ishi, TW: Towada-ishi, and AN: Ashino-ishi.

3.2 Effect of water repellent coating

Compared to uncoated stone, the part of the water repellent coating part is less crystalline and less aesthetically pleasing than uncoated stone. The applied stone was found to be more effective in maintaining the aesthetic appearance of the stone than the uncoated stone, as no crystals were deposited on the surface (Figure 1). The weathering of the stone was delayed by the protective agent (Figures 2 and 3). The weathering of some stones (NK, TY) was delayed by the protective agent, while others (AN, TW) were accelerated. The weathering of some stones (NK, TY) was delayed by the protective agent, while others (AN, TW) were accelerated (Table 1). The coated stones except for OY were not affected by weathering. The coated stones except for OY deteriorated more rapidly than the uncoated stones once weathering had started. The appearance and P-wave velocity values of the coated stones except for OY, showed that they deteriorated more rapidly than the uncoated stones once weathering started. The appearance and P-wave velocity values showed that the stones coated with OY deteriorated more rapidly than those without OY once weathering started.

All these stones had a more severely degraded and reduced appearance and P-wave velocity at the end of the cycle than the stones without coating. P-wave velocity at the end of the cycle was more severely degraded and reduced than that of the uncoated stone (Table 1). The applied stone is consequently more severely degraded than the uncoated stone. The resulting degradation is due to the larger crystalline pressure that breaks the surface-hardening zone formed by the protectant. The reason for this is that the salt crystal pressure is large enough to break the surface hardening zone formed by the protectant, which occurs before the hardening zone. This is because the salt crystal pressure is large enough to break the surface hardening zone formed by the protectant. In other words, the total salt crystal pressure is greater before the hardening zone than the total force of the crystalline pressure of the uncoated stone. The total salt crystalline pressure accumulated before the

hardening zone is consequently greater than the total crystalline pressure of the uncoated stone. The total force of the crystalline pressure of the salt accumulated before the hardening zone is consequently greater than the total force of the crystalline pressure of the uncoated stone, which can cause severe fracture. If the protective agent is left in place for a longer period than this, the presence of the protective agent may cause deterioration. This suggests that the presence of a protective agent may contribute to degradation if the protective agent is left on for a long period of time. The results of this study suggest that the presence of a protective agent may instead contribute to degradation if the protective agent is left applied for a long time.

4 CONCLUSION

The use of a protective agent is a major risk when using a rock When using a protective agent, it is important to consider the rock It is important to understand the combination of rock properties such as pore size distribution, strength and mineralogy of the rock sample and crystal pressure when using a protectant.

ACKNOWLEDGEMENTS

We would like to thank Mr. Yoshimura and Dr. Fukumura at Perfect Wash Co. for their full cooperation in the application of the water repellent coating.

REFERENCES

[1] S. Date, Y. Goryouzono, S. Hashimoto and S. Miyazato (2012)： The Evaluation of Performance of Hydrophobic Impregnation—Comparison with European Norm (EN 1504-2)— Concrete Journal, 50, 331−337 (in Japanese with English abstract).

[2] Y. Nakamura, S. Matsui, A. Suzuki (1981): Geology of the Oya Area. Utsunomiya City. Bulletin of Faculty of Education, Utsunomiya University, 31, 105-106 (in Japanese with English abstract).

[3] M. Sawazaki, T. Kunimoto, Y. Kusakabe (1993): Studies on the Mechanical Proerties of Rhyolitic Tuff (Nilkka Stone) in Kanagaso District, Komatsu City, Ishikawa Prefecture. Memoirs of the Fukui Institute of Technology. 23, 153-160 (in Japanese with English abstract).

[4] H. Yoshida, M. Takahashi (1991): Geology of the eastern part of the Shirakawa pyroclastic flow field. Jour. Geol. Soc. Japan, 97, 231-249 (in Japanese with English abstract).

[5] R. Kobayashi (2001): Tatsuyama-ishi － Stone in Kinki district in Japan, Chishitsu news, 557, 26-32 (in Japanese).

[6] Towada-ishi <https://towadaishi.jp/about/> (2023.8.23)

[7] S. Yu and C. T. Oguchi (2010): Role of pore size distribution in salt uptake, damage, and predicting salt susceptibility of eight types of Japanese building stones. Engineering Geology, 115, 226−236.

FUNDAMENTAL STUDY ON DESALINATION METHODS FOR BRICK CHIMNEYS PART 2 DIFFUSION VERSUS ADVECTION

Masaru Abuku[1], Takayuki Fumoto[2], Tomoko Uno[3], and Chiemi Iba[4]

KEYWORDS

Desalination rate, Sodium sulfate, Masonry systems

ABSTRACT

Some of brick chimneys built after modern times in Japan have been deteriorated due to salt weathering. Although dissolution and removal of salts by water is generally useful for desalination to inhibit salt weathering of bricks, previous studies [1-2] have shown that salt crystals change the strength of the porous material and cause cracks. When structural materials of buildings are desalinated, careful attention needs to be paid to the structural strength.

Desalination of brick walls is usually done mainly by two methods: desalination by poulticing [3-4] and electric desalination [5-8]. In both methods, diffusion and advection of salt ions would play an important role. Our previous experimental study of desalination of a brick specimen containing sodium sulfate [9], which was done for purpose of desalination of brick chimneys, showed that 75 % of the salt contained in the specimen was desalted after 15 days during which the specimen was dried once a day, then absorbed pure water, and was immersed in pure water. This experiment also showed that the rate of desalination significantly decreased when the process of pure water absorption was omitted. This means that advection of salt ions during pure water absorption played an important role in the desalination. In the experimental study presented here, we quantified the rate of desalination during which either diffusion or advection would mainly occur, in order to compare desalination due to diffusion and advection.

[1] Faculty of Architecture, Kindai University, Osaka, Japan, abuku@arch.kindai.ac.jp
[2] Faculty of Science and Engineering, Kindai University, Osaka, Japan
[3] School of Architecture, Mukogawa Women's University, Hyogo, Japan
[4] Graduate School of Engineering, Kyoto University, Kyoto, Japan

Specimens were cut from a brick (100 × 60 × 210 mm^3), resulting in the dimensions of 50 × 60 × 30 mm^3. All the surfaces of the specimens except the two 60 × 30 mm^2 surfaces were made vapor-proofed.

Two different desalination experiments were conducted as illustrated in Figure 1. In the former case (case A), the specimen was completely immersed into pure water, so that salt ion diffusion from the inside of the specimen to the surrounding water would occur. In the latter case (case B), only the bottom of the specimen was immersed, so that pure water is continuously absorbed into the specimen and evaporates at and near the top surface and, as a result, ion advection from the bottom to the top surface and salt crystallization on and near the top surface would occur. In case A, three specimens A1-A3 were desalinated at 24 °C, while A4-A6 were at 40 °C; in case B, four specimens A1-A4 were desalinated at 24 °C, while A5-A8 were at 34 °C. The average density and porosity of the specimens are 1877 kg/m^3 and 0.28 (-) for case A and 1843 kg/m^3 and 0.27 (-) for case B. The capillary absorption coefficients of specimens for pure water $A_{cap,w}$ and for saturated salt solution $A_{cap,s}$ were measured at 24 °C (Figure 2). After the salt solution uptake tests, the specimens were desalinated. The temperature and time of desalination and the final percentage of desalination of the specimens are summarized in Table 1.

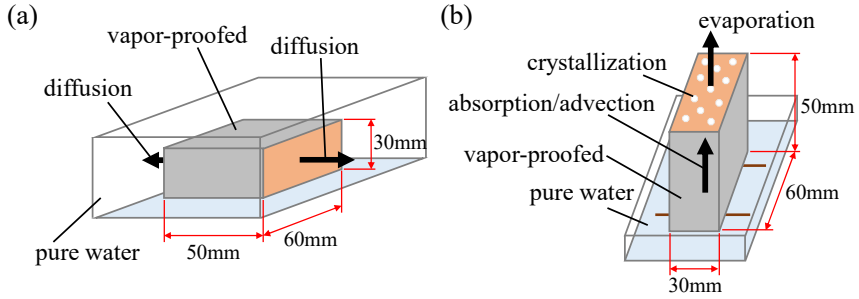

Figure 1: Schematic diagram of experiments of desalination due to (a) diffusion (case A) and (b) advection (case B).

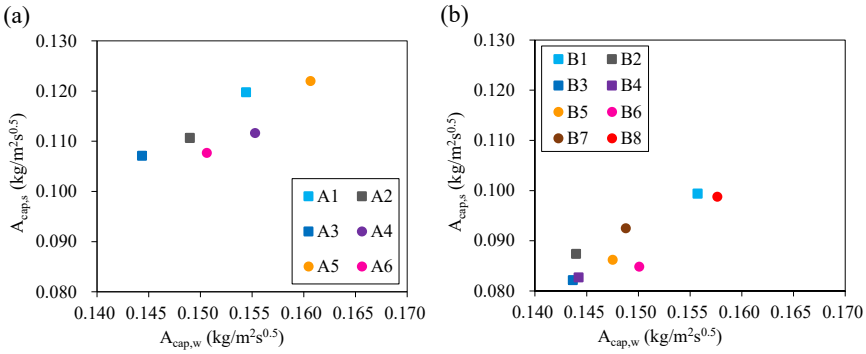

Figure 2: Capillary absorption coefficients of specimens for pure water $A_{cap,w}$ compared to that for saturated salt solution $A_{cap,s}$. (a) Case A and (b) case B.

Table 1: Desalination temperature, desalination time, and final percentage of desalination.

specimen	desalination temperature (°C)	desalination time (h)	final percentage of desalination (%)
A1	24	480	62.1
A2		480	60.7
A3		336	50.5
A4	40	480	77.7
A5		480	81.8
A6		168	45.3
B1	24	24	19.7
B2		192	70.3
B3		192	66.7
B4		72	32.2
B5	34	24	7.7
B6		72	54.3
B7		222	67.9
B8		312	97.9

The measured desalination rate and percentage of desalination of the two cases at two different ambient air temperatures are plotted in Figure 3. Each line in Figure 3 shows the average value of three specimens for case A and four specimens for base B. The results show that desalination due to advection is much faster than that due to diffusion and desalination is faster at the higher temperatures. However, specimens B2 and B3 were cracked at 192 hours. Figure 4(a) shows a photograph of the top surface of specimen B2 taken after desalination; Figure 4(b) and Figure 4(c) display X-ray CT images near the top surface and approximately 3.5 mm below the top surface. The crack of specimen B3 was similar to that of specimen B2. Comparison of Figure 4(b) and Figure 4(c) shows that the crack is larger near the top surface of the specimen. Desalination at a higher temperature does not only lead to a high desalination rate but also to avoiding cracking during desalination.

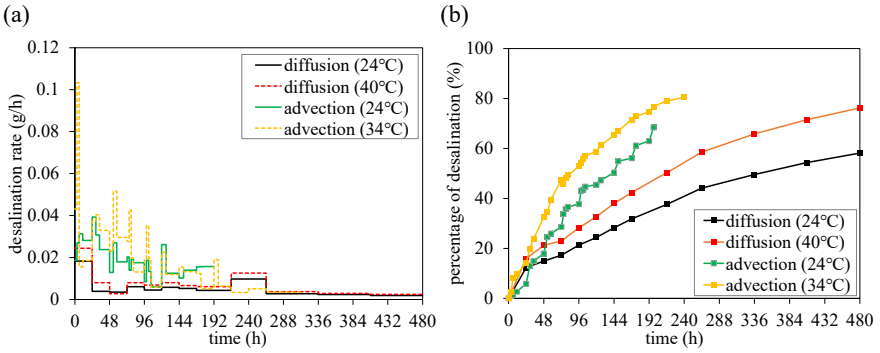

Figure 3: (a) The average desalination rate and (b) percentage of desalination of the two cases at two different ambient air temperatures.

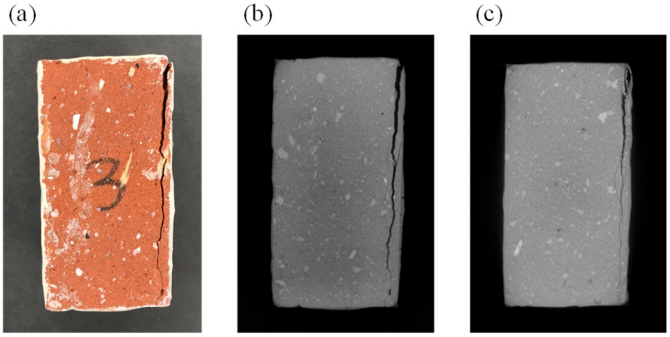

Figure 4: (a) A photograph of the top surface of specimen B2 taken after desalination and X-ray CT images (b) near the top surface and (c) approximately 3.5 mm below the top surface. The number 3 written on the top surface does not mean the number of the specimen used in this paper and thus should be omitted.

REFERENCES

[1] D. K. Knöfel, D. Hoffmann, and R. Snethlage, "Physico-chemical weathering reactions as a formulary for time-lapsing ageing tests," *Materials and Structures*, vol. 20, pp.127-145, 1987.

[2] F. Paolo and V. Alessia, "Experimental investigation on bricks from historical Venetian buildings subjected to moisture and salt crystallization," *Engineering Failure Analysis*, vol. 45, pp.185-203, 2014.

[3] V. Vergès-Belmin, "Desalination of Masonries and Monumental Sculptures by Poulticing: A Review," *Restoration of Buildings and Monuments*, vol. 11(6), pp.391-408, 2005.

[4] I. Rörig-Dalgaard, "Development of a poultice for electrochemical desalination of porous building materials: desalination effect and pH changes," *Materials and Structures*, vol. 46, pp.959-970, 2013.

[5] J. M. Paz-García, "Simulation-based analysis of the differences in the removal rate of chlorides, nitrates and sulfates by electrokinetic desalination treatments," *Electrochimica Acta*, vol. 89, pp.436-444, 2013.

[6] N. Husillos-Rodríguez, "Sacrificial mortars for surface desalination," *Construction and Building Materials*, pp.452-460, 2018.

[7] G. Skibsted, "Electrochemical desalination of bricks - Experimental and modeling," *Electrochimica Acta*, vol. 181, pp.24-30, 2015.

[8] J. Feijoo, "Electrokinetic desalination of a farmhouse applying a proton pump approach. First in situ experience," *Construction and Building Materials*, 243, pp. 1-14, 2020.

[9] A. Kimura, M. Abuku, T. Fumoto, T. Uno, and C. Iba, "Fundamental study on desalination methods for brick chimneys, Part 1 Desalination by ion diffusion," in Proceedings of SWBSS 2021 (Fifth International Conference on Salt Weathering of Buildings and Stone Sculptures), pp. 273–274, 2021.

INSIGHT ON ZWITTERIONIC POLYMER-TERMINATED CALCIUM CARBONATE OLIGOMER AS SALT-RESISTANT MATERIALS FOR SANDSTONE HERITAGE

Junyan Liang[1] and Ling He[1*]

KEYWORDS

Zwitterionic polymers, Calcium carbonate oligomers, Sandstone heritage, Protective materials, Resistance to salt weathering

ABSTRACT

Outdoor immovable sandstone grotto sites are abundant in number and type in China. Despite the great historical, artistic and scientific value, they generally suffer from severe weathering damage. For example, salt weathering has been implicated as a cause of disintegration of the Leshan Giant Buddha, a world cultural and natural heritage in Sichuan province, due to the salt crystallization pressure and hydration. Salt damage could be weakened by protective materials that reinforce the fragile sandstone and simultaneously promote the migration of soluble salts towards the sandstone surface via water without crystallization inside the sandstone. However, the reported protective materials accelerate sandstone deterioration by hindering water/salt migration or peel from the sandstone to reduce their service life. To address this issue, our project proposed to design and synthesize a novel zwitterionic polymer-terminated $CaCO_3$ oligomer. Specifically, the water/salt affinity of zwitterionic polymer facilitated the water/salt migration and the small size effect and crosslinking property of $CaCO_3$ oligomer facilitated the interfacial adhesion towards sandstone. The specific research work and main research results are as follows:

(1) Methacryloyloxyethyl phosphorylcholine (MPC) containing zwitterionic groups and methacryloxypropyl trimethoxylsilane (MPS) containing Si-OR active groups were used as functional monomers to prepare the zwitterionic copolymer P(MPC-*ran*-MPS) by free radical polymerization. Meanwhile, $CaCO_3$ oligomers were prepared by using triethylamine (TEA) as end-capping agent. Subsequently, zwitterionic polymer-terminated $CaCO_3$ oligomer [P(MPC-*ran*-MPS)/$CaCO_3$] (Figure 1) was obtained by replacing end-capping agent TEA of $CaCO_3$ oligomers

[1] School of Chemistry, Xi'an Jiaotong University, Xi'an 710049, China. E-mail: heling@mail.xjtu.edu.cn

with P(MPC-*ran*-MPS). Specifically, P(MPC-*ran*-MPS)/$CaCO_3$ was further cross-linked by tetramethoxysilane (TMOS) to create P(MPC-*ran*-MPS)/$CaCO_3$-TMOS composite. The results showed that the adhesion strength of composite first increased and then decreased with increasing MPS or $CaCO_3$ content. The maximum adhesion strength of composite was 1.176 MPa (Figure 2). In addition, it was found that the wettability of the composite coatings could change from hydrophobicity with a contact angle of 108.4° to hydrophilicity with a contact angle of 12.5° as the molar ratio of MPC to MPS in zwitterionic polymer increased from 4:6 to 8:2.

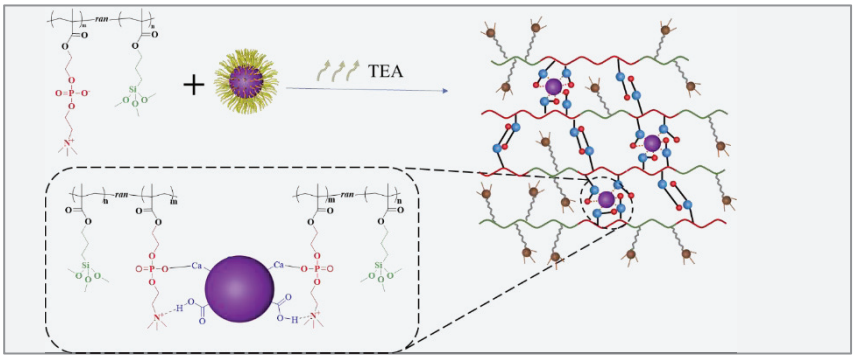

Figure 1: Synthetic routes to P(MPC-*ran*-MPS)/$CaCO_3$.

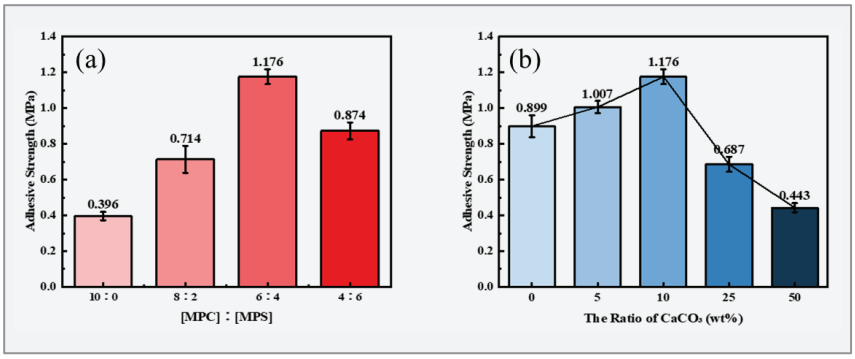

Figure 2: The effect of MPC: MPS feed molar ratios (a) and content of $CaCO_3$ (b) on the adhesion strength of P(MPC-*ran*-MPS)/$CaCO_3$-TMOS coating towards the glass plate.

(2) To further improve the adhesion strength of P(MPC-*ran*-MPS)/$CaCO_3$-based coatings, methacryloyl POSS (MA-POSS) and diethylenetriamine (DETA) were selected to synthesis POSS-DETA through Michael addition reaction, followed by replacing end-capping agent TEA of $CaCO_3$ oligomers in P(MPC-*ran*-MPS)/$CaCO_3$ with DETA to obtain P(MPC-*ran*-MPS)/$CaCO_3$-POSS (Figure 3). The results revealed that the P(MPC-*ran*-MPS)/$CaCO_3$-POSS exhibited an adhesion strength of 1.303 MPa due to the hydrogen bonding provided by a large number of -NH_2 groups in POSS-DETA. However, the presence of hydrophobic POSS-DETA induced an increase in water contact angle of P(MPC-*ran*-MPS)/$CaCO_3$-POSS coating.

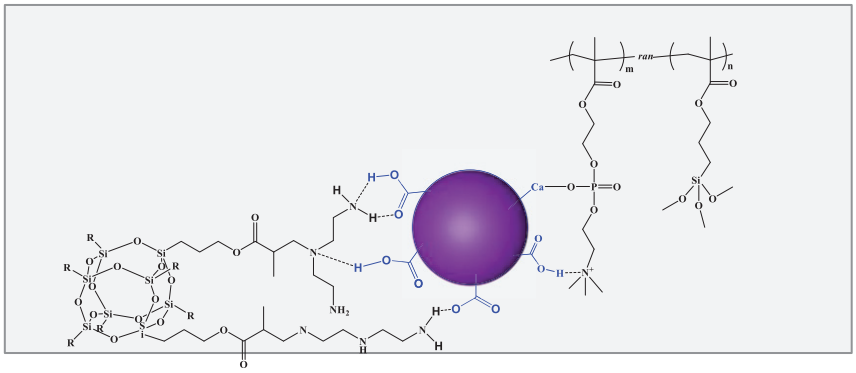

Figure 3: Structural depiction of P(MPC-*ran*-MPS)/$CaCO_3$-POSS.

(3) Obtained P(MPC-*ran*-MPS)/$CaCO_3$, P(MPC-*ran*-MPS)/$CaCO_3$-TMOS, P(MPC-*ran*-MPS)/ $CaCO_3$-POSS and POSS-DETA were used as protective materials to resist salt weathering of sandstone. The physical properties, surface microstructure and the resistance to freeze-thaw and salt crystallization aging cycle for sandstone before and after protection were evaluated at lab-scale. It demonstrated that the surface microstructures of sandstones protected by P(MPC-*ran*-MPS)/$CaCO_3$-TMOS and P(MPC-*ran*-MPS)/$CaCO_3$-POSS were most similar to that of original sandstones. The protective materials all enabled the sandstone to perform good water permeability except for POSS-DETA (Figure 4). The cholinesterase-inhibition assay indicated that the P(MPC-*ran*-MPS)/$CaCO_3$-based composite could be dissolved out after treated sandstone samples was immersed in water and the dissolution rate was 5.2-5.6 wt% within a week. However, the number of freeze-thaw cycles and salt-resistant crystallization aging cycles on the sandstone treated with these four protective materials was more than double those on the untreated sandstone.

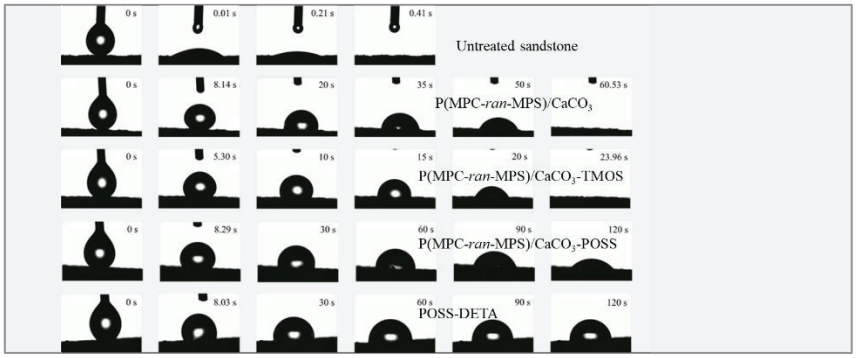

Figure 4: The observation of water permeability on untreated sandstone and treated sandstone by different P(MPC-*ran*-MPS)/$CaCO_3$-based materials and POSS-DETA material.

(4) The ability of protective coatings to delay and inhibit salt crystallization, to reduce salt crystallization pressure and to promote water and salt migration was elaborately evaluated by investigating the salt crystallization characteristics in air

and in a limited region, and testing the salt migration rate inside the sandstone after protection. Obviously, the Na_2SO_4 crystallization started at 50 min on the surface of glass plate but started at 80 min on the surfaces of P(MPC-*ran*-MPS)/$CaCO_3$-based coatings. Moreover, Na_2SO_4 crystals were dispersed on the surfaces of protective coatings. Importantly, the protective coating could also induce a lower crystallization force of 35.7 mN (3.64 g) and a shorter crystallization duration of 100 min than the glass plate with a crystallization force of 459.1 mN (46.85 g) and a crystallization duration of 24 h (Figure 5). In addition, P(MPC-*ran*-MPS)/$CaCO_3$ and P(MPC-*ran*-MPS)/$CaCO_3$-TMOS could significantly enhance the salt migration towards the surface of sandstone (Figure 6). Typically, the salt migration rates of treated sandstone samples were measured as 97.7 mg/d and 91.3 mg /d, respectively. In contrast, the sandstone treated with P(MPC-*ran*-MPS)/$CaCO_3$-POSS had a lower salt migration rate at 14.2 mg/d than untreated sandstone with a salt migration rate at 78.0 mg/d.

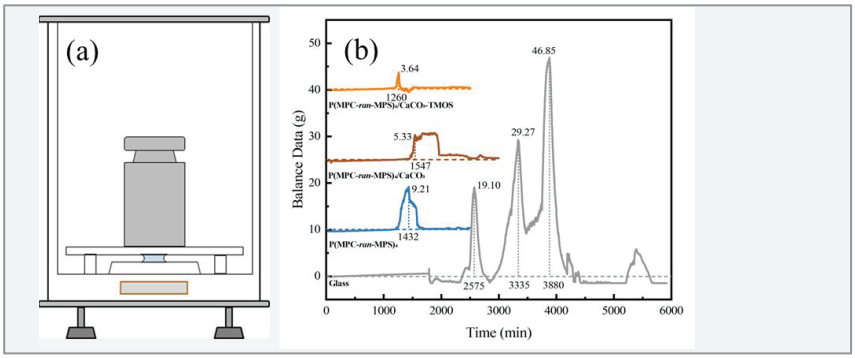

Figure 5: (a) Schematic representation of a self-made device used for evaluating the salt crystallization pressure; (b) the salt crystallization pressure of three coatings.

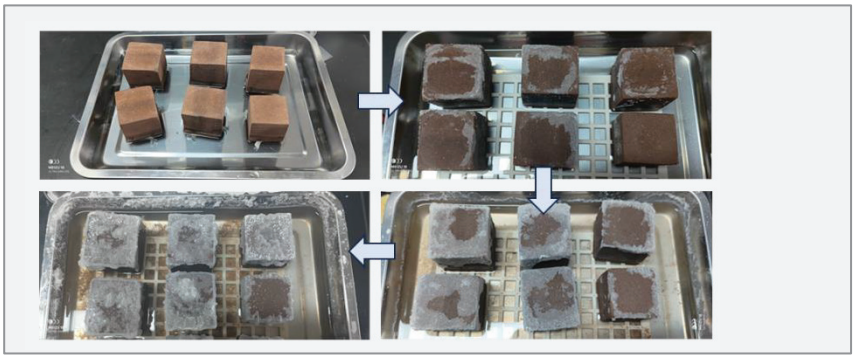

Figure 6: Enhanced water/salt migration for sandstone treated by P(MPC-*ran*-MPS)/$CaCO_3$ and P(MPC-*ran*-MPS)/$CaCO_3$-TMOS.

CHALLENGES AND INTERVENTION STRATEGY IN MANAGING SALT DAMAGE FOR THE BRICK WALLS HIDDEN IN THE SUB-FLOOR OF THE 135-YEAR-OLD COLONIAL HERITAGE HOTEL IN SINGAPORE

Ryanne H.S. Tang[1] and C.W. Wong[1]

KEYWORDS

Salt simulation, Hygrothermal monitoring, Sub-floor microclimate, Salt crystallization attack

ABSTRACT

In 2017, a major retrofitting and restoration exercise was commissioned to be carried out for the oldest and iconic colonial heritage hotel in Singapore. The Hotel with colonial architecture was opened in 1887 and remains to be one of the few surviving greatest 19th century hotels in the world. It has welcomed many famous personalities over the decades, from celebrities to politicians, and members of royalty. With its significant history for the country, it has been gazetted as a National Monument.

Inevitably, there were a number of technical challenges encountered during the restoration stage, and one of the toughest were the sub-floor spaces present below the guestrooms of the Hotel. The sub-floor was constructed of old brick masonry walls with arched openings. The brick masonry walls extended up to 2 storeys above and served as the load bearing walls between guestrooms. Though salt damage and uprising damp problem were evident the existing building construction complicated the design of intervention approach to address the issues. The access to the sub-floor space is highly limited with the lowest height/headroom clearance of only about 0.7m. There was also no thorough connectivity in the sub-floor spaces among all the guestrooms. In addition, active condensation occurred on the soffit of structural steel decking slab ("BONDEK") inside the sub-floor space, where the excessive moisture aggravated salt crystallization attack on the old brick walls.

While it was viable to perform necessary treatment to eliminate the penetration of uprising water and address the salt damage for the brick walls at the first storey, application of any repair required for the sub-floor appeared to be comparatively

[1] MAEK Consulting Pte Ltd, 18 Boon Lay Way #07-101, Singapore 609966, ryannetang@maek.com.sg

unfeasible. With the findings from the detailed condition assessment completed using combined methods of non-destructive equipment and laboratory tests, this paper discusses few options of intervention strategy which were developed and evolved then to overcome the site constraint and technical challenges in the sub-floor restoration.

Consideration had been given for application of electrokinetic desalination method to extract soluble salts from the wall surface under influence of an applied voltage gradient, so as to minimize the need of labour-intensive work in the sub-floor. On the other hand, an option had also been explored to introduce sacrificial plaster system designed with macro-pore structure for the walls, to accommodate any residual salt crystals formed in the future instead of allowing them to deposit and damage the brick substrate.

The other aspect was to understand the risk of further salt attack on and within the old brick walls during hotel operation in future, given the possibilities that thorough and substantial removal of salts from the sub-floor walls would be difficult to achieve. The risk assessment was made using salt simulation software "RUNSALT" based on the sub-floor microclimate as established by hygrothermal monitoring across the periods of hotel in operation and closure. This presents a clearer picture for the potential threat and increased severity in salt-related damages on the sub-floor walls over time. A monitoring program was also developed for mitigation measure to protect the heritage fabrics.

1 INTRODUCTION

The 135-year-old iconic colonial heritage hotel comprises of different blocks within its compound. While all the blocks appeared with grand presentation on their façade, there were unexpected deterioration going on inside the historic building elements, concealed behind the heavily loaded interior fit-out in the hotel, over the past decades. After dismantling of surface finishes from the walls and floors as part of the preparation for the subsequent restoration work, all the petrifying problems from which the old building materials were suffering were eventually revealed.

Amongst all the blocks, one of the buildings was constructed of load bearing masonry columns and walls, which had extended downwards with arch-openings in the subfloor and likely continued to the footing in the ground. The existence of subfloor was first uncovered by the presence of a row of ceramic perforated vents located along the bottom edge of the inner façade walls, which were likely designed for cross-ventilation to provide cooling to the internal space. This is a common vernacular design for hot humid tropical climate. The actual construction system was only unearthed fully after an opening was made on the level 1 flooring for a breakout inspection to the sub-floor. Unfortunately, there was no as-built drawing or archival documentation record showing more structural details of the building. Besides, it was also noted from the breakout inspection to the subfloor that, some alterations were made in the past upgrading work for the flooring at Level 1 where structural steel decking slab ("BONDEK") had been introduced. See Figure 1.

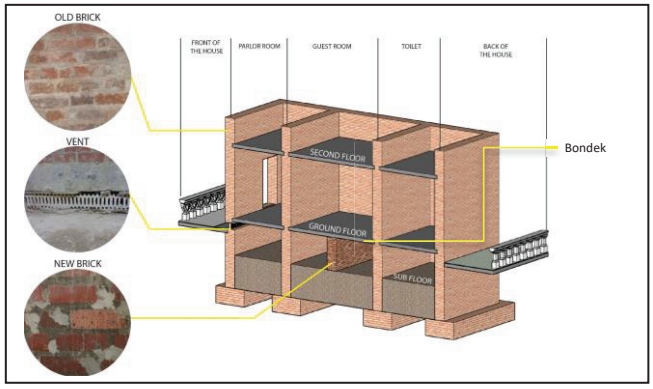

Figure 1: Cross-sectional view showing the actual construction of the historic two-storey building.

Through the pre-restoration inspection made to the sub-floor, signs of severe salt attack and moisture damage were evident on the surface of historic brick walls [1]. This led to the suspection of prolonged rising dampness and salt attack. Other defects like corrosion were noticed on the Bondek system. There were also other walls with clay brick units in different dimensions and colour from those historic ones, remaining in good condition without any visual defect. These were latter-day added, likely to support the added Bondek slab system.

Figure 2: Typical view of a narrow space between the old and new masonry walls. Note also the corroded Bondek slab along the side with the historic masonry wall.

The restricted height clearance inside the subfloor which ranged from 0.7m to 1.4m only made any subsequent restoration strategy to tackle the salt crystallization attack and rising dampness issue of the brick masonry structure rather challenging. Moreover, the existence of newly erected brick walls next to the historic structure had further narrowed the working space inside the sub-floor, adding to the poor accessibility for restoration work.

This paper discusses the investigative assessment and design consideration for the restorative treatment in view of the challenges highlighted earlier. The likely causes and extent of the salt crystallization attack and moisture-related problems such as rising damp and condensation issues were determined with the aids of some non-destructive testing on site and laboratory tests of extracted samples [2]. With the spatial challenges in addressing the problems in the sub-floor, several treatment options with minimum requirement of access had then been explored for execution in consideration of the established condition of walls. Apart from that, as part of the effectiveness monitoring program for the completed restoration work, the risk of salt recurrence during the hotel operation was also studied via salt simulation model in consideration of micro-climate of the involved spaces.

2 UNCOVERED SALT AND OTHER DETERIORATIONS IN THE SUB-FLOOR

During the visual inspection inside the sub-floor, efflorescence was evident on some bricks of the historic walls, as observed from the formation of whitish salt crystals on their surfaces. Such whitish salts mostly manifested as cluster or bundle of needle-like crystals, growing out of and breaking through the surface of clay bricks. As a result, the integrity of brick surface had been compromised with flaky and friable surfaces. This is often attributed to uprising dampness when moisture is transported from the ground upwards via capillary. In the process soluble salts from the ground are dissolved and carried up the wall which then re-crystallizes when water evaporates. The zone where water evaporates is governed by numerous factors which include, the pore characteristics of the substrate, surface finishes, environmental conditions. In this Hotel, the distribution of salt crystallization attack appeared to be random without a distinct pattern. They are found widespread in the sub-floor and at various heights and locations above the sub-floor. The micro climate in the sub-floor with ventilated air flow and yet at times humid condition as seen from the condensation depending the external weather could indeed have

resulted in the formation of efflorescence at one time and crypto-fluorescence at another in the wall. These could have also led to salt crystallizing out from the wall above the sub-floor space, in the air conditioned guest rooms.

Figure 3: Left image - Efflorescence on the surface of the bricks accompanied by flaking or stratification of the surface layers. Middle image - Large crusts of salt crystals which have crystallized out from the surface of the bricks. Right image - Typical symptoms of friable clay and flaking of the bricks caused by salt crystallization.

Condensation found on the underside of the Bondek are indications of humid environment within the sub-floor which impedes drying. However, the presence of efflorescence infers that there could have been local drying for salts with high equilibrium relative humidity, possibly contributed by a fluctuating microclimate in the sub-floor. Severe corrosion of the galvanized steel Bondek along the edges that is supported by the old masonry wall indicates prolonged dampness.

Figure 4: Left image shows condensation on the Bondek at the historic masonry wall side. The condensate water could lead to more water being absorbed by the historic wall. Right image shows the corrosion of the galvanised steel of the bondek especially where the deck buts the wall.

3 SCIENTIFIC ASSESSMENT OF SALT RELATED PROBLEM

3.1 Moisture Distribution

A non-destructive equipment, microwave moisture sensor was deployed to map the moisture distribution within the walls. Since water has a very high dielectric constant, the electric field generated by the microwave will result in the molecules of water trapped inside the materials to vibrate and rearrange. Probe with 110 mm detection depth was used. After all readings were collected, the measurement points were mapped with software to generate a tomographical matrix showing the moisture distribution and any trapped moisture.

Trend of rising damp could be captured from within the walls inside the sub-floor, as higher concentration of moisture was encountered within the bottom half of the wall. See Figure 5.

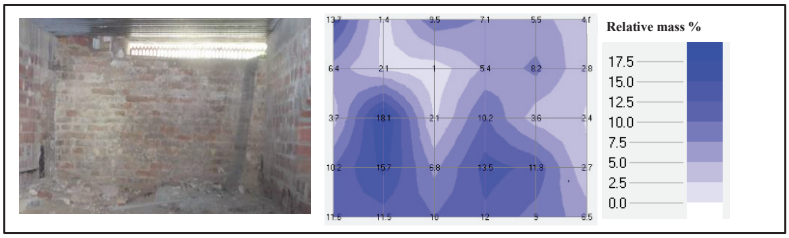

Figure 5: Microwave tomograph of location with rising damp trend detected.

At another wall in the sub-floor, higher moisture content was determined at both the bottom edge, as well as just below the underside of the Bondek. See Figure 6. The latter suggested the possibility of brick wall absorbing the condensate water from the Bondek surface.

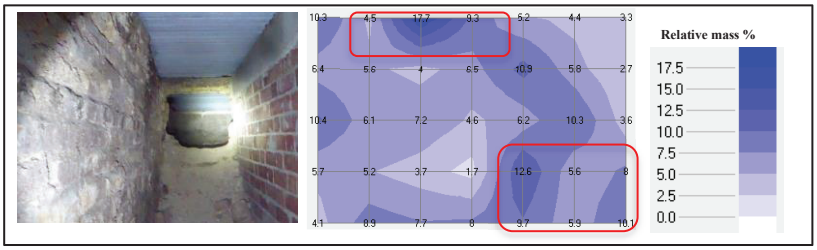

Figure 6: Microwave tomograph of location with moisture concentration at the bottom edge of wall as well as near the underside of Bondek.

Brick powders were drilled from the mid-depth of the walls across different heights spanning from within the sub-floor to Level 1 of the hotel room. Total and hygroscopic moisture contents (TMC and HMC) of the samples were then determined in accordance with BRE Digest 245 [3], whereby 2g of brick powder was conditioned under relative humidity above 75% and temperature of 30◦C for 3 days to obtain HMC of the sample. From the example of results as shown in Figure 7, the total moisture content in the brick wall within the sub-floor is much higher than that in Level 1. Nevertheless, the total moisture content above at Level 1 slab is still high, which is above 5%. This finding implies the presence of rising damp affecting the walls from sub-floor up to Level 1. At location MW10, higher total moisture content was found just below the Bondek slab, possibly attributed to moisture absorbed from the ground through capillary and condensation from the Bondek slab. The absorption of moisture from the condensate at the underside of the Bondek slab and any resulting downward migration of moisture will alter the pattern of salt distribution. This makes tracing the salt pattern and distribution difficult. At location MW8, the higher HMC as compared to the TMC in the sub-floor may indicate that the relative humidity within the masonry is higher than the test condition as specified in BRE Digest 245 of 75% RH. This shows that within the sub-floor, the masonry wall will remain at elevated degree of dampness over prolonged duration.

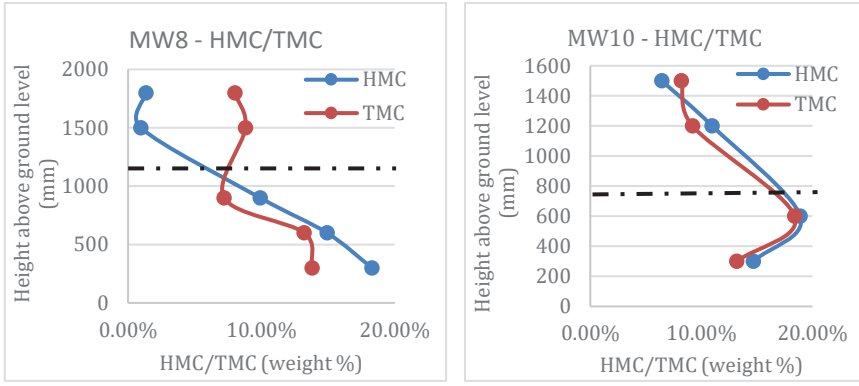

Figure 7: TMC and HMC results of the walls MW8 and MW10 inside sub-floor.

3.2 Salt Analysis

Powder samples within the brick surface zone at locations where high hygroscopic moisture content was found, were extracted for ion chromatography. 1g of sample was adequately mixed with 50ml of deionized water, where the solution was extracted by filtration before the test. This was to check for salt species and concentration, which included cations of sodium, potassium, magnesium and calcium, and anions of chloride, sulphate and nitrate. The results from locations MW8 and MW 10 with HMC ranging from 15%-18% at the mid-depth are shown in Table 1.

Table 1: Ion chromatography result of powder samples MW8 and MW10.

Unit #/ Location	Height/ mm	Ion concentration (weight %)						
		Cl^-	SO_4^{2-}	NO_3^-	K^+	Na^+	Ca^{2+}	Mg^{2+}
111/MW8	300	0.13	1.14	0.09	0.44	0.70	1.38	0.08
118/MW10	300	0.01	1.67	0.01	0.43	0.10	2.25	0.09

The key salt species present is likely sulphate. These salts could well originate from the ground and be carried upward into the bricks via uprising damp as they are commonly encountered in the soil. However, it is also possible that there was some salt inherent within the clay used in the bricks manufacturing. The salt may be water soluble especially when the clay has not been sufficiently fired or vitrified.

4 DESIGN CONSIDERATION FOR TREATMENT

It had been established that the brick walls in the sub-floor were suffering from rising dampness and severe salt attack. The pattern and distribution of salt attack within the sub-floor could not be clearly identified due to the rife dampness. The salt damage above the sub-floor at Level 1 on the other hand could be defined because of the drier and controlled air conditioned environment, and certainly needed to be treated as these are the locations of the guest rooms. Rising damp treatment was subsequently executed by chemical injection to the foot of the wall at Level 1, just above the sub-floor. Salt treatment was also carried out on the walls at Level 1. However, the dampness and accumulated salt within the wall in the sub-floor

could not be tackled without adequate work access. To do this would require complete ripping out the entire Level 1 floor.

As it was not possible to treat the uprising damp and dampness in the sub-floor wall due to the poor access, several options of treatment had been considered in order to manage the salt crystallization issue. Due to the construction and layout of the building, no practical method to address the uprising dampness and moisture problem in the sub-floor such as drying stone and wall based ventilation is feasible. Instead, it was decided to at least focus on managing the salt problem. The options deliberated included electrokinetic desalination method and application of sacrificial plaster. Moreover, any attempt to arrest the uprising damp and dampness issue without addressing the salt problem could lead to greater damage when the salt crystallizes when the wall dries [4].

4.1 Electrokinetic Desalination Method

Electrokinetic desalination is designed to remove salts by applying direct current electric field to the brick substrate, which allows electric current to transport the ions to the respective electrodes [5]. Nonetheless, pH change during the electrolysis of water could retard electrical transport process and thus desalination efficiency [6]. Furthermore, acidification built up at the anode could decay the lime bedding mortar of the walls. Hence, pH neutralization control is very crucial.

There were a number of benefits to consider this option. Firstly, there was no necessity to cover the entire surface of brick walls for this treatment, where only some parts of the walls were involved for electrode installation. Secondly, the efficiency to remove salts from the brick surface is supposed to be high, without any specific climatic condition such as relative humidity and temperature. It could also work for clay bricks with different porosities. Lastly, it should have a possibly deeper effective zone of the brick surface thickness to remove salts.

Notwithstanding, this technique was considered too new and thus not mature locally for application in the construction field. This was particularly challenging when the balanced pH of the electrical transport process needs to be controlled. Besides, while active rising damp in the brick wall may benefit the electrolysis process, the harmful gases formed during the process could also be a critical safety hazard in the confined space of the sub-floor. In addition, rising dampness within the walls at the sub-floor were unable to be treated and eliminated due to the floor difference between the sub-floor and the front of house. Moisture supply from the ground in the wall at the sub-floor was then expected to continue, and same applied to salt transport in the walls.

Given the circumstances above, the alternative treatment was then considered.

4.2 Sacrificial Plaster Method

Since it was technically impossible to halt the moisture movement inside the walls at the sub-floor, application of sacrificial plaster became a more feasible method to address salt attack issue in this case [7]. Consideration was given for natural hydraulic lime mortar with specially designed macro-pore structure. The macro pores in this sacrificial plaster are meant to promote water evaporation and thus accom-

modate salt crystallization if it occurs. This helps to prevent any salt-related damage on the historic brick substrate. Such structure also moderates transportation of vapors so as to make the plaster layer "breathable" and allow excessive moisture to escape from the brick substrate. Renewal of such sacrificial plaster is anticipated after cycle of several years once the layer is saturated and loaded with salts. One example of application of lime-based sacrificial plaster for salt accommodation is presented in Figure 8.

Given the tight project timeline, limited resources to be deployed for treatment and restrained headroom for complex work execution, application of one layer of sacrificial plaster over the existing historic brick walls directly was chosen as the best and most viable option to mitigate salt recurrence and attack on the historic brick fabric at the point of the project progress.

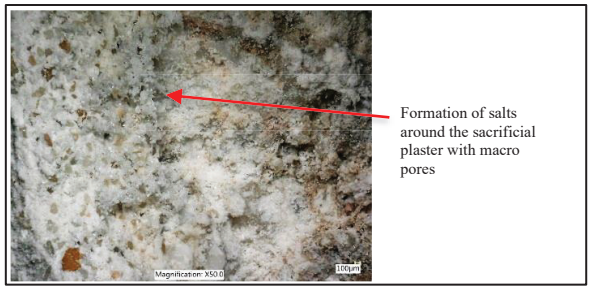

Figure 8: Microscopic view showing one example of salt formation in the sacrificial plaster with macro pores applied onto a historic building with salt problem.

5 MONITORING PROGRAM FOR EFFECTIVENESS

Risk of salt recurrence remained an unanswered question, even with sacrificial plaster applied onto the brick surface in the sub-floor. Further monitoring program of salt recurrence was therefore instituted to facilitate the essential maintenance of the building health after treatment was completed.

5.1 Temperature and Relative Humidity (RH) Logging

Environmental condition of the sub-floor was monitored before and after handover of the hotel to the Contractor for restoration works. Changes in relative humidity and temperature were first logged. See the logged results in Figure 9.

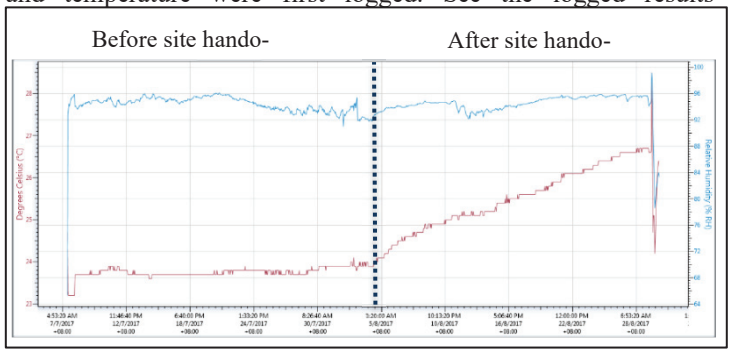

Figure 9: RH and temperature logged before and after site handover.

It was established that temperature in the sub-floor had risen from 23ºC (with air-conditioned hotel room situated above) gradually to 27ºC after hotel has ceased operation for commencement of restoration. However, relative humidity in the sub-floor remained unchanged and high above 90% throughout the transition process. This was despite the natural ventilation of the sub-floor, possibly due to the continued supply of humid air within the confined space.

5.2 Runsalt Model

Taking consideration of the environmental condition in the sub-floor during hotel operation, a salt simulation model [8] [9] was made to check for the risk of salt formation on the historic walls in the future.

With reference to the data logged in Figure 9, the temperature was set as 23ºC for operational hotel condition, while the exposed relative humidity was anticipated to range from 90% to 98% in accordance with the logged data. In the prediction model, influence of calcite and gypsum was not considered fully due to their low water solubility. Nonetheless, given the extremely high humidity present in the tropical climate, it is also possible to have gypsum salts crystallized. See salt models made for locations MW8 and MW10 are shown in Figure 10.

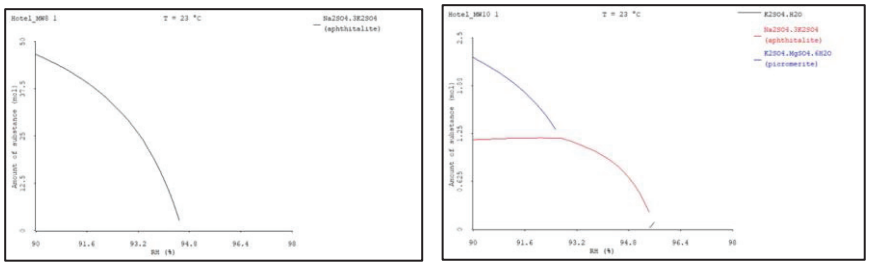

Figure 10: Salt simulation models for locations MW8 (left) and MW10 (right).

According to the models, aphthitalite ($Na_2SO_4 \bullet 3K_2SO_4$) was predicted to form at both locations, while growth of potassium sulphate hydrate and picromerite ($K_2SO_4 \bullet MgSO_4 \bullet 6H_2O$) was also possible at location MW10. Risk of salt recurrence in the future is thus present.

Some easing measures were proposed to monitor the growth of salt crystals on the brick surface. It included making provision to have openable inspection panel at certain intervals on the level 1 flooring, to check sign of salt attack periodically.

6 DISCUSSION AND RECOMMENDATION

The effectiveness of sacrificial plaster to accommodate salt formation had been proven in other local restoration projects. While it remained to be the most feasible option at the time of project, its efficiency should be monitored in a longer term due to the dynamic climatologic condition inside the sub-floor and its connection with the hotel room condition above. This includes periodic visual inspection via inspection panel, and occasional sampling of sacrificial plaster from the sub-floor

brick wall to check for salt content. On the other hand, it would be also beneficial to be able to make known the porosity of the clay bricks, in order to validate the anticipated capillary movement of salts from bricks into the sacrificial plaster. When time permits, salt profile at different depths of the brick wall should also be assessed to understand salt movement for better risk assessment of salt recurrence. It is seen from this project, it is not always possible to implement the usual methods of addressing uprising damp and salt attack in historic building. Occasionally, there will be cases where different tacks are required. This case also demonstrated the importance of having post-restoration monitoring program which should be designed into at the onset of the project and not as an after-thought.

7 REFERENCES

[1] H. S. Tang and C. W. Wong, "Managing Recalcitrant Rising Damp and Salt Attack Problems in Heritage Buildings in the Tropics," in *International Academic Forum on Built Heritage: A Cultural Motivator for Urban and Rural Development*, Shanghai, 2017.

[2] C. W. Wong and H. S. Tang, "Diagnostic Condition Assessment of a 180 Year Old Church in Singapore for the Purpose of Restoration," in *International Conference on Sustainable Building Restoration and Revitalization*, Shanghai, 2013.

[3] *Rising Damp in Walls: Diagnosis and Treatment - Digest 245,* UK: Building Research Establishment, 2007.

[4] J. M. P. Q. Delgado, A. Guimarães, V. de Freitas, I. Antepara, V. Kocí and R. Cerný, "Salt Damage and Rising Damp Treatment in Building Structures," *Advances in Materials Science and Engineering,* 2016.

[5] M. Yasir, M. Ayyaz, K. Karman, M. Ishaq and F. Rasool, "Electrokinetic Desalination of Compound Building Materials by Applying Electric Field," *Advances in Sciences and Engineering,* vol. 13, no. 1, pp. 10-16, 2021.

[6] L. Ottosen, A. Pedersen and I. Rörig-Dalgaard, "Salt-related problems in brick masonry and electrokinetic removal of salts," *Journal of Building Appraisal,* vol. 13, no. 3, pp. 10-16, 2007.

[7] K. Leiten, H. Sirelpuu and M. Kiviste, "Desalination using clay and lime sacrificial plasters with additives on field stone wall and fired clay bricks," *Journal of Physics: Conference Series (8th International Building Physics Conferences),* p. 2069, 2021.

[8] D. Bionda, "RUNSALT - A graphical user interface to the ECOS thermodynamic model for the prediction of the behaviour of salt mixtures under changing climate conditions.," http://science.sdf-eu.org/runsalt/, 2005.

[9] C. A. Price, "An expert chemical model for determining the environmental conditions needed to prevent salt damage in porous materials. European Commission Research Report No 11, (Protection and Conservation of European Cultural Heritage)," Archetype Publications, London, 2000.

CONSERVATION APPROACHES OF THE HERITAGE BUILDINGS INSIDE THE PALACE MUSEUM: AGAINST SALT DAMAGE OF THE FLOOR BRICKS BY ENVIRONMENTAL IMPROVEMENT

Xiaogu Zhang[1] **and Shuang Zhang**[2]

KEYWORDS

Brick Weathering, Environment Monitoring and Control, Simulation, Preservation

ABSTRACT

The deterioration caused by salting out is a common occurrence of brick materials. Most of the heritage buildings inside the Palace Museum were paved with bricks. In the buildings with living function, the heating facilities were also set up below the indoor ground. They were called “kang and flues”. All of them have been no longer in use for more than 100 years and in poor condition. Due to the water and salt transport through the kang and flue structure, the indoor environment is not conducive to the preservation of cultural relics and the floor bricks and other building materials are also damaged. In order to improve the environment inside the building and in the kang and flues, we have chosen Tihe Hall as an experimental and study case and put a ventilation equipment inside the flues to reduce the humidity. Based on real-time monitoring data of the exterior and internal environment and CFD simulation and modeling analysis, we can dynamically adjust the air circulation direction throughout a 2-way fan and optimized the equipment parameters so as to effectively improve the internal environment while protecting the original structure.

[1] Department of Architectural Heritage, the Palace Museum, Beijing, China, ninagugu@qq.com
[2] Digital Wave (Beijing) Technology Co., Ltd., Beijing, China

1 INTRODUCTION

In the ancient Chinese architecture with wood, brick and stone as the main architectural structure system, porous materials such as stone and brick are often affected by salt damage. Under the action of capillarity, the water transfer inside and outside the material will precipitate the soluble salt in the form of crystalline salt, then form a white or yellow powder or flocculent crystal on the surface of the masonry [1][2]. The accumulation of crystalline salt will produce accumulated stress inside the material, destroy the microporous structure of the material, and cause cracking and pulverization on the surface of the material, resulting in material damage and strength reduction.

In the process of surveying and protecting the heritage buildings of the Palace Museum in Beijing, we found a kind of typical phenomenon of salt damage of indoor floor bricks, which showed seasonal regularity: it repeatedly appeared in the spring and autumn seasons every year, and in summer the floor bricks were very wet. Because there are precious cultural relics on display in the room, salt crystals on the ground will also erode the parts of the cultural relics in contact with the ground (figure 1).

Figure 1: Indoor damages of building material: salt damage of floor bricks, cracking and mildew of wallpaper.

Since we've already known that the most important environmental impact factor of crystalline salt is water and salt transport, salt damage can cause sustained, long-term and irreversible damage to cultural heritage if the environmental problems are not solved [3]. In order to understand the source of water, through site investigation, ground penetrating radar, local excavation and other methods, we found that there were similar underground building structures in such buildings with salt damage of indoor floor bricks: Kang and flues (figure 2).

Kang and flues were heating facilities widely used in the imperial palaces during Ming and Qing dynasties [4]. Due to the change of building function, the kang and flues has long been abandoned and no longer assumes the function of heating. Because the they are located below the indoor floor, it is easy to be ignored and not easy to repair, and most of them are in poor preservation condition. Meanwhile, due to their structural characteristics, building environment problems have been caused, resulting in rising water vapor and indoor humidity.

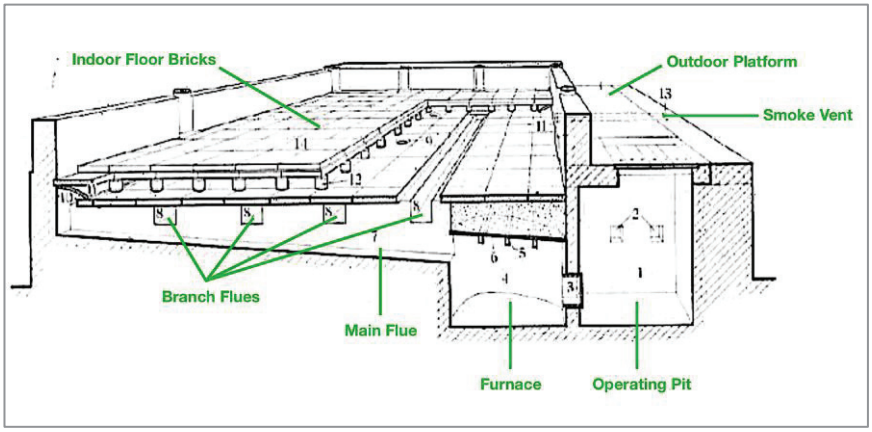

Figure 2: Structure diagram of kang and flues underneath the heritage buildings inside the Palace Museum [5].

In order to solve the above problems, we decided to choose Tihe Hall as a study case to carry out environmental analysis and assessment work, and use the internal channel of its kang and flues to carry out environmental treatment, and designed a set of ventilation experiment method, in order to improve the indoor environment of the building and protect the heritage buildings and cultural relics.

2 SITE SURVEY AND ENVIRONMENTAL ASSESSMENT

2.1 Survey of the Current State of Kang and Flues of Tihe Hall

Using ground penetrating radar, photogrammetry, endoscope shooting, local excavation and other technical means, we investigated the preservation status of the kangs and flues in Ti He Hall. According to the investigation results, there are a set of kang and flues on both east and west ends of the building (figure 3). After partial excavation, the operation pit and the furnace opening can be seen under the eaves in front of the building (figure 4).

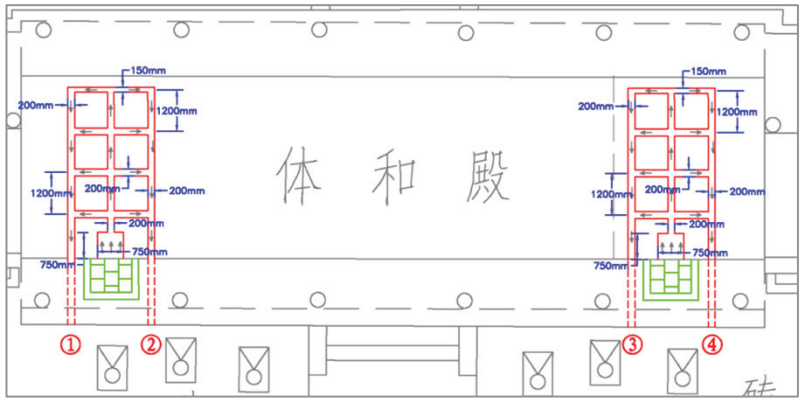

Figure 3: Ground penetrating radar mapping of kang and flues of Tihe Hall.

Figure 4: Photo of operation pit and the furnace.

2.2 Monitoring of the Interior Environment

In order to continuously monitor the environmental changes inside the Tihe Hall, we set up a three-dimensional grid temperature and humidity monitoring instrument inside the building (figure 5).

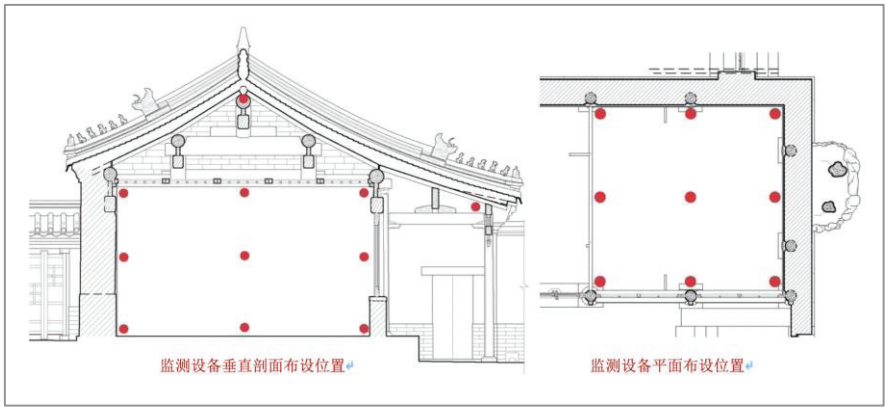

Figure 5: Diagram of three-dimensional grid environmental monitoring instruments layout inside the building

2.3 Environmental Analysis and Impact Assessment of Tihe Hall

Through the analysis of a year of environmental data, the following conclusions can be drawn：

1. The east-west side of Tihe Hall is 5 rooms wide, and the doors are in the center room (both north and south side, but normally the building is not open), and the

kangs and flues is located underneath the east-end and west-end rooms, so the interior temperature and RH are obviously uneven. That is because the kang and flues are hollow and have poor moisture insulation performance. In addition, the underground structure has high moisture content, deep depth and high heat capacity, especially in winter, the ability to maintain high temperature is strong, and the ground moisture evaporation is large, so the temperature and relative humidity are high. In the east and west, due to the lateral migration of underground water in the east and west, the underground moisture content is high, but the depth is shallow, the high moisture volume is small, the heat capacity is relatively small, and the ability of insulation and evaporation in winter is relatively weak. The center room is not affected by the kangs and flues, the underground moisture content is the smallest, and the ventilation condition is better than other rooms, so the temperature and humidity are the lowest in winter. From the monitoring data, the temperature difference between the east-end and west-end rooms and the center room can reach 3-4 degrees Celsius, and the relative humidity difference may reach 25% (figure 6).

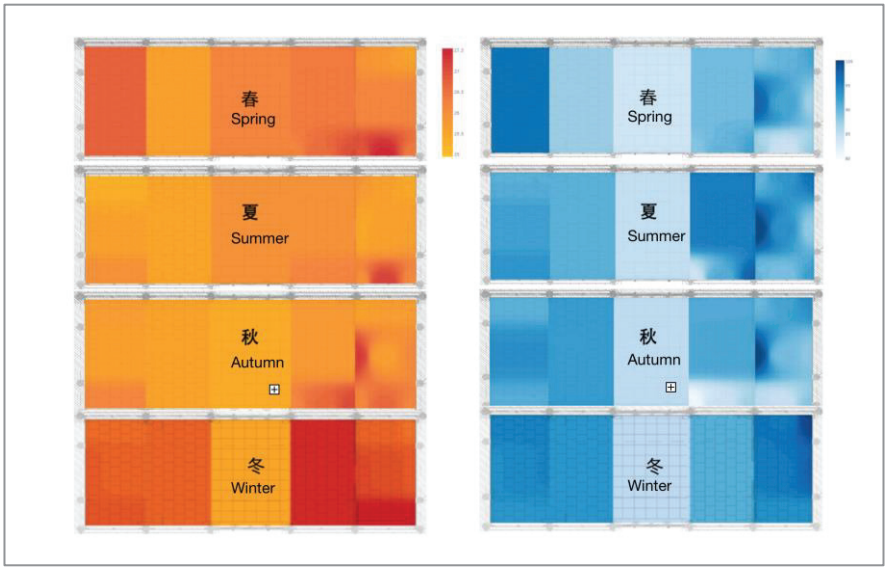

Figure 6: Plane distribution of four seasons of temperature and relative humidity near the ground (left: temperature distribution, right: humidity distribution)

2. The circulation of moisture in the building environment, combined with fluctuations in environmental conditions, leads to a concentrated outbreak of salt damages during autumn and winter. This is because during autumn and winter, the underground space of the kang and flue structure has an average temperature higher than the indoor average temperature, and the underground space remains in a high relative humidity state exceeding 95%. This relatively high temperature and humidity create an environment with strong condensation and weak evaporation.

3. The analysis of the surrounding environment showed that if the rainwater from the courtyard is not quickly drained away by the ground surface, the rainwater would gradually seep into the ground, which is easy to form shallow underground

water retention, resulting in the long-term wet foundation environment of the ancient building foundation. Meanwhile, the natural ventilation and infiltration wind inside and outside the building drive the migration of water and heat in the building envelope, and the water and heat in the foundation migrate upward and enter the building through the floor bricks, resulting in changes in the indoor temperature and humidity environment (figure 7). In the process of repeated evaporation and water and salt transport, salt crystallization of the floor bricks resulted in repeated salt damage and continuous deterioration of building materials [6].

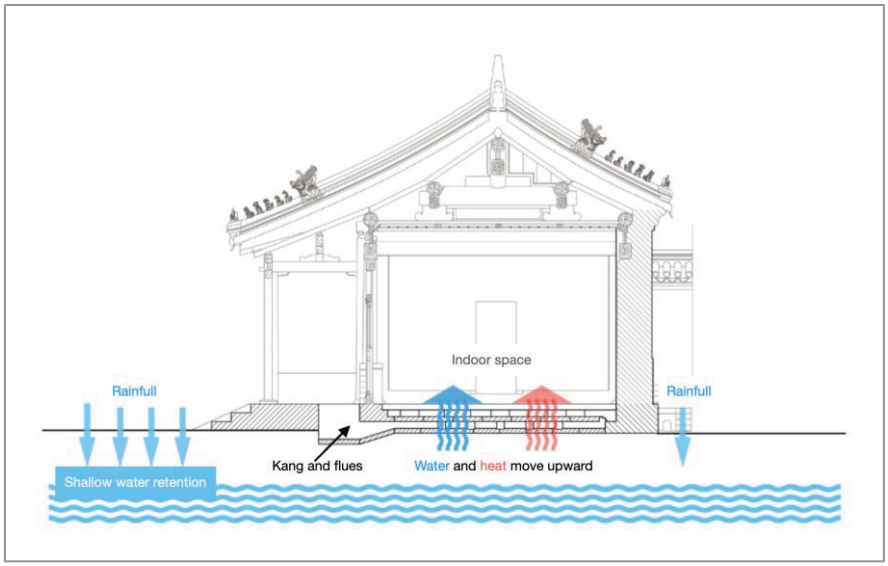

Figure 7: Environmental impact analysis and assessment

3 ENVIRONMENTAL IMPROVEMENT APPROACHES

Based on a clear understanding of the interaction mechanism between the kang, flues and the environment, we have developed a comprehensive environmental improvement plan. Utilizing the flues as an existing passage, we progressively reduce the high humidity inside the kang and flues through air ventilation and circulation, aiming to reduce the indoor dampness from its source.

3.1 Ventilation System and Ways of Air Circulation

Starting from 2021, the ventilation experiment was carried out on the kang and flues on the east side of Tihe Hall. Based on the real-time monitoring data of the external and internal environment of the flue, we dynamically adjusted the air circulation pattern: (1) when the ambient temperature and relative humidity exceed the threshold, such as in the case of high humidity, the fan equipment will use positive pressure form to transport air to the flue with relative humidity below 50% (RH) and temperature above 10°C (T) until the internal environment of the flue and the indoor environment of the building reach the ideal state; (2) when the outdoor ambient temperature and relative humidity conditions are good, such as in the case of dry and warm external environment, the form of negative pressure is used to

extract the humid air inside the flue, while driving the air circulation in the flue, and the outdoor dry air is introduced into the flue by the exhaust port, thus forming an air circulation and replacement cycle (figure 8).

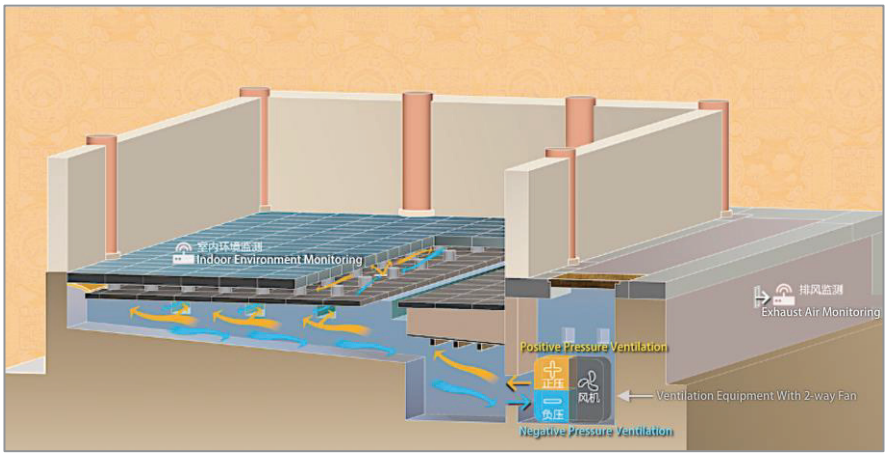

Figure 8: Ventilation experiment diagram of kang and flues

3.2 CFD Simulation and Calculation of the Environment

Aiming at the key external environment variables, CFD modeling, simulation and calculation analysis of the interior space of the kang and flue structure are carried out. Firstly, the ventilation effect under different wind speed is simulated. The results show that when the inlet wind speed is 1, 5 and 10m/s respectively, the average air flow velocity in the whole space inside is 0.31m/s, 1.59m/s and 3.23m/s respectively. On the one hand, this indicates that the double-layer structure of the flue will bring greater friction and return resistance to the internal air flow. On the other hand, it also shows that increasing the inlet wind speed can significantly improve the displacement efficiency. Secondly, the ventilation effect at different temperatures is simulated. The results showed that the dehumidification efficiency of the flue's internal environment can be improved by increasing the input air temperature. The higher inlet air temperature reduces the inlet air humidity, and when the mixture with the air inside the flue reaches a steady state, the low humidity area underground is larger, the average humidity level in the flues is lower, and the removal effect of the condensation is improved. However, due to the electricity power restrictions in the Palace Museum, ventilation cannot be continued after closing the museum everyday, so in order to ensure the environmental balance inside the flues and avoid temperature and humidity fluctuations or condensation caused by violent hot and cold alternation, the medium intake air temperature is selected in actual operation to keep the dew point temperature of the mixed state air lower than the inner surface temperature. (figure 9)

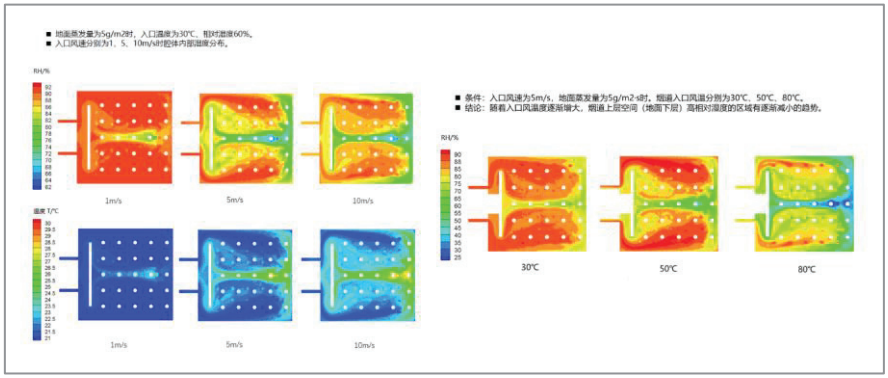

Figure 9: CFD modeling and simulation of the interior space in the flues (left upper and down: temperature and relative humidity changes under different velocity of ventilation; right: temperature changes under different ventilation temperature).

3.3 Results of Improvement Effect

After nearly two year of air ventilation and circulation inside the kang and flues, there has been some improvement of the indoor environment of Tihe Hall. When comparing to the west part of the building, there has been a significant reduction in the floor bricks' humidity of the east-end room. Correspondingly, the relative humidity of the interior environment has also significantly decreased, and temperature fluctuations have been reduced.

4 CONCLUSION

At present, we still actively optimize the ventilation and air circulation measures of kang and flues according to the site working conditions, the environmental monitoring data, the CFD simulation and analysis results. We believe that it is a scientific, reasonable and sustainable preventive protection mode for heritage buildings to make full use of the positive utilization value of the kang and flues by using the structural characteristics of the building itself without destroying the building itself. This is also a worthy concept of cultural heritage protection, in line with the principle of minimal intervention. In the future, we hope to promote this set of methods and concepts in the Palace Museum and even other heritage sites, so as to realize the scientific and effective protection and utilization of cultural heritage.

REFERENCES

[1] Kegui Zhang (张克贵), "Study on salt damage of the exterior wall of ancient buildings (古建筑干摆外墙泛碱病害的研究)," *Ancient Architecture Garden Technology (古建园林技术)*. vol.1, pp. 12-16，2010.

[2] Kamh G. M. E., "Salt weathering, bio-deterioration and rate of weathering of dimensional sandstone in ancient buildings of Aachen City, Germany," *Int. J. Water Res. Environ. Eng.* vol. 3(5), pp. 87-101, 2011.

[3] Salvador Ordóñez et al., "Mineralogical evolution of salt over nine years, after removal of efflorescence and saline crusts from Elche's Old Bridge (Spain)," *Construction and Building Materials*. vol. 112, pp. 343–354, 2016.

[4] Yanchun Wang (王艳春), "Fire Kangs in the Ancient Buildings of the Imperial Palace of Shenyang(沈阳故宫建筑中的火地与火炕)," *Proceedings of the Forbidden City Society of China. Vol 6* (*中国紫禁城学会论文集 第六辑下*), The Forbidden City Publishing House (紫禁城出版社), pp. 550-558. 2011.

[5] The insititute for history of natural sciences, Chinese Academy of Sciences, (中国科学院自然科学史研究所), "History of ancient Chinese architectural technology" (中国古代建筑技术史), Science Press (科学出版社), pp. 323–328, 2000.

[6] Christopher Hall, William Hoff, "Water Transport in Brick, Stone and Concrete", 3rd ed. CRC Press, 2021.

EFFECT OF INTERIOR AND EXTERIOR ENVIRONMENTS ON SALT MIXTURE PRECIPITATION IN BRICK MASONRY WITH WALL PAINTINGS

E. Mizutani[1,2], D. Ogura[3], and J. Sasaki[4]

KEYWORDS

Salt mixture, exfoliation, phase diagram, wall painting, brick masonry

ABSTRACT

The deterioration of walls in Hagia Sophia caused by the precipitation of several types of salts and the environmental factors that affected this deterioration were investigated by comparing the phase diagrams, temperature, and relative humidity for the building and within the walls. The temperature and relative humidity within the walls were calculated using a numerical model that considered the indoor and outdoor temperatures, humidity, sunlight, and rainfall. For two types of salt, sodium nitrate and sodium sulfate, the timings of salt deposition and disappearance and the damage patterns on the wall surface were confirmed to be dependent on the type of salt precipitated. Differences of rain loads on the wall surface were shown to have influenced the location and timing of the two types of precipitation. The results yield fundamental information for the development of effective conservation and restoration protocols for historical buildings.

[1] NICH, Tokyo National Institute for Cultural Properties, Uenokoen13-43, Taito City, Tokyo, Japan; mizutani-e7k@nich.go.jp

[2] NICH, Cultural Heritage Disaster Risk Management Center, Nara City, Japan

[3] Graduate school of Engineering. Kyoto University, Kyoto City, Japan

[4] Tohoku University of Art and Design, Yamagata, Japan

1 INTRODUCTION

Salt precipitation is one of the main causes of deterioration in buildings made of porous materials, such as bricks, stones, and mortar. Multiple types of salt precipitation are usually observed at sites where salt weathering occurs, owing to the presence of several types of soluble ions resulting from rain, groundwater, and material contamination. The impact of material damage depends on the type of precipitated salt on material damage which are affected by the composition of the dissolved ions and environmental factors. Therefore, developing appropriate conservation and restoration protocols for historical sites and buildings facing salt weathering needs to consider the characteristics of the precipitating salts and the causes of their precipitation.

Hagia Sophia (Ayasofya Camii) in Istanbul, which is the subject of this study, has suffered damage to wall surfaces from salt precipitation. Wall conditions and deterioration factors in the northwest exedra wall at the second cornice, where spalling of the inner finishing materials is particularly noticeable, have been scientifically investigated [1,2].

The following studies were carried out with the aim of understanding the deterioration of properties due to salt precipitation in the walls of Hagia Sophia and identifying the environmental factors that affect salt precipitation.

First, the distribution of precipitate salts and the pattern of wall damage in the northwest exedra were summarised based on the results of the chemical analysis of the precipitates and visual observation of wall conditions. Second, the measured indoor temperature and humidity and the phase diagram were compared to investigate their effects on seasonal changes in salt precipitation. Furthermore, to elucidate the influence of the outdoor environment on the temperature and humidity of the wall and the salt precipitation properties, the temperature and humidity distributions within the wall were calculated for a numerical model with simultaneous heat and moisture transfer equations, and the degradation mechanism was investigated by comparing it with the phase diagram.

2 FIELD SURVEY OF THE WALL DAMAGE IN AYA SOPHIA

2.1 Outline of Hagia Sophia and its wall structure

Hagia Sophia is located in a historically important area of Istanbul and is surrounded by the sea on all sides except the west. It has four floors, as illustrated in Figure 1: ground floor, gallery, second cornice, and dome cornice. The central dome measures 55.6 m from the floor and is approximately 33 m in diameter. The second cornice has semicircular walls called exedras, which are the focus of this study. Hagia Sophia has a brick masonry architecture with inner and outer finishing materials, as shown in Figure 2. The inner surface is decorated with paint and mosaics. In general modern masonry, the connection mortar is approximately 1 cm thick, whereas that in Hagia Sophia has a considerable thickness of 3–5 cm. The brick was approximately 3–5 cm thick and thus thinner than the typical bricks currently in use. The mortar used in Hagia Sophia is pozzolanic mortar, which does

not react with water-yield cementitious phases, and is not a pure lime mortar; pozzolanic mortar comprises crushed brick [3].

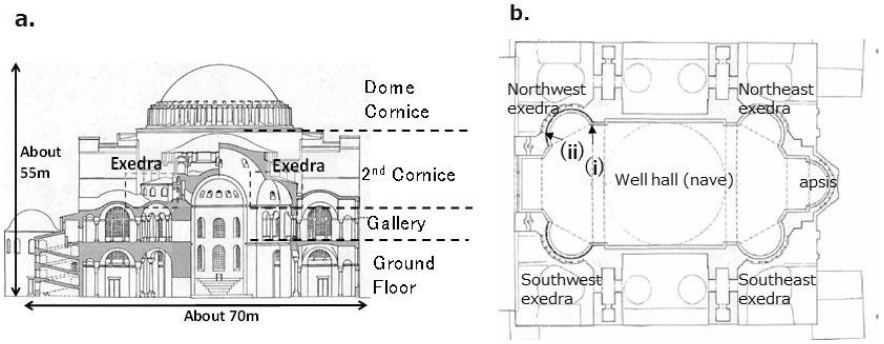

Figure 1：(a) A section of the Aya Sophia and (b) plan of the second cornice [3]

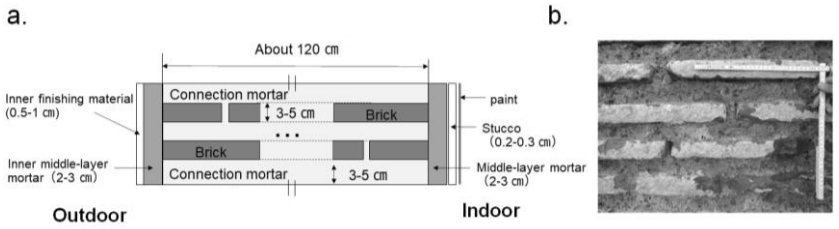

Figure 2: (a) Wall components in the exedra walls and (b) outer appearance of the wall in 2012

2.2 Types of precipitated salts

A total of 55 samples of salt deposited on the inner walls of the northwestern exedra were collected in 2011 and 2012, and the relationship between the distribution of salt on the walls and the distribution of the wall material was studied in detail. The salt types were identified by elemental detection using X-ray fluorescence (XRF), followed by identification of the crystalline phase by X-ray diffraction (XRD). Among the identified salts, Na_2SO_4 (thenardite) and $CaSO_4{\cdot}2H_2O$ (gypsum) were the most widely deposited. Other identified salts included $NaNO_3$ (nitrite), $CaCO_3$ (calcite), and $MgSO_4$ (epsomite). Based on the relationship between the type of precipitate and the distribution of restoration materials, $MgSO_4$ (epsomite) has been identified among the precipitates in areas where the restoration material has been used, and an influence of the elements derived from this material is suspected [4].

2.3 Deterioration patterns and seasonal change of the wall in the northwest exedra

Visual surveys of the degradation and identification of the precipitated salts have been continuously conducted since 2010. Visual inspection revealed that the deterioration progressed over time, especially at the precipitation points of sodium nitrate and sodium sulfate. Figure 3 shows examples of the conditions of the inner wall surfaces under which sodium nitrate and sodium sulfate precipitate. Sodium

nitrate precipitated mainly in the easternmost part of the northwest exedra indicated by (i) in Figure 1, where the paint layer had peeled off. Observations at the same locations also showed seasonal changes, with precipitation in February 2011 and November 2013, disappearance of the precipitate in August 2014, and re-precipitation in December 2014, confirming a gradual thinning of the paint. Sodium sulfate precipitated over a wide area of the northwest exedra, not only on the surface paint but also between the stucco and middle layer mortar, with many instances of stucco exfoliation seemingly associated with this. In some areas, the middle layer mortar has also been exfoliated [2, 4].

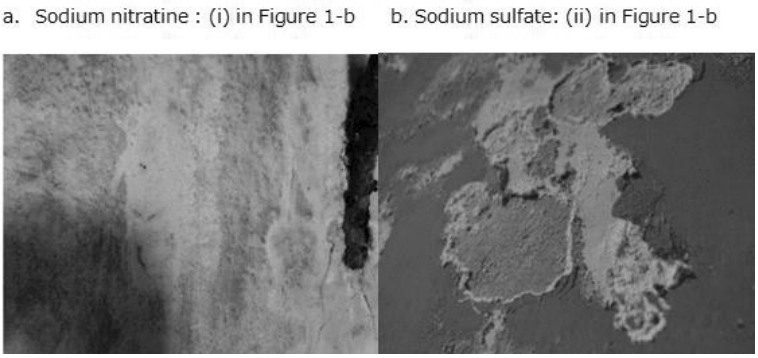

Figure 3 Wall conditions of the (a) sodium nitrate precipitation site and (b) sodium sulfate precipitation site

3 COMPARISON BETWEEN PHASE DIAGRAM AND INSIDE TEMPERATURE/HUMIDITY

Salt crystallisation behaviour is quite complex because all factors, such as the changing climate conditions and the composition and ion concentration of the salt solution, influence it. A thermodynamic model, the environmental control of salts (ECOS), can analyse the crystallisation behaviour of mixed salt solutions as a function of temperature and relative humidity and has been used to study several salt weathering sites [5, 6]. One of the limitations of ECOS is that it is only compatible with electrically neutral solutions. Ion-chromatographic analysis of soluble chemical components in the material stripped from the northwest exedra wall showed that the total number of anions analysed was approximately twice that of cations, probably because of the surface charge of the clay minerals and undetectable ions [2]. Therefore, the present study was designed to investigate the salt precipitation properties of two salts, sodium nitrate and sodium sulfate, by comparing their phase diagrams with the indoor temperature and humidity [7, 8]. The monthly average values of temperature and relative humidity in the second cornice are plotted against the phase diagrams of sodium nitrate and sodium sulfate in Figure 4. For the salt to precipitate, the ambient relative humidity must be below the equilibrium relative humidity of the saturated salt solution. Sodium nitrate is more likely to precipitate during autumn and winter because the ambient relative humidity is below the equilibrium relative humidity, whereas deliquescence is more likely to occur during spring and summer. Sodium sulfate is likely to exist as mirabilite ($Na_2SO_4 \cdot 10H_2O$) from January to May and as thenardite (Na_2SO_4) from June to

December. The ambient relative humidity did not exceed the equilibrium relative humidity of the saturated salt solution throughout the year. This means that only the hydration and efflorescence trends of sodium sulfate salts already deposited on the wall surface can be studied, and the mechanism by which salt precipitation occurs is unknown. Therefore, for a more detailed study, the temperature and relative humidity within the walls were determined by numerical analysis, considering the outdoor and indoor environment.

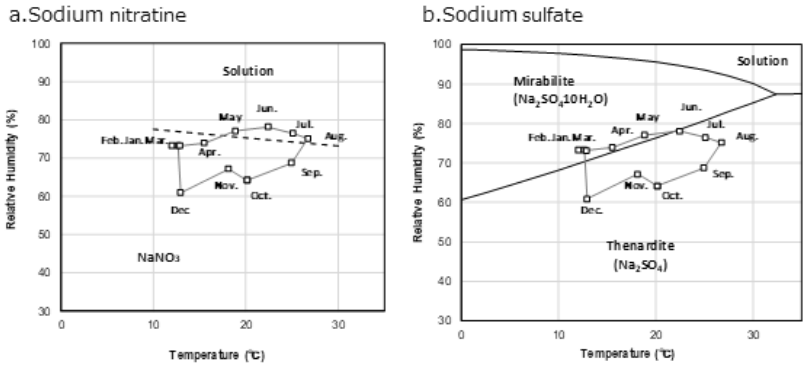

Figure 4: Comparison of the phase diagrams of (a) sodium nitrate and (b) sodium sulfate with the monthly average values of indoor temperature and relative humidity

4 ANALYTICAL INVESTIGATION ON THE EFFECT OF THE INTERIOR AND EXTERIOR CLIMATE ON SALT PRECIPITATION

4.1 Governing equations

In this section, we describe the simulations performed for heat and moisture transfer in porous materials, where the simultaneous heat and moisture transfer equations [9] are applied as the fundamental equations. The heat and moisture balance equations are as follows:

$$\rho_w \frac{\partial \psi}{\partial t} = \nabla \cdot \left[\lambda'_\mu (\nabla \mu - g) + \lambda'_T \nabla T \right] \quad (1)$$

$$(c\rho)_{app} \frac{\partial T}{\partial t} = \nabla \cdot \left[(\lambda + \lambda'_{Tg}) \nabla T + r \lambda'_{\mu g} (\nabla \mu - g) \right] \quad (2)$$

Where c, ρ, $(c\rho)_{app,}$ T, λ, r, μ, ρ_w, and φ refer to the specific heat capacity [J/(kgK)], the density[kg/m^3], the apparent specific heat capacity for volume [J/(m^{3}K)], temperature [K], thermal conductivity [W/(mK)], latent heat of water [J/kg], water chemical potential [J/kg], water density [kg/m^3], and moisture content [m^3/m^3], respectively; λ'_T and λ'_μ are the moisture conductivity related to the temperature and water chemical potential gradient [kg/(ms(J/kg))], respectively; and subscripts g and l indicate water vapor and liquid water.

4.2 Simulated wall structure and boundary conditions

The severely deteriorated vertical walls of the exedra facing north were analysed. Figure 5 shows a schematic of the exedra wall and the boundary conditions. During the analysis, the outer finishing materials of the northwest exedra wall were removed; therefore, the numerical wall model assumed no outer finishing materials.

The third boundary condition is applied to the inner and outer surfaces of the walls. The air temperature and relative humidity were measured every 30 min inside and outside Hagia Sophia between 26 September 2012 and 25 September 2013; these measurement data were used as the boundary conditions. The horizontal rainfall intensity and total horizontal solar radiation were measured simultaneously. The vertical surface solar radiation for walls facing north was derived using Bouguer's and Berlarge's equations by dividing the total horizontal solar radiation into direct and diffuse components.

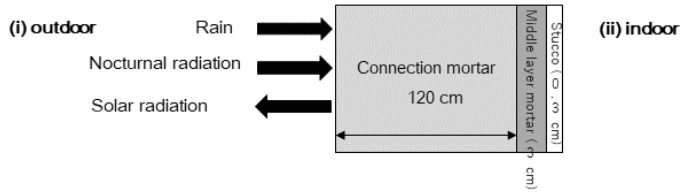

Figure 5: schematic diagram of the wall of the exedra and boundary conditions

4.3 Material properties

The liquid water diffusivity and moisture retention curve of the connection mortar, which is the main component of the wall, were determined for the material used in Hagia Sophia. Other hydrothermal properties were obtained from literature [10, 11]. The moisture diffusivities of general stucco and mortar reported by Kumaran [10, 11] were used for the stucco and middle-layer mortar. These moisture diffusivities fall below the lower limit identified by the infiltrometer. Thus, the relative ease of liquid water transfer in the inner finishing materials can be reproduced [2, 12].

4.4 Results and discussion

The hourly calculated values of the temperature and relative humidity within the wall at depths of 0 to 3.5 cm from the inner wall surface are plotted as a phase diagram in Figure 6. The analysis was performed by assuming locations where rainwater runoff was concentrated on the exterior wall surface. A comparison with the phase diagram of sodium nitrate shows that the calculated values do not fall below the relative humidity at which the saturated salt solution equilibrates. Therefore, precipitation is unlikely in areas where a large amount of rainwater infiltrates, as assumed in the present analysis. The area where deterioration due to the precipitation of sodium nitrate has been observed is the easternmost part of the northwest exedra, labelled as (i) in Figure 1b. This location protrudes from the inner side of the wall, where rainwater runoff is concentrated. Therefore, the amount of moisture infiltration is assumed to be low.

Comparison of calculated temperatures and relative humidity with the phase diagram of sodium sulfate shows that the calculated relative humidity from the surface to the middle-layer mortar is below the equilibrium relative humidity of the saturated salt solution, indicating that salt can precipitate at these depths. The results agree with visual observations showing that not only the surface paint layer but also the stucco and middle layer mortar are peeled off in areas with sodium sulfate precipitates, suggesting that sodium sulfate precipitates more easily at higher humidity and therefore tends to precipitate internally, possibly causing the interior materials to peel off. The analysis results suggest the following timing of salt precipitation: from September to November, mirabilite ($Na_2SO_4 \cdot 10H_2O$) precipitates in the stucco and the middle layer mortar as the wall dries out; in late November, dissolution or deliquescence occurs once as the wall becomes more humid; and when the temperature drops in early December, mirabilite ($Na_2SO_4 \cdot 10H_2O$) precipitates again in the stucco (see b and c in Figure 6). Therefore, salt precipitation within the wall may occur as a result of drying of the wall body and a temperature decrease in areas where rainwater infiltration is concentrated.

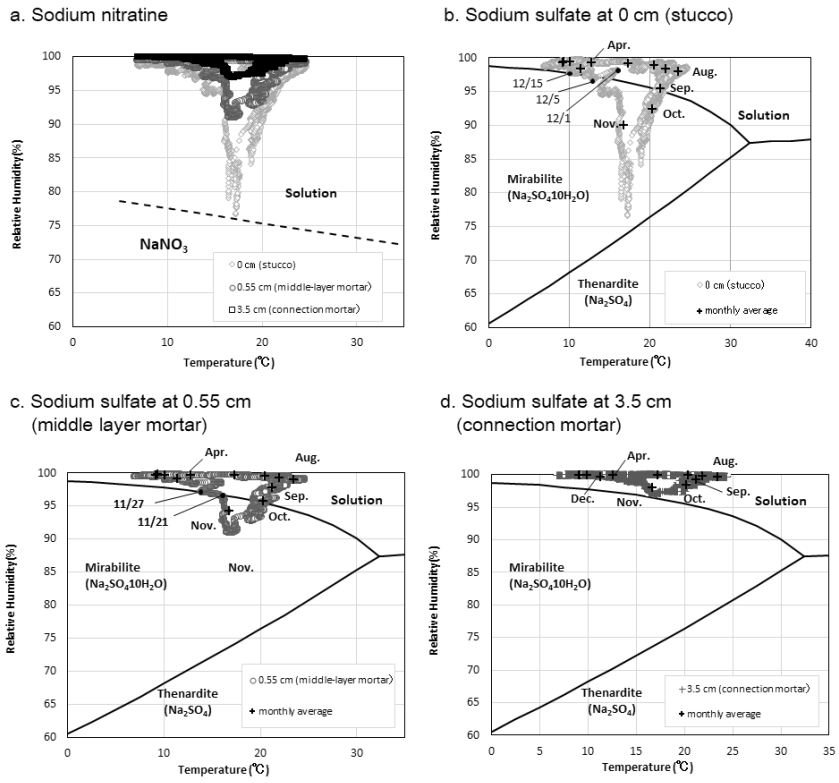

Figure 6: Comparison of the calculated values of temperature and relative humidity in the wall and the phase diagrams: (a) sodium nitrate and (b-d) sodium sulfate

5 CONCLUSION

To elucidate the deterioration mechanism of the wall paintings in Hagia Sophia due to salt precipitation, the relationship between the indoor and outdoor environments and salt precipitation properties was investigated using phase diagrams for sodium nitrate and sodium sulfate, which were found to deteriorate at the precipitation points for the salts. It was shown that the internal temperature, humidity, and exterior environment affect the type and location of salts precipitated as well as the precipitation time. In the future, detailed studies will likely be carried out by considering differences in wall precipitation, the state of peeling of interior surfaces and salt transfer in the analytical model, which will be useful for proposing countermeasures for each type of salt and for setting standards for temperature, humidity, and effective moisture penetration control.

ACKNOWLEDGEMENTS

This work was supported by JSPS KAKENHI, Grant Numbers 18H01596 and 20K14892.

REFERENCES

[1] J. Sasaki, et al., "Research on the Degradation and Materials of the Inner Walls in Hagia Sofia and Other Historic Buildings of Turkey", *Science for Conservation*，Vol.54，pp.303-312，2015

[2] E. Mizutani, "Study on the mechanisms of salt weathering of historic masonry buildings and the diffusivity of salt solutions in porous materials", Ph.D Thesis, Kyoto University, pp.259, 2022

[3] R.J. Mainstone, "HAGIASOPHIA Architecture, Structure and Liturgy of Justinian's Great Church", *Thames & Hudson*, 1988（reprinted 2006）

[4] J. Sasaki, et al.,"Salt Crystallization in Hagia Sophia, Istanbul, Turkey" *Annual Meeting of the Japan Society for Scientific Studies on Cultural Property Abstracts*, 56-57, 2015

[5] Bionda, D. RUNSALT—A Graphical User Interface to the ECOS Thermodynamic Model for the Prediction of the Behaviour of Salt Mixtures under Changing Climate Conditions (2005). Available online: http://science.sdf-eu.org/runsalt/ (accessed on May 2023)

[6]S. Gods, et al, "Modeling Salt Behavior with ECOS/RUNSALT: Terminology, Methodology, Limitations, and Solutions", *Heritage*, 5(4), 3548-3663, 2022

[7] Lewis Greenspan, "Humidity Fixed Points of Binary Saturated Aqueous Solutions", *Journal of research of the national bureau of standards-A. Physics and Chemistry*, Vol.81A, No.1, 1977

[8] M. Steiger and S. Asmussen, "Crystallization of sodium sulfate phases in porous materials: The phase diagram Na2SO4–H2O and the generation of stress", *Geochimica et Cosmochimica Acta*, 72, 4291–4306, 2008

[9]Matsumoto M, “Simultaneous heat and moisture transfer in porous wall and analysis of internal condensation. In: Hoogendoorn CJ, Afgan NH (eds), Energy of conservation in heating, cooling, and ventilating buildings: heat and mass transfer techniques and alternatives”, Washington, DC: Hemisphere Publishing Corporation, pp.45–58, 1978

[10]Kumaran MK, “IEA Annex 24. Final report, vol. 3, Task 3 Material Properties”, Print Acco IÍuven, 1995

[11]M.K. Kumaran, “A Thermal and Moisture Transport Property Databases for Common Building and Insulating Materials”, *Final Report from ASHRAE Research Project*, 1018-RP, 2002

[12]E. Mizutani, et.al, “Influence of wall composition on moisture related degradation of the wall surfaces in Hagia Sophia, Istanbul”, *Journal of Building Physics*,Volume 45, Issue 3, 2020, https://doi.org/10.1177/1744259121996

OPTIMIZING EXHIBITION METHODS FOR THE REMAINS IN THE ICHIJODANI ASAKURA FAMILY SITE MUSEUM, FUKUI PREFECTURE, JAPAN

Sayuri Fujii[1], Soichiro Wakiya[2], Akinobu Yanagida[2], and Takeshi Ishizaki[3]

KEYWORDS

salt deterioration, heat and moisture environment, reburying methods

ABSTRACT

This study aimed to prevent salt deterioration and maintain a balance between the conservation and exhibition of remains in the Fukui Prefectural Ichijodani Asakura Family Site Museum, Japan. The remains are exhibited in the museum, and consist of river stones and cohesive soil. There is no air-conditioning system in the exhibition room, but a louver has been installed to ensure natural ventilation. In consideration that salt precipitation is considered to be a major factor in the deterioration of this site in the future, we measured the environmental conditions inside an exhibition room and attempted several reburying methods to suppress salt deterioration. The results showed that salt deterioration may occur in the exhibition room in the future because the temperature and humidity inside the room were affected by air flowing through the louvers, and the soil moisture content on the surface of the remains was always high. To suppress the precipitation of salts, it is effective to reduce the evaporation rate from the surface of the remains. Therefore, the surface of the remains was covered with materials (cohesive soil, sand, and gravel) of different water permeabilities, and the moisture content of each soil layer was measured. The results showed that covering the remains with cohesive soil and gravel was the most effective way to suppress water evaporation from the surface of the remains. This is due to the effect of the capillary barrier because the grain size of gravel is larger than that of other materials.

[1]Fukui Prefectural Ichijodani Asakura Family Site Museum, Fukui, Japan, address, s-fujii-fw@pref.fukui.lg.jp
[2]Nara National Research Institute for Cultural Properties, Nara, Japan
[3]Institute for Conservation of Cultural Property, Tohoku University of Art and Design, Yamagata, Japan

SWBSS ASIA 2023 – Nara, Japan. September 20-22, 2023.

1 INTRODUCTION

The Ichijodani Asakura Family Site was a castle town in the Sengoku period (15–16th centuries A.C.). In 2022, new museum was opened to exhibit the remains of a river port for goods transported by river. Salt deterioration is often a problem in museum exhibitions. Salt precipitation and deliquescence are related to environmental conditions, such as temperature, humidity, and soil moisture content. Therefore, we conducted a field survey and analyzed ways to reduce the risk of salt deterioration in the future.

2 THE REMAINS AND EXHIBITION ROOM

The museum is located next to a river at the entrance of a valley. The remains on display consist of river stones (approximately 20 cm in diameter) and cohesive soil. The exhibition area is about 990m^2, and in the center of the room, there are remains of river stones on cohesive soil (approximately 35m long and 3.5m wide), with cohesive soil spread around it. For exhibition, the stones are exposed and the soil around them reburied with cohesive soil from the excavation. There is no air-conditioning system in the exhibition room; however, there is a louver always open to ensure natural ventilation.

3 SURVEY METHODS

Fig. 1 shows the measurement points in the room. Temperature and relative humidity were measured using a temperature/relative humidity data logger (T & D corporation, TR-72nw). The chemical potential of the soil moisture inside the remains was measured using a soil water potential sensor (METER, MPS-2). The dissolved ion in groundwater was analyzed using ion chromatography (Thermo Fisher Scientific, ICS-2000). Furthermore, to protect the remains of the river from salt deterioration, we tried several reburying methods (Fig. 2). At the Ichijodani Asakura Family Site, the remains are reburied with sand and excavated soil for protection (Condition B). Laying sandy soil with high water permeability on the exposed surface of the remains could suppress drying [1]; thus, the remains were covered with gravel (Condition C). The chemical potential of each soil layer was measured using a soil water potential sensor (METER,

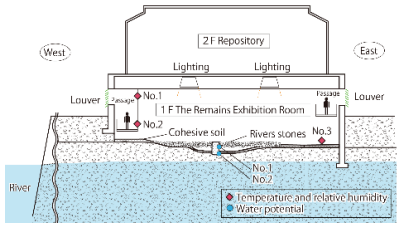

Fig. 1: Cross-sectional view of the exhibition room showing the facility and the data loggers

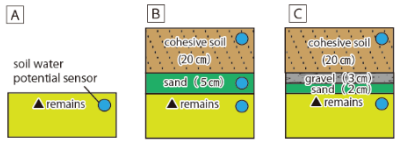

Fig. 2: Cross-sectional view of a comparison test of reburying methods of the remains made of soils: A) exposing; B) reburying with cohesive soil and sand; C) reburying with cohesive soil, gravel, and sand

TEROS21). The coefficient of permeability of the soil of the remains and that used for reburying was obtained by a constant head permeability test.

4 RESULTS AND DISCUSSION

4.1 Micro-environmental factors inside the exhibition room

In summer (Fig. 3A), the temperature inside the room was vertically stratified owing to the inflow of warm air from the louvers. The absolute humidity inside the room equaled or exceeded that of the outside air, indicating that water constantly evaporated from the surface of the soil. However, in winter (Fig. 3B), the temperature difference between upper and lower of the room was reduced, suggesting that outside air promoted vertical mixing of indoor air. The absolute humidity in the room and outside decreased, possibly accelerating evaporation from the remains.

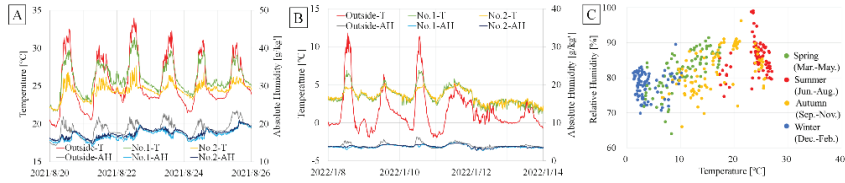

Fig. 3: Temperature and absolute humidity inside, and outside the exhibition room; A) in summer; B) in winter; C) Temperature and relative humidity of daily average inside the exhibition room

The water potential of the remains was high (Fig. 4). In particular, the upper part of the remains (Fig. 4, No. 1) appears to have been affected by precipitation. Although the water supply route needs further consideration, it was found that the remains always maintained a high-water potential.

Fig. 5 shows the results of quantitative analysis of the dissolved ions in the groundwater and river water, which are almost the same as for the river. Additionally, Fig. 3C shows that the relative humidity inside the room ranged 70%–100% during the year, which might cause precipitation of salts such as sodium chloride, magnesium chloride, sodium sulfate, and calcium sulfate on the surface of the remains.

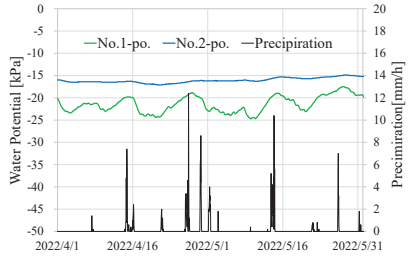

Fig. 4: Soil water potential of the remains and precipitation

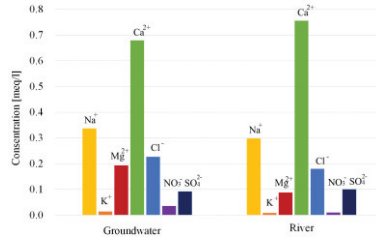

Fig. 5: Dissolved ions of the groundwater and river water

4.2 Reburying methods to reduce evaporation

To reduce salt precipitation, it is effective to suppress evaporation from the surface of the remains, which were thus covered with materials (cohesive soil, sand, and gravel) of different water permeabilities (Fig. 2 and Table 1). Fig. 6 shows the water potential of each soil layer. First, condition C is the most effective of the three in suppressing evaporation from the remains, because it maintains the highest potential. The water potential of cohesive soil B increased more than C. This is because the sand under the cohesive soil B appears to have high water retention because it contains clayey soil and grain size is not sufficient to induce capillary barrier. Conversely, although the gravel under the cohesive soil C has larger particles and higher permeability than sand, its permeability decreases due to a significant decrease of the moisture content. we posit that the water potential of cohesive soil C on the gravel decreased owing to the capillary barrier of the gravel. Therefore, covering the remains with gravel and cohesive soil is the most effective way to control water evaporation from the surface of the remains.

Table 1: Soil permeability coefficient

Sample name	Coefficient of permeability [m/s]
Remains soil	1.35E−5
Cohesive soil	3.62E−6
Sand	1.11E−4

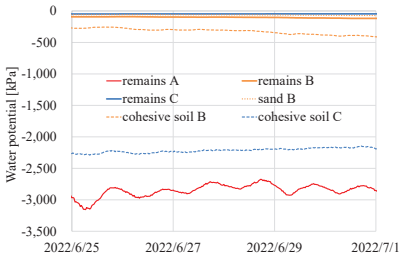

Fig. 6: Water potential of each soil layer; A) exposing; B) reburying with cohesive soil and sand; C) reburying with cohesive soil, gravel, and sand

CONCLUSIONS

We measured the environmental conditions inside an exhibition room and attempted several reburying methods to suppress salt deterioration. According to the results of our field survey, the conditions inside the exhibition room may lead to salt deterioration of the remains in the future because of microclimate changes inside the exhibition room. The main factors are as follows: (1) the temperature and humidity inside the room are influenced by ventilation from the louver; (2) as groundwater is supplied to the remains throughout the year, the soil moisture content of the surface of the remains is high. According to the results of several reburying methods, covering the surface of the remains with cohesive soil and gravel is the most effective way to suppress water evaporation from the surface of the remains. This is due to the effect of the capillary barrier because the grain size of gravel is larger than that of sand. In the future, it will be necessary to investigate ideal conditions and methods for operating exhibition rooms.

REFERENCES

[1] S. Wakiya, T. Ishizaki, Y. Kohdzuma and S. Aoki “Study on Preservation Methods of Imperial Citadel of Thang Long based on heat and moisture movement in the remains,” Proceedings of the International Conference on Conservation of Stone and Earthen Architectural Heritage, 97-104, 2014.

THREE-DIMENSIONAL MODELLING OF COASTAL TAFONI: A CASE STUDY INVESTIGATING APPLICABILITY OF LIDAR-SLAM TECHNOLOGY TO WEATHERING FEATURES

Masato Sato[1], Shingo Tomidokoro[2], Tsuyoshi Hattanji[3], and Takuro Ogura[4]

KEYWORDS

mobile laser scanner, low-cost, SLAM, SfM, Boso Peninsula

ABSTRACT

The most basic survey of weathering features is to determine their geometry, and SfM photogrammetry and laser scanning are used specifically for three-dimensional geometry surveys. The purpose of this paper is the verification of a 3D measurement method with low-cost mobile LiDAR and SLAM (Simultaneous Localization and Mapping) technology. LiDAR-SLAM is a technology that acquires point cloud data while moving, self-positioning and mapping simultaneously.

The targets for 3D modelling were tafone and honeycombed coastal cliff located on the south-east coast of the Boso Peninsula in central Japan. The point clouds were acquired using a low-cost mobile LiDAR scanner and a laptop PC. The acquired point cloud data can be verified in real time. From the acquired point cloud data, we were able to identify tafoni of about 10 cm or more in width. Those of a few centimeters were difficult to identify. The distance to the target ranged from a few meters to about 100 meters and did not affect the size of the identified tafoni. In order to represent the complex structure of weathering features, it would be necessary to optimize the modelling parameters for SLAM.

[1] National Research Institute for Earth Science and Disaster Resilience, 3-1 Tennodai, Tsukuba, Ibaraki, Japan, m-sato@bosai.go.jp

[2] Graduate School of Life and Environmental Sciences, University of Tsukuba, 1-1-1 Tennodai, Tsukuba, Ibaraki, Japan.

[3] Faculty of Life and Environmental Sciences, University of Tsukuba, 1-1-1 Tennodai, Tsukuba, Ibaraki, Japan.

[4] Graduate School of Education, Hyogo University of Teacher Education, 942-1 Shimokume, Kato, Hyogo, Japan.

1 INTRODUCTION

Geometry is one of the most fundamental elements in the study of weathered features. A variety of methods have been used for a long time, and non-destructive methods such as photo-geometry and laser scanning have been widely used in recent years [1], [2]. SLAM (Simultaneous Localization and Mapping) is a technology that acquires point cloud data while moving, self-positioning and mapping simultaneously. SLAM technology has been widely used in the field of robotics, such as self-driving. Compared to SfM (Structure from Motion) photogrammetry, SLAM can acquire 3D models in a short time and the acquired point cloud data can be referenced in real time. In this study, we attempted to acquire 3D models of the coastal tafoni using a low-cost mobile laser scanner and SLAM technology.

2 STUDY SITE AND METHOD

The targets for 3D modelling were tafone and honeycombed coastal cliff, located on the south-east coast of the Boso Peninsula in central Japan. Marine terraces and rocky coasts formed by seismic uplift are widespread in the area. Kedoura, a rocky coast consists of a shelf platform with tens of meters wide and a rock cliff over ten meters high. The cliffs are composed of Neogene sandstones and mudstones, and honeycomb features have developed mainly on the sandstone layer. Another site is Nojimazaki, which located at the southern end of the Boso Peninsula. The small cape consists of a present-day shore-platform and several uplifted marine terraces. Tafoni of various sizes are found on the shore-platform and marine terraces [3].

Figure 1: Targets of Three-dimensional modelling.

Point clouds of the weathering features were acquired using a mobile LiDAR scanner (Livox Avia) and a laptop PC. The PC was running Ubuntu OS, and FAST-LIO, a package of real-time odometry and mapping algorithms [4], was installed. If limited to LiDAR data collection without real-time SLAM, the laptop PC could be replaced by a RaspberryPi 4B, a low-cost single-board computer. The point cloud was acquired by moving parallel to the wall at a distance of about 10 m from the coastal cliff in Kedoura. In the case of Nojimazaki, we moved around the tafoni to obtain a point cloud in all directions. In each case, the data acquisition time was approximately five minutes.

At the same time, photographs of the weathering features were taken for comparison between SLAM and SfM. The point cloud data were processed using CloudCompare, a point cloud processing software. Agisoft's Metashape Pro was used for SfM processing.

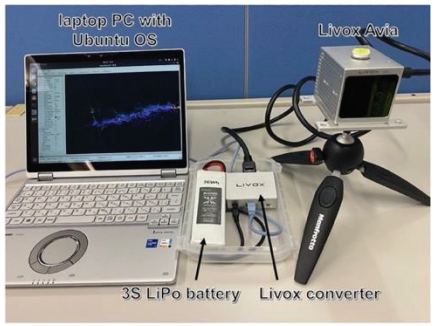

Figure 2: Low-cost mobile LiDAR scanner (Livox Avia) and equipment.

3 RESULT

Figure 3. shows acquired point clouds of the honeycombed coastal cliff, which has several steps of uplifted bench. From the acquired point cloud data, we were able to identify depressions in the sandstone layers due to honeycomb weathering (Figure 3(b)). The depths of the depressions were 10 cm or more. Honeycomb features ranging in size from a few centimeters to tens of centimeters were developed on the surface of the sandstone. These could not be identified from the point cloud. Figure 3(c) shows point clouds obtained by fixed point observation. The surface structures were less clear than in the SLAM point cloud.

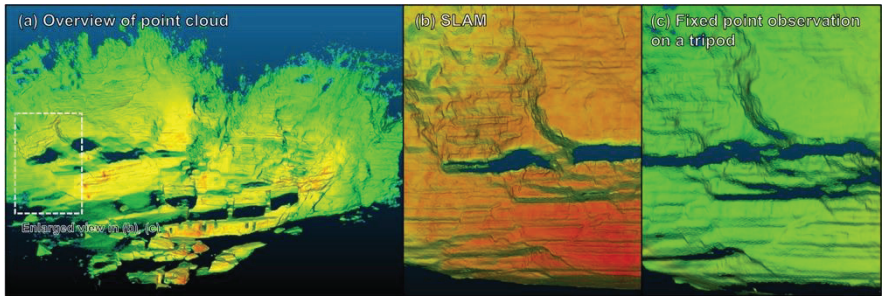

Figure 3: Acquired point clouds of honeycombed coastal cliff in Kedoura.

A comparison between SLAM and SfM is shown in Figure 4. The upper part of the tafoni is missing. This is because the photographs used for SfM were taken from the underside of the tafoni. There are three modes of LiDAR reflectance point selection. Cross-sections were generated for each mode and compared to the SfM. The profile of the first return mode was most similar to that of SfM when comparing the three modes. In the strongest return mode, there are fewer points in depressions and complex geometries. 3D model based SfM showed the shape of the tafoni more clearly. The SLAM algorithm was optimised for self-driving. In order to represent the complex structure of weathering features, it would be necessary to optimise the modelling parameters, as the range precision of the LiDAR used in this study is 2 cm at 20 m distance.

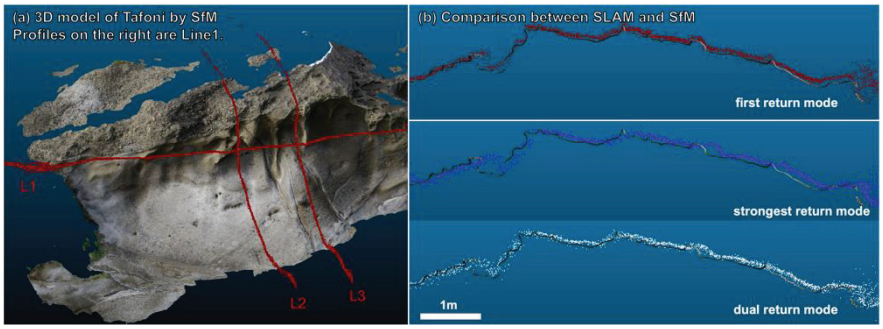

Figure 4: SLAM and SfM comparison.

4 CONCLUSION

We applied LiDAR SLAM technology and obtained a 3D point cloud of the honeycombed coastal cliff and tafoni. From the acquired point cloud data, we were able to identify tafoni of about 10 cm or more in width. Those of a few centimetres were difficult to identify. Currently, SfM is superior in terms of model clarity, but it would be possible to identify tafoni less than 10 cm wide by revising the SLAM parameter.

5 ACKNOWLEDGEMENTS

This study was funded by a JST aXis programme "Implementation experiment of volcano, earthquake and disaster monitoring technology using the latest UAV, RTKGNSS and sensors".

6 REFERENCES

[1] T. Caputo et al. “Terrestrial Laser Scanning (TLS) data for the analysis of coastal tuff cliff retreat: application to Coroglio cliff, Naples, Italy, ” *Ann. Geophysics.*, vol. 61, No. 1, 2018.

[2] L. Mol and L. Clarke, “Integrating structure-from-motion photogrammetry into rock weathering field methodologies,” Earth. Surf. Proc. Land., vol. 44, No. 13, pp. 2671–2684, 2019.

[3] Y Matsukura and N. Matsuoka, “Rates of tafoni weathering on uplifted shore platforms in Nojima-Zaki, Boso Peninsula, Japan,” Earth. Surf. Proc. Land., vol. 16, No. 1, pp. 51–56, 1991.

[4] W. Xu and F. Zhang, “Fast-lio: A fast, robust lidar-inertial odometry package by tightly-coupled iterated kalman filter,” *IEEE Robot. Autom. Lett.*, vol. 6, No. 2, pp. 3317–3324, 2021.

ISBN 978-4-600-01329-5